Geomechanical-numerical modeling of the crustal stress state of Germany

TECHNISCHE UNIVERSITÄT DARMSTADT

Genehmigte Dissertation zur Erlangung des wissenschaftlichen Grades Doktor-Ingenieur (Dr.-Ing.)

Vorgelegt von

Steffen Ahlers

Fachbereich 11, Material- und Geowissenschaften

Referent: Prof. Dr. Andreas Henk

Korreferent: Prof. Dr. Oliver Heidbach (GFZ Potsdam, TU Berlin)

Darmstadt, September 2022

Ahlers, Steffen: Geomechanical-numerical modeling of the crustal stress state of Germany
Darmstadt, Technische Universität Darmstadt
Jahr der Veröffentlichung auf TUprints: 2023
URN: urn:nbn:de:tuda-tuprints-230291
URL: https://tuprints.ulb.tu-darmstadt.de/id/eprint/23029/
Tag der mündlichen Prüfung: 02.12.2022

Statement of Authorship

I, Steffen Ahlers, hereby declare that I have, with the exception of the help that has been clearly mentioned in the thesis, completed this work on my own. I have included a list of all references used in my doctoral thesis.

_____ _____

Ort, Datum Unterschrift

Acknowledgements

This study is part of the SpannEnD project which is supported by Federal Ministry for Economic Affairs and Energy (BMWI) and managed by Projektträger Karlsruhe (PTKA) (project code: 02E11637A).

I would like to thank the entire SpannEnD team (Andreas Henk, Karsten Reiter, Tobias Hergert, Luisa Röckel, Birgit Müller, Frank Schilling, Oliver Heidbach and Sophia Morawietz) for the good cooperation over the last four years. The numerous discussions, comments and ideas have contributed a lot to this thesis; it has been a great pleasure for me!

I would especially like to thank my supervisor Andreas Henk for the excellent support and the great freedom you gave me during the work for this thesis.

Abstract

The stress state in the earth crust is an important quantity for many scientific and technical questions, e.g., seismic hazard assessment, borehole stability and underground storage. However, the level of knowledge about the recent stress field in Germany is still limited. There are basically two larger data sets available: (1) the World Stress Map (WSM) providing mainly information about the orientation of the maximum horizontal stress (S_{Hmax}) as well as the stress regime and (2) a stress magnitude database of Germany providing magnitude information about the individual components of the absolute stress tensor. However, the data are sparse, pointwise and unequally distributed. Therefore, a continuous prediction of the recent crustal stress state of Germany by linear interpolation between these data points is not suitable, in particular due to vertical and lateral inhomogeneities, e.g., mechanical properties, or faults leading to stress variations within in the crust.

The presented cumulative dissertation is part of the SpannEnD project that aims to enhance the state of knowledge of the stress field in Germany. This dissertation contains three manuscripts: two dealing with the continuous prediction of the recent crustal stress state of Germany by large scale (1000 x 1250 x 100 km^3) geomechanical-numerical models and one with the analysis of slip tendency (T_S) of faults in Germany using results of one of these models. The two geomechanical-numerical models contain units describing the present geological conditions, which are parameterized with individual rock properties. Linear elasticity is assumed and the Finite Element Method (FEM) is used to solve the equilibrium of forces. The models enable a continuous prediction of the absolute stress state based on continuum mechanics within the upper lithosphere for the entire area of Germany for the first time.

The first model presented in this cumulative dissertation contains seven units: a sedimentary unit, four laterally overlapping units of the upper crust, the lower crust and parts of the lithospheric mantle. It is calibrated against magnitudes of the minimum horizontal stress (S_{hmin}) and compared with orientations of S_{Hmax} of the WSM and some additional data. The results show an overall good fit to the orientation of S_{Hmax} with a mean of the absolute deviations of 15.6° and a median of 5.6° and to the S_{hmin} magnitudes with a mean of the absolute differences of 3.3 MPa used for calibration. However, the S_{Hmax} magnitudes show some larger differences especially too low values within the upper part of the model.

The second model is an improved version of the first model with focus on a higher stratigraphic resolution of the sedimentary unit, containing 22 units. In combination with an 18-time higher mesh resolution and an additional calibration with S_{Hmax} magnitudes the results show an overall good fit to the magnitudes of all principal stresses (S_{hmin}, S_{Hmax} and the vertical stress (S_V)) and the WSM orientation data. This is indicated by absolute differences of 0.0 MPa for S_V, 4.6 MPa for S_{hmin} and 6.4 MPa for S_{Hmax} and by a median of 0.3° and absolute differences of 11.9° for the S_{Hmax} orientations within the central part.

The third manuscript shows a possible application for the results of a large-scale geomechanical-numerical model. It is a T_S analysis of faults for Germany using the results of the first model of this

study and three different sets of faults with increasing complexities. The analysis show a good spatial agreement between the calculated T_S and earthquakes within the study area. However, the fit between the depth of earthquake occurrence and the highest predicted T_S show some discrepancies. In general, the study shows the influence of the fault geometry, the fault orientation in relation to the stress field and the crucial influence of the pore pressure.

The results of this cumulative dissertation are a step towards a better understanding of the recent stress field of Germany. By two geomechanical models providing - for the first time the 3D stress tensor - and results, which are in good agreement with different calibration and comparison data sets. However, there are still some local and few general deviations that need to be further investigated, for example, with smaller more complex models, for which the stress field of this study can be used as an initial stress state.

Zusammenfassung

Der Spannungszustand in der Erdkruste ist eine wichtige Größe für viele wissenschaftliche und technische Fragestellungen, z.B. für die Beurteilung der seismischen Gefährdung, die Bohrlochstabilität und die Untertagespeicherung. Der Kenntnisstand über das rezente Spannungsfeld in Deutschland ist jedoch noch begrenzt. Es gibt im Wesentlichen zwei größere Datensätze: (1) Die World Stress Map (WSM), die vor allem Informationen über die Orientierung der maximalen Horizontalspannung (S_{Hmax}) sowie das Spannungsregime liefert und (2) eine Spannungsmagnitudendatenbank für Deutschland, die Magnituden der einzelnen Komponenten des absoluten Spannungstensors liefert. Die Daten sind jedoch spärlich, punktuell und ungleichmäßig verteilt. Eine kontinuierliche Vorhersage des rezenten Krustenspannungszustandes Deutschlands durch lineare Interpolation zwischen diesen Datenpunkten ist deshalb und insbesondere aufgrund von vertikalen und lateralen Inhomogenitäten, z.B. mechanischen Kontrasten oder Störungen, die zu Spannungsvariationen innerhalb der Kruste führen, nicht sinnvoll.

Die vorliegende kumulative Dissertation ist Teil des SpannEnD-Projekts, das den Wissensstand über den rezenten Spannungszustand in Deutschland verbessern soll. Diese Dissertation enthält drei Manuskripte, von denen sich zwei mit der kontinuierlichen Vorhersage des rezenten Spannungszustandes Deutschlands mit Hilfe von großskaligen (1000 x 1250 x 100 km^3) geomechanisch-numerischen Modellen befassen und eines mit der Analyse der Versagenswahrscheinlichkeit (T_S) von Störungen in Deutschland unter Verwendung der Ergebnisse eines dieser Modelle. Die beiden geomechanisch-numerischen Modelle enthalten Schichten, die die heutige Geologie repräsentieren und mit individuellen Gesteinseigenschaften parametrisiert sind. Es wird lineare Elastizität angenommen und die Finite-Elemente-Methode (FEM) wird zur Lösung des Kräftegleichgewichts verwendet. Die Modelle ermöglichen erstmals eine kontinuierliche Vorhersage des absoluten Spannungszustandes auf der Basis der Kontinuumsmechanik innerhalb der oberen Lithosphäre für ganz Deutschland.

Das erste in dieser kumulativen Dissertation vorgestellte Modell enthält sieben Einheiten: Eine sedimentäre Einheit, vier lateral überlappende Einheiten der oberen Kruste, die untere Kruste und Teile des lithosphärischen Mantels. Es wird anhand der Magnituden der minimalen horizontalen Spannung (S_{hmin}) kalibriert und mit den Orientierungen von S_{Hmax} aus der WSM und einigen zusätzlichen Daten verglichen. Die Ergebnisse zeigen insgesamt eine gute Übereinstimmung mit der Orientierung von S_{Hmax} mit einem Mittelwert der absoluten Abweichungen von 15,6° und einem Median von 5,6° und mit den S_{hmin}-Magnituden (die zur Kalibrierung verwendet werden) mit einem Mittelwert der absoluten Differenzen von 3,3 MPa. Die S_{Hmax}-Magnituden weisen jedoch einige größere Abweichungen auf, insbesondere zu niedrige Werten im oberen Teil des Modells.

Das zweite Modell ist eine verbesserte Version des ersten Modell mit Fokus auf einer stratigraphischen Verfeinerung der sedimentären Einheit mit insgesamt 22 Einheiten. In Kombination mit einer 18-fach höheren Netzauflösung und der zusätzlichen Kalibrierung an S_{Hmax}-Magnituden

zeigen die Ergebnisse eine insgesamt gute Übereinstimmung mit den Magnituden aller Hauptspannungen (S_{hmin}, S_{Hmax} und der Vertikalspannung (S_V)) und den Orientierungsdaten aus der WSM. Dies zeigt sich in absoluten Differenzen von 0,0 MPa für S_V, 4,6 MPa für S_{hmin} und 6,4 MPa für S_{Hmax}, sowie in einem Median von 0,3° und absoluten Differenzen von 11,9° für die S_{Hmax}-Orientierungen innerhalb des zentralen Modellteils.

Das dritte Manuskript zeigt eine mögliche Anwendung für die Ergebnisse großräumiger geomechanisch-numerischer Modelle. Es ist eine T_S-Analyse von Störungen innerhalb Deutschlands unter Verwendung der Ergebnisse des ersten Modells dieser Studie und dreier verschiedener Störungssätze mit ansteigender Komplexität. Die Ergebnisse der Analyse zeigen eine gute räumliche Übereinstimmung zwischen der berechneten T_S und dem Auftreten von Erdbeben im Untersuchungsgebiet. Die Tiefe der Erdbebens und der höchsten vorhergesagten T_S unterscheiden sich jedoch. Im Allgemeinen zeigt die Studie den Einfluss der Störungsgeometrie, der Störungsorientierung in Bezug auf das Spannungsfeld und den entscheidenden Einfluss des Porendrucks.

Die Ergebnisse dieser kumulativen Dissertation sind ein Schritt zu einem besseren Verständnis des rezenten Spannungsfeldes in Deutschland. Durch zwei geomechanische Modelle, die zum ersten Mal den vollständigen 3D-Spannungstensor für Deutschland bereitstellen und deren Ergebnisse in guter Übereinstimmung mit verschiedenen Kalibrierungs- und Vergleichsdatensätzen sind. Es gibt jedoch noch einige lokale und wenige systematische Abweichungen, die weiter untersucht werden müssen, zum Beispiel mit kleineren, komplexeren Modellen, für die die Ergebnisse dieser Studie als initiales Spannungsfeld verwendet werden können.

Contents

List of figures

List of tables

List of abbreviations

3DD - 3D Deutschland

ALCAPA - Alps-Carpathian-Pannonian

ASZ - Albstadt Shear Zone

ATA - Armorican Terrane Assemblage

b - Load vector

BF - Black Forest

BM - Bohemian Massif

BO - Borehole breakout

BPF - Bavarian Pfahl fault

BT - Boppard thrust

c - Cohesion

CEBS - Central European Basin System

CG - Central Graben

C_{ijkl} - Stiffness tensor

DIF - Drilling induced fracture

E - Young's modulus

EEC - East European Craton

EG - Eger Graben

EI - Eifel

F - Force

FBF - Formation breakdown pressure

FCP - Fracture closure pressure

FEM - Finite Element Method

FL - Franconian Line

FM - Focal mechanisms

FMA - Average/composite focal mechanism

FMF - Formal inversion focal mechanism

FMS - Single focal mechanism

FP - Fracture potential

g - Gravitational acceleration

GG - Glückstadt Graben

HF - Hydraulic fracturing

HG - Horn Graben

HSBF - Hunsrueck Southern Border fault

HTPF - Hydraulic testing of pre-existing faults

HZ - Harz Mountains

i - Node index

ISIP - Instantaneous shut-in pressure

j - Element index

k - Ratio between vertical and horizontal stresses

K - Stiffness matrix

KTB - Kontinentale Tiefbohrung

L - Length of an element

LAB - Lithosphere-Asthenosphere-Boundary

LNF - Landshut-Neuötting fault

LRG - Lower Rhine Graben

M - Massif

MAT - Midi-Aachen thrust

MB - Molasse Basin

MDZ - Moldanubian Zone

MGCH - Mid German Crystalline High

MLF - Mariánské Lázne fault

Moho - Mohorovičić discontinuity

n - Stress regime index

NEGB - North East German Basin

NF - Normal faulting regime

NGB - North German Basin

NHBF - Northern Harz Boundary fault

OD - Odenwald

OG - Ohře Graben

OS - Osning fault

P_p - Pore pressure

P_r - Re-opening pressure

RF - Rodl fault

RG - Roer Graben

RHZ - Rhenoherzynian Zone

RMB - Rheder Moor-Blenhorst fault

RSR - Regime Stress Ratio

RT - Rheinsberg through

S - Reduced stress tensor

S_{Hazi} - Orientation of S_{Hmax}

S_{Hmax} - Maximum horizontal stress

S_{Hmean} - Mean of horizontal stresses

S_{hmin} - Minimum horizontal stress

SL - Swabian Lineament

SNB - Saar-Nahe Basin

SP - Spessart

SS - Strike-slip regime

S_V - Vertical stress

SXZ - Saxothuringian Zone

T_S - Slip tendency

TF - Thrust faulting regime

T_{Seff} - Slip tendency (effective normal stress)

T_{Snorm} - Normalized slip tendency

$T_{Snormeff}$ - Normalized slip tendency (effective normal stress)

TVD - True vertical depth

TW - Tauern Window

u - Displacement

U – Unknown stress regime

URG - Upper Rhine Graben

VB - Vogelsberg Complex

VG - Vosges

WF - Wittenberg fault

WSM - World Stress Map

z - Depth

δ - Kronecker delta

ε - Strain

λ, μ - Lame constants

μ - Coefficient of static friction

ν - Poisson's ratio

ρ - Density

σ_{ij} - Stress tensor

σ'_{ij} - Transformed stress tensor

σ_1, σ_2, σ_3 - Principal stresses (maximum, medium, minimum)

σ_{11}, σ_{22}, σ_{33} – Normal stress components

σ_{12}, σ_{13}, σ_{21}, σ_{23}, σ_{31}, σ_{32} – Shear stress components

σ_n – Absolute normal stress

σ_{neff} – Effective normal stress

τ - Shear stress

τ_f – Frictional resistance

φ - Friction angle

ϕ - Ratio of stress differences

X_i – Body forces

χ_j – Cartesian coordinates

∇ – Nabla operator

1 Introduction

1.1 Motivation

A reliable prediction of the stress state within the upper crust is of great importance for many economic and scientific issues, in particular for the exploration and operation of geothermal or hydrocarbon reservoirs (Henk, 2009; Altmann et al., 2014; Smart et al., 2014) and seismic hazard assessment. This includes for example, the wellbore stability (Bell, 2003; Azzola et al., 2019), the understanding and mitigation of induced seismicity (Segall and Fitzgerald, 1998; Gaucher et al., 2015; Walsh and Zoback, 2016; Müller et al., 2020) and the slip and dilation tendency of existing faults and fractures (Worum et al., 2004; Moeck et al., 2009a; Hettema, 2020). Furthermore, for gas storage (Konstantinovskaya et al., 2012), caverns (Hudson and Harrison, 1997a), underground mining (Brady and Brown, 2004) or tunneling (Hudson and Harrison, 1997a; Diederichs et al., 2004). In addition, the stress state is of great interest for construction and long-term safety of a high-level nuclear waste deposit (Hudson and Harrison, 1997a; IAEA, 2011). Short-term safety during the excavation of the repository itself and long-term safety until the radioactive radiation subsides. For example, about 40 % of the Swiss location identifiers are directly or indirectly influenced by the stress state (nagra, 2008). Similar proportions are found for the criteria in Belgium, France, Germany, Sweden or the United States (BGR, 2015; StandAG, 2017). Criteria whose prediction quality depends largely on the recent stress state are, for example, the integrity of the host rock due to the activation or reactivation of faults and associated fluid pathways during the excavation of the repository, possible ice loads, uplift and erosion, or changes in the regional stress field.

However, information of the crustal stress field of Germany is so far sparse and usually only locally and pointwise available. Basically two data sets are available: the World Stress Map (WSM; Heidbach et al., 2016a) mainly providing the orientation of the maximum horizontal stress (S_{Hmax}) as well as the stress regime and a stress magnitude database of Germany - providing magnitude information - of Morawietz and Reiter (2020). Therefore, the aim of this study is a continuous 3D prediction of the absolute crustal stress state of Germany. Since an interpolation between those sparse data records is not suitable due to vertical and lateral inhomegeneities, e.g., density or stiffness contrasts, or faults leading to stress variations within in the crust geomechanical-numerical models are used. These geomechanical-numerical models with increasing complexities include the geological structure, are parameterized with individual rock properties for each unit and are calibrated and validated with available stress magnitudes and orientations. This study is part of the SpannEnD project (Reiter et al., 2022), which aims to increase the knowledge of the recent upper crustal stress state in Germany, by the first magnitude database for Germany (Morawietz and Reiter, 2020; Morawietz et al., 2020), geomechanical-numerical modeling (Ahlers et al., 2021a; 2021b; 2022a; 2022b), slip tendency (T_S) analysis on faults (Röckel et al., 2022a; 2022b) and a generic study (Reiter, 2021).

1.2 Structure of the thesis

The main part of this thesis consists of three published article (Chapter 4, 5 and 6). Introductory chapters, discussion and outlook frame these chapters. The introductory chapters describing fundamentals of the crustal stress field (Chapter 2.1), available data records and former models (Chapter 2.2) and the modeling approach (Chapter 3) used for the studies in Chapter 4 and 5.

Chapter 4 contains the study of the first 3D geomechanical-numerical model (Ahlers et al., 2021a, 2021b) giving a continuous prediction of the complete 3D stress tensor for the entire area of Germany. The model contains seven units: a sedimentary unit, four lateral overlapping units of the upper crust, the lower crust and a part of the lithospheric mantle. It is calibrated with magnitudes of the minimum horizontal stress (S_{hmin}) and compared with orientations of S_{Hmax} of the WSM project. The second published model (Ahlers et al., 2022a; 2022b; Chapter 5) is a significantly improved version of the model of Ahlers et al. (2021b). An 18-time higher resolution of the mesh, a subdivision of the sedimentary unit in 15 stratigraphic subunits and an additional calibration with S_{Hmax} magnitudes improve the prediction reliability, especially within the sedimentary units. The third publication of Röckel et al. (2022b) (Chapter 6) shows a possible application for the result of such large-scale geomechanical numerical models. Since induced or natural seismicity is often linked to the reactivation of pre-existing faults (Sibson, 1985), the results of Ahlers et al. (2021b), are used to analyze the T_S of major faults in Germany. Three different fault sets, with increasing complexities, are build and then the modeled stress field - partly enhanced with pore pressure - is used to calculate the T_S.

Chapter 7 compares and discusses the results of the two models and the T_S analysis using results from former models, some extra calculations, a detailed analysis of the calibration data and some additional stress data sets. In addition, model uncertainties are discussed. Chapter 8 summarizes the results of all studies and provides an outlook on how the models could be improved and the prediction reliability of all studies could be increased. A DVD is attached to this work, which provides model geometries and results.

2 Fundamentals and state of the art

2.1 Fundamentals of the crustal stress field

2.1.1 Reduced stress tensor

The stress state at an arbitrary point - visualized as an infinitesimal cube (Figure 2.1a) - can be described by the second rank stress tensor (σ_{ij}) with three normal stress components (σ_{11}, σ_{22}, σ_{33}) and six shear stress components (σ_{12}, σ_{13}, σ_{21}, σ_{23}, σ_{31}, σ_{32}):

$$\sigma_{ij} = \begin{pmatrix} \sigma_{11} & \sigma_{21} & \sigma_{31} \\ \sigma_{12} & \sigma_{22} & \sigma_{32} \\ \sigma_{13} & \sigma_{23} & \sigma_{33} \end{pmatrix} \tag{2.1}$$

However, due to the symmetry of the matrix ($\sigma_{12} = \sigma_{21}$, $\sigma_{13} = \sigma_{31}$, $\sigma_{23} = \sigma_{32}$) only six of nine components are independent. A further simplification can be made by defining a principal stress system, i.e., through rotation of the coordinate system (Figure 2.1b: x_1, x_2, x_3 to x'_1, x'_2, x'_3). This reduces the necessary stress components to three principal stresses (σ_1, σ_2, σ_3):

$$\sigma'_{ij} = \begin{pmatrix} \sigma_1 & 0 & 0 \\ 0 & \sigma_2 & 0 \\ 0 & 0 & \sigma_3 \end{pmatrix} \tag{2.2}$$

However, for the complete description of the stress state additionally to the magnitudes of the principal stresses also their orientations (α, β, γ) are necessary. Due to the fact, that within the earths crust usually the vertical stress (S_V) - mainly derived from the weight of the overburden - is one of these principal stresses, S_{hmin} and S_{Hmax} are principal stresses, too:

$$S = \begin{pmatrix} S_V & 0 & 0 \\ 0 & S_{Hmax} & 0 \\ 0 & 0 & S_{hmin} \end{pmatrix} \tag{2.3}$$

This so-called reduced stress tensor (S; Figure 2.1c) can fully be described by four components: the magnitudes of S_V, S_{hmin} and S_{Hmax} and the orientation of one of the horizontal stresses (S_{hmin} or S_{Hmax}). However, the assumption that S_V is vertical is not always valid, e.g. high topographic gradients or salt diapirs (e.g., Schutjens et al., 2012; Carruthers et al., 2013) can tilt S_V. (Zang and Stephansson, 2010)

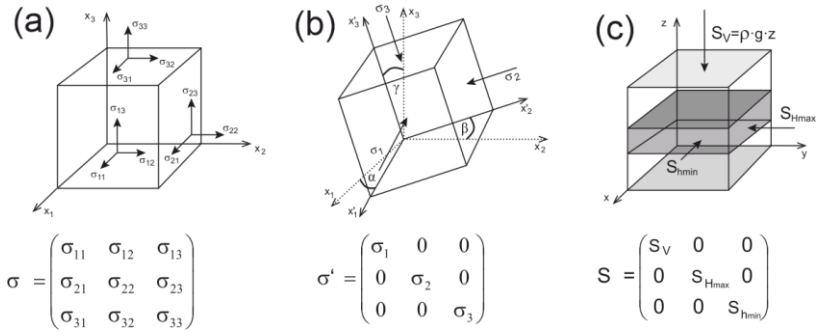

Figure 2.1: The stress tensor, based on Zang and Stephansson (2010) and Heidbach et al. (2018). a) General coordinate system, b) principal axes coordinate system, c) coordinate system for simplified definition of stress in the crust ('Reduced stress tensor').

The relative proportions between the principal stress magnitudes (S_V, S_{hmin}, S_{Hmax}) can be described simplified with three tectonic regimes (Figure 2.2): normal faulting ($S_V > S_{Hmax} > S_{hmin}$), strike-slip ($S_{Hmax} > S_V > S_{hmin}$) and thrust faulting ($S_{Hmax} > S_{hmin} > S_V$).

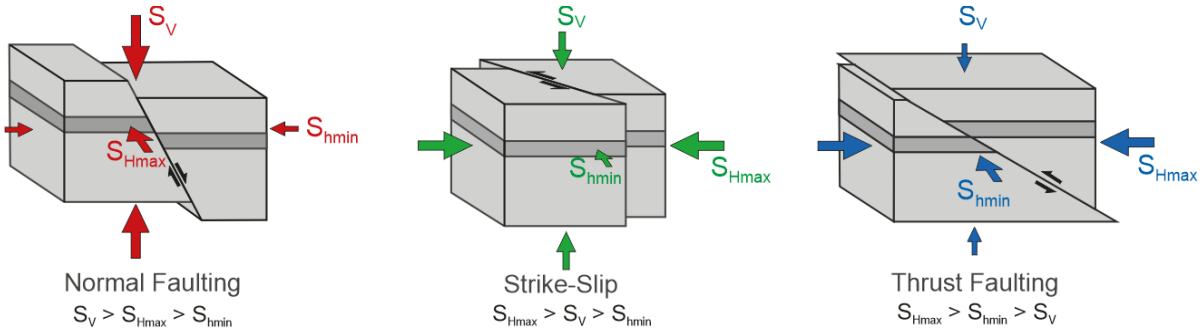

Figure 2.2: Stress regimes indicating the relative proportions between the principal stress magnitudes (S_V, S_{hmin}, S_{Hmax}). Based on Heidbach et al. (2018).

2.1.2 Stress state of the earth's crust

Assuming a perfect spherical earth with an isotropic and homogenous crust the crustal stress field would be laterally homogenous with vertically increasing magnitudes due to increasing load and confining pressure with depth, but without lateral variations and with equal horizontal stresses. Such an undisturbed stress state has been described by Sheorey (1994) as a semi-empirical function of *k*, which is defined as the ratio between the vertical and horizontal stresses:

$$k = \frac{S_{Hmean}}{S_V} = \frac{S_{Hmax} + S_{hmin}}{2S_V} \tag{2.4}$$

depending on the Young's modulus (E) and the depth (z) as:

$$k = 0.25 + 7E\left(0.001 + \frac{1}{z}\right) \tag{2.5}$$

However, the earth is not such a homogenous, isotropic body. Figure 2.3 shows in addition to calculated k-values of Sheorey (1994) a compilation of k-values from different regions, tectonic settings and lithologies. Although a clear trend is visible from higher to lower k-values with increasing depth, the k-values show a wide range, indicating inhomogeneities. Several orders of inhomogeneities, i.e., stress sources perturbating the undisturbed stress state, can be distinguished with respect to their scale of influence (e.g., Heidbach et al., 2007; Rajabi et al., 2017). First-order stress sources are plate boundary forces like ridge push or slab pull forces (Müller et al., 1992; Richardson, 1992; Zoback, 1992) which can influence the stress field over 100s to 1000s of kilometers (Figure 2.4). Second-order sources are large volume forces which can influence the stress field over 100s of kilometers, e.g., mountain chains (Tingay, 2009; Tingay et al., 2010; Pierdominici and Heidbach, 2012). More local – third- or fourth-order - stress sources can occur due to geological structures, like faults (e.g., van Mount and Suppe, 1987; Bell, 1996; Yale, 2003) or diapirs (King et al., 2012; Carruthers et al., 2013), due to detachment zones, e.g., caused by clays (Cornet and Röckel, 2012; Meixner et al., 2014) or

evaporites (Grote, 1998; Röckel and Lempp, 2003; Hillis and Nelson, 2005; Tingay et al., 2011; Hübner et al., 2015; Williams et al., 2015) or man made pressure changes (e.g., Rajabi et al., 2017).

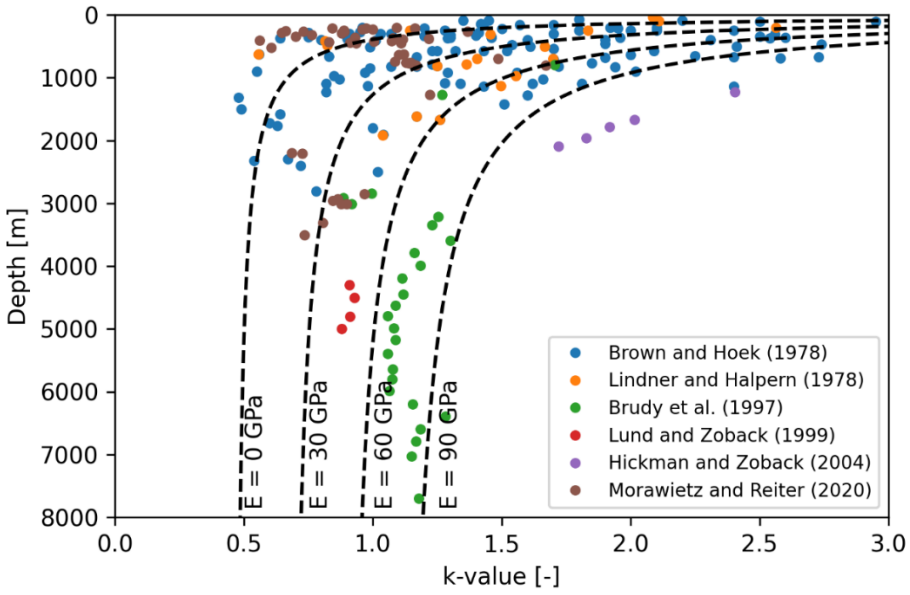

Figure 2.3: k-values versus depth from different sources and theoretical values based on Sheorey (1994). Color-coded dots show in situ k-values of Brown and Hoek (1978), Lindner and Halpern (1978), Brudy et al. (1997), Hickman and Zoback (2004), Lund and Zoback (1999) and Morawietz and Reiter (2020). Black dotted lines show the theoretical values of Sheorey (1994) for four different Young's moduli.

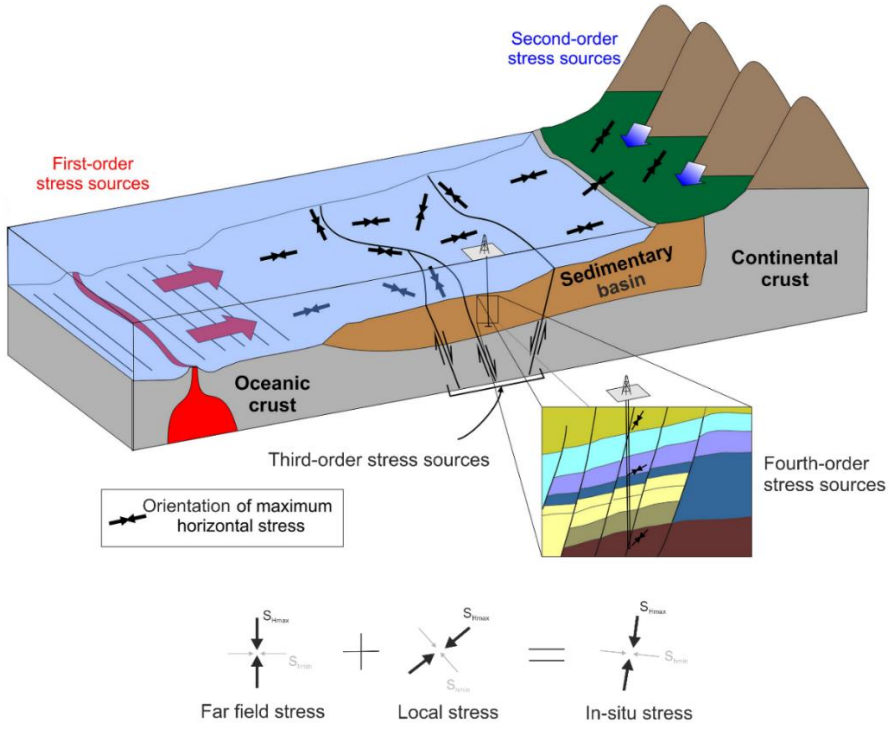

Figure 2.4: Sketch showing different orders of stress sources influencing the stress field. Based on Tingay (2009) and Rajabi et al. (2017).

However, these stress sources do not only lead to reorientations of S_{Hmax}, they can have an influence on all three principal stresses (S_V, S_{hmin}, S_{Hmax}). Accordingly, the description of the stress state using the k-value is only of limited value, since it describes the relationship between S_V and the horizontal stresses, but does not take into account the relationship between S_{hmin} and S_{Hmax}. However, a 3D representation is essential, since only the knowledge of the magnitudes of all three principal stresses allows a statement about the differential stresses or the stress regime. Furthermore, third- or fourth-order stresses, e.g. salt diapirs can tilt S_V (e.g., Schutjens et al., 2012) so that the assumption made for the reduced stress tensor is no longer valid.

2.1.3 Measurement techniques

This chapter is intended to provide a brief introduction to various measurement methods used to determine the orientation of S_{Hmax} and absolute values of the stress magnitudes. Only the most frequent measurements methods regarding the data used during this study are described. For a more detailed and comprehensive description, please refer to other textbooks or literature, like Zoback (2007), Zang and Stephansson (2010), Schmitt et al. (2012), Heidbach et al. (2016b) or Morawietz et al. (2020).

2.1.3.1 Focal mechanisms (FM)

The majority of information about the orientation of the horizontal stresses are derived from earthquake FM, especially at greater depths below 5 km. (Heidbach et al., 2018; Figure 2.8). FM describe the spatial radiation pattern of seismic waves from which the coseismic strain and thus orientation of the displacement on fault planes can be derived. Therefore, it should be noted that the stress orientation could differ from the deformation direction significantly, if the fault is not optimally oriented in the contemporary stress field. Based on the WSM three different data types of FM can be distinguished: Single (FMS), formal inversion (FMF) and average/composite (FMA). The most common methods to derive FMS are the first motion detection of p-waves and the moment tensor inversion. For the first method the first motion of p-waves – compressional or dilatational – at different seismometers are detected and projected on a theoretical sphere at the hypocenter of the earthquake. Displayed as a lower-hemisphere stereographic projection the strain axes and the type of motion can be derived. For the moment tensor inversion also the radiation pattern is used, but the projection to the hypocenter is more reliable since the waveform data is inverted to match synthetic waveforms derived from a reference model. (Barth et al., 2016)

The FMA data type includes two methods. For the average FM, the data of different earthquakes within a region are averaged. The composite FM method uses additional data from aftershocks or different earthquakes of the same fault segment to derive a FM. For the FMF several FMS from a region with an assumed homogenous stress field are combined and the orientations of the principal stress axes are derived by a formal stress inversion. Thus, this data type is the only one where the stress orientation is derived explicitly and therefore FMF are rated as A or B quality in the WSM

(Barth et al., 2016). Both, FMS and FMA data records do not consider the differences between the deformation and stress pattern. Therefore, they are in the WSM rated as maximum C. (Barth et al., 2016)

2.1.3.2 Borehole breakouts (BO) and drilling induced fractures (DIF)

Within the upper 5 km depth the most common data source to estimate the orientation of the horizontal stresses are BO (Heidbach et al., 2018, Figure 2.8). BO are stress-induced widenings of boreholes which are - within vertical wells – oriented parallel to S_{hmin} and perpendicular to S_{Hmax}, respectively (Figure 2.5). There are also methods to estimate stress ratios between S_{hmin} and S_{Hmax} from breakout dimensions, e.g., by Barton et al. (1988) or Shen (2008). However, those derived stress ratios or magnitudes should be used with caution due to several assumptions that have to be made (Schmitt et al., 2012; Morawietz et al., 2020). Another stress-induced damage indicating the stress state so-called drilling induced fractures (DIF) can occur along boreholes parallel to S_{Hmax}, i.e., perpendicular to BO (Schmitt et al., 2012; Tingay et al., 2016; Figure 2.5). DIF and BO can be observed on resistivity, acoustic, optical or density image logs (Tingay et al., 2016), BO additionally also by caliber logs (Reinecker et al., 2016).

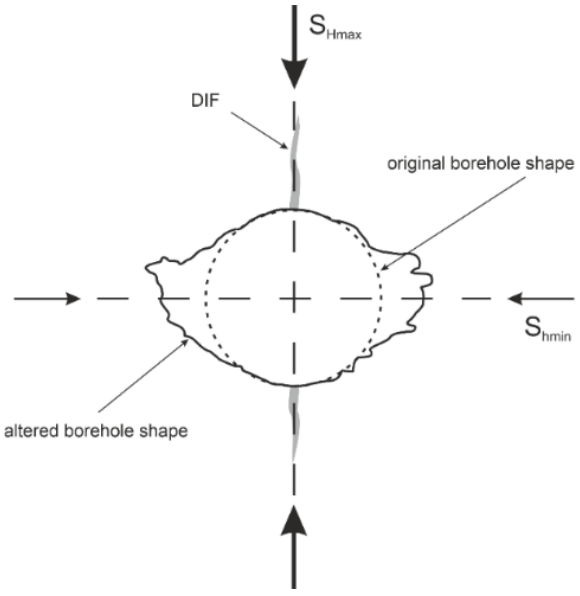

Figure 2.5: Sketch of the relationship between borehole breakouts (BO), drilling induced tensile fractures (DIF) and horizontal stresses assuming a vertical well. Based on Morin and Wilkens (2005) and Schmitt et al. (2012).

2.1.3.3 Hydraulic fracturing (HF)

HF tests are used to determine the minimum principal stress (σ_3). Therefore, assuming the reduced stress tensor S_{hmin} can directly be derived in case of a normal faulting ($S_V > S_{Hmax} > S_{hmin}$) or strike-slip ($S_{Hmax} > S_v > S_{hmin}$) regime, i.e., if σ_3 does not correspond to S_V. For a HF test a part of the borehole is

sealed by two packers and then the fluid pressure within this part is increased until rock failure occurs. Afterwards, the created fractures are usually reopened several times. Figure 2.6 shows an example of a HF test as a pressure-time diagram with one re-opening cycle.

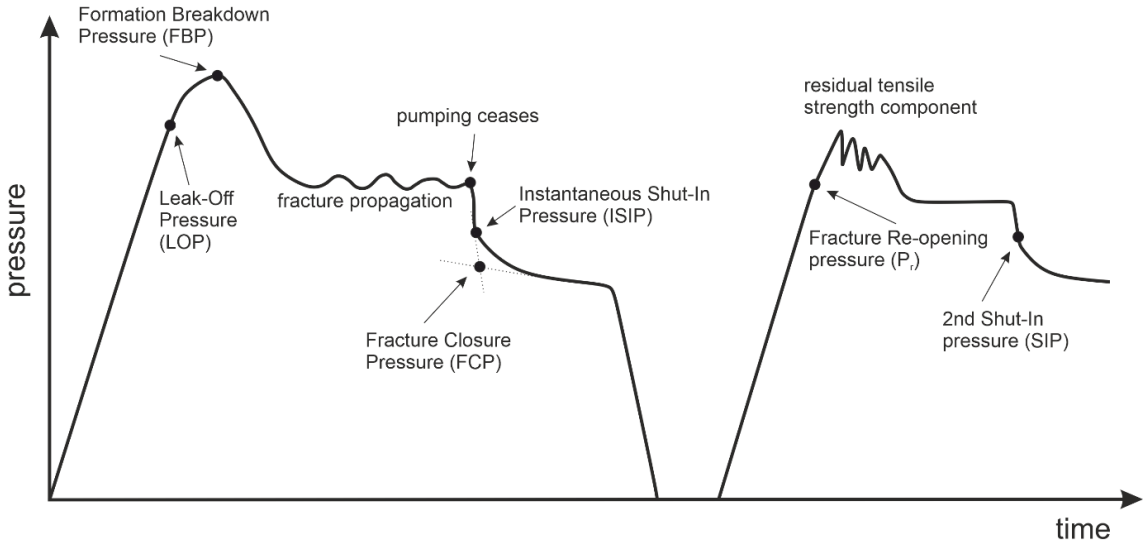

Figure 2.6: Temporal evolution of pressure in a well during a hydraulic fracturing (HF) test. Based on White et al. (2002) and Morawietz et al. (2020).

The pressure increases until a fracture is initiated, i.e., the tensile strength of the rock is exceeded. This pressure is the formation breakdown pressure (FBP). Then the pressure is kept constant and the fracture propagates. Finally, the pumping is ceased, the pressure decreases and the fracture is closed marked by the instantaneous shut-in pressure (ISIP) and followed by the fracture closure pressure (FCP). Afterwards the re-opening cycle starts by increasing the pressure again until the fracture re-opens (re-opening pressure (Pr)). The fractures propagates again and the pumping is seased. This re-opening cycles should be repeated at least once (Haimson and Cornet, 2003). Since the fracture width depends on the difference between fluid pressure and the stress acting on the fracture surface, the fluid pressure equals the stress when the aperture is zero. Therefore, the FCP and Pr can be taken as lower and upper boundaries of S_{hmin}. (Desroches et al., 2021). A direct determination of S_{Hmax} is not possible with a HF test, but S_{Hmax} can be estimated from the results.

2.1.3.4 Hydraulic testing of pre-existing fractures (HTPF)

One method with which the full stress tensor can be determined is the hydraulic testing of pre-existing fractures (HTPF) method. The basic principle is the same as for the HF method but instead of creating new fractures existing ones are used. To determine the full stress tensor, at least six tests on different oriented fractures are required. In case of a combination with a HF test, this number can be reduced to three to five. In general, such a combination of HF and HTPF tests is recommended, as it reduces the uncertainties of the measurement results. (Haimson and Cornet, 2003)

2.1.3.5 Overcoring

Another method of determining the stress state is called overcoring. In this method, a strain gauge is installed in a small diameter hole and then the rock containing the gauge is drilled over. The resulting stress relief is recorded by the gauge and the complete stress tensor as a result of the relief can be derived. (Morawietz et al., 2020)

2.2 State of knowledge of the stress field in the model area

2.2.1 Available data records

For the model area, information of the crustal stress field is available from basically two datasets. The WSM (Heidbach et al., 2016a; 2018) and a stress magnitude database of Germany (Figure 2.7; Morawietz and Reiter, 2020; Morawietz et al., 2020). The WSM project was initiated in 1986 providing quality-ranked data of the orientation of S_{Hmax} and frequently the stress regime. The latest database release 2016 contains 42.870 data records globally, of which 32.465 data records have an A to C quality, i.e., an uncertainty of up to 25°.

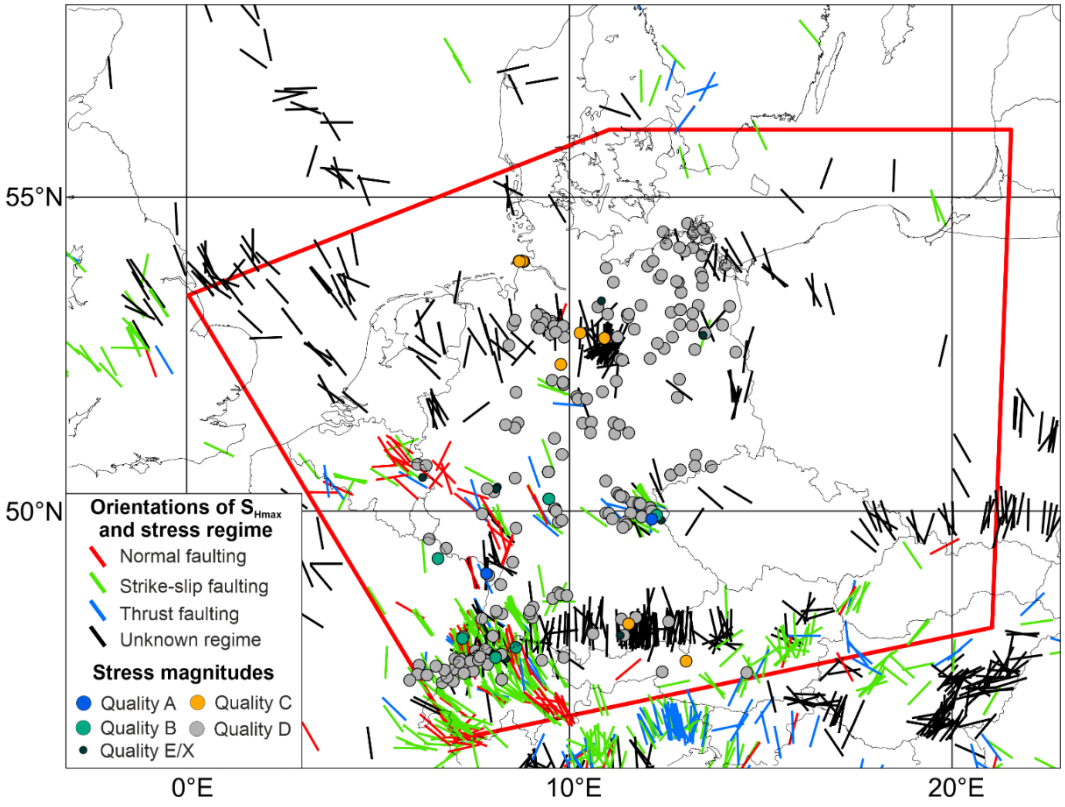

Figure 2.7: Map showing the orientation of S_{Hmax} of the WSM (Heidbach et al., 2016a) and some additional data of Levi et al. (2019) and data records of Morawietz and Reiter (2020). The orientations of S_{Hmax} are color-coded according to their stress regime. Only data of WSM quality (Heidbach et al., 2018) A to C are shown. Data records from the supra salinar of the North German Basin (NGB) are not displayed. The stress magnitudes are color-coded according to their quality. All data records of Morawietz and Reiter (2020) are shown.

Most of the data records are from FM (72 %) and BO (14 %) basically within the upper 5 km of the crust (Heidbach et al., 2018). In addition, a dataset of S_{Hmax} orientations of Levi et al. (2019) from Austria - not included in the WM database so far - is used in this study. Furthermore, for the second study (Ahlers et al., 2022a; Chapter 5), data from the supra salinar units within the North German Basin (NGB) are excluded. Since, within the NGB thick salt deposits act due to their visco-elastic properties as a mechanical decoupling horizon between the units above and below, i.e., data above and below the salt unit represents different stress fields (e.g., Grote, 1998; Röckel and Lempp, 2003; Heidbach et al., 2007). However, since the salt units of the models are not parameterized with visco-elastic properties, these data are excluded. For the study the WSM and the dataset of Levi et al. (2019) include 1094 data records with a quality of A to C and without data from the supra salinar within the NGB. These data records are mainly from FM (46 %), BO (44 %) and HF (5 %) (Figure 2.8).

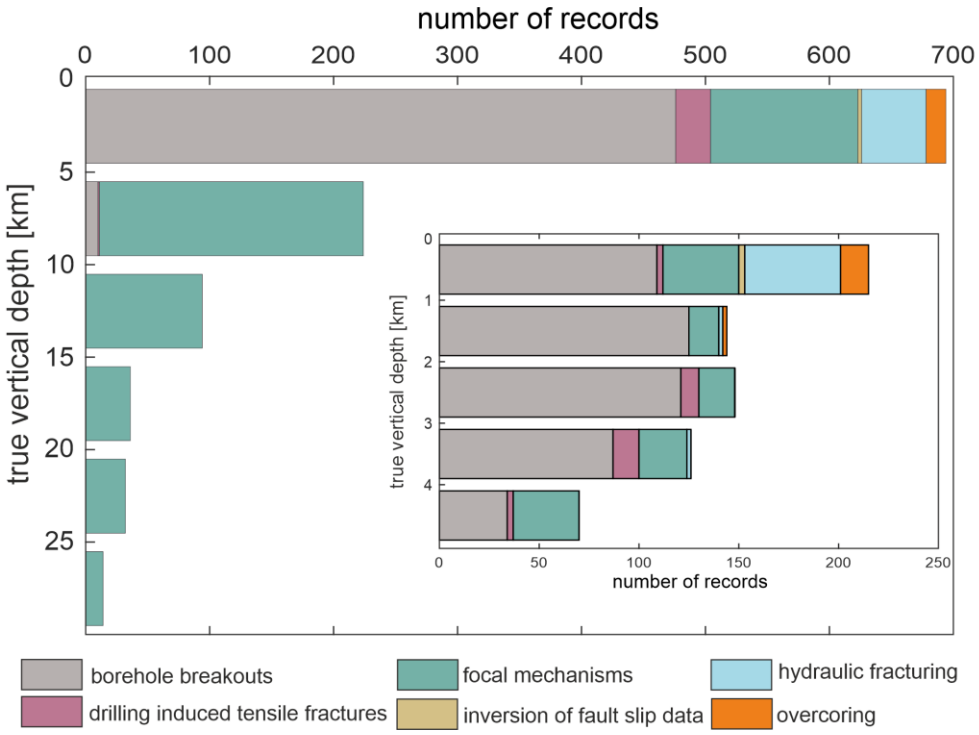

Figure 2.8: Histograms showing the frequency of data – color-coded depending on measurement techniques - for the WSM data (Heidbach et al., 2016a) and data of Levi et al. (2019) used for this study. Displayed are data records with a quality of A to C. Data from the supra salinar units of the North German Basin (NGB) are excluded. Overall 1094 data records are displayed.Large histogram: all data. Small histogram: only data from the upper 5 km true vertical depth.

However, the WSM does not provide many stress magnitude data and the quality ranking scheme does not consider them either (Heidbach et al., 2018). The magnitude database by Morawietz and Reiter (2020) provides the first comprehensive dataset for Germany and adjacent regions including a quality assessment of the data records. This database contains 568 data records, mainly from HF, HTPF and different types of borehole fluid measurements from depths up to 9 km. About half of the data records are from the upper 500 m of the crust and 20 % of the data are rated as A to C quality

only. Even though the different qualities are not related to a specific uncertainty assessment, the qualities A to C are considered reliable (Morawietz et al., 2020). Thus, for this study only these A to C ranked data records are used and additionally only data records from a depth >200 m to avoid topographic effects to ensure that S_V is vertical. In the end 73 S_{hmin} magnitudes, 56 S_{Hmax} magnitudes and 71 S_V magnitudes are used (Figure 2.9).

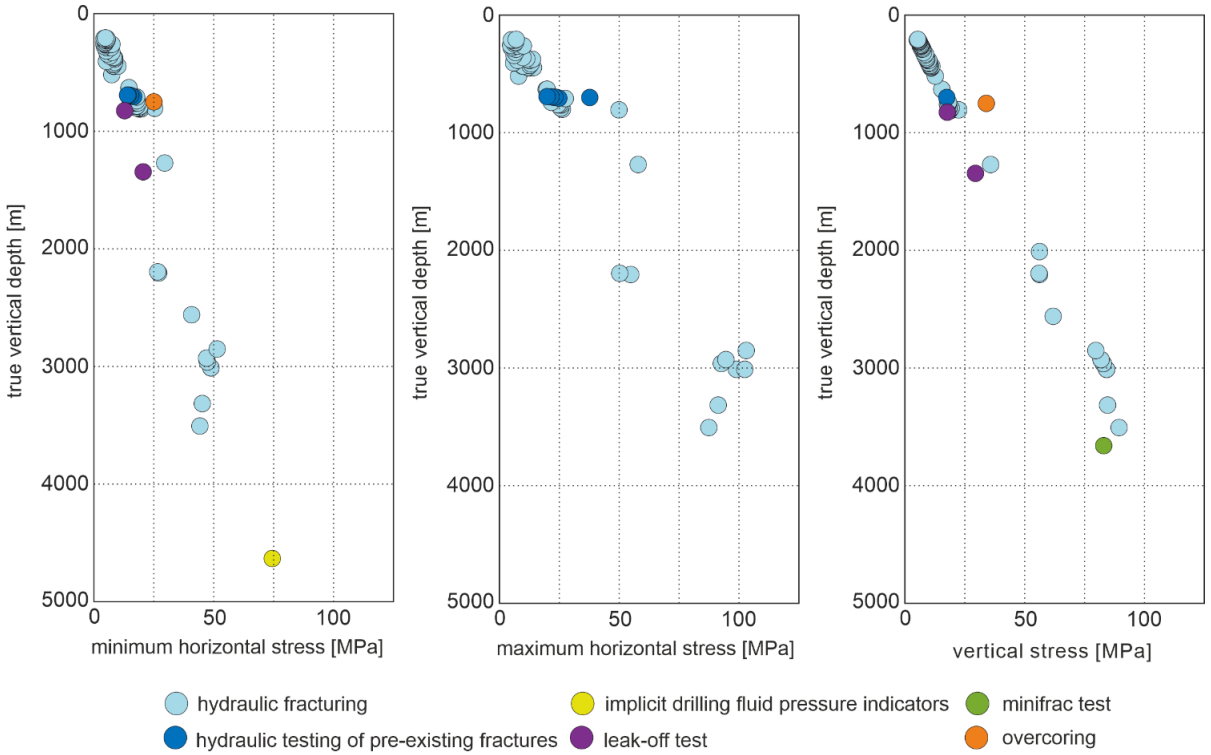

Figure 2.9: Depth distribution of stress magnitude data (S_V, S_{hmin} and S_{Hmax}) from the magnitude database of Morawietz and Reiter (2020) used. The magnitudes are color-coded regarding their measurement techniques. Shown are only data qualities A to C and from a true vertical depth of >200 m. The magnitudes of S_{hmin} and S_{Hmax} are used for calibration.

2.2.2 Former numerical models

Since the mid-1980s several large-scale numerical models have been published dealing with the stress field of the study area (Grünthal and Stromeyer, 1986, 1992; 1994; Goelke and Coblentz, 1996; Marotta et al., 2001; 2002; Kaiser et al., 2005; Jarosiński et al., 2006; Buchmann and Connolly, 2007; Cacace, 2008; Cacace et al., 2008; Warners-Ruckstuhl et al., 2013), in particular with focus on the fan like pattern of the orientation of S_{Hmax} in north Germany (Roth and Fleckenstein, 2001). Except for the model of Buchmann and Connolly (2007) of the Upper Rhine Graben (URG) all models are 2D and therefore they only provide the orientation of S_{Hmax} or sometimes averaged differential stresses, but no complete 3D stress information.

The first model has been published by Grünthal and Stromeyer (1986), followed by two updated versions of this model in 1992 and 1994 investigating the stress field of east and central Europe. The

first model (Grünthal and Stromeyer, 1986) is a 2D model with a lateral resolution of 2° and homogeneous elastic properties (E = 75 GPa, Poisson's ration (ν) = 0,23). The pattern of the stress field in northeastern Germany could be reproduced by a fixed northeastern model boundary. 1992 an updated model version has been published, still with a resolution of 2° and a mainly homogenous crust (E = 75 GPa, ν = 0,23) but including three stiffness contrasts. For the Bohemian Massif (BM) and the Adriatic Indenter a higher Young's modulus of 100 GPa is defined and for the Pannonian Basin a reduced Young's modulus of 40 GPa. The stiffness contrasts show significant effects on the stress field, e.g., due to the stiff Adriatic indenter the radial stress pattern along the Alpine chain could be reproduced. However, the stress pattern in northern Germany was again reproduced by the fixed northeastern model boundary, without any stiffness contrasts. In 1994 Grünthal and Stromeyer published a second update of their model, with additional extensional features in the Pannonian Basin and a shear zone at the northeastern margin of the BM.

Goelke and Coblentz (1996) developed a 2D model of the European part of Eurasia with homogeneous elastic properties (E = 70 GPa, ν = 0.25) and a spatial resolution of 1° which incorporates buoyancy forces due to lateral density contrasts at continental margins and topography. They predict a horizontal compression of 10-20 MPa averaged over a 100 km thick lithosphere. They could show the effect of their implemented density contrasts on the stress magnitudes, e.g., by near isotropic horizontal stresses within the Alps or in Scandinavia. However, the implemented density contrast does not lead to a significant change of the orientation of S_{Hmax}.

A model dealing with the stress field in Germany has been developed by Marotta et al. (2001) and (2002). They assume a viscous lithosphere with varying crustal thicknesses but constant lithosphere thicknesses. The model has a spatial resolution of 0.5°. Below the NGB, varying lithospheric strengths have been tested. A special feature is the usage of the convergence of the past 32 Ma (0.4 cm/y) during the Alpine collision as boundary conditions for the model, in contrast to recent plate boundary forces or displacements used in previous studies. They conclude that their boundary conditions and a stiff lithosphere below the NGB are suitable since they can reproduce the fan like pattern of S_{Hmax} in northern Germany.

In 2005 a study of Kaiser et al. investigates the stress field of northern Germany and southern Scandinavia. Their model has a lateral resolution of approximately 0.27°, a laterally homogeneous crust and lithospheric mantle, and contains 22 faults and fault zones. They assume inelastic, temperature dependent material properties. Three boundary conditions – no displacement, pure alpine compression, displacements derived from GPS measurements – are tested. They conclude that the displacements derived from GPS are the most suitable boundary conditions, in particular the influence of the movements due to the isostatic rebound in Scandinavia. Furthermore, the fault zones are interpreted as a significant impact factor.

A larger-scale study investigating the stress state of central and eastern Europe has been conducted by Jarosiński et al. (2006). Their model with a maximum lateral resolution of 50 km contains 24

tectonic units and 16 faults. They assume elastic properties with a constant Poisson's ratio of 0.25 and varying Young's moduli for each tectonic unit. They also define different lithospheric thicknesses for each unit. As boundary conditions, external tectonic forces and topographic induced stresses are applied. Several models with varying boundary forces, varying friction coefficients, varying Young's moduli and varying lithospheric thicknesses are tested. Their results predict a stress field with differential stresses of 10 to 60 MPa averaged over a 30 to 80 km thick lithosphere. From their results they conclude that the overall stress state can be explained by tectonic forces and topographic induced stresses. However, they also conclude that faults zones play a prominent role in generating second-order stresses and that stiffness contrasts have only minor effects. A conclusion which differs from all previous studies mentioned.

A study dealing with the stress state within the Central European Basin System (CEBS) has been published by Cacace et al. (2008) and Cacace (2008). They use a thin sheet approach, with varying crustal and mantle thicknesses and a lateral subdivided lower crust. Temperature dependent creep parameters are used and plate boundary displacements are defined as boundary conditions. Their results show a significant impact of the Lithosphere-Asthenosphere-Boundary (LAB) - defined as 1600 K border - due to the significant impact on their temperature dependent material properties, especially between the deep LAB of the East European Craton (EEC) and the shallower LAB of Avalonia. In addition, implemented rheological contrasts within the crust and the mantle implemented influence their results.

As mentioned, the first 3D model investigating the stress state within the study area on a regional-scale has been published by Buchmann and Connolly (2007). They presented a geomechanical-numerical model of the URG region with an average resolution of 1500 m, which decreases with increasing depth. They use a similar workflow as this study (Chapter 3.1). First, an initial stress state is established and then boundary conditions are varied until a best fit with in situ stress magnitudes is achieved. Their model predicts the orientation of S_{Hmax} and the magnitudes of all three principal stresses (S_V, S_{hmin} and S_{Hmax}). Therefore, they are also able to predict the stress regime and the fracture potential for the entire model volume.

The most recent study, dealing with the stress state of the entire Eurasian plate, has been published by Warners-Ruckstuhl et al. (2013). Their results indicate a high impact of collision forces action on the southern margin of the Eurasian plate and a minor effect of lithospheric density contrasts and mantle flow. In addition, they show that some implemented faults can influence the stress field significantly but only at a short distance compared to the scale of the model.

Three additional models which investigate factors influencing the crustal stress state that partly overlap with the model area of this study, but whose focus lies beyond it, are the stress models of the Pannonian Basin of Bada et al. (1998) and (2001) and of the Iberian Peninsula of Andeweg (2002).

A generic study of Reiter (2021) motivated by stress perturbations in Germany investigate effects of stiffness contrasts, Poisson's number variations, density contrasts and faults on the stress field.

3 Modeling Approach

For the geomechanical-numerical models, (Chapter 4 and 5) linear elasticity is assumed and thermal stresses and pore pressure effects are neglected. The Finite Element Method (FEM) is used to solve the partial differential equation of the equilibrium of forces. In this chapter, the technical procedure is presented and the equilibrium of forces and the FEM is described. The conceptual modeling approach is described in Chapter 4.3.1 and 5.2.1.

3.1 Workflow

The first step is the creation of a consistent geometry. This is done with *GOCAD* based on existing models and additional geometry data, e.g., interpreted seismic sections. The created geometry is exported as xyz-files and processed in two ways. Topography and the Mohorovičić discontinuity (Moho) are used as input data for the discretization in *HyperMesh*. All other surfaces of the geometrical model are used as input data for the subdivision of the discretized model later on. For a smooth use of the topography and Moho in *HyperMesh*, first IGES files are created with *Point Cloud to NURBS*. After imported in *HyperMesh*, the model is discretized in two parts: the crust and the lithospheric mantle. In addition, the model is extended for the setting of an initial stress state, with an underburden, a sideburden, a conic shell and contact elements connecting model and 'box'. To avoid misunderstandings, the actual 'core model' will be referred to as model in the following, the extension as box and both together as extended model. The extended model is exported as an *Abaqus* file. In the next step the crust unit of the discretized model is subdivided with the Python script *ApplePY* (Ziegler et al., 2019). During this process each element of the crust is assigned to a subunit (Upper crust, Lower crust, …) based on the surface information of the geometrical model. After this step all units are parametrized with elastic parameters (Young's modulus, Poisson's ratio) and an individual density.

The next step of the workflow is the set of an initial stress state describing an only gravity-driven, undisturbed stress state of the earth's crust. Background and assumptions are described in Chapters 4 and 5, here the focus is on the technical implementation. The three components of the box – shell, underburden, sideburden - have different functions. The conic shell - with a theoretical intersection point at the center of the earth – emulates the increasing confining pressure with increasing depth (Zang and Stephansson, 2010). The elastic properties of the underburden and sideburden are used as adjusting screws to find a best fit with calibration values derived from Sheorey (1994). Since the conic shell and the underburden and sideburden are combined with frictionless contact elements, the Young's modulus of the underburden defines the sink-in depth and therefore the confining pressure. An increase of the Young's modulus results in a reduction of the sink-in depth and a reduction of the confining pressure, respectively and a decrease of the Young's modulus increases the sink-in depth and the confining pressure, respectively. Within the sideburden the Poisson's ratio is varied to increase (higher Poisson's ratio) or decrease (lower Poisson's ratio) the influence of S_V on the horizontal stresses. In addition, the Poisson's ratios of the model units are also varied. The whole calibration process of the initial stress state is only gravity-driven.

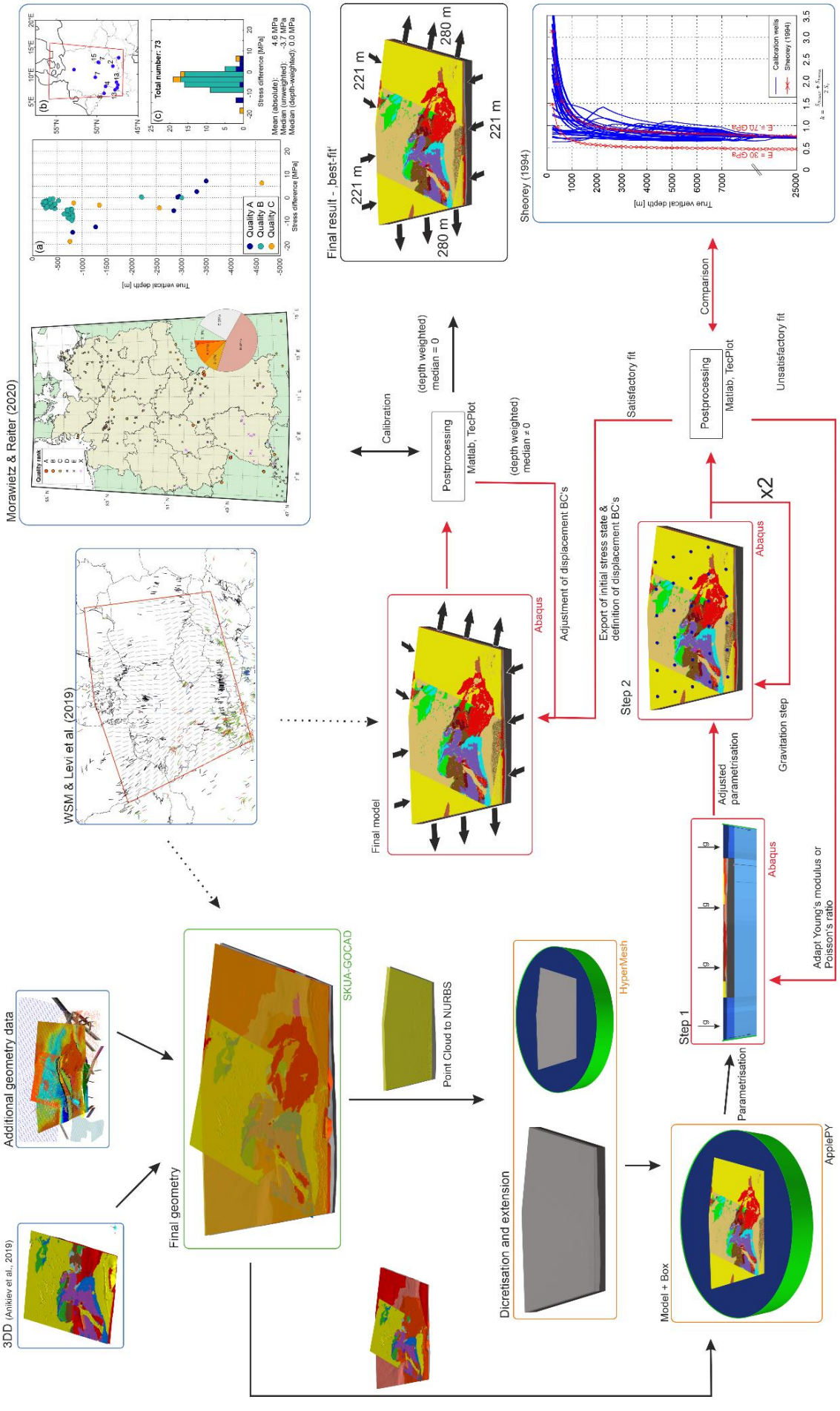

Figure 3.1: Description see next page.

Figure 3.1: Workflow of the geomechanical-numerical modeling approach used in Chapter 4 and 5. Blue framed boxes show data used for the model geometry, the calibration process and for comparison. The green framed box describes the geometry build up, orange boxes the discretization of the model and red boxes the set of the initial stress state and the calibration of the final model. The best fit is shown in the black box.

However, the gravity induced compaction changes the original geometry and the defined Poisson's ratios within the model do not correspond to reality. Therefore, a so-called gravity step is implemented in the calibration process. Hereby, the stress field of the model is used as input data for a 'new' uncompressed model without box, parameterized with 'real' material parameters. This 'new' model is then again compressed under the effect of gravity. This gravity step is repeated until the model compaction is sufficiently small (<1 m), i.e., usually two gravity steps are needed. Afterwards, the results are compared with the semi-empirical function of Sheorey (1994) and if necessary the process is repeated with adjusted parameters until a best fit is achieved.

After a satisfactory initial stress state is achieved, displacement boundary conditions are defined at the model edges. As with the previous step *Abaqus* is used as Solver and the post processing is mainly done with *Tecplot* enhanced with the GeoStress add-on (Stromeyer and Heidbach, 2017) and *Matlab*. The polarities of the boundary conditions are defined with respect to a mean orientation of S_{Hmax} derived from the WSM (details in Chapter 4.4.1 and 5.3.1) but they are not used for calibration. As calibration data magnitudes with a quality of A to C and from depths >200 m from the database of Morawietz and Reiter (2020) are used. The displacement boundary conditions are varied until a best fit with these calibration data is achieved. The magnitudes used for calibration (S_{hmin} and/or S_{Hmax}) and the decisive statistical calibration value (median or depth weighted median) varies between the two model versions developed in this study.

3.2 Linear elasticity

The equilibrium of forces (body and surface forces) to be solved can be described by the following set of partial differential equations:

$$\frac{\partial \sigma_{ij}}{\partial x_j} + \rho X_i = 0 \tag{3.1}$$

With the stress tensor (σ_{ij}), the Cartesian coordinates (χ_j), the density (ρ) and the body forces (X_i). Assuming linear elasticity, the stress tensor (σ_{ij}) can be described by Hooke's Law as a linear function of the strain tensor (ε_{kl}) and the stiffness tensor (C_{ijkl}):

$$\sigma_{ij} = C_{ijkl}\varepsilon_{kl} \tag{3.2}$$

For the isotropic case - assumed in this study - this can be simplified to:

$$\sigma_{ij} = \lambda \varepsilon_{kk}\delta_{ij} + 2\mu\varepsilon_{ij} \tag{3.3}$$

With the Kronecker delta (δ) and the Lame constants (λ) and (μ). The two Lame constants can also be described with Young's modulus (E) and Poisson's ratio (ν) as:

$$\lambda = \frac{\nu E}{(1+\nu)(1-2\nu)} \tag{3.4}$$

$$\mu = \frac{E}{2(1+\nu)} \tag{3.5}$$

Since, displacement boundary conditions are used in this study ε_{ij} must be defined in terms of displacements. Under the simplifying assumption of infinitesimal strain theory, i.e., that the displacements are small in contrast to the dimension of the structure, the strain tensor can be defined in terms of the spatial derivatives of the displacement vectors ($u_{i,j}$, $u_{j,i}$) as follows:

$$\varepsilon_{ij} = \frac{1}{2}\left(u_{i,j} + u_{j,i}\right) \tag{3.6}$$

Inserted into Hook's law (Equation 3.3), the equilibrium of forces (Equation 3.1) can be formulated in terms of Navier equations as follows (Jaeger et al., 2011):

$$(\lambda + \mu)\,\nabla(\nabla \cdot u) + \mu\nabla^2 u + X_i = 0 \tag{3.7}$$

3.3 Finite Element Method (FEM)

3.3.1 Principles

Since a global approximation function, i.e., a discrete solution of the set of partial differential equation (Equation 3.1), is almost impossible - in any case very impractical - for a large model to find, the FEM is used. For a comprehensive description of the method, please refer to textbooks, such as Merkel and Öchsner (2014) or Zienkiewicz et al. (2013).

The first step for the application of the FEM is the subdivision (discretization) of the model volume into small - in comparison to the model volume - subvolumes (finite elements). Therefore, this method is called **Finite Element Method**. The elements are defined by their vertices, so called nodes. Through the subdivision, the approximation function within an element can be assumed to be simple, e.g., linear. The next step is the assignment of material properties for each element and the definition of boundary conditions. All this information is combined in a global (g) matrix equation, with the stiffness matrix (K) describing the material behavior, the displacement vector (u) and the load vector (b):

$$b^{(g)} = K^{(g)} u^{(g)} \tag{3.8}$$

Then a so-called FEM solver is used to find a solution for this matrix equation.

3.3.2 1D example

The basic idea of the FEM in more detail can be easily described by a simple 1D example. A 1D bar subdivided into elements (j), constrained by nodes (i), fixed on the left side and a force (F) acting on the right side.

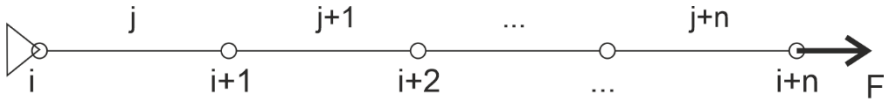

Figure 3.2: Sketch of a 1D bar subdivided into elements (j), constrained by nodes (i), fixed on the left side and a force (F) acting on the right side.

Assuming linear elastic behavior, Hooke's law in 1D is:

$$\sigma = E\varepsilon \tag{3.9}$$

The forces acting on one element can then be written as:

$$F_i = \sigma_i = E_j \frac{u_i - u_{i+1}}{L_j} \tag{3.10}$$

$$F_{i+1} = \sigma_{i+1} = E_j \frac{u_{i+1} - u_i}{L_j} \tag{3.11}$$

With the forces (F_i, F_{i+1}) - in 1D equal to the stresses (σ_i, σ_{i+1}) - acting on the nodes on the left and right side of the element, the Young's modulus (E_j) and the length (L_j) of the element and the displacements (u_i, u_{i+1}) at the nodes on the left and right side. These two equations can also be written as one in matrix form:

$$\begin{pmatrix} F_i \\ F_{i+1} \end{pmatrix} = \frac{E_j}{L_j} \begin{pmatrix} 1 & -1 \\ -1 & 1 \end{pmatrix} \begin{pmatrix} u_i \\ u_{i+1} \end{pmatrix} \tag{3.12}$$

The ratio between the material properties (in this case E) can also be written as:

$$k_j = \frac{E_j}{L_j} \tag{3.13}$$

Inserted into Equation 3.12:

$$\begin{pmatrix} F_i \\ F_{i+1} \end{pmatrix} = \begin{pmatrix} k_j & -k_j \\ -k_j & k_j \end{pmatrix} \begin{pmatrix} u_i \\ u_{i+1} \end{pmatrix} \tag{3.14}$$

This matrix containing the material properties and describing the mechanical behavior is the stiffness matrix (K):

$$K^{(j)} = \begin{pmatrix} k_j & -k_j \\ -k_j & k_j \end{pmatrix} \tag{3.15}$$

Equation 3.12 or 3.14 can therefore also be written as:

$$b^{(j)} = K^{(j)} u^{(j)} \tag{3.16}$$

The matrix equations for each single element (j) can then be combined in a global **finite element** matrix equation:

$$\begin{pmatrix} F_j \\ \vdots \\ F_{j+n} \end{pmatrix} = \begin{pmatrix} u_j \\ \vdots \\ u_{j+n} \end{pmatrix} \begin{pmatrix} k_j & -k_j & & & & 0 \\ -k_j & k_j + k_{j+1} & -k_{j+1} & & & \\ & -k_{j+1} & k_{j+1} + k_{j+2} & \ddots & & \\ & & \ddots & \ddots & & \\ & & & & k_{j+n-1} + k_{j+n} & -k_{j+n} \\ 0 & & & & -k_{j+n} & k_{j+n} \end{pmatrix} \tag{3.17}$$

In a more generalized form, the combination is displayed in Figure 3.3.

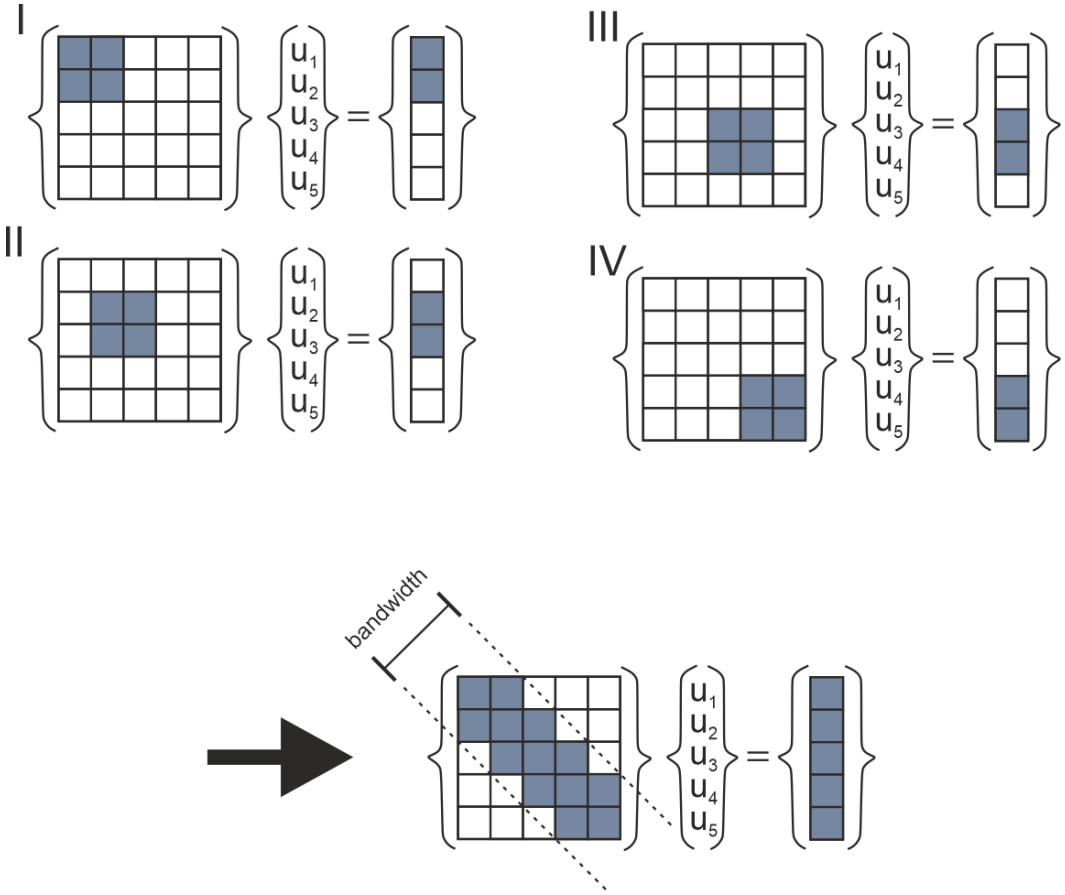

Figure 3.3: Sketch of the combination of four matrices of individual elements (I to IV) into a global finite element matrix similar to Equation 3.17. Based on Zienkiewicz et al. (2013).

4 3D crustal stress state of Germany according to a data-calibrated geomechanical model

Steffen Ahlers[1], Andreas Henk[1], Tobias Hergert[1], Karsten Reiter[1], Birgit Müller[2], Luisa Röckel[2], Oliver Heidbach[3,4], Sophia Morawietz[3,4], Magdalena Scheck-Wenderoth[5,6], Denis Anikiev[5]

[1]Engineering Geology, Institute of Applied Geosciences, TU Darmstadt, 64287 Darmstadt, Germany

[2]Technical Petrophysics, Institute of Applied Geosciences, KIT, 76131 Karlsruhe, Germany

[3]Seismic Hazard and Risk Dynamics, GFZ German Research Centre for Geosciences, 14473 Potsdam, Germany

[4]Institute for Applied Geosciences, TU Berlin, 10587 Berlin, Germany

[5]Basin Modelling, GFZ German Research Centre for Geosciences, 14473 Potsdam, Germany

[6]Department of Geology, Geochemistry of Petroleum and Coal, Faculty of Georesources and Material Engineering, RWTH Aachen University, Aachen, Germany

Published in Solid Earth (https://doi.org/10.5194/se-12-1777-2021)

Received: 30 November 2020, Accepted: 7 July 2021, Published: 11 August 2021

Abstract

The contemporary stress state in the upper crust is of great interest for geotechnical applications and basic research alike. However, our knowledge of the crustal stress field from the data perspective is limited. For Germany basically two datasets are available: orientations of the maximum horizontal stress (S_{Hmax}) and the stress regime as part of the World Stress Map (WSM) database as well as a complementary compilation of stress magnitude data of Germany and adjacent regions. However, these datasets only provide pointwise, incomplete and heterogeneous information of the 3D stress tensor. Here, we present a geomechanical-numerical model that provides a continuous description of the contemporary 3D crustal stress state on a regional scale for Germany. The model covers an area of about 1000 x 1250 km² and extends to a depth of 100 km containing seven units, with specific material properties (density and elastic rock properties) and laterally varying thicknesses: a sedimentary unit, four different units of the upper crust, the lower crust and the lithospheric mantle. The model is calibrated by the two datasets to achieve a best fit regarding the S_{Hmax} orientations and the minimum horizontal stress magnitudes (S_{hmin}). The modeled orientations of S_{Hmax} are almost entirely within the uncertainties of the WSM data used and the S_{hmin} magnitudes fit to various datasets well. Only the S_{Hmax} magnitudes show locally significant deviations, primarily indicating values that are too low in the lower part of the model. The model is open for further refinements regarding model

geometry, e.g., additional layers with laterally varying material properties, and incorporation of future stress measurements. In addition, it can provide the initial stress state for local geomechanical models with a higher resolution.

4.1 Introduction

Knowledge about the stress state in the upper crust is of great importance for many economic and scientific questions. Some examples are wellbore stability (Bell, 2003; Kristiansen, 2004), operation and stimulation of hydrocarbon and geothermal reservoirs (Altmann et al., 2014; Azzola et al., 2019; Henk, 2009; Smart et al., 2014), slip and dilation tendency of existing faults and fractures (Hettema, 2020; Konstantinovskaya et al., 2012), underground mining (Brady and Brown, 2004) and deep tunneling (Diederichs et al., 2004). Furthermore, it plays a decisive role in the search for a disposal site for high-level radioactive waste, since it is crucial for the short and long-term safety of a possible repository (StandAG, 2017; nagra, 2008; BGR, 2015). For all these applications the contemporary stress state is a key parameter, and thus the quantification of the complete 3D stress tensor is essential.

However, from the data perspective, our knowledge of the stress state in western central Europe is limited in particular regarding stress magnitude information. Public stress information is provided by the World Stress Map (WSM) project, which supplies a global database of the orientation of the maximum horizontal stress (S_{Hmax}) and the stress regime (Heidbach et al., 2016a) and by a compilation of stress magnitude data for Germany and adjacent regions of Morawietz and Reiter (2020). However, these two datasets contain only pointwise information, which is incomplete as only a subset of the stress tensor components is provided and their spatial distribution is sparse and irregular (Figure 4.1a).

To provide a continuous description of the 3D stress tensor in the upper crust on a regional scale, we developed the first 3D geomechanical model covering Germany (Figure 4.1). Our model comprises seven units, with specific material properties and laterally varying thicknesses: a sedimentary unit, four different units of the upper crust, the lower crust and the lithospheric mantle. The finite element method (FEM) is used to solve the partial differential equation which describes the equilibrium of body and surface forces within an inhomogeneous medium. Our input parameters are density and elastic material properties (Young's modulus and Poisson's ratio). The model is calibrated using appropriate initial conditions and displacement boundary conditions to find a best fit with respect to the stress orientation and magnitude datasets described above. This modeling approach has been used for a wide range of scales and different tectonic settings (Buchmann and Connolly, 2007; Heidbach et al., 2014; Hergert and Heidbach, 2011; Hergert et al., 2015; Reiter and Heidbach, 2014).

4.2 Fundamentals and state of the art

4.2.1 Geology and tectonic setting of the study area

The crustal and lithospheric structure in the model domain reflects the complex geodynamic evolution of central Europe since Precambrian times (McCann, 2008; Meschede and Warr, 2019) (Figure 4.1c and d). The north-eastern part of the study area belongs to the cratonic unit of Baltica and, more specifically, the East European Craton (EEC). This unit consists mainly of high-grade magmatic and metamorphic rocks of Precambrian and early Paleozoic age. Crustal thickness in the area is about 50 km, and a thick mantle lithosphere down to depths of 200 km has been observed (Mazur et al., 2015). The EEC is separated from the Avalonia microplate to the south-west by the Tornquist Suture and the Thor Suture, respectively (e.g., Linnemann et al., 2008, and various references therein). At this boundary, a sharp transition to the significantly thinner crustal and lithospheric thicknesses typical for Paleozoic and Mesozoic Europe can be observed (Ziegler and Dèzes, 2006). Western Baltica and eastern Avalonia got into contact during closure of the Tornquist Ocean during Ordovician to Silurian times and the Caledonian orogeny, respectively. At this stage, Laurussia (composed of Laurentia, Baltica and Avalonia) was formed, whose continental crust makes up the northern and eastern part of the study area.

The central part of the model domain comprises the southern part of Avalonia as well as Armorica – microplates and terrane assemblages - which collided during the Variscan orogeny in Late Paleozoic times (Franke, 1989, 2006; Meschede and Warr, 2019). The low-grade metamorphic rocks of the Rhenohercynian Zone (sensu Kossmat, 1927) represent passive margin sediments which were deposited on thinned crust of south-eastern Avalonia. South-eastward-directed subduction and closure of the Rheic Ocean led to the formation of an active margin at the northern rim of Armorica, which nowadays comprises the medium-grade metamorphic and magmatic rocks of the so-called Mid German Crystalline High (Oncken, 1997). Further to the south, the Saxothuringian and Moldanubian Zone represent the remnants of the internal zone of the Variscan orogen with medium- to high-grade metamorphic rocks and abundant granitoids presently exposed at surface. Crustal thickness in this part of the model domain and outside the areas affected by Cenozoic rifting and mountain building is typically on the order of 30 km (Ziegler and Dèzes, 2006). The late Cretaceous to Paleogene evolution was influenced by NE-directed Africa-Iberia-Europe convergence which led to intraplate contraction and inversion of NW-SE-striking structural elements (Kley and Voigt, 2008). The final stage of this phase coincides with W-E to NW-SE directed extension and the onset of rifting in the Upper Rhine Graben (URG) and Eger Graben, among others (Kley et al., 2008).

The southernmost parts of the study area are located in the so-called ALCAPA (Alps–Carpathians–Pannonian) unit or terrane (e.g., Brückl et al., 2010; Schmid et al., 2004). Its geodynamic evolution is closely related to the collision between Europe and the Adriatic-Apulian microplate leading to the Alpine orogeny. Since Eocene times, its northern foreland has been characterized by N-S to NW-SE directed compression and thrusting, respectively (Reicherter et al., 2008).

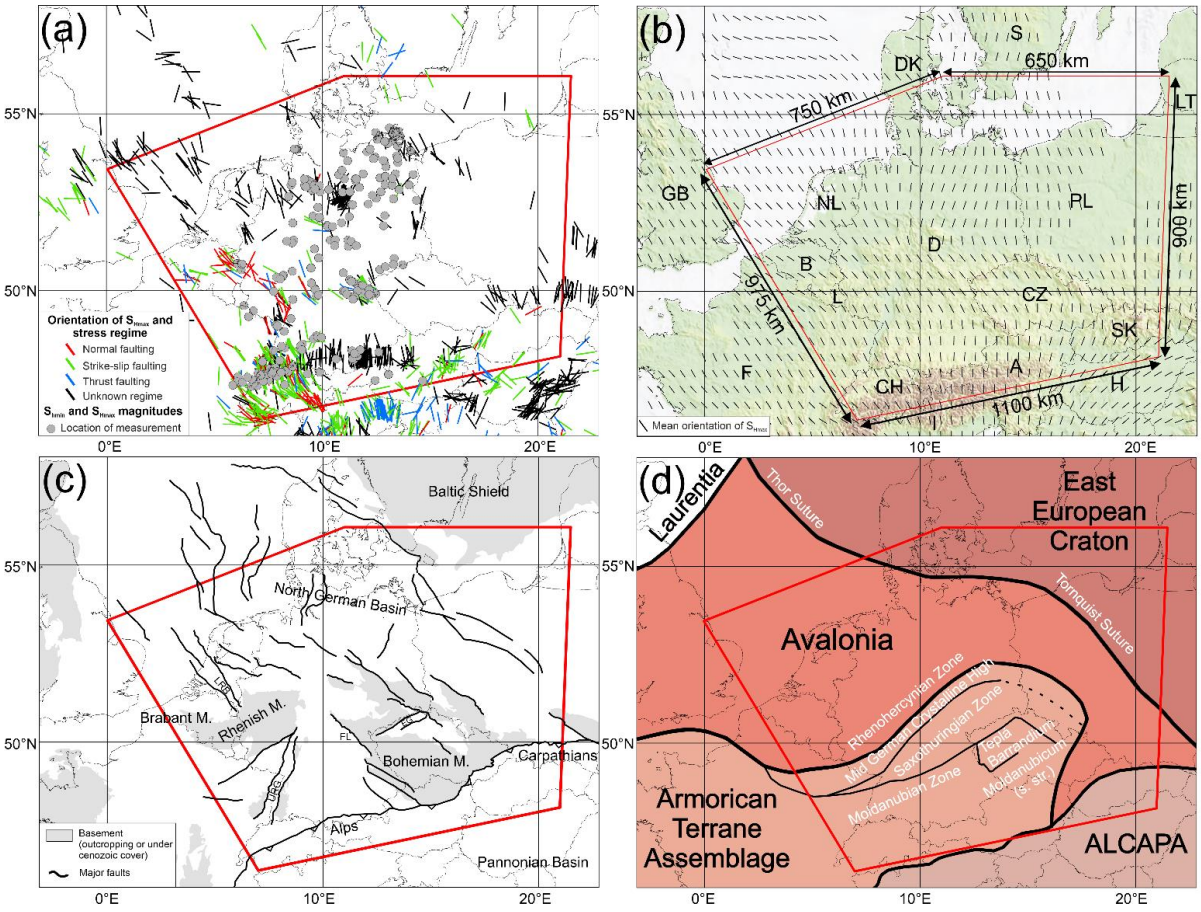

Figure 4.1: Maps of western central Europe. The red polygon indicates the model area. (a) Overview of calibration data used. Color-coded lines indicate the orientation of S_{Hmax} and the stress regime of the WSM (Heidbach et al., 2016a) and additional data of Levi et al. (2019). Grey dots show the positions of stress magnitude data of Morawietz and Reiter (2020). (b) Topography and mean S_{Hmax} orientations on a regular 0.5° grid derived from the WSM. Each grid point requires at least 10 data points within a fixed search radius of 200 km (details in Chapter 4.1). The topography is based on Smith and Sandwell (1997). (c) Tectonic framework of the model area based on Asch (2005) and Kley and Voigt (2008). EG - Eger Graben, FL - Franconian Line, LRB - Lower Rhine Basin, M - Massif, URG - Upper Rhine Graben. (d) Overview of the crustal units in central Europe (modified after Kroner et al., 2010 and Brückl et al., 2010). Black titles show tectonic units and white titles sutures and Variscan units.

4.2.2 Basics of the crustal stress state

The stress state at a given point can be described by a second rank tensor (Figure 4.2a) with the pascal (1 Pa = N m^{-2}) as the basic unit. Due to its symmetry properties, only six out of nine components are independent of each other (e.g., Jaeger et al., 2011). In the principal axis system, the off-diagonal components vanish and the remaining three components are the principal stresses σ_1, σ_2 and σ_3. Their orientations and magnitudes describe the absolute stress state (Figure 4.2b). Assuming that the vertical stress (S_V) is one of the three principal stresses (Figure 4.2c), the orientation of this so-called reduced stress tensor is determined by the orientation of S_{Hmax}. Given that S_V can be approximated by

depth and density of the overburden, the remaining unknowns are the magnitudes of S_{Hmax} and the minimum horizontal stress (S_{hmin}).

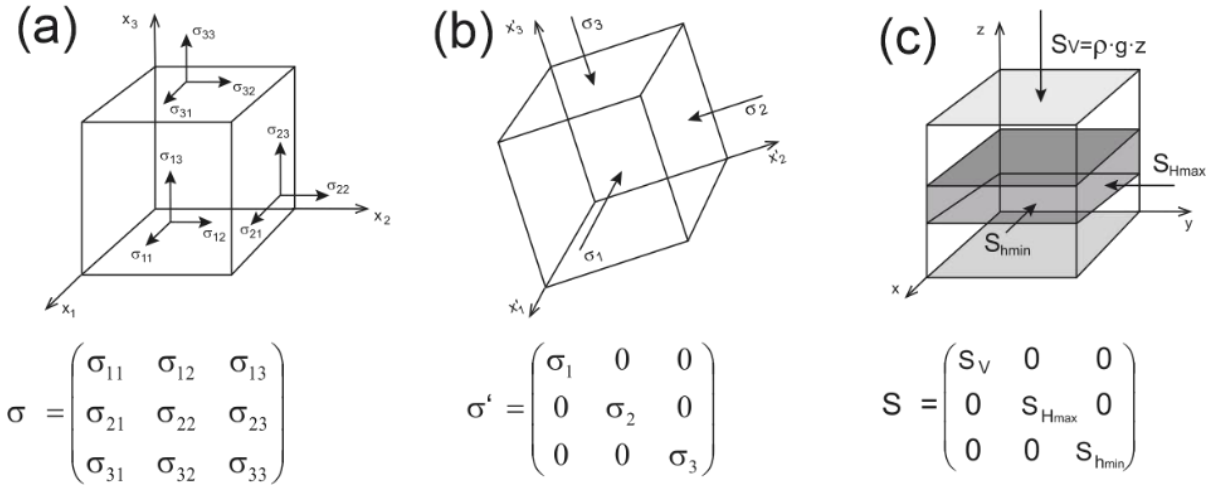

Figure 4.2: (a) The nine components of the stress tensor define the stress state at an arbitrary point and enable to compute the stress vector on any surface through that point. To describe the stress tensor components an infinitely small cube with uniform surfaces is used. (b) Due to the conservation of momentum, the stress tensor is symmetric and thus a coordinate system exists where shear stresses vanish along the faces of the cube. In this principal axis system, the remaining three stresses are the principal stresses. (c) Assuming that the vertical stress (the overburden) in the Earth crust $S_V = g \cdot \rho \cdot z$ is a principal stress (g is gravitational acceleration, ρ is the rock density, z is depth), the two horizontal stresses S_{hmin} and S_{Hmax}, the minimum and maximum horizontal stress, respectively, are principal stresses as well. This so-called reduced stress tensor is fully determined with four components: the S_{Hmax} orientation and the magnitudes of S_V, S_{hmin} and S_{Hmax}. (Heidbach et al., 2018)

The stress state of the continental crust is influenced by stress sources on different scales from several meters up to several thousand kilometers: first-order stress sources (>100 km) related to plate boundary forces, e.g., ridge push or slab pull, second-order stress sources (~100 km) related to large volume forces, e.g., lithospheric flexure due to mountain ranges or deglaciation and third-order stress sources (< 100 km) related to local density or stiffness contrasts, e.g., faults or diapirs. Second- and third-order stress sources are able to disturb the overall stress orientation trend from regional through local to reservoir scale (Heidbach et al., 2007).

4.2.3 Data compilation of stress tensor components

The orientation of the stress tensor in the Earth's crust is provided by the WSM database, which is a global compilation providing data on the S_{Hmax} orientation and the stress regime (Heidbach et al., 2016a). This stress information is derived from a variety of methods, primarily earthquake focal

mechanism solutions, borehole breakouts and drilling-induced tensile fractures (from borehole image or multi-arm caliper log data), in situ stress measurements (overcoring or hydraulic fracturing) and geologic indicators, such as fault slip and volcanic vent alignment (Amadei and Stephansson, 1997; Ljunggren et al., 2003; Schmitt et al., 2012). The stress information in the WSM database is compiled in a standardized format and quality-ranked for reliability and comparability on a global scale (Heidbach et al., 2010; Zoback, 1992). For Germany and adjacent regions, the S_{Hmax} orientations have been re-evaluated recently (Reiter et al., 2016; Reiter et al., 2015). The new data have been integrated in the latest WSM database release (Heidbach et al., 2016a). For stress magnitude data, Morawietz et al. (2020) published a publicly accessible database with 568 data records including a quality assessment of the data for Germany and adjacent regions. These two datasets (Figure 4.1a) - the S_{Hmax} orientation of the WSM with some additional data of Levi et al. (2019) and the stress magnitude database (Morawietz and Reiter, 2020) - are used to calibrate the geomechanical model.

4.2.4 Previous models

Modeling the contemporary crustal stress in western central Europe has been addressed by various authors since the mid-1980s. However, except the model of Buchmann and Connolly (2007), who provide a 3D model of the broader URG, all models are 2D and with a strong emphasis on the S_{Hmax} orientation and little regarding the stress magnitudes. Table 4.1 gives a short overview of their key technical characteristics. If several model versions are published by one author, the most current one is listed. In general, different plastic and elastic material properties have been tested so far and also various boundary conditions have been applied. For a detailed overview we refer to, e.g., Cacace (2008), Heidbach et al. (2007) or Jarosiński et al. (2006).

The results indicate different main factors influencing the contemporary stress state. The majority of the studies have found lateral stiffness contrasts in the lithosphere, such as the Bohemian Massif, the Elbe Fault Zone or the Avalonia-EEC boundary (Cacace, 2008; Grünthal and Stromeyer, 1994; Jarosiński et al., 2006; Marotta et al., 2002) and isostatic effects (Bada et al., 2001; Kaiser et al., 2005; Jarosiński et al., 2006) to be the main cause of stress perturbations. In addition, faults or fault zones are held responsible for third- or second-order stresses, respectively (Jarosiński et al., 2006; Kaiser et al., 2005). An indirect influence of the depth of the asthenosphere lithosphere boundary (LAB) and the resulting temperature contrasts and changed mechanical properties are described by Cacace (2008).

Table 4.1: Overview of regional-scale stress models within the model area. If several model versions are published, the most current one is listed. The (X) is used for Buchmann and Connolly (2007), since the boundary conditions are not derived from the plate boundary forces, but still represent them.

Author	Model area	Model dimension	Material law		Boundary and initial conditions		Variations			
			elastic	plastic	plate boundaryforces	Gravity-induced forces	density	friction coefficient (faults)	thickness	plastic or elastic material parameters
Andeweg, 2002	European part of Eurasia	2D	X			X	X		X	
Bada et al., 2001	Pannonian Basin and surrounding orogens	2D	X		X					X
Buchmann and Connolly, 2007	Upper Rhine Graben	3D	X	X	(X)		X			X
Cacace, 2008	Central European Basin System	2D, thin sheet		X	X					X
Goelke and Coblentz, 1996	European part of Eurasia	2D	X		X		X			
Grünthal and Stromeyer, 1994	East and central Eurasia	2D	X		X					X
Jarosiński et al., 2006	East and central Europe	2D	X			X		X		X
Kaiser et al., 2005	Northern Germany and southern Scandinavia	2D, thin plate		X	X	X		X		X
Marotta et al., 2002	Germany	2D, thin sheet		X	X				X	X
Warners-Ruckstuhl et al., 2013	Eurasia	2D, thin shell	X		X		X	X	X	

4.3 Model setup

4.3.1 Conceptual modeling approach

To model the contemporary 3D stress field of the upper crust we assume linear elasticity and neglect thermal stresses and pore pressure effects. With these assumptions, the partial differential equation of the equilibrium of forces has to be solved (Jaeger et al., 2007). The two contributing forces are volume forces from gravitational acceleration and surfaces forces that are mainly attributed to plate tectonics.

The latter are key drivers for the tectonic stress that we observe and they are parameterized with displacement boundary conditions that are chosen in a way that the resulting stresses deliver a best fit with respect to the model-independent stress data. Although these displacement boundary conditions are mainly representing the tectonic stresses, they are not derived from these. Accordingly, our results do not allow any conclusions regarding the sources of crustal stress in the model area. This process is called model calibration, which can also be used to estimate model uncertainties by means of standard deviation (Ziegler et al., 2016; Ziegler and Heidbach, 2020). The technical procedure is presented in Figure 4.3 with a schematic general workflow. The individual text boxes are color-coded indicating the four major steps.

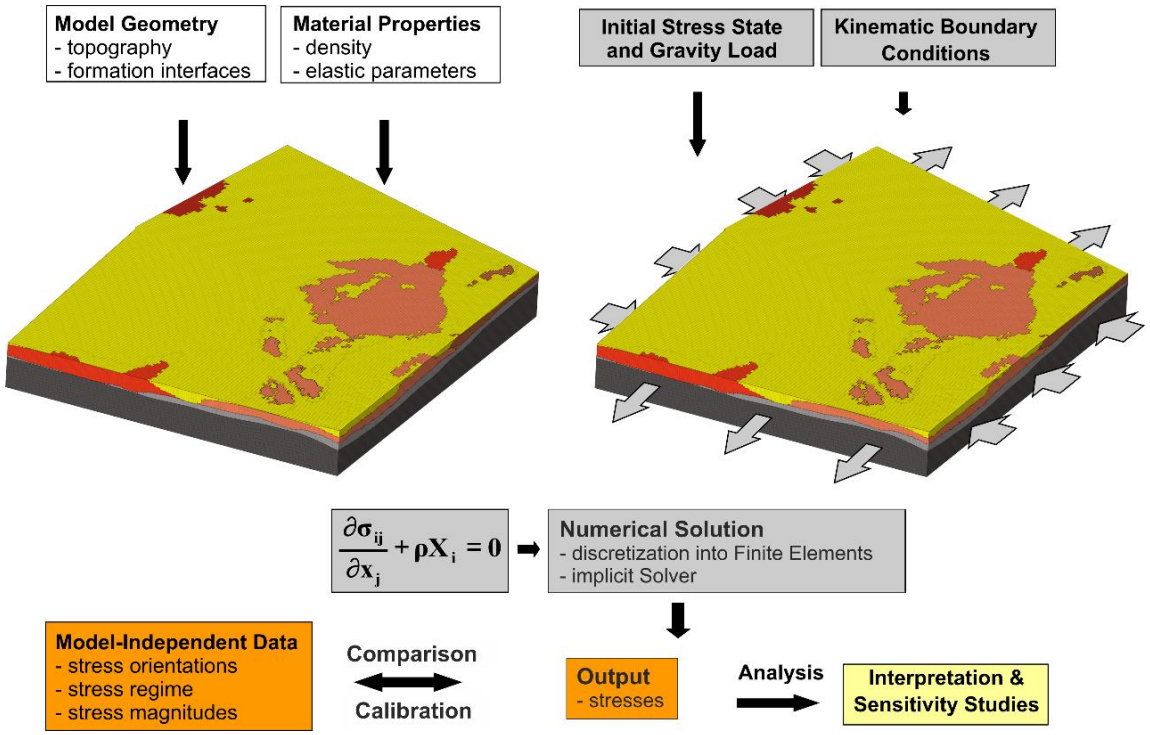

Figure 4.3: General workflow of 3D geomechanical-numerical modeling. White boxes: assembly of model geometry and rock properties. Left figure: 3D view of the discretized model volume. Grey boxes: Initial stress field and kinematic boundary conditions, gravity load and numerical solution. An appropriate initial stress state and kinematic boundary conditions are determined and applied as well as gravity load. Right figure: discretized model volume including boundary conditions used. The partial differential equation of the equilibrium of forces in 3D is solved using the FEM (σ_{ij} stress tensor, x_j Cartesian coordinates, ρ density, and X_i body forces). Orange boxes: model results are calibrated against model-independent observations. Yellow box: once the fit to the model-independent observations is acceptable, i.e., within their uncertainties, an interpretation and analysis of the model results can be performed.

The model geometry reflects the contemporary distribution of rock properties such as density and stiffness and Poisson's ratio. An appropriate initial stress equilibrates the gravitational stresses and resembles a reference stress state (Fischer and Henk, 2013; Hergert et al., 2015; Reiter and Heidbach, 2014). The orientations of the lateral model boundaries where the displacement boundary conditions

are applied are chosen in such a way that the mean S_{Hmax} orientation (Figure 4.1b) is perpendicular or parallel to them. For the solution of the partial differential equation of the equilibrium of forces, we use the FEM to estimate an approximated numerical solution. The FEM is appropriate as it allows discretizing complex geometries with unstructured meshes. The commercial FEM software package Abaqus™ v2019 is used. For post-processing we are using Tecplot 360™ enhanced with the GeoStress add-on (Stromeyer and Heidbach, 2017). For the construction and discretization of the 3D model geometry, GOCAD™ and HyperMesh™ are used.

4.3.2 Model geometry

The model geometry extends over 1250 km in east-west direction from eastern Poland to western France and by 1000 km in north-south direction from southern Scandinavia to northern Italy, covering an area of about 1.25 million km². This area was chosen with regard to the orientation of S_{Hmax} to simplify the definition of boundary conditions later on and with regard to important crustal structures which may affect the recent stress field in Germany, e.g., the Bohemian Massif, the Avalonia-EEC suture and the European Cenozoic Rift System. Additionally, model boundaries are selected distal to the German border to avoid possible boundary effects in the area of main interest. (Figure 4.1)

The model geometry contains seven units: a sedimentary cover, the upper crust subdivided into four units, the lower crust and parts of the lithospheric mantle. The units are bounded by five surfaces: the topography, the top of the crystalline basement, the top of the lower crust, the Mohorovičić discontinuity (Moho) and the model base at 100 km depth. The bottom of the model is thus not defined as the LAB, and therefore the thickness of the lithospheric mantle can deviate from its real thickness. The Moho was chosen as the deepest surface since almost all calibration data are from above, and also the depth interval of greatest interest is the upper 10 km of the crust. Although deeper structures may exert a long-wavelength effect on the stress state in the upper crust, we expect that the primary contributions to the stress field are captured by the considered interfaces. The upper crust is laterally sub-divided into four parts: the EEC, Avalonia, the Armorican Terrane Assemblage and the ALCAPA unit referring to the tectonic units displayed in Figure 4.1d.

Figure 4.4: Database and depth maps of the top of the crystalline basement, the top of the lower crust and the Mohorovičić discontinuity. We used the color map 'roma' of Crameri (2021). Sources of used data are as follows. Crystalline basement: Anikiev et al. (2019) (dark green), Diebold et al. (1991) (brown), GeORG-Projektteam (2013) (light blue), Geothermieatlas Bayern (2004) (pink), Hurtig et al. (1992) (blue green), Kirsch et al. (2017) (red), Korsch and Schäfer (1995) (light green), Lindner et al. (2004) (grey), Maystrenko and Scheck-Wenderoth (2013) (dark blue), Reinhold (2005) (orange), Rupf and Nitsch (2008) (cyan), Sommaruga (1999) (yellow), Tašárová et al. (2016) (light red), and black profiles (Behr et al., 1994; Bokelmann and Bianchi, 2018; Cazes et al., 1985; Freeman and Mueller, 1992; Grad et al., 2009a; Heinrichs et al., 1994; Hirschmann, 1996; Janik et al., 2011; Meschede and Warr, 2019; Oncken et al., 2000; Reinhold, 2005; Schintgen, 2015; Wenzel and Brun, 1991). A labeled, larger

size map of this database is available in the supplementary data. Top of the lower crust: Anikiev et al. (2019) (dark green), Maystrenko and Scheck-Wenderoth (2013) (dark blue), Tašárová et al. (2016) (light red), and Valasek and Mueller (1997) (cyan). Mohorovičić discontinuity: Anikiev et al. (2019) (dark green), Grad et al. (2009b) (red), Maystrenko and Scheck-Wenderoth (2013) (dark blue), and Wagner et al. (2012) (pink).

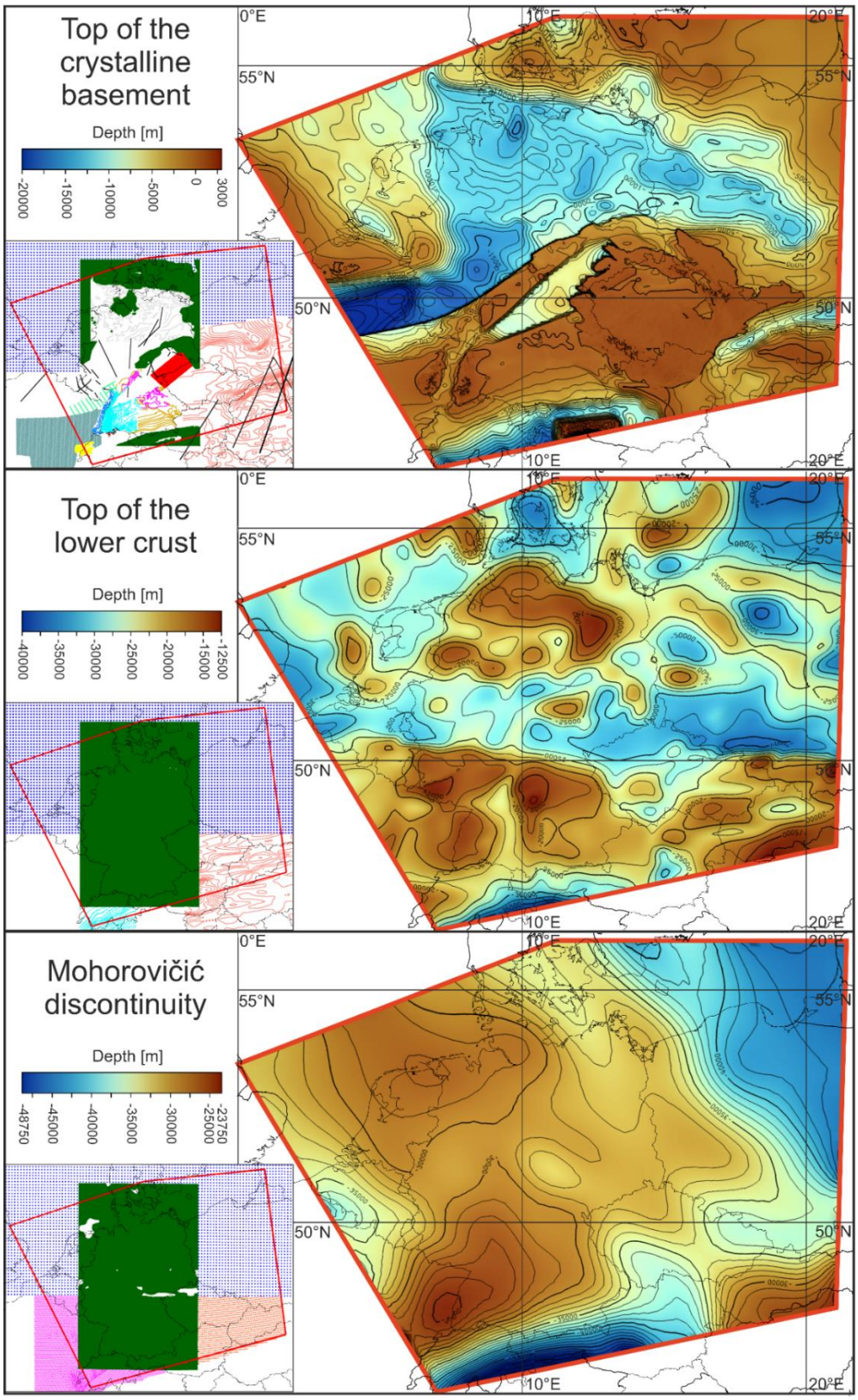

Figure 4.4 shows the depth maps of the top of the crystalline basement, the top of the lower crust and the Moho with the corresponding database used. The model is mainly based on three existing models: the 3D Deutschland model (Anikiev et al., 2019), the Central European Basin model (Maystrenko and Scheck-Wenderoth, 2013) and the central Europe model of Tašárová et al. (2016). The key challenge was the construction of the top of the crystalline basement. In all the models used and also in most other datasets, the base of the sedimentary layer is defined as the top of the basement regardless of whether the basement consists of crystalline or low-grade metamorphic rocks. This is an assumption which is not sufficient to represent the stiffness contrast correctly. The main reason for this assumption is the lack of data due to the usually great depths and the lack of economic interest in these units. Especially in the Rhenohercynian and Saxothuringian Zone (Figure 4.1c) only a few seismic profiles exist from research projects like DEKORP (Meissner and Bortfeld, 1990), EGT (Freeman and Mueller, 1992) or ZENTROSEIS (Bormann et al., 1986). Despite the uncertainties due to this poor amount of data, the use of the sediment-crystalline boundary is necessary for a geomechanical-numerical model, because of the strongly different mechanical properties. An extreme example within our model area is the western part of the Rhenohercynian Zone. Here the basement is outcropping, e. g. in the Rhenish Massif, but the top of the crystalline crust is suspected to be at about 20 km depth (Schintgen, 2015; Oncken et al., 2000). Therefore, in those areas where the definition of the basement does not correlate to the top of the crystalline basement, we constructed this surface to obtain a mechanically uniform surface; data used are shown in Figure 4.4. The boundaries between the Variscan basement units are simplified as vertical due to the poor knowledge.

4.3.3 Model discretization

Our final mesh shown in Figure 4.5 comprises 1.32 million hexahedral elements with a lateral homogenous resolution of approximately 6×6 km^2. The vertical resolution decreases with depths from 800 m near the surface up to 7500 m at the base of the model. An exception is the uppermost element layer, which is only 50 m thin to reduce the impact of free surface effects in the uppermost units. Due to the complex geometry of our model we decided not to use the common approach in the upper units in which each unit is meshed individually. Only the mantle and the crust are meshed as whole. Then we use the tool ApplePy (Ziegler et al., 2019) to assign each finite element to the respective subunits and the appropriate rock properties.

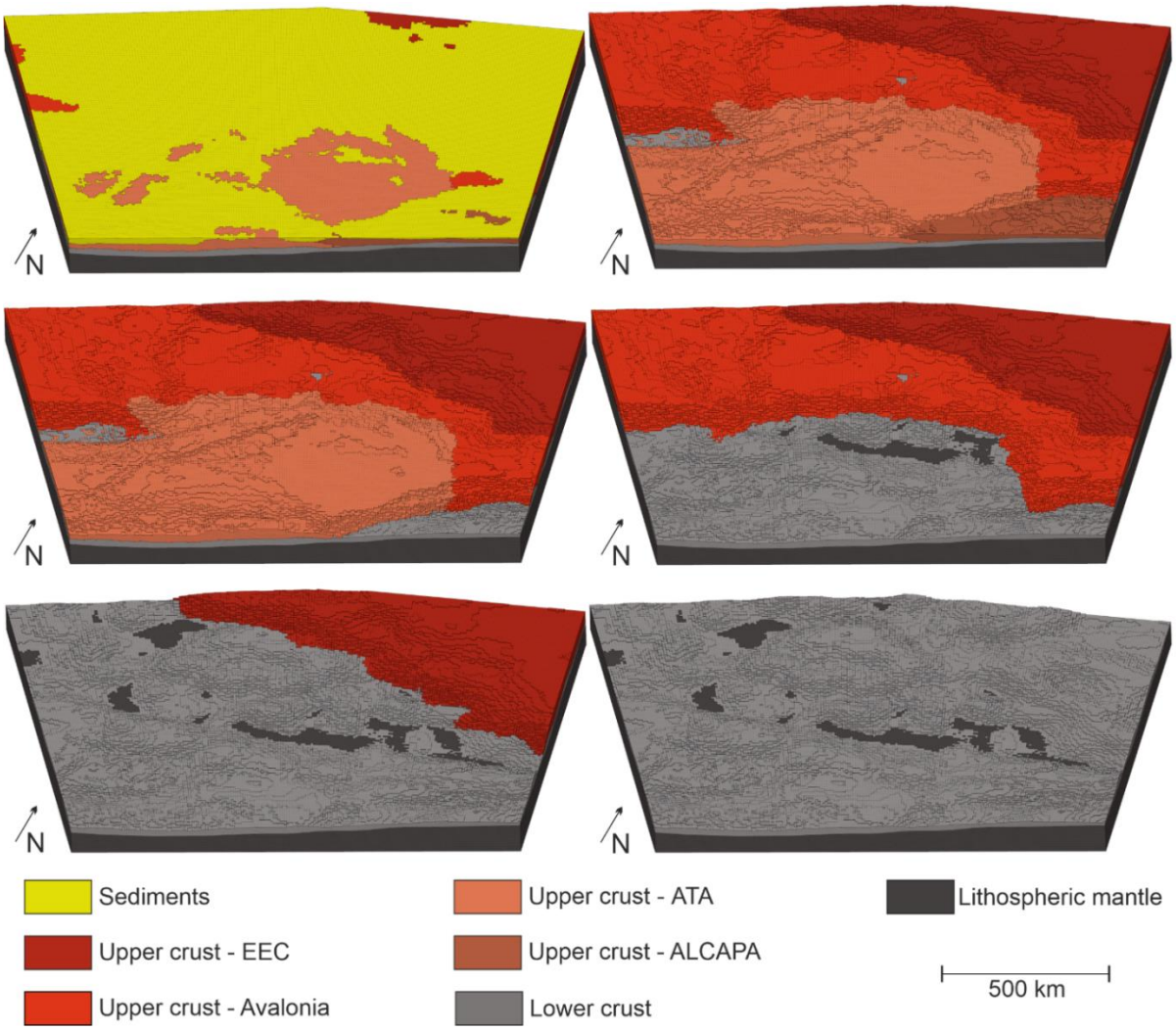

Figure 4.5: Six different views of the discretized model showing the internal model structure. The sedimentary unit is colored in yellow, the upper crust in different red shades regarding to different tectonic units (Figure 4.1c), the lower crust in light grey and the lithospheric mantle in dark grey. The dimension of the model is 1000 x 1250 x 100 km^3 comprising 1.32 million hexahedral elements. ALCAPA - Alps-Carpathians-Pannonian, ATA - Armorican Terrane Assemblage, EEC - East European Craton.

4.3.4 Rock properties

The material properties used in the model and corresponding references are shown in Table 4.2. The assignment of mean rock properties to the sediment unit is a difficult task, due to the large number of different rock types represented by unconsolidated rocks, claystones, sandstones, salt or limestones. Therefore, the values are approximate mean values. For the upper crust we applied a different density for each tectonic unit in the range of 2750 to 2820 kg m^{-3}. Young's modulus and Poisson's ratio are values for granodiorite as the characteristic rock of the upper crust. For the lower crust density we use the results of Maystrenko and Scheck-Wenderoth (2013) and Tašárová et al. (2016), but since, unlike them, we have only one uniform unit, we use an average of 3000 kg m^{-3}. Young's modulus and Poisson's ratio are again values for the characteristic rock of the unit, in this case gabbro.

Table 4.2: Overview of the parameters used for the parametrization. [a]Turcotte and Schubert (2014), [b]Maystrenko and Scheck-Wenderoth (2013), [c]Tašárová et al. (2016), [d]Przybycin et al. (2015)

Unit	Density [kg m^{-3}]	Young's modulus [GPa]	Poisson's ratio [-]
Sediments	2300	30	0.25
Upper crust			
ALCAPA	2750[b]	70[a]	0.25[a]
Armorican Terrane Assemblage	2790[c]	70[a]	0.25[a]
Avalonia	2820[b]	70[a]	0.25[a]
East European Craton	2810[b]	70[a]	0.25[a]
Lower crust	3000[b,c]	80[a]	0.25[a]
Lithospheric mantle	3300[c,d]	130	0.28[a]

4.3.5 Initial stress state

Before applying displacement boundary conditions to the model an initial stress state is generated representing a reference stress state. We use a simple semi-empirical function by Sheorey (1994) for the stress ratio k depending on depth (z) and Young's modulus (E) which can be considered as being representative of tectonically inactive regions with low lateral density contrasts:

$$k = 0.25 + 7E\left(0.001 + \frac{1}{z}\right) \quad (4.1)$$

To achieve our initial stress state we compare the k-values defined as

$$k = \frac{S_{Hmean}}{S_V} = \frac{S_{Hmax} + S_{hmin}}{2\,S_V} \quad (4.2)$$

from 29 synthetic profiles with the stress ratio calculated for a Young's modulus of 30 and 70 GPa, representing the sedimentary and upper crust units.

In order to establish the initial stress state, an underburden and a sideburden are added and this extended model is implemented in a conic shell (Figure 4.6a and b). Then, the model has to settle down frictionless within this conical shell. During that procedure, Young's modulus in the underburden as well as Poison's ratio in all units is varied until the virtual wells fit the Sheorey equation (Equation 4.1; Figure 4.6c). This procedure has been used and described several times (Buchmann and Connolly, 2007; Hergert, 2009; Hergert and Heidbach, 2011; Reiter and Heidbach, 2014). The resulting stress state represents the initial stress state, which is subsequently perturbed by applying displacement boundary conditions that impose the tectonic stress.

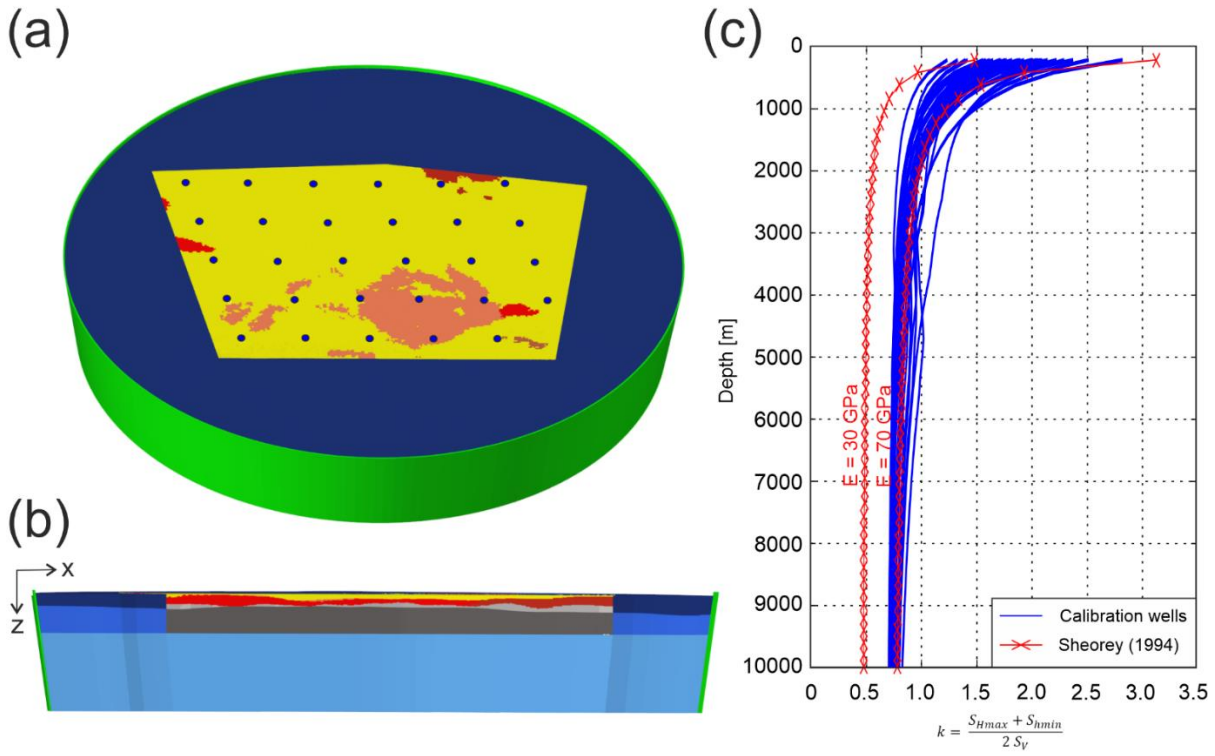

Figure 4.6: (a) Top view of the model implemented in the shell (green) and the sideburden (dark blue). Blue dots indicate the synthetic calibration wells. (b) Side view of the model implemented in the shell, the sideburden and the underburden (bright blue) (c) k-values of the calibration wells (blue curves) in comparison with k-values calculated with a semi-empirical function by Sheorey (1994) for a Young's modulus of 30 and 70 GPa representing the sedimentary and the upper crust units (red curves).

4.3.6 Displacement boundary conditions

The base of the model is fixed vertically, lateral movements are allowed and the model surface is free. At the five lateral boundaries of the model, displacement boundary conditions are applied to parametrize past and ongoing tectonic kinematics. The orientations of the model boundaries are chosen parallel or perpendicular to the mean S_{Hmax} orientation (Figure 4.1b). The eastern and western lateral model boundaries are aligned parallel and the northern and southern boundaries perpendicular to the mean S_{Hmax} orientation. Accordingly, extension is applied to the eastern and western boundaries and shortening to the northern and southern ones (Figure 4.3).

We use a two-stage approach to find a good agreement with the stress orientation and stress magnitude datasets. First a best fit with respect to a mean S_{Hmax} orientation (see details in Chapter 4.4.1) is estimated by an appropriate ratio between the extension and shortening applied. In a second step we vary the magnitude of these displacements on the model boundaries while keeping the ratio constant so that a best fit with the stress magnitude data is achieved as well. The calibration is mainly based on the S_{hmin} magnitude due to the larger amount of data from the compilation of Morawietz and Reiter (2020) and the fact that S_{Hmax} magnitudes are often calculated and not measured

and therefore less reliable. For the best fit model a total extension of 465 m in east-west direction and a total shortening of 325 m in north-south direction are applied.

4.4 Results

4.4.1 Orientation of the maximum horizontal stress (S_{Hmax})

We compare our model results with the stress orientation from the WSM database (Heidbach et al., 2016a) and some additional data by Levi et al. (2019) from western Austria (Figure 4.1a). From the WSM database we use only S_{Hmax} orientations that have a WSM quality A to C. However, we do not use individual data records but a mean S_{Hmax} orientation on a regular 0.5° grid (Figure 4.1 and 4.7c). Using a mean S_{Hmax} orientation avoids effects of data clustering which is often the case in the WSM database and it filters the data for a wavelength of the stress pattern that is representative of the resolution of the model. For the estimation of the mean S_{Hmax} values, we use the tool stress2grid from Ziegler and Heidbach (2019b). The S_{Hmax} data records are weighted according to their quality and their distance to the grid points. Each grid point requires at least 10 data points within a fixed search radius of 200 km. The resulting mean orientation of S_{Hmax} has a median standard deviation of ~28° using the statistics of bi-polar data (Mardia, 1972). The model results are interpolated linearly on a plane at 5 km depth, and then the nearest value to each grid point is chosen for the comparison with the mean WSM data.

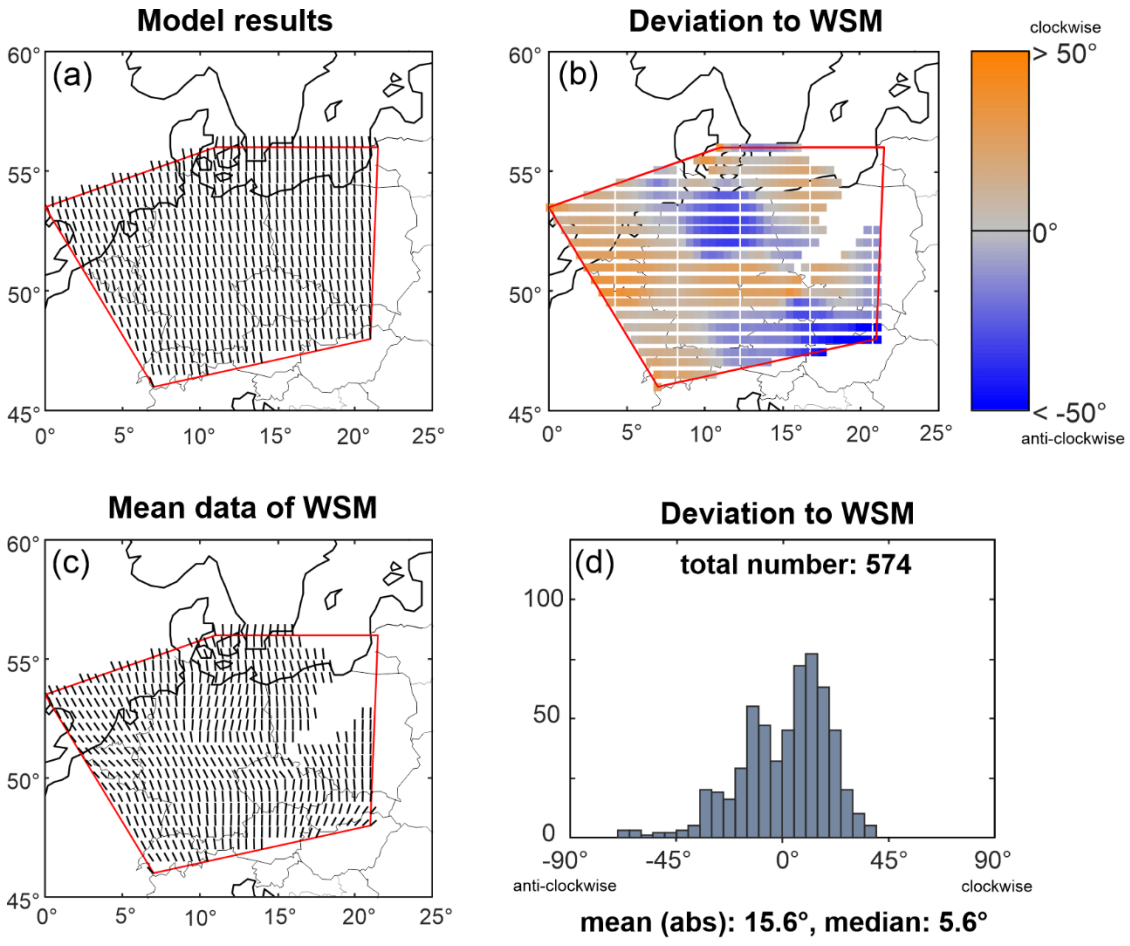

Figure 4.7: Comparison of S_{Hmax} orientation of the model results with the mean S_{Hmax} orientation derived from WSM data (Heidbach et al., 2016a). (a) S_{Hmax} orientation of the model at 5 km depth. (b) Deviation of the model result relative to the mean S_{Hmax} orientation derived from WSM data. (c) Orientation of the mean S_{Hmax} of WSM data (details are described in the text). (d) Histogram of the deviation of the modeled S_{Hmax} orientation to the mean S_{Hmax} orientation derived from WSM data.

Figure 4.7a displays the S_{Hmax} orientation of the model at 5 km depth, whereas Figure 4.7c shows the calculated mean S_{Hmax} orientation of the WSM data within the model area. The modeled S_{Hmax} orientations at the model boundaries are controlled by the assigned boundary conditions; thus the orientations are perpendicular to the northern and southern boundaries and parallel to the eastern and western edges. Within the model area the orientation of S_{Hmax} shows a homogenous pattern with a dominant NNW-SSE orientation which rotates slightly to a north-south orientation at the eastern boundary. Figure 4.7b visualizes the deviation of the model results from the mean WSM data. Blue indicates regions where the model results are rotated anti-clockwise with respect to the mean WSM data and orange regions with a clockwise rotation. There are three areas with larger deviations: one with primarily clockwise rotation in the area of Belgium and the two other areas, located in the northern and south-western part of the model, including the NGB (North German Basin), the eastern part of the Alps and western part of the Carpathians showing an anti-clockwise rotation. Apart from these two areas, the dominant color is orange, conterminous with a slight clockwise rotation. This trend is also visible in Figure 4.7d, where the histogram of the deviation between the mean S_{Hmax} orientation derived from the WSM data and the modeled orientation is shown with a median deviation of 5.6° and a mean deviation, calculated from the absolute differences, of 15.6°.

4.4.2 Stress magnitudes

4.4.2.1 Minimum horizontal stress (S_{hmin}) magnitudes

The modeled magnitudes of S_{hmin} in comparison to stress magnitude data of Morawietz and Reiter (2020) are shown in Figure 4.8. The figure is divided into three subfigures displaying the differences depending on depth and quality (Figure 4.8a), the spatial distribution of the calibration data (Figure 4.8b) and a histogram showing the distribution of the differences between the modeled and observed S_{hmin} magnitudes (Figure 4.8c). The differences are calculated as interpolated model results minus data: thus positive differences correspond model values that ate too large and negative ones to model values that are too low. We use only data from Morawietz and Reiter (2020) with a quality of A, B and C and from depths >200 m, to avoid topographic effects. Thus, we use 74 S_{hmin} magnitude data records from a depth of 200 to 4600 m, most of them from the upper 1000 m.

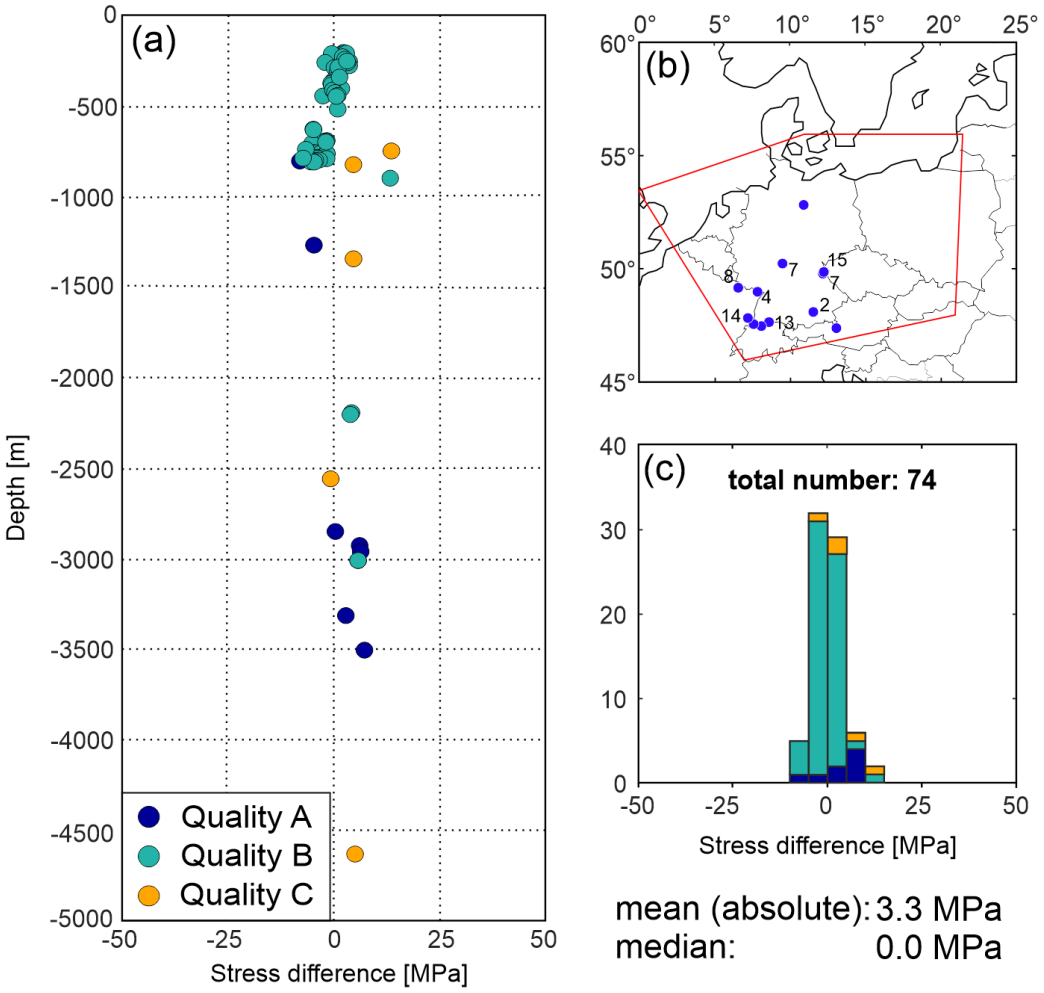

Figure 4.8: S_{hmin} magnitudes of the model in comparison to the data of Morawietz and Reiter (2020). The differences are calculated as model results minus calibration data. (a) Depth depending differences. Color of dots indicates the quality of the calibration data. (b) Spatial distribution of the calibration data used, numbers indicating localities with multiple data used. (c) Histogram of the differences displayed in (a).

As shown in Figure 4.8b the data are mainly located within the southwestern part with the exception of one measurement from the NGB. With 42 data records, more than half of all data records originate from three localities: from Falkenberg near the German-Czech border (Baumgärtner et al., 1987), from Benken in Switzerland (nagra, 2001) and from Wittelsheim in eastern France (Cornet and Burlet, 1992). Due to the calibration process described in Chapter 4.3.6 a median difference of 0 MPa is achieved. The differences are, with two exceptions, in a range of -10 to 10 MPa and seem to be independent of depth and quality. This together with a mean difference of 3.3 MPa indicates a very good fit with the data of Morawietz and Reiter (2020).

4.4.2.2 Maximum horizontal stress (S_{Hmax}) magnitudes

For the model calibration regarding the S_{Hmax} magnitudes 57 data records are used from the database of Morawietz and Reiter (2020). Again, only data with a quality of A to C and from a depth of >200 m

are used. Similar to the S_{hmin} data they are mainly located in the southwestern part of the model area (Figure 4.9b). The data are from seven different localities, whereby the data from Falkenberg near the German-Czech border (Baumgärtner et al., 1987) and from Benken in Switzerland (nagra, 2001) with 25 data records make up almost half of the comparison data used. The mean of the absolute difference is 20.6 MPa, and the median difference is 19.3 MPa. This difference can be explained by the asymmetric depth distribution of the values (Figure 4.9a). There are significantly more data records from shallower depths (200 to 1000 m), which indicate model results that are too than from the greater depths (>1000 m), which indicate results that are too low. Regardless of this, a trend is visible from positive to negative stress differences with increasing depth, i.e., the model seems to predict too large values of S_{Hmax} in the upper part of the model and too low values of S_{Hmax} in the deeper part. Furthermore, it is striking that the differences of quality A data are almost all negative and almost all of quality B and C are positive.

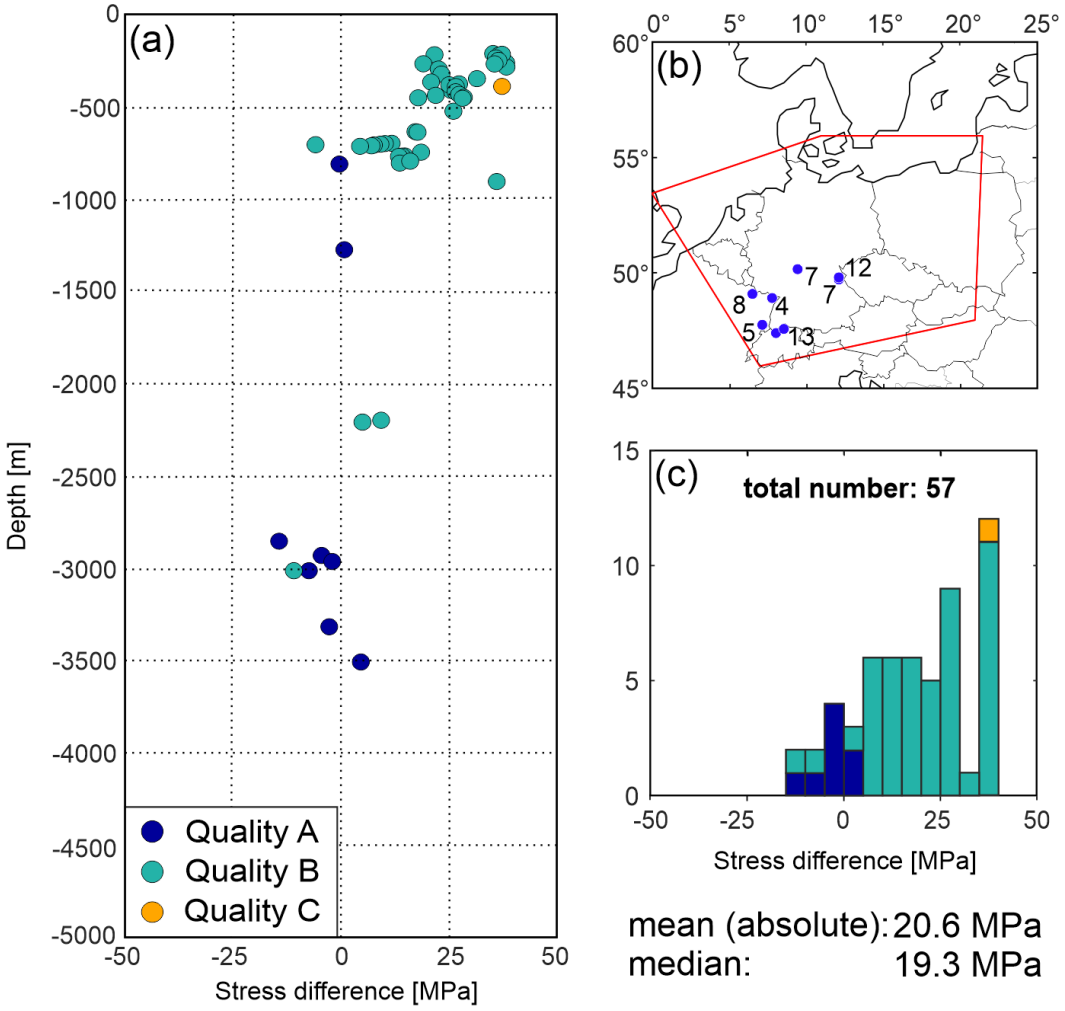

Figure 4.9: S_{Hmax} magnitudes of the model in comparison to the data of Morawietz and Reiter (2020). The differences are calculated as model results minus calibration data. (a) Depth depending differences. Color of dots indicates the quality of the calibration data. (b) Spatial distribution of the calibration data used, numbers indicating localities with multiple data used. (c) Histogram of the differences displayed in (a).

4.4.2.3 Stress gradients and stress regime

In addition to the calibration and comparison of the model with stress magnitude data of Morawietz and Reiter (2020), the absolute stress magnitudes of S_V, S_{hmin} and S_{Hmax} for three hypothetical wells up to 10 km depth are shown in Figure 4.10. We have chosen these three locations (Figure 4.11) due to the availability of stress data for a comparison later on, the quite uniform distribution over Germany (north, southwest and southeast) and the different depths of the crystalline surface. The hypothetic well 1 is entirely within the crystalline basement, well 2 entirely within the sedimentary unit and well 3 partly within the sediment unit and partly within the crystalline basement. As with the previous results we do not show the results of the upper 200 m. The depths are relative to the model surface and do not correspond to the z values of the model.

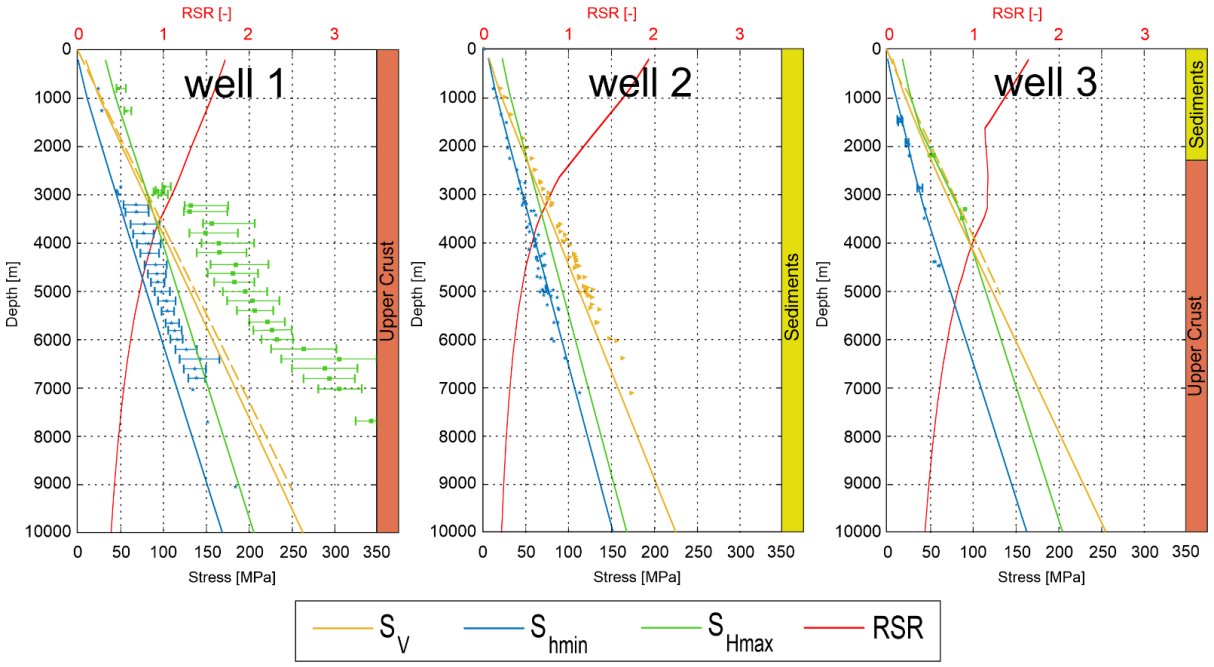

Figure 4.10: Gradients of regime stress ratio (RSR), S_V, S_{hmin} and S_{Hmax} for three hypothetic wells in comparison with data. The orientation of S_{Hmax} (not shown here) is constant over the entire depth (well 1: 161°, well 2: 163°, well 3: 162°). The colored lines show the RSR (red), the stresses of S_V (yellow), S_{hmin} (blue) and S_{Hmax} (green). Blue stars and green rectangles show measured respectively calculated magnitude of S_{hmin} and S_{Hmax}. The uncertainties of the magnitudes if specified are displayed as error bars. Yellow dotted lines are calculated S_V from density data. Well 1: comparison data from the 'Kontinentale Tiefbohrung' (KTB) of Brudy et al. (1997). Well 2: comparison data from the NGB of Röckel and Lempp (2003). Well 3: comparison data from Soultz-sous-Forêts and Rittershoffen. Measured S_{hmin} magnitudes of Valley and Evans (2007), calculated S_{Hmax} values of Klee and Rummel (1993), and calculated S_V magnitudes based on density values of Azzola et al. (2019).

The S_V gradients of well 1 and 2 are constant with the exception of a slight increase in the upper 1000 m, which is related to free surface effects. Well 3 also shows this effect but with an additional gradient change at 1500 to 3500 m depth. Above 1500 m depth the gradient corresponds to well 2 and below 3500 m to well 1. Overall well 2 shows the lowest S_V gradient of about 22.5 MPa km^{-1}, well 1

the highest S_V gradient of about 27 MPa km^{-1} and well 3 is with ~25.5 MPa km^{-1} in between. The horizontal stresses of S_{hmin} and S_{Hmax} have almost constant gradients in well 1 and 2; only the absolute stresses differ. In well 1 we have a gradient of about 17 MPa km^{-1} resulting in 170 MPa at 10 km depth for S_{hmin} and about 205 MPa at 10 km for S_{Hmax}. Due to the identical gradients the differential stress between S_{Hmax} and S_{hmin} is constant 35 MPa all over the well path. Well 2 shows a similar pattern with a S_{hmin} and S_{Hmax} gradient of about 15 MPa km^{-1} and a constant differential stress between S_{hmin} and S_{Hmax} of about 15 MPa. The gradients of well 3 are, as with the S_V magnitudes, a combination of well 1 and 2. This can be seen particularly clearly by the S_{hmin} values of well 3. From the surface to a depth of ~1500 m the gradient is quite similar to well 2 and below ~3500 m to well 1. In between, the gradient increases to ~25 MPa km^{-1}, which is the highest gradient of all horizontal stresses displayed. As a result, the differential stress in well 3 between S_{Hmax} and S_{hmin} also changes with depth. It amounts to 20 MPa at 1500 m depth, increasing with depth to about 40 MPa at 4000 m and then remains constant leading to 165 MPa for S_{hmin} and 205 MPa for S_{Hmax} at 10 km depth. Well 3 thus shows the only significant change of horizontal differential stress with depth of all three wells shown and also the highest differential stress with a maximum of about 40 MPa below 4000 m depth.

All three wells show a change of the stress regime from strike-slip to normal faulting, with S_V becoming greater than S_{Hmax}. In well 1 the transition is at about 3500 m, in well 2 at about 2500 m and in well 3 at about 4000 m depth. But despite these minor differences in depth, there are almost no differences between the stress regimes.

As an additional result the regime stress ratios (RSRs) (Simpson, 1997) for four model sections and for the three wells are shown in Figure 4.10 and 4.11. The RSR (Equation 4.3) is a unitless value combining the stress regime index n (Equation 4.4) of Anderson (1905) and the ratio of stress differences ϕ (Equation 4.5):

$$RSR = (n + 0.5) + (-1)^n(\phi - 0.5) \text{ (Simpson, 1997)} \quad (4.3)$$

$$n = \begin{cases} 0 & S_{hmin} < S_{Hmax} < S_V \\ 1 & S_{hmin} < S_V < S_{Hmax} \\ 2 & S_V < S_{hmin} < S_{Hmax} \end{cases} \text{ (Anderson, 1905)} \quad (4.4)$$

$$\phi = \frac{(\sigma_2 - \sigma_3)}{(\sigma_1 - \sigma_3)} \text{ (Angelier, 1979)} \quad (4.5)$$

The resulting value between 0 and 3 is the RSR indicating the stress regime divided into six classes from radial extension over extension, transtension, transpression and compression to constriction.

The results in Figure 4.11 show with the exception of peripheral areas, displaying some boundary effects, a rather uniform change of the stress regime from strike-slip to normal faulting with increasing depth. Starting with a RSR of 1 to 2 at 1000 m resulting in a RSR of 1 to 0.25 at 10 km depth. The two sections in between at 2000 and 4000 m show the transition with a dominant RSR of 1 to 1.5 and 0.75 to 1.25, respectively. The RSRs of the three wells displayed in Figure 4.10 confirm this observation. In the shallower parts the RSR lies between 1.75 and 2 then decreasing with depth to

values smaller than 0.5. A special aspect is visible in well 3, where the RSR is almost constant over 2 km along the transition between the sedimentary and the upper crust unit. The lowest RSR occurs in well 2, which is located entirely within the sedimentary unit. This correlation is also visible in Figure 4.11, where the lower RSR is related to areas with high sediment thicknesses, e.g., the NGB. On the other hand, a higher RSR seems to correlate with basement areas like the Bohemian Massif or the Mid German Crystalline High, well visible at 2000 and 4000 m depth.

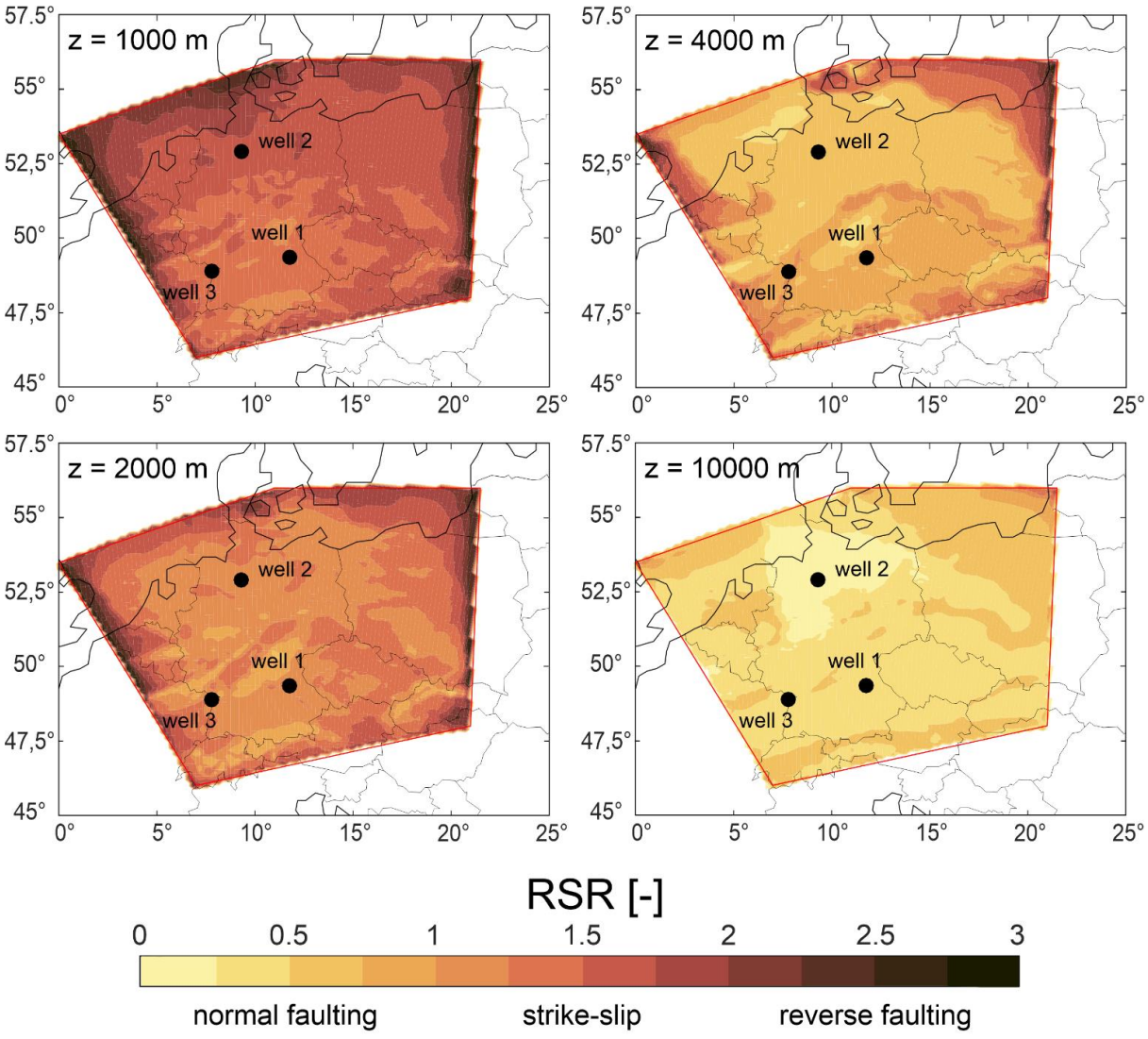

Figure 4.11: RSR indicating the stress regime for four model sections for different depths. The three black dots show the locations of the three hypothetical wells in Figure 4.10. The high RSR values at the model edges in the upper 4000 m, representing a constriction, are edge effects due to the applied boundary conditions. We used a color map based on 'lajolla' of Crameri (2021).

4.5 Discussion

4.5.1 Orientation of the maximum horizontal stress (S_{Hmax})

The results of the S_{Hmax} orientation are in comparison to the mean WSM data quite good with a median deviation of 5.6° and an absolute mean deviation of 15.6° (Figure 4.7). Therefore, the results are within the error range of the used WSM A to C quality data records which have uncertainties of 15 to 25° (Heidbach et al., 2018). Apart from some reorientation at the model edges in the upper 100s of meters, the orientations are almost constant over the entire model depth. For example, the S_{Hmax} orientations of our three hypothetical wells are 161°, 163° and 162° (Figure 4.10).

However, there are three areas with noticeable lateral deviations: in the north-eastern part of Germany, in Belgium and along the Carpathians. The region in north-eastern Germany belongs to the NGB in which there are thick salt deposits. Salt can act as a mechanical decoupling horizon between the layers above and below (Ahlers et al., 2019; Bell, 1996; Cornet and Röckel, 2012; Heidbach et al., 2007; Hillis and Nelson, 2005; Tingay et al., 2011). In such cases, the stress state below represents the regional trend transferred through the crust, while the stress state above is only affected by local sources often controlled by local density and strength contrasts. More than 20 % of the data from this region are above the salt and mostly E-W oriented, in contrast to the data below, which are more N-S oriented (e.g., Cornet and Röckel, 2012; Grote, 1998; Röckel and Lempp, 2003; Roth and Fleckenstein, 2001). However, since we do not distinguish between the data from these different layers the derived mean S_{Hmax} values are influenced by these data above the salt layer. Possibly the misfit in this area can also be explained by the Pritzwalk anomaly, a positive gravity anomaly due to high-density lower crust (Krawczyk et al., 2008).

The deviations in Belgium and adjacent areas can have several reasons. This region is the border between two massifs, the Rhenish and the Brabant Massif (Pharaoh, 2018), and the strength contrast between these two massifs may play a role. Such contrasts are often considered to be responsible for reorientations in the stress field (e.g., Adams and Bell, 1991; Heidbach et al., 2007; Rajabi et al., 2017). Another reason could be the tectonically active Lower Rhine Basin nearby or the uplift of the Rhenish Massif (Reicherter et al., 2008). Possible boundary effects can be excluded, since the orientation of S_{Hmax} is uniform along the entire western boundary of the model. The deviations in the south-eastern part of the model are located along the Carpathians and the adjacent Pannonian Basin. This is possibly an area with low far-field or first-order horizontal stress sources resulting in a near-isotropic stress state (Heidbach et al., 2007), and thus the topography contrast between the mountain range and the Pannonian Basin probably has a dominant influence (Bada et al., 2001; 1998). Furthermore, the NE-SW-oriented S_{Hmax} indicated by the WSM data implies an NW-SE extension in this area, which is in agreement with the orientation of back-arc extension arising from the retreating slab beneath the Carpathians in Romania (Sperner et al., 2001), which the model does not account for.

In general, our modeled S_{Hmax} orientations show a rather simple stress pattern without local perturbations. This is to a certain extent an expectable result since our model is in equilibrium with

gravitation. Therefore neither isostatic effects as described by, e.g., Kaiser et al. (2005), Bada et al. (2001) or Jarosiński et al. (2006) nor local perturbations due to faults or fault zones (Kaiser et al., 2005; Jarosiński et al., 2006) can be considered since such structural elements are not implemented. Nevertheless, our model results also show no impact of mechanical contrasts on the orientation of S_{Hmax}, e.g predicted by Grünthal and Stromeyer (1994), Marotta et al. (2002) or Cacace (2008) despite mechanical contrast, e.g., a Young's modulus difference of 40 GPa between the sedimentary (30 GPa) and the upper crust units (70 GPa). Probably a lateral stiffness difference and a weak unit seems to be necessary to get some perturbation due to a stiffness contrast (Reiter, 2021). To test this thesis, we defined an unrealistic low Young's modulus of 30 GPa to the upper crust unit of Avalonia (Figure 4.5). In this case we could see perturbations at the border between the upper crust units of Avalonia and the EEC.

Although our kinematic boundary conditions applied are not derived from plate tectonic forces, they fit in general the tectonic setting of the model area. A shortening in N-S direction can be related to the alpine orogeny in the south and an extension in E-W direction correlates with the evolution of several extensional structures like the Cenozoic Rift System or the Eger Graben since the Paleogene (Kley et al., 2008).

4.5.2 Magnitudes of S_{hmin}, S_{Hmax} and S_v

The S_{hmin} magnitudes (Figure 4.8a) in general show a very good correlation with the data of Morawietz and Reiter (2020) with a mean difference of 3.3 MPa, a median difference of 0 MPa and an almost even distribution independent of data quality and depth. However, the model was calibrated with these values, so the almost perfect match should not be overrated.

The comparison of the S_{Hmax} magnitudes does not show such a good match with a mean difference of 20.6 MPa and a median difference of 19.3 MPa (Figure 4.9). Due to the calibration process described a much better fit should be achieved. But we have decided not to force a median of 0 MPa for various reasons. Compared to the S_{hmin} magnitude data, the scattering is significantly larger and the distribution is less even. This is an expectable result since S_{Hmax} values are usually calculated and not measured and therefore S_{Hmax} magnitudes have a lower reliability compared to S_{hmin} values (Morawietz et al., 2020),but additionally there seems to be a dependency on depth and quality. A major part of the data indicating S_{Hmax} magnitudes that are too large are from shallow depths (200 to 1000 m) (Figure 4.9a). It can be assumed that the median and mean difference would be significantly better for a uniform depth distribution of the S_{Hmax} values since the results below 1000 m show a good match. A reduction of the S_{Hmax} magnitudes in our model and thus a statistically better fit would therefore only lead to a better fit of the model result in the upper part of the model. Whether there is a dependency of the results on quality is difficult to assess, although data of quality B and C tend to show larger deviations than data of quality A. But most quality B and C data are also from shallow depths. Therefore, the depth dependency may overlay the quality dependency.

The stress magnitudes of the three hypothetical wells displayed in Figure 4.10 show by and large the expected results. Since S_V is only dependent on the density the gradients of well 1 and 2 located in a single unit are constant all over the total well depth. The gradient of well 3 changes in between 1500 and 3500 m depth due to the change of units. The transition zone is quite large because of the vertical element resolution of about 800 m. Based on the sum of the overburden, the maximum S_V at 10 km depth is the highest in well 1, followed by well 3 and 2. The stress differences between S_{Hmax} and S_{hmin} are dependent on the elastic rock properties. Therefore, these results again are mainly based on the unit the well is located in. Since the Poisson's ratio is constant for the units involved (0.25), Young's modulus is probably the decisive parameter. This explains the constant horizontal stress differences within well 1 and 2 and the variations over the length of well 3. In addition, the maximum stress differences seemed to be mainly dependent on Young's modulus. Well 2 shows the smallest stress differences of 15 MPa, and well 1 shows differences of 35 MPa according to Young's modulus of 30 and 70 GPa, respectively. An exception is well 2 with the highest total stress differences of up to 40 MPa.

Also the RSRs displayed in Figure 4.10 and 4.11 indicate a strong dependency on Young's modulus since the highest values occur usually in the units of the upper crust characterized by a Young's modulus of 70 GPa and the lowest values are visible in areas with a high sediment thicknesses with a Young's modulus of 30 GPa. This correlation is almost perfectly visible in 4000 m depth in Figure 4.11 in comparison to the depth of the top of the crystalline basement shown in Figure 4.4. This stiffness difference between these two units is also responsible for the constant RSR in well 3 in the transition zone between these units in 1500 to 3500 m depth (Figure 4.10). The explanation for this correlation between the RSR and Young's modulus is larger horizontal stresses due to a higher Young's modulus, which lead to a more compressive regime and vice versa. In addition, our results indicate a change of the stress regime with depth for the whole model area from a dominant strike-slip regime ($1 < RSR < 2$) to a normal faulting regime ($RSR < 1$) (Figure 4.10 and 4.11). This change occurs, with few exceptions, between 2000 and 4000 m depth. The stress regime and thus in particular a change with depth is a decisive factor, e.g., for the wellbore stability, especially in case of directional or deviated drilling (Rajabi et al., 2016) or the stimulation of enhanced geothermal reservoirs (Azzola et al., 2019). Such depth-dependent stress regimes are for example described by Brooke-Barnett et al. (2015), Cornet et al. (2007), Rajabi et al. (2016) and Rajabi et al. (2017).

To get a more detailed insight we compare our hypothetic wells 1, 2 and 3 with local magnitude data (Figure 4.10). The model results of the hypothetic well 1 are displayed in comparison to values of the 'Kontinentale Tiefbohrung' (KTB), a major scientific drilling project in Germany (Brudy et al., 1997). Our results of S_V are in a very good agreement with the S_V calculated from a mean density value. Only at greater depths does the difference increase to about 5 MPa, and in the uppermost 750 m our results are too large, possibly due to free surface effects caused by our model resolution. The results of S_{hmin} and S_{Hmax} show significantly larger differences to the data of Brudy et al. (1997). Except for the values at 3000 m depth the S_{hmin} magnitudes of Brudy et al. (1997) are at least 15 MPa larger than the model results. The maximum difference of about 35 MPa is at 6400 m depth. The results of S_{Hmax} show even

greater deviations. All values of Brudy et al. (1997) are at least 15 MPa larger than the model results. The maximum difference is about 180 MPa at 7800 m depth and thus larger than our model results with 160 MPa. Remarkable is the change in the horizontal stress magnitudes of Brudy et al. (1997) at 3000 m depth. The S_{hmin} magnitudes increase from 50 to 70 MPa within 200 m, and S_{Hmax} increases even by 30 MPa from 100 to 130 MPa. At the same time the inaccuracies also increase significantly. This can be attributed to the fact that the values between 3000 and 7000 m depth are only calculated and not directly measured (Brudy et al., 1997), which is why the values only got a quality of worse than C (Morawietz et al., 2020) and are not used by us for calibration. A remarkable difference between our model and the geomechanical properties at the KTB site is the values of Young's modulus. The calculated values of Brudy et al. (1997) are about 90 GPa on average between 3000 and 8000 m depth, which is about 20 MPa larger than our model assumption of 70 GPa in this area. Furthermore, in our model a normal faulting regime is established from about 3500 m depth downwards (Figure 4.11), which is contrary to the stress regime of Brudy et al. (1997) showing a strike-slip regime from 1 km depth downwards. This indicates that our S_{Hmax} values are possibly too low within this model area. In general, our model results show a constant differential stress between S_{hmin} and S_{Hmax} of 35 MPa, whereas the data of the KTB indicate an increasing differential stress with depth. The fact that our model does not include faults can also have an effect. The KTB is located above the Franconian Line and even intersecting it (Wagner et al., 1997). The Franconian Line is a major fault zone at the south-western margin of the Bohemian Massif with a polyphase development from late Paleozoic to Neogene times (Zulauf, 1993; Peterek et al., 1997). In the end it is probably a combination of the lower Young's modulus in the model, the very large uncertainties of the calculated values and S_{Hmax} values that are too low in our model, which may explain the differences of up to 180 MPa for the S_{Hmax} magnitudes.

The stress magnitudes of the hypothetic well 2 are shown in comparison with S_V and S_{hmin} data from the NGB of Röckel and Lempp (2003). The S_V values are in good agreement with our results down to ~2000 m depth, whereas the difference increases below this level. This shows that the density chosen for the sedimentary unit is at least appropriate for the upper part of this unit. A larger density would lead to better results at greater depths, but since our calibration data mainly comes from depths shallower than 3500 m (Figure 4.8 and 4.9), we consider assuming a density of 2300 kg m^{-3} for the sedimentary unit is reasonable. The S_{hmin} values indicate a good fit with our results across the entire depth range to 7000 m, which agrees with our general comparison shown in Figure 4.8. Due to missing data, a comparison is not possible for the S_{Hmax} values. However, Röckel and Lempp (2003) mention that the actual stress regime in the NGB can be characterized as normal faulting for the sub-salt level. At an average depth of the salt layer in the NGB of 4 km (Scheck-Wenderoth and Lamarche, 2005), our results show a normal faulting regime beneath 4 km depth too (Figure 4.10 and 4.11).

For the comparison of our hypothetic well 3, we use data from the geothermal project in Soultz-sous-Forêts and some values from Rittershoffen, another geothermal project nearby both located at the western edge of the URG. The URG is part of the major European Cenozoic Rift System located in south-western Germany and eastern France (Ziegler and Dèzes, 2006). The dashed S_V gradients in

Figure 4.10 are calculated on the basis of density values of Rittershoffen (Azzola et al., 2019) correlated to the stratigraphic column of Soultz-sous-Forêts based on Aichholzer et al. (2016) up to 5080 m, the total depth of the deepest well in Soultz-sous-Forêts. Despite the density change between the sedimentary unit and the crystalline basement, the S_V magnitudes of the model are in good agreement. An exception is the upper 750 m, where modeled S_V magnitudes are slightly too low. The data of Valley and Evans (2007) show measured S_{hmin} magnitudes between 1500 and 4500 m depth. They are in very good agreement with our model results within the upper 3000 m. In between 3500 and 4500 m depth the agreement is slightly worse but with a maximum difference of about 10 MPa at 4500 m depth still good. For the validation of the S_{Hmax} magnitudes, we use four calculated values of Klee and Rummel (1993) between 2200 and 3500 m. Within this depth interval our model results show a good correlation with a maximum deviation of about 5 MPa. Due to the small amount of data available for S_{Hmax}, a comparison with some calculated stress gradients can be helpful. Assumptions for stress gradients of Heinemann (1994), Klee and Rummel (1993), and Valley and Evans (2007) result in S_{Hmax} magnitudes of 35 up to 55 MPa at a depth of 2000 m, of 95 up to 143 MPa at 5000 m and of 195 up to 310 MPa at 10 km. Even though these values show a quite wide range, the comparison of the model results allows the conclusion that our S_{Hmax} values show a quite good agreement in the upper 5000 m but tend to be too low with increasing depth. This is also supported by the observation of seismic events which show a slight dominance of strike-slip versus normal faulting focal mechanisms at depths of 8 to 10 km in the URG (Cornet et al., 2007). In contrast, our results show a normal faulting regime, which implies S_{Hmax} values that are too low.

In general, the model results show a good agreement with real magnitude data. The S_V magnitudes show a good correlation for all three described cases of the KTB, the NGB and the Soultz-sous-Forêts site (Figure 4.10). The modeled S_V magnitudes appear to be only slightly too low with increasing depth, but in general the densities seem to be quite well chosen. A better agreement would probably only be possible with a higher stratigraphic resolution in the sedimentary unit and a density gradient within the upper crust. Such a simple gradient, which could also reduce the differences in the sedimentary unit, would be less useful in this case, because densities between two sedimentary units can differ considerably, independent of their depth. Overall, the S_{hmin} magnitudes show a very good correlation. This can be seen in the general location-independent comparison in Figure 4.8, as well as with regard to the Soultz-sous-Forêts and NGB location in Figure 4.10. Only the results for the KTB site show some considerable differences, with the greatest deviations from calculated S_{hmin} values (3000 to 7000 m depth) that have not been directly measured and are of rather questionable quality. The S_{Hmax} magnitudes show the largest deviations, both in the general comparison (Figure 4.9) and in the local comparisons (Figure 4.10). The general comparison shows that our values in the upper part are rather too large and at greater depths rather too small. The results of S_{Hmax} at the KTB and Soultz-sous-Forêts sites only confirm the trend of values that are too low in the deeper parts but not the trend of values that are too large in the shallower parts. In contrast, the S_{Hmax} magnitudes at Soultz-sous-Forêts show a good agreement down to 2000 m depth and the values at the KTB site even indicate

magnitudes down to 800 m depth that are too low. An indication of S_{Hmax} magnitudes that are generally too small with increasing depth is also the RSR values at 10 km depth (Figure 4.10), which show larger areas of values lower than 0.5 indicating a radial extension, an uncommon stress regime in the upper crust. In the upper part of the model up to 4000 m, the rather uniform tectonic regime, between normal faulting and transtensional, corresponds mainly to the tectonic conditions expected (Röckel and Lempp, 2003; Cornet et al., 2007). However, in detail, e.g., for the KTB site, the model cannot reflect differing local conditions. This could simply be a consequence of the simplifications made, which cannot resolve all local conditions, e.g., differing rock properties or nearby faults.

4.6 Conclusion

The model presented is the first 3D geomechanical model for Germany predicting the first-order 3D stress tensor. The model is calibrated with S_{Hmax} orientations from the WSM database (Heidbach et al., 2016a) and compilation of S_{hmin} and S_{Hmax} stress magnitude data from Morawietz and Reiter (2020). Overall, our model shows good results regarding the orientation of S_{Hmax} and S_{hmin} magnitudes despite the necessary simplifications due to the model resolution and rock property distributions as well as the highly irregular spread of the calibration data and their varying quality. The S_{Hmax} orientations of the model are to a large extent within the uncertainty of the mean S_{Hmax} orientations that are derived from the A to C quality data of the WSM database. Furthermore, the S_{hmin} magnitudes show a quite good fit to various datasets (Röckel and Lempp, 2003; Valley and Evans, 2007), but the S_{Hmax} magnitude results show locally significant differences. Modeled S_{Hmax} magnitudes are too small in the lower part of the model, whereas some results indicate values that are to high in the upper part. But in general, our model describes the regional 3D contemporary stress state quite well. Some larger deviations due to local structures are expectable. Therefore, the model results cannot be used for stress prediction on a local or reservoir scale as the resolution is not sufficient, but it can deliver initial stress conditions for smaller-scale models that contain little or no stress magnitude data at all.

To improve our large-scale model a better stratigraphic resolution of the sedimentary unit and thus a better representation of the lithologies has to be implemented. This would increase the reliability of the comparison between measured stress magnitude data and the modeled ones. In addition to a vertical refinement, resolving lateral variations of the rock properties would be useful and these potentially account for lateral variability of the stress tensor.

Data availability

The results of our model have been published and are publicly available (see Ahlers et al., 2021b).

Supplement

The supplement related to this article is available online at: https://doi.org/10.5194/se-12-1777-2021-supplement.

Author contribution

Conceptualization of the project was done by AH, TH, KR, OH and BM. Construction and discretization of the model were done by SA. Data for the model and its calibration were collected and provided by SA, TH, LR, SM, MS and DA. Evaluation of the model results and their interpretation were performed by SA with the support of AH, TH, KR, BM, LR, OH and SM. SA wrote the paper with help from all coauthors. All authors read and approved the final paper.

Acknowledgements

This study is part of the SpannEnD Project (www.SpannEnD-Projekt.de, last access: 02 August 2021), which is supported by Federal Ministry for Economic Affairs and Energy (BMWI) and managed by Projektträger Karlsruhe (PTKA) (project code: 02E11637A).

Coastlines and borders used in the figures are based on the Global Self-consistent Hierarchical High-resolution Geography (GSHHG) of Wessel and Smith (1996).

5 The crustal stress field of Germany: a refined prediction

Steffen Ahlers[1], Luisa Röckel[2], Tobias Hergert[1], Karsten Reiter[1], Oliver Heidbach[3,4], Andreas Henk[1], Birgit Müller[2], Sophia Morawietz[3,4], Magdalena Scheck-Wenderoth[5,6], Denis Anikiev[5]

[1]Engineering Geology, Institute of Applied Geosciences, TU Darmstadt, 64287 Darmstadt, Germany

[2]Technical Petrophysics, Institute of Applied Geosciences, KIT, 76131 Karlsruhe, Germany

[3]Seismic Hazard and Risk Dynamics, GFZ German Research Centre for Geosciences, 14473 Potsdam, Germany

[4]Institute for Applied Geosciences, TU Berlin, 10587 Berlin, Germany

[5]Basin Modelling, GFZ German Research Centre for Geosciences, 14473 Potsdam, Germany

[6]Department of Geology, Geochemistry of Petroleum and Coal, Faculty of Georesources and Material Engineering, RWTH Aachen University, Aachen, Germany

Published in Geothermal Energy (https://doi.org/10.1186/s40517-022-00222-6)

Received: 1 December 2021, Accepted: 10 June 2022, Published online: 25 June 2022

Abstract

Information about the absolute stress state in the upper crust plays a crucial role in the planning and execution of, e.g., directional drilling, stimulation and exploitation of geothermal and hydrocarbon reservoirs. Since many of these applications are related to sediments, we present a refined geomechanical-numerical model for Germany with focus on sedimentary basins, able to predict the complete 3D stress tensor. The lateral resolution of the model is 2.5 km, the vertical resolution about 250 m. Our model contains 22 units with focus on the sedimentary layers parameterized with individual rock properties. The model results show an overall good fit with magnitude data of the minimum (S_{hmin}) and maximum horizontal stress (S_{Hmax}) that are used for the model calibration. The mean of the absolute stress differences between these calibration data and the model results is 4.6 MPa for S_{hmin} and 6.4 MPa for S_{Hmax}. In addition, our predicted stress field shows good agreement to several supplementary in situ data from the North German Basin, the Upper Rhine Graben and the Molasse Basin.

5.1 Introduction

The prediction of the recent crustal stress field is important for many applications regarding the exploitation or use of the subsurface, particularly for directional drilling, stimulation and exploitation of geothermal or hydrocarbon reservoirs. Another currently important application is the search for and long-term safety assessment of a high-level nuclear waste deposit. However, up to now the knowledge of the crustal stress field for Germany is limited. It is essentially based on two major databases regarding stress tensor orientations and stress magnitudes (Heidbach et al., 2016a; Morawietz et al., 2020), several 2D numerical models (Grünthal and Stromeyer, 1994; Marotta et al., 2002; Kaiser et al., 2005; Jarosiński et al., 2006; Cacace et al., 2008) and some regional scale 3D geomechanical-numerical models (Buchmann and Connolly, 2007; Heidbach et al., 2014; Hergert et al., 2015; Ziegler et al., 2016). The only large scale 3D model that covers entire Germany has been presented by Ahlers et al. (2021a). However, this model focuses on the large-scale stress pattern in the entire crust with low resolution in sediments that are represented with homogeneous mean rock properties.

To take a further step towards a robust prediction of the recent crustal stress state, we developed a geomechanical-numerical model of Germany based on Ahlers et al. (2021a). It provides a continuous prediction of the crustal stress in 3D with focus on the sedimentary basins. The work of Ahlers et al. (2021a) also provided a continuous description of the stress state of Germany but focused on basement structures and included a homogenous sedimentary layer without mechanical stratification in a coarse resolution. The model presented here has been significantly improved with a differentiated sedimentary layer, consisting of 15 units with specific material properties (density, Poisson's ratio and Young's modulus) and an 18-time higher resolution in the upper part of the crust. An improved differentiation of the sedimentary layer is essential, since the majority of applications focuses on sedimentary basins particularly for geothermal and hydrocarbon exploitation. At the same time, stress conditions within sedimentary units can be particularly challenging due to structural, lithological and mechanical variability. Mechanical properties varying with depth - mainly stiffness contrasts – can lead to differing stress magnitudes, differential stresses and perturbations in the orientation of the maximum horizontal stress (S_{Hmax}) (Cornet and Röckel, 2012; Heidbach et al., 2014; Hergert et al., 2015). Extreme cases include very weak layers of salt or clay, leading to a nearly lithostatic stress state, which can mechanical decouple the overburden from the underburden layers (Roth and Fleckenstein, 2001; Röckel and Lempp, 2003; Heidbach et al., 2007; Ahlers et al., 2019). Furthermore, our new model is calibrated with minimum horizontal stress (S_{hmin}) and S_{Hmax} magnitudes which significantly improve the reliability of the predicted stress state compared to the model Ahlers et al. (2021a), which could only be calibrated with S_{hmin} values.

5.2 Model setup

5.2.1 Method

We assume linear elasticity and use the finite element method to solve the partial differential equations of the equilibrium of forces. First, an appropriate initial stress state is defined representing an undisturbed state of stress governed by gravity. In a second step, the stress state in the model is calibrated with magnitude data by varying displacement boundary conditions defined at the model edges. This modeling approach has been used for different tectonic settings and scales and is described in detail in Buchmann and Connolly (2007), Hergert and Heidbach (2011), Heidbach et al. (2014), Reiter and Heidbach (2014), Hergert et al. (2015) and Ahlers et al. (2021a). For the construction and discretization of the 3D model geometry and the assignment of rock properties to individual finite elements the software packages GOCAD™, HyperMesh™ and ApplePY (Ziegler et al., 2019) are used. As solver, we use the commercial finite element software package Abaqus™ v2019. For post-processing Tecplot 360™ enhanced with the GeoStress add-on (Stromeyer and Heidbach, 2017) is used.

5.2.2 Geology of the study area

The diverse history of the model area lead to the complex geological structure observed today (Figure 5.1c, d). The upper crust can be subdivided into four parts: the East European Craton (EEC) in the northeast amalgamated with Avalonia further south during the Caledonian orogeny, the Armorican Terrane Assemblage (ATA) added during the Variscan orogeny and finally the Alp-Carpathian-Pannonian (ALCAPA) part as a result of the Alpine orogeny (Ziegler and Dèzes, 2006; McCann, 2008; Linnemann and Romer, 2010). Since these units are identical to Ahlers et al. (2021a) we refer to this publication for further information. The basement of the model area is mainly covered by late Paleozoic to Cenozoic sediments, with the exception of the Rhenish and Bohemian massifs commonly interpreted as long-lived highs (e.g., Eynatten et al., 2021), the Alpine mountain chain and parts of the Mid German Crystalline High (MGCH) and Moldanubian Zone (MDZ).

Figure 5.1: Overview of the geology of the model region and stress data used for comparison and calibration. The black frame shows the key area of the model with increased stratigraphic resolution based on Anikiev et al. (2019). (a) Distribution of the stress magnitude data of Morawietz and Reiter (2020). The color-coded dots indicate the quality assigned by Morawietz et al. (2020). Displayed are all data from a true vertical depth (TVD) >200 m. (b) Data of the World Stress Map (WSM) of Heidbach et al. (2016a) and Levi et al. (2019). Color-coded lines indicate the stress regime and the orientation of S_{Hmax}. Grey lines show the mean orientation of S_{Hmax} on a regular grid (Details see Chapter 5.3.1). (c) Geological framework of the model area based on Asch (2005) and Kley and Voigt (2008). BF – Black Forest, CG – Central Graben, EI – Eifel, HG – Horn Graben, HZ – Harz Mountains, GG – Glückstadt Graben, LRG – Lower Rhine Graben, OD – Odenwald, OG – Ohře Graben, SNB – Saar-Nahe Basin, SP – Spessart,

TW - Tauern Window, URG - Upper Rhine Graben, VB - Vogelsberg Complex, VG - Vosges. (d) Overview of the basement structures based on Kroner et al. (2010) and Brückl et al. (2010). The red frame shows the entire model area. ALCAPA - Alps-Carpathian-Pannonian, ATA - Armorican Terrane Assemblage, EEC - East European Craton.

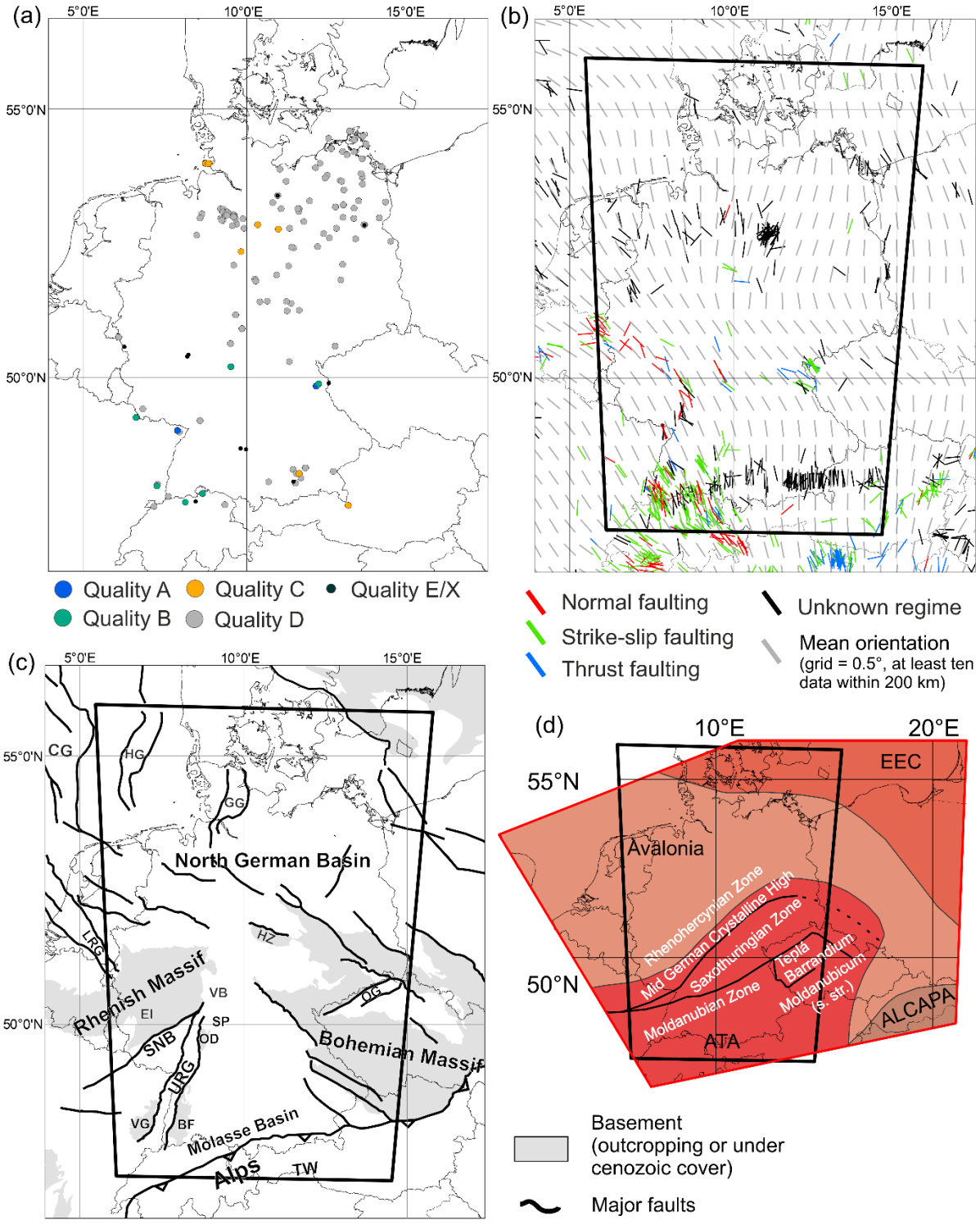

During the final phase of the Variscan orogeny from the late Carboniferous to Permian time the model area was affected by extension leading to the origin of several basins filled up with debris of the eroding Variscan orogeny and contemporaneous volcanic activity mainly located in NE Germany (McCann et al., 2008; Scheck-Wenderoth et al., 2008). Due to the large amount of mostly reddish clastic and

volcanic rocks deposited, this time period is called Rotliegend. The largest basin developed was the Southern Permian Basin with a maximum extent of ~1700 km covering large areas of the northern model area (Stollhofen et al., 2008). During the late Permian, this basin was flooded from the north leading to the deposition of the so-called 'Zechstein' evaporites (McCann et al., 2008). The following Triassic development of the model area was controlled by the breakup of Pangea and the westward opening of the Tethys leading to an E-W dominated extensional tectonic regime and the development of N-S oriented graben systems mainly in the north, e.g., the Central Graben or the Glückstadt Graben (Figure 5.1c) (Scheck-Wenderoth and Lamarche, 2005; Kley et al., 2008). During this time period the southern 'Alpine' part of the model area was characterized by open marine conditions of the Tethys shelf, whereas continental to shallow marine conditions by repeated incursions of the Tethys dominated the northern 'Germanic' domain (Feist-Burkhardt et al., 2008). The Jurassic was dominated by the progressive breakup of Pangea and mostly marine conditions (Pienkowski et al., 2008). Central Europe was still affected by extensional tectonics but the extension direction changed to NW-SE during the Late Jurassic (Kley et al., 2008). During the Early Cretaceous this development continued with depocenters in the northern part of the model area (Voigt et al., 2008). However, the deposition of sediments was restricted to these depocenters that evolved as en echelon subbasins along the southern margin of the Permian Basin in a transtensional regime (Scheck-Wenderoth et al., 2008).The largest part of the former Permian Basin area in the northern domain of the model area was uplifted during Late Jurassic to Early Cretaceous times. In the Late Cretaceous the tectonic setting and depositional conditions changed. Due to an eustatic sea-level rise large parts of Central Europe were flooded and predominantly carbonates and sandstones were deposited (Scheck-Wenderoth et al., 2008). The rotation of Iberia reversed the tectonic regime leading to the inversion of former depocenters, the formation of thrust faults and basement uplifts, e.g., the Harz mountains (Kley et al., 2008). Additional processes for the Late Cretaceous to Paleogene exhumation are still discussed (Eynatten et al., 2021). The Cenozoic development of the model area was mainly influenced by the collision of Africa and Eurasia leading to the rise of the Alpine mountain chains and the evolution of the Molasse Basin (MB). In addition, the Cenozoic Rift System developed, e.g., the Upper Rhine Graben (URG) and the Lower Rhine Graben (LRG) (Ziegler and Dèzes, 2006) and the uplift of the Rhenish Massif began (Reicherter et al., 2008). Except the sedimentary basins of the MB, the URG, the LRG and the North German Basin (NGB) large parts of the model area were affected by erosion (Rasser et al., 2008). The Cenozoic tectonics north of the Alps were accompanied by various volcanic activities, e.g., the Vogelsberg Complex, the Eifel, Ohře Graben or in the vicinity of the URG (Litt et al., 2008; Reicherter et al., 2008).

5.2.3 Model geometry

All basic information about the model area and geometry is described in Ahlers et al. (2021a). However, in order to refine the resolution w.r.t. to the former model we subdivide the sediment layer. The subdivision is based on the 3D-Deutschland (3DD) model of Anikiev et al. (2019) and is therefore only

resolved in the key area of our model (Figure 5.2). We did not extend the higher stratigraphic resolution to the whole model area since the data availability is poor and our focus area is covered by the 3DD data. Thus, the sedimentary units outside of the 3DD area are combined to a single unit. Furthermore, the stress data used for calibration are mainly located within the 3DD model area. The geometry data include a gap between the base of the Rotliegend - the deepest layer almost completely contained in the 3DD model - and the surface of the crystalline basement of Ahlers et al. (2021a). All lithological units between are represented by one unit named Pre-Permian unit though we aware that this is a very heterogeneous unit comprising early- to mid-Paleozoic low-grade metamorphic sediments and late-Paleozoic sediments.

5.2.4 Model discretization

The average lateral resolution of the model is 2.5 km and constant over the entire depth range of the model, the vertical resolution varies with depth. The mesh is divided into three vertical zones with a decreasing resolution with increasing depth. The deepest and most coarsely resolved unit is the lithospheric mantle limited by the bottom of the model and the Mohorovičić discontinuity with five element layers leading to a vertical resolution of 10 to 15 km. The mesh of the crust is subdivided at 10 km depth. Below 10 km depth the mesh contains ten element layers with a vertical resolution between 2.5 and 4 km. Above 10 km depth the mesh contains 43 element layers with a vertical resolution of about 240 m. Overall, the mesh contains about 11.1 million hexahedral elements.

Due to the complex geometry of the individual layers, especially of the sedimentary units, we did not create an individual mesh for each of them. We use ApplePY (Ziegler et al., 2019) to assign the individual mechanical properties of each unit to the finite elements of the mesh. Therefore apart from the lithospheric mantle, which is the deepest meshed zone, the geometry of the individual units are not directly represented by the mesh.

The final model consists of 22 units (Table 5.1): the lithospheric mantle, the lower crust, four units of the upper crust (EEC, Avalonia, ATA, ALCAPA), the Pre-Permian unit, Rotliegend volcanics and sediments, Zechstein carbonates and salt, Mesozoic units of the Triassic, Jurassic and Cretaceous, thrusted units of the Alps, folded units of the MB, three lateral subdivided units of Cenozoic sediments (NGB, URG and MB), Cenozoic volcanics and the sediments outside the 3DD area. Additionally, there are some relict elements (Table 5.1, Layer ID: 2) which arise from the element assignment with ApplePY if the surface of the mesh does not fit perfectly to the surface defined by the geometry used. This occurs because the geometry of the 3DD model has a higher resolution (1 x 1 km) than the mesh of our model (~2.5 x 2.5 km).

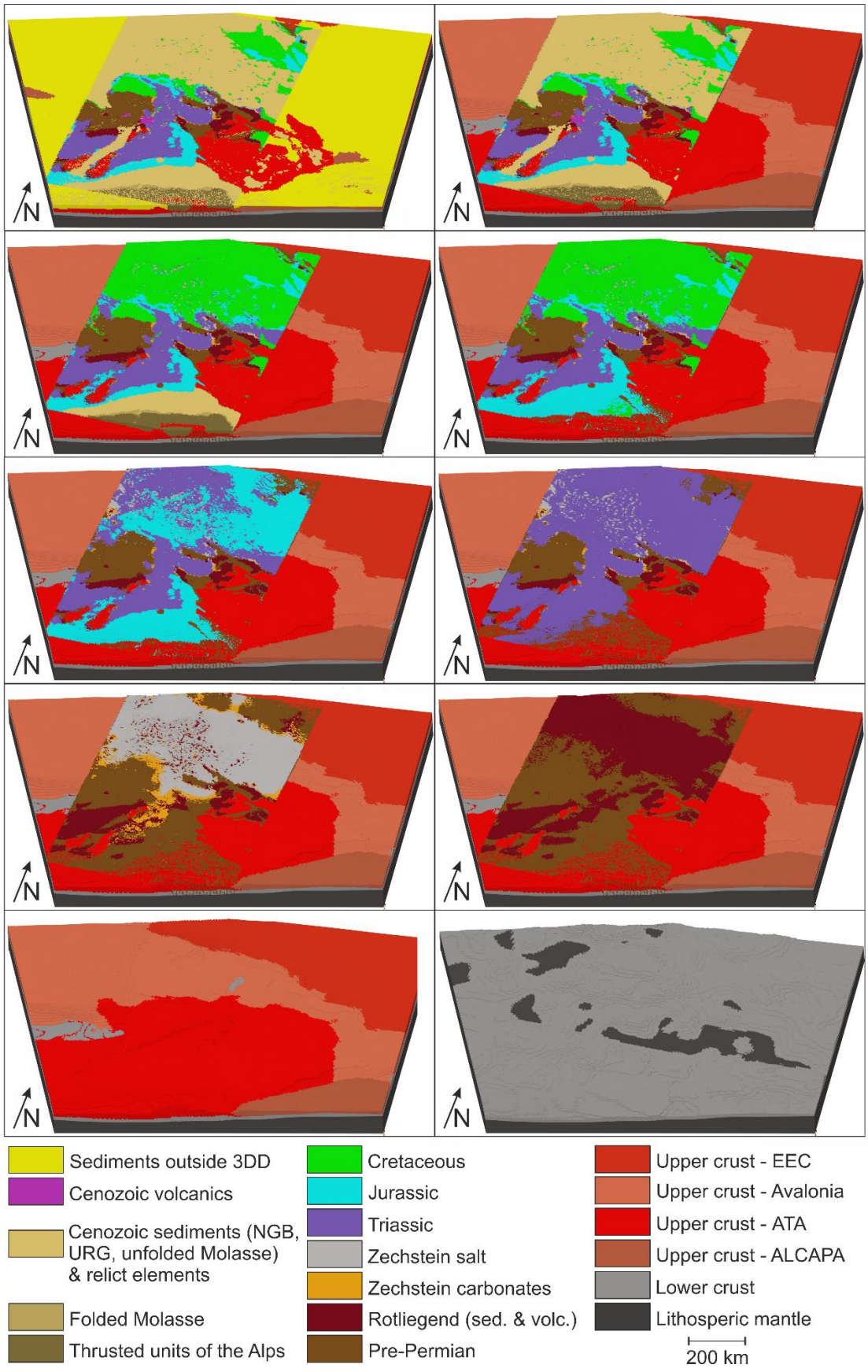

Figure 5.2: Overview of the discretized model showing the internal structure including 22 units. ATA - Armorican Terrane Assemblage, ALCAPA - Alpine-Carpathian-Pannonian, EEC - East European Craton, NGB - North German Basin, URG - Upper Rhine Graben.

5.2.5 Rock properties

Individual material properties are assigned to all 22 units of the model (Table 5.1). The density and the elastic properties (Young's modulus and Poisson's ratio) are defined as material properties for the numerical calculation, i.e., linear-elastic material behavior is assumed. Friction angle, cohesion and tensile strength are only used for post-processing analysis later on. Although our model contains 22 units, the Triassic and Jurassic units still contain mechanically very different subunits. For example, the Triassic unit comprises the sandstone-dominated Buntsandstein, the carbonate- and evaporate-dominated Muschelkalk and the claystone-dominated Keuper (Feist-Burkhardt et al., 2008). Therefore, we calculated the arithmetic mean of the subunits for the mechanical properties of these two units. Another challenge was the parametrization of the thrusted units of the Alps, the sediments outside the 3DD area and the relict elements unit. Since the relict elements can only occur at the top of the model, we used an average value of the three Cenozoic sedimentary units (NGB, URG and MB). For the sediments outside of the 3DD model area, we have chosen roughly estimated values. For the thrusted units of the Alps, we decided to use the mean of the Mesozoic units with the exception of the density. As for almost all other units, we use the density values from the 3DD model of Anikiev et al. (2019). The elastic properties are mainly based on the P^3 database (Bär et al., 2020) and Hergert et al. (2015). In addition, the friction angle and cohesion are mainly based on the latter. The tensile strength is assumed to be 5 MPa for almost all units, since available data are limited. In general, all values in Table 5.1 without a reference are roughly estimated. The friction angle, cohesion and tensile strength of the Zechstein salt are not defined due to the visco-elastic properties of salt (e.g., Urai et al., 2008).

In addition, we defined a Young's modulus gradient for all units with the exception of the sediments outside 3DD as it led to convergence problems at the model edges. The Young's modulus gradient should mimic the tendency of the rock mass to strengthen with increasing depth due to compaction and increasing confining pressure. An effect that can be seen, for example, in the decrease of porosity and permeability with increasing depth (Ingebritsen and Manning, 1999). Our Young's modulus gradient reaches from 1.5 km depth to the surface, describing a reduction of the Young's modulus from 100% (of the values in Table 5.1) to 10 % at the surface. The reduction to 10% is derived from Hudson and Harrison (1997b) and the depth of the gradient was iterated by preliminary tests.

Table 5.1: Overview of all units defined in the model and parameters used. For abbreviations, see Figure 5.2. Further detailed information on the individual units can be found in Anikiev et al. (2019) and Ahlers et al. (2021a).

Layer ID	Name	Density [kg/m³]	Young's modulus [GPa]	Poisson's ration [-]	Friction angle [°]	Cohesion [MPa]	Tensile Strength [MPa]
2	Relict elements	2400[a]	15[b]	0.29[b]	38[b]	10[b]	5
3	Sediments outside 3DD	2700	30	0.25	38[b]	10[b]	5
4	Cenozoic volcanics	2860[a]	54[c]	0.25[c]	50[i]	39[i]	5
5	Cenozoic sediments of the NGB	2480[a]	15[b]	0.29[b]	38[b]	10[b]	5
6	Cenozoic sediments of the URG	2300[a]	15[b]	0.29[b]	38[b]	10[b]	5
7	Cenozoic sediments of the Molasse Basin	2350[a]	15[b]	0.29[b]	38[b]	10[b]	5
8	Folded Molasse	2400[a]	15[b]	0.29[b]	38[b]	10[b]	5
9	Thrusted units of the Alps	2700[a]	23[c]	0.25[c]	40	25	5
10	Cretaceous	2590[a]	20[c]	0.25[c]	40[j]	18[j]	7[k]
11	Jurassic	2600[a]	20[c]	0.26[c]	36[b,j]	15[b,j]	5
12	Triassic	2650[a]	28[c]	0.25[c]	36[b,j]	31[b,j]	5
13	Zechstein salt	2100[a]	25[g]	0.27[g]	-	-	-
14	Zechstein carbonates	2400[a]	30[c]	0.25[c]	50[i]	18[i]	5
15	Rotliegend sediments	2600[a]	15[c]	0.19[c]	43[l,m]	25[l,m]	5[l,m]
16	Rotliegend volcanics	2650[a]	26[c]	0.25[c]	40[l]	57[l]	15[l]
17	Pre-Permian	2670[a]	40[c]	0.25[h]	40[l,n]	15[l,n]	5[l,n]
18	Upper crust ALCAPA	2750[d]	70[h]	0.25[h]	40[b,c]	30[b,c]	5
19	Upper crust ATA	2790[e]	70[h]	0.25[h]	40[b,c]	30[b,c]	5
20	Upper crust AV	2820[d]	70[h]	0.25[h]	40[b,c]	30[b,c]	5
21	Upper crust EEC	2810[d]	70[h]	0.25[h]	40[b,c]	30[b,c]	5
22	Lower crust	3000[d,e]	80[h]	0.25[h]	40[b,c]	30[b,c]	5
1	Lithospheric mantle	3300[e,f]	130	0.25[h]	40[b,c]	30[b,c]	5

[a]Anikiev et al. (2019), [b]Hergert et al. (2015), [c]Bär et al. (2020), [d]Maystrenko and Scheck-Wenderoth (2013), [e]Tašárová et al. (2016), [f]Przybycin et al. (2015), [g]Wenting et al. (2017), [h]Turcotte and Schubert (2014), [i]Zoback (2007), [j]Reyer (2013), [k]Dubelaar and Nijland (2016), [l]Alber et al. (2015), [m]Stöckhert et al. (2013), [n]Alber and Solibida (2017).

5.2.6 Initial stress state

An initial stress state is established, describing an only gravity-driven undisturbed, non-tectonic stress field within the upper crust before the displacement boundary conditions are applied. To achieve such an initial stress state, we extend our model with a sideburden (dark blue), an underburden (light blue) and a stiff shell (green) (Figure 5.3a, b). The shell has a conic shape with a theoretical intersection point at the center of the earth emulating the naturally increasing confining pressure with depth (Zang and Stephansson, 2010). The elastic properties (Young's modulus and Poisson's ratio) of the sideburden and underburden are the adjusting screws to set a best fit initial stress state. For calibration we use a semi-empirical function of Sheorey (1994) describing the undisturbed stress state of the earth as stress ratio (k):

$$k = \frac{S_{Hmean}}{S_V} = \frac{S_{Hmax}+S_{hmin}}{2S_V} \tag{5.1}$$

depending on depth (z) and Young's modulus (E):

$$k = 0.25 + 7E\left(0.001 + \frac{1}{z}\right) \tag{5.2}$$

we compare the theoretical k-values with k-values of our model using 29 virtual wells up to 25 km true vertical depth (TVD) (blue dots in Figure 5.3a). Subsequently, we vary the gravity-driven settlement of the model by varying the Young's modulus of the underburden and increase or decrease the influence of S_V on the horizontal stresses by varying the Poisson's ratio within the model and the sideburden. This workflow has been used and described in detail by several authors before, e.g., Buchmann and Connolly (2007), Hergert (2009), Hergert and Heidbach (2011), Reiter and Heidbach (2014) or Ahlers et al. (2021a).

Our best fit regarding the theoretical stress state of Sheorey (1994) is displayed in Figure 5.3c. There is a change of scale along the depth axis below 7000 m TVD since a uniform stress state and an almost perfect fit to the theoretical curve (red curve) is achieved at greater depths when all wells reach the upper crustal units (Layer ID: 18 - 21) with a homogeneous Young's modulus of 70 GPa. About half of the calibration wells (blue curves) show an almost vertical progression within the upper 1500 m, while the other half follows the progression of the theoretical curve of Sheorey (1994) to higher k-values with decreasing depth. This effect occurs due to the Young's modulus gradient defined within the main area of our model up to 1500 m TVD. Figure 5.3c includes the function of Equation 5.2 for a Young's modulus of 30 GPa typical for the sediments and a Young's modulus of 70 GPa representing crystalline basement units.

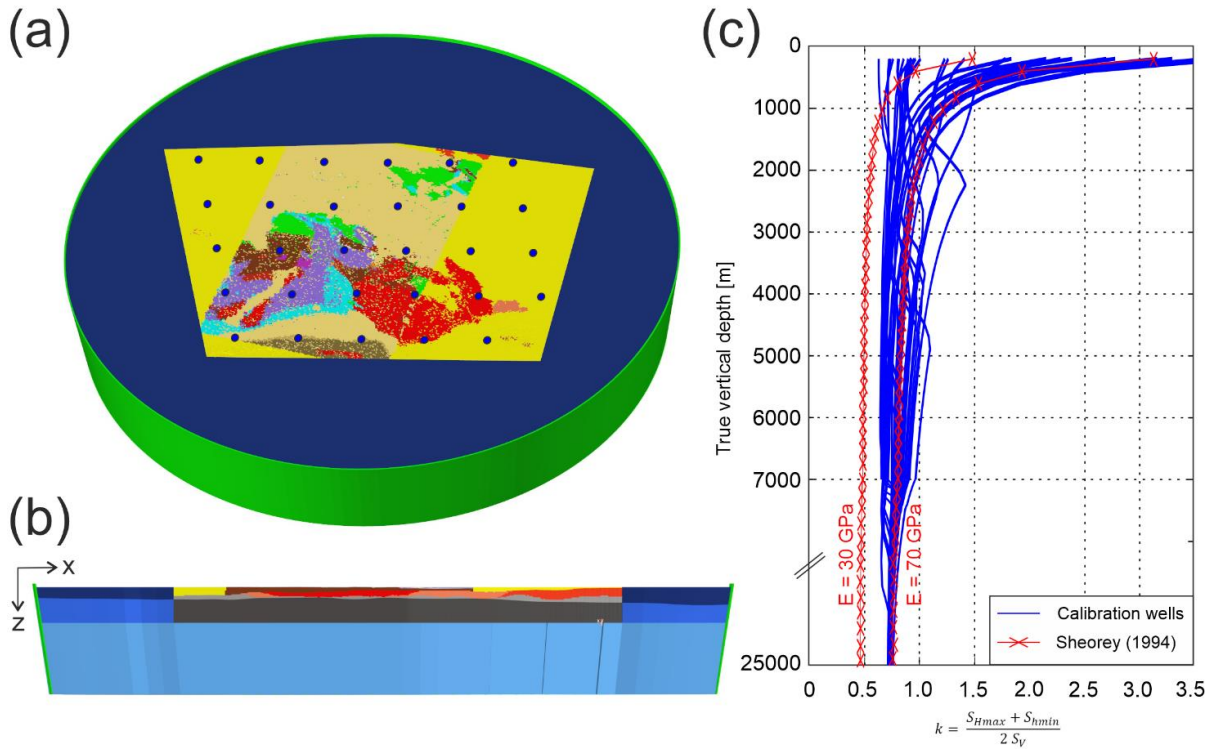

Figure 5.3: Top (a) and side view (b) of the extended model box used to achieve an initial stress state. (c) Best fit of 29 virtual wells (blue curves and blue dots in (a)) in comparison to calculated curves (red) for a Young's modulus of 30 and 70 GPa based on Sheorey (1994). There is a change of the scale of the depth axis below 7000 m TVD.

5.2.7 Displacement boundary conditions and calibration

After the initial stress state is reached, the model is calibrated with measured in situ stress data using variable displacement boundary conditions. The bottom of the model is fixed vertically, horizontal displacements are allowed and the model surface is free. Displacement boundary conditions are defined at the five vertical model edges (Figure 5.4). The directions of displacements are predefined by the mean S_{Hmax} orientation derived from the *World Stress Map (*WSM, Heidbach et al., 2016a) data (Figure 5.1b). At the northern and southern edges, where S_{Hmax} is oriented perpendicular to the model boundary, compression is applied. Accordingly, extension is applied at the western and eastern edges, where S_{Hmax} is parallel to the model boundary. The magnitudes of the displacement boundary conditions are derived through a calibration process using in situ stress magnitudes from the database of Morawietz and Reiter (2020). Since S_V is based almost entirely on density and is not influenced by displacement boundary conditions applied, only the S_{Hmax} and S_{hmin} magnitudes are used for calibration. We use only data qualities from A to C and values from TVDs >200 m to minimize possible topographical effects. Thus, in total 73 S_{hmin} and 56 S_{Hmax} magnitudes from 200 to ~4700 m TVD are available from the database of Morawietz and Reiter (2020). Since the calibration data are unevenly distributed with depth (Figure 5.6 and 5.8) a depth-weighted median for depth intervals of 500 m is

used as decisive calibration value. The best fit is achieved with a total shortening of 442 m in N-S direction and an extension of 560 m in E-W direction (Figure 5.4).

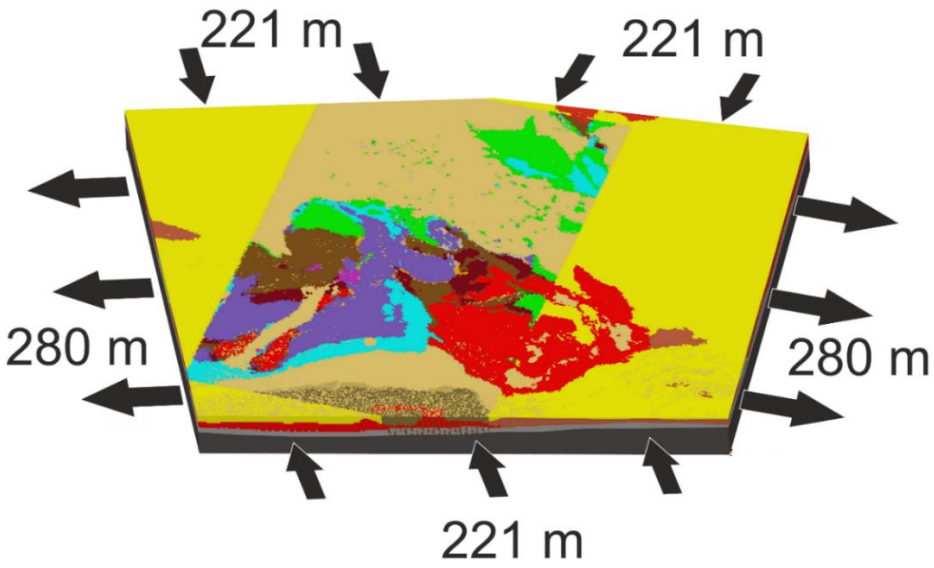

Figure 5.4: Displacement boundary conditions applied at the discretized model. Arrows indicate direction of the displacements applied, numbers the magnitudes of displacements defined for the best fit.

5.3 Results

5.3.1 Orientation of S_{Hmax}

The orientations of S_{Hmax} in comparison to the mean orientation of S_{Hmax} derived from the WSM (Heidbach et al., 2016a) and additional data by Levi et al. (2019) are displayed in Figure 5.5. Figure 5.5a shows the modelled S_{Hmax} orientation at 5000 m TVD (red lines) and the mean S_{Hmax} orientation (black lines) with standard deviation (grey wedges) based on the WSM data. The angular deviation between these two are displayed as a color plot (Figure 5.5b) and a histogram (Figure 5.5c). The mean orientation of S_{Hmax} and standard deviation based on the WSM data is calculated using the stress2grid script of Ziegler and Heidbach (2019b) that uses the statistics for circular data (Mardia, 1972). Input data within a 200 km search radius are weighted by data quality and distance to a point of the 0.5° x 0.5° grid (Ziegler and Heidbach, 2019a). Furthermore, at least 10 data records - with a quality of A to C - within the search radius must be available to return a mean S_{Hmax} orientation. In addition, data from the NGB within or above the Zechstein salt are sorted out to avoid effects due to salt decoupling (e.g., Roth and Fleckenstein, 2001; Röckel and Lempp, 2003; Heidbach et al., 2007), since visco-elastic properties are not included in our model. For comparison, we use model results interpolated to 5000 m TVD.

As shown by Figure 5.5a, our model predicts an almost homogeneous N-S orientated stress pattern. The median deviation of 0.3° indicates an overall good fit to the mean WSM data. Furthermore, almost all results are within the standard deviation of the mean WSM data. However, Figure 5.5a and b

indicate several model regions with significant deviations. For example, the local perturbations in the southern part of the model area where NNW-SSE orientations of S_{Hmax} dominate in the west and N-S orientations in the east or the NW-SE orientations in central Germany. In addition, the histogram (Figure 5.5c) shows an uneven distribution of the deviation.

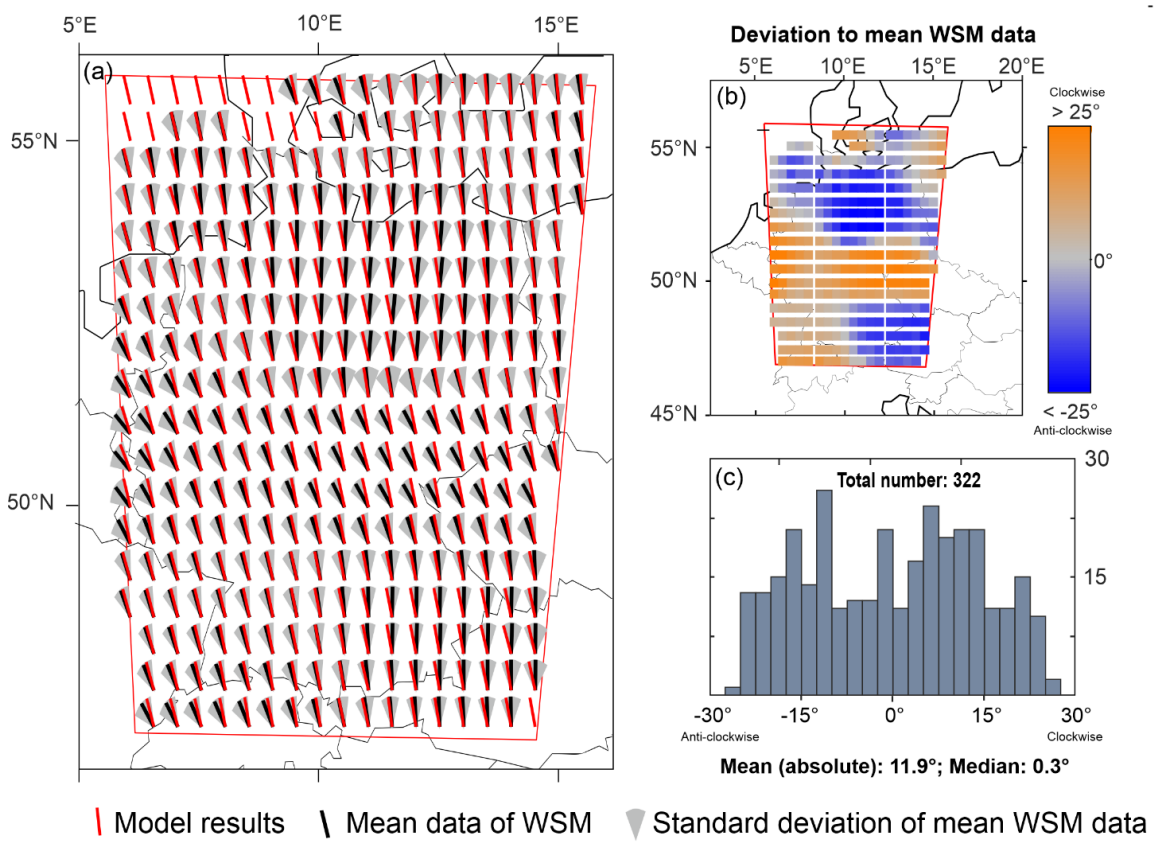

Figure 5.5: Orientation of S_{Hmax} predicted by the model in comparison to the mean orientation of the WSM (Heidbach et al., 2016a) and Levi et al. (2019). Details are described in the text. (a) Model results at 5 km TVD (red lines), the mean orientation derived from the WSM (black lines) with standard deviation (grey wedges). (b) Color-coded deviation between the results and the mean orientation of the WSM. Blue indicates an anti-clockwise rotation of the model results and orange a clockwise rotation of the model results w.r.t the mean orientation of the WSM. (c) Histogram showing the deviation displayed in (a) and (b).

5.3.2 Stress magnitudes and absolute stress state

5.3.2.1 Magnitudes of S_{hmin}

The magnitudes of S_{hmin} predicted by the model are displayed in comparison to calibration data by Morawietz and Reiter (2020). The differences are calculated as model results minus calibration data. Thus, positive differences indicate too high values predicted by the model and negative differences too low values. The differences in Figure 5.6a and Figure 5.6c are color-coded regarding their qualities. We use 73 values, from TVDs >200 m, with a quality of A to C from twelve localities mainly located in south Germany with the exception of a data record from Peckensen (Röckel and Lempp, 2003). The

localities are displayed in Figure 5.6b with numbers indicating multiple magnitudes from different depths at one location. In general, the fit regarding the S_{hmin} magnitudes of Morawietz and Reiter (2020) is good with differences in the range of -20 to 7.5 MPa and a mean of the absolute differences of 4.6 MPa. Figure 5.6a shows a depth trend from negative differences in the upper 1500 m indicating too low magnitudes predicted by the model to positive differences in greater depths indicating slightly too high magnitudes predicted. Due to the large amount of data in the upper 1000 m this leads to the unweighted median of -3.7 MPa and skewed histogram with a peak at -2.5 to -5 MPa. Therefore, we decided to use a depth-weighted median during the model calibration (Chapter 5.2.7). A dependency on data qualities is not recognizable.

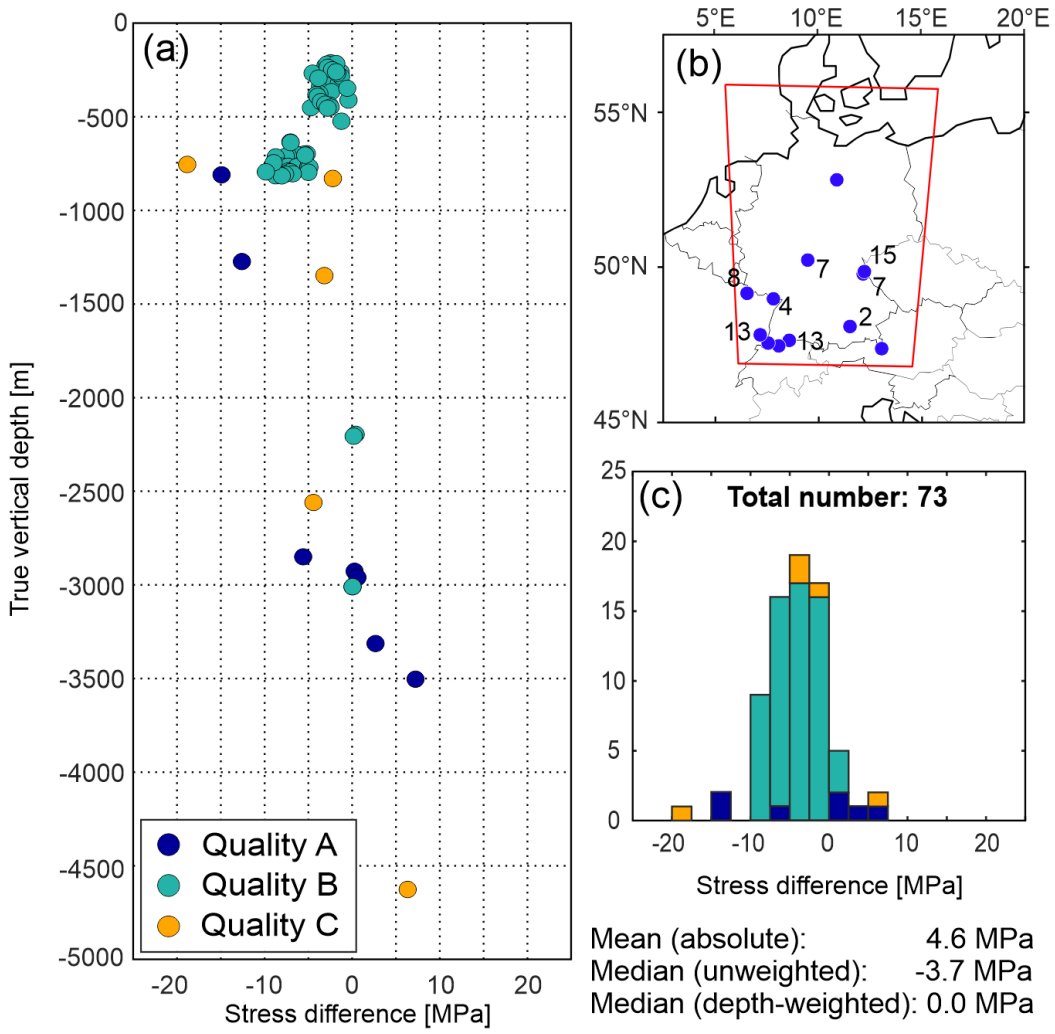

Figure 5.6: S_{hmin} magnitudes of the model in comparison to data of Morawietz and Reiter (2020) used for calibration. (a) Color-coded differences versus depth. Differences are calculated as model results minus calibration data. (b) Spatial distribution of stress magnitude data, used for calibration. Numbers indicate localities with multiple data records. (c) Color-coded histogram of the differences displayed in (a).

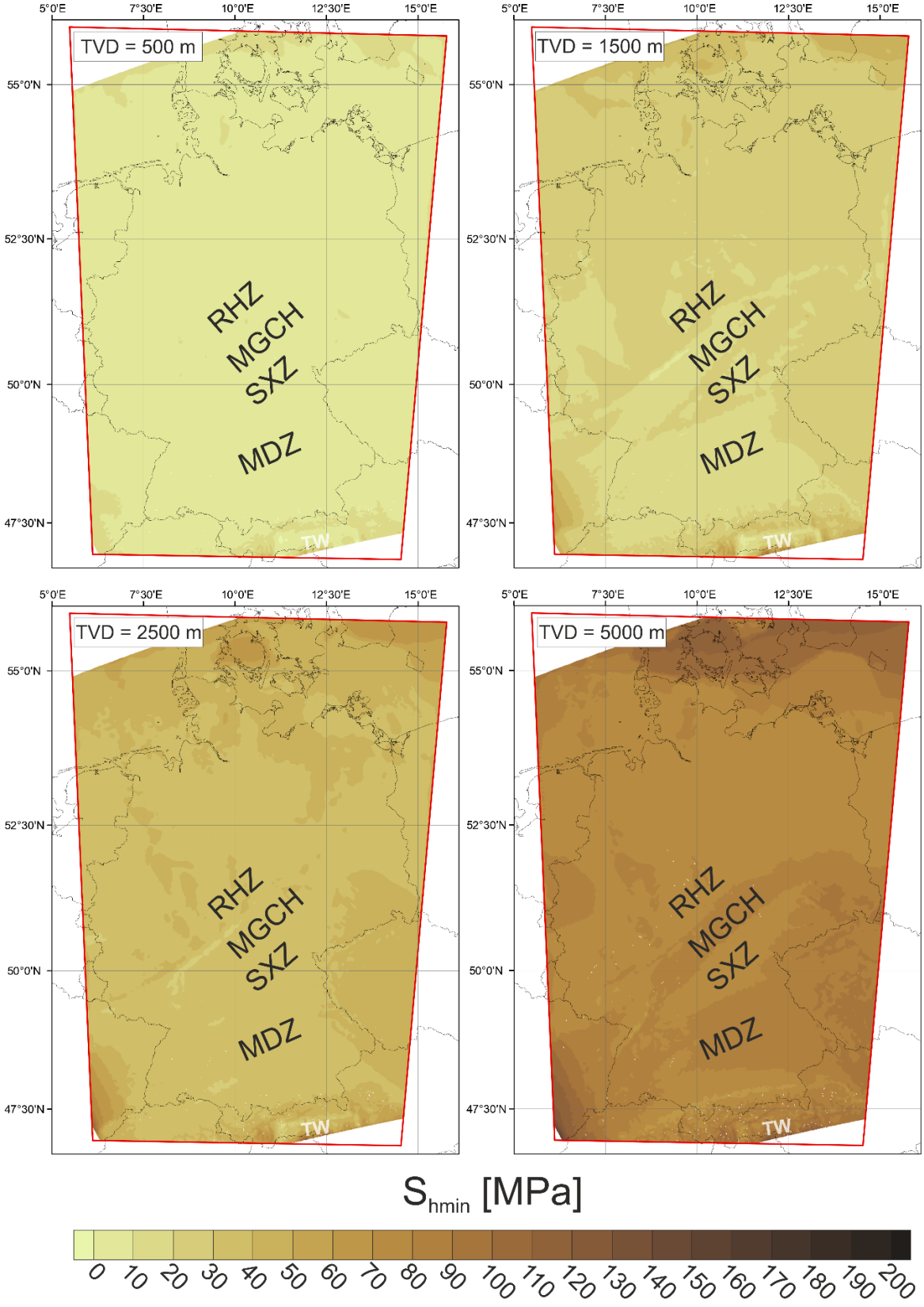

Figure 5.7: Depth sections showing the lateral distribution of the S_{hmin} magnitudes predicted by the model at four depth sections. TVD – true vertical depth. Black titles (details in Figure 5.1d): MDZ – Moldanubian Zone, MGCH – Mid German Crystalline High, RHZ – Rhenoherzynian Zone, SXZ – Saxothuringian Zone. White title (details in Figure 5.1c): TW – Tauern Window.

The depth sections displayed in Figure 5.7 show the S_{hmin} magnitudes at 500, 1500, 2500 and 5000 m TVD. The S_{hmin} at 500 m TVD shows a homogeneous stress distribution with values mainly between 0 and 10 MPa. Only the northern and southern model edges show some larger magnitudes with the exception of the Tauern Window showing lower stresses equal to the main part of the model section. The section at 1500 m shows a less homogeneous stress distribution with dominant values between 10 and 30 MPa. The highest values, up to 70 MPa in the southeast, are again, related to the model boundaries. The lowest values (0 to 10 MPa) occur along the border between the Rhenoherzynian zone (RHZ) and the MGCH (Figure 5.1d) and in the western part of the Tauern Window. Striking are the lower values (10 to 20 MPa) within the area of the MDZ and the MGCH. Sine, at 2500 m TVD these regions show the same magnitudes as the adjacent regions, in general, a homogeneous distribution with values between 30 and 40 MPa. The lowest values with 20 to 30 MPa again occur in the western part of the Tauern Window and at the border between RHZ and MGCH. The highest values are associated with the model edges. At 5000 m TVD, the stress distribution within the area of the MDZ and the MGCH seems to be inverted in comparison to the distribution at 1500 m TVD since the stress magnitudes are larger than in the adjacent areas, e.g., the Saxothuringian zone (SXZ). In general, the four depth sections of the model show a quite homogeneous distribution of S_{hmin} indicated by a maximum range of 20 to 30 MPa for each depth section, except for the model edges.

5.3.2.2 Magnitudes of S_{Hmax}

Figure 5.8 shows the S_{Hmax} magnitudes of the model in comparison to the calibration data of Morawietz and Reiter (2020). Differences displayed in Figure 5.8a and 5.8c are calculated as model results minus calibration data. Thus, positive differences indicate too high values of S_{Hmax} predicted by the model and negative differences too low S_{Hmax} magnitudes predicted. The differences are color-coded depending on their qualities defined in the magnitude database by Morawietz et al. (2020). The localities of the data used are displayed in Figure 5.8b. All data used, with a quality of A to C and from a TVD >200 m are located at eight localities in southern Germany. The differences versus depth (Figure 5.8a) and the histogram (Figure 5.8c) show a uniform distribution with a scattering of +/- 20 MPa. A dependency of depth or quality is not visible. The homogeneous fit between the model results and the calibration data is also indicated by the (unweighted) median of -0.9 MPa, which is almost equal to the depth-weighted median of 0.0 MPa. However, we also use the weighted median for the calibration with the S_{Hmax} magnitudes as for the S_{hmin} magnitudes to use a constant calibration value.

To show the lateral distribution of the S_{Hmax} magnitudes four horizontal sections at 500, 1500, 2500 and 5000 m TVD are displayed in Figure 5.9. At 500 m TVD, the magnitudes range from 0 to 30 MPa. The lowest magnitudes with 0 to 10 MPa are located within the MGCH in the vicinity to the RHZ and in the Tauern Window. The highest values of >20 MPa are associated with the model edges in the north and south and the basement outcrops of the southwestern Rhenish Massif, the Bohemian Massif, the Vosges, the Black Forest, the Odenwald and the Spessart. The section at 1500 m TVD

shows a more differentiated distribution of S_{Hmax} with values ranging from 20 to 60 MPa, with some exception along the model edges. The higher values are again associated with outcropping basement structures like the Bohemian Massif. Regions with lower S_{Hmax} magnitudes between 20 and 40 MPa are located in the MB, the URG, the Saar-Nahe Basin (SNB), the NGB and the northern part of the MGCH in the vicinity of the RHZ. The results at 2500 and 5000 m TVD confirm the trend of higher magnitudes within the areas belonging to basement structures and lower magnitudes belonging to sedimentary units. An exception is the southwestern part of the Rhenish Massif, where the magnitudes do not increase as much as within the areas of crystalline basements. Finally, at 5000 m TVD the higher S_{Hmax} magnitudes correspond to areas with outcropping or shallow lying crystalline basement structures and lower S_{Hmax} magnitudes to sedimentary or low-grade metamorphic units.

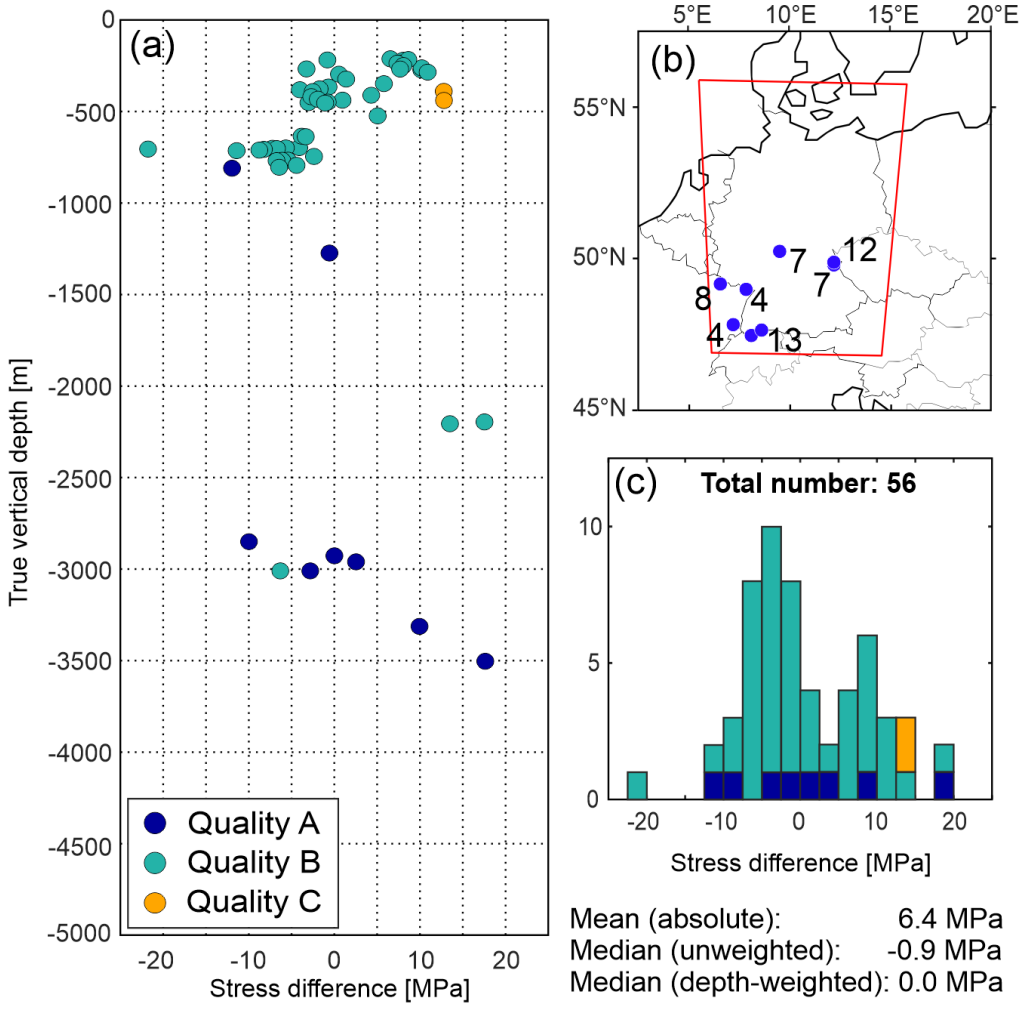

Figure 5.8: S_{Hmax} magnitudes of the model in comparison to data of Morawietz and Reiter (2020) used for calibration. (a) Color-coded differences versus depth. Differences are calculated as model results minus calibration data. (b) Spatial distribution of stress magnitude data, used for calibration. Numbers indicate localities with multiple data records. (c) Color-coded histogram of the differences displayed in (a).

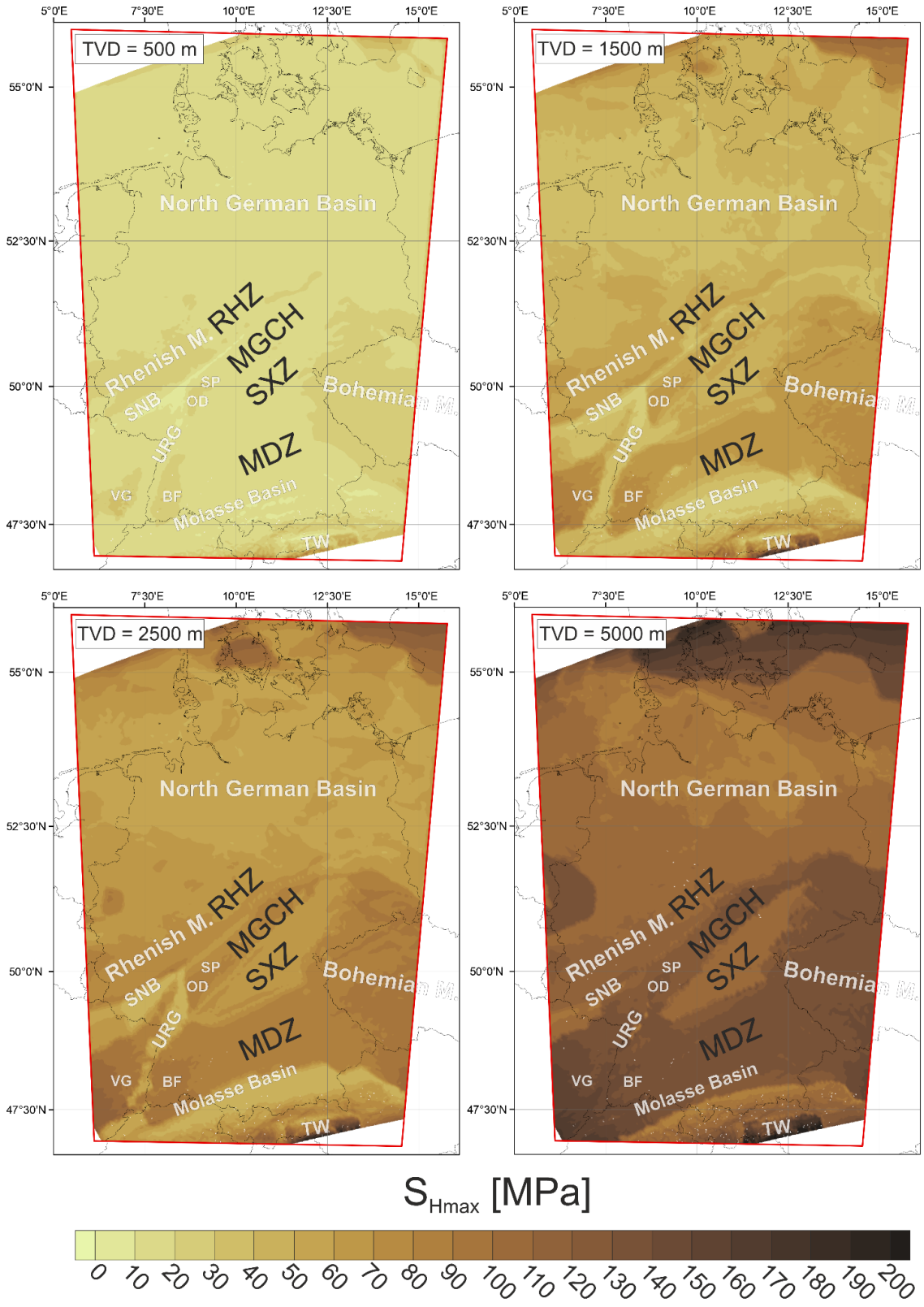

Figure 5.9: Depth sections showing the lateral distribution of the S_{Hmax} magnitudes predicted by the model at four depth sections. TVD – true vertical depth. Black titles (details in Figure 5.1d): MDZ – Moldanubian Zone, MGCH – Mid German Crystalline High, RHZ – Rhenoherzynian Zone, SXZ – Saxothuringian Zone. White titles (details in Figure 5.1c): BF – Black Forest, M – Massif, OD – Odenwald, SNB – Saar-Nahe Basin, SP – Spessart, TW – Tauern Window, URG – Upper Rhine Graben, VG – Vosges.

5.3.2.3 Magnitudes of S_V

The differences between S_V magnitudes and the data by Morawietz and Reiter (2020) are displayed in Figure 5.10. They are calculated as model results minus data of the magnitude database. Thus, too high model results lead to positive differences, too low model results to negative differences. Since the S_V magnitudes depend almost entirely on the density and are not influenced by displacement boundary conditions applied, we did not use these data for calibration but for validation to check if the densities chosen are reasonable. We use 71 values of Morawietz and Reiter (2020) from twelve localities (Figure 5.10b). As the results show, the data used from the 3DD model (Anikiev et al., 2019) are very appropriate. With the exception of two values at 750 and 3700 m TVD all differences are in the range of -2.5 to 2.5 MPa, resulting in a mean of the absolute differences of 1.1 MPa and a median of 0.0 MPa.

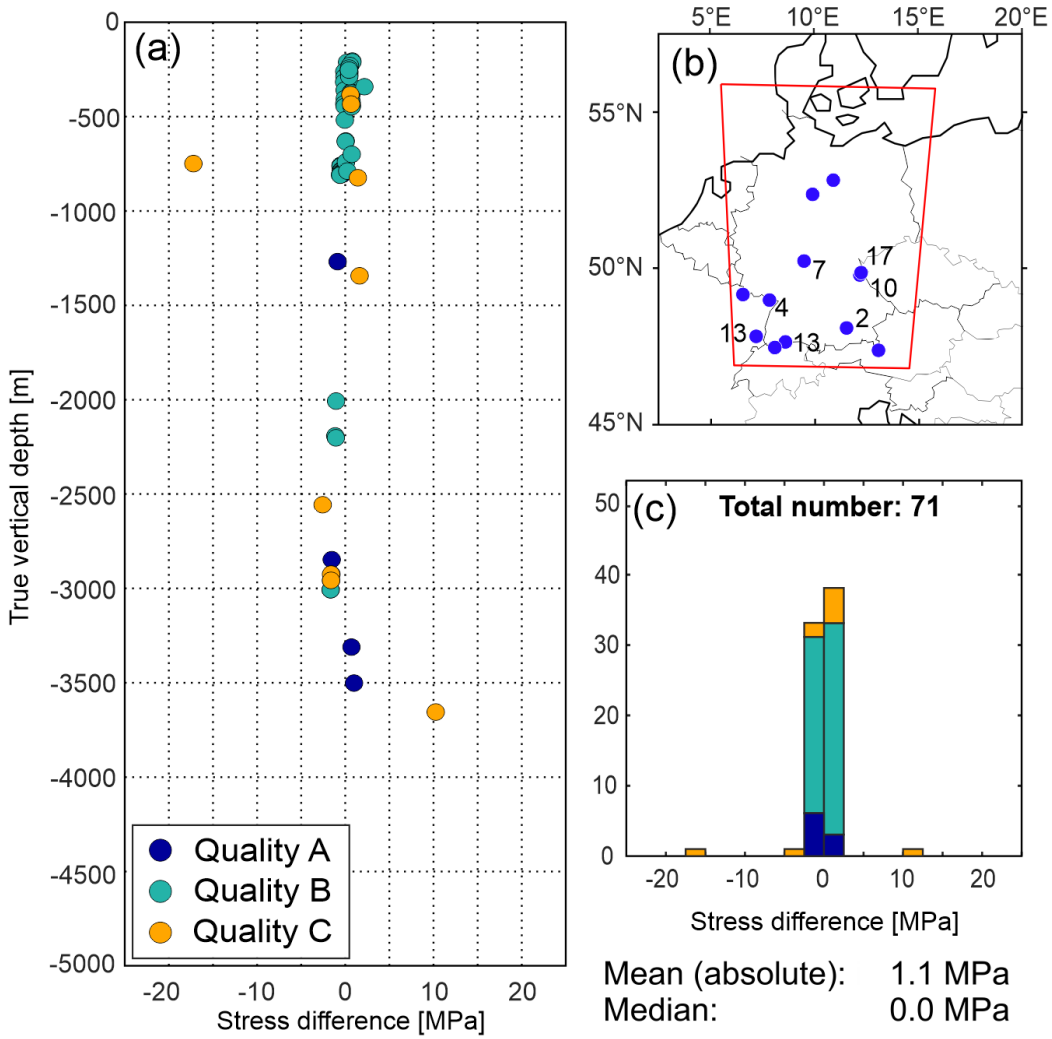

Figure 5.10: S_V magnitudes of the model in comparison to data of Morawietz and Reiter (2020). (a) Color-coded differences versus depth. Differences are calculated as model results minus data of Morawietz and Reiter (2020). (b) Spatial distribution of stress magnitude data. Numbers indicate localities with multiple data. (c) Color-coded histogram of the differences displayed in (a).

5.3.2.4 Regime Stress Ratio

To indicate the stress regime predicted by the model, the Regime Stress Ratio (RSR) for four model sections at 500, 1500, 2500 and 5000 m TVD is shown in Figure 5.11.

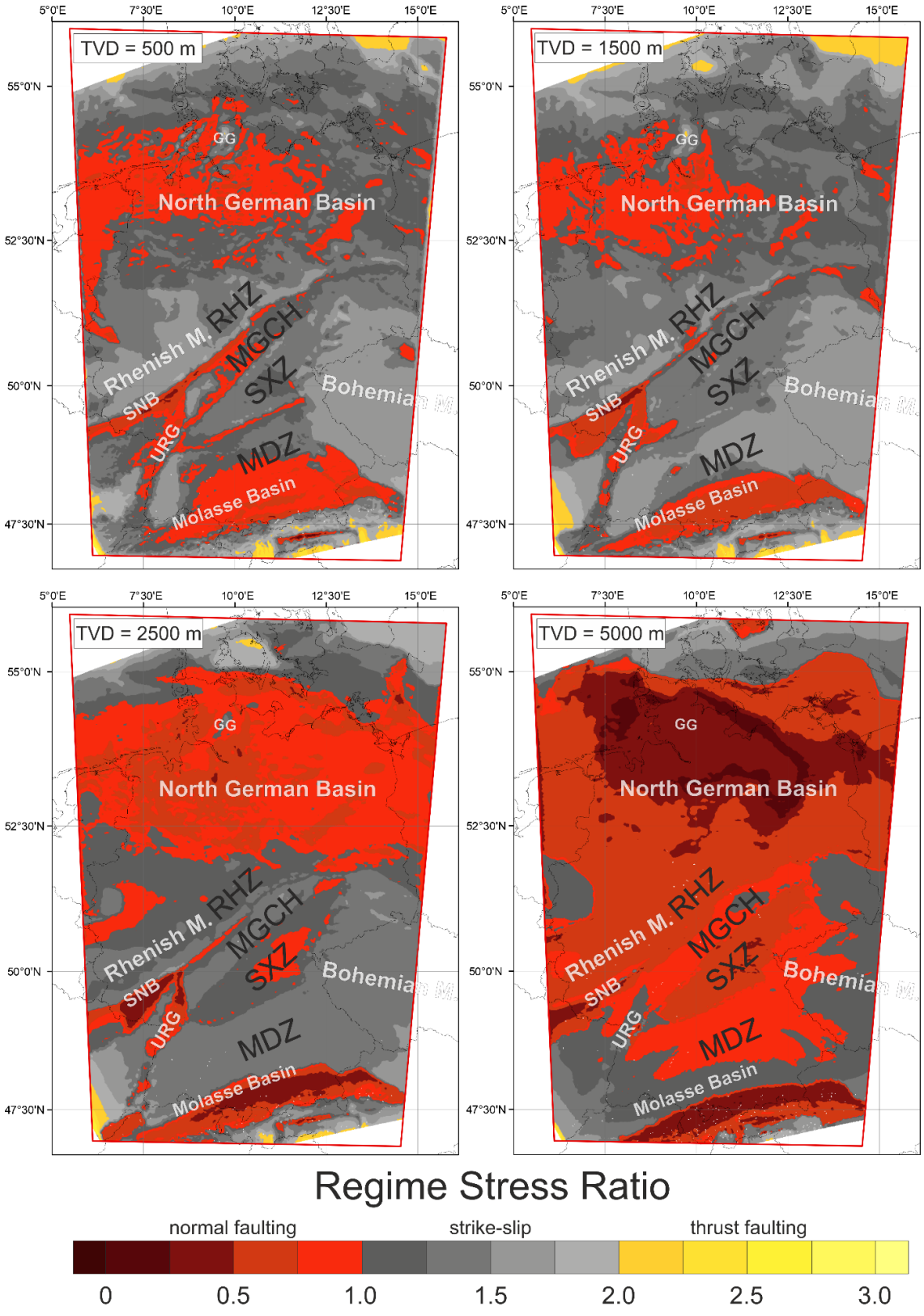

Figure 5.11: Four depth sections showing the lateral distribution of the Regime Stress Ratio (RSR) predicted by the model. TVD – true vertical depth. Black titles (details

in Figure 5.1d): MDZ – Moldanubian Zone, MGCH – Mid German Crystalline High, RHZ – Rhenoherzynian Zone, SXZ – Saxothuringian Zone. White titles (details in Figure 5.1c): GG – Glückstadt Graben, M – Massif, SNB – Saar-Nahe Basin, TW – Tauern Window, URG – Upper Rhine Graben.

The RSR is a unitless value between 0 and 3 describing seven stress states defined by Simpson (1997): radial extension (0), pure normal faulting (0.5), transtension (1), pure strike-slip (1.5), transpression (2), pure reverse faulting (2.5) and constriction (3). The RSR is derived from the regime index n (Anderson, 1905) and the ratio of stress differences ϕ (Angelier, 1979):

$$RSR = (n + 0.5) + (-1)^n(\phi - 0.5) \text{ (Simpson, 1997)} \quad (3.3)$$

$$n = \begin{cases} 0\ S_{hmin} < S_{Hmax} < S_V \\ 1\ S_{hmin} < S_V < S_{Hmax} \\ 2\ S_V < S_{hmin} < S_{Hmax} \end{cases} \text{ (Anderson, 1905)} \quad (3.4)$$

$$\phi = \frac{(\sigma_2 - \sigma_3)}{(\sigma_1 - \sigma_3)} \text{ (Angelier, 1979)} \quad (3.5)$$

The calculated RSR values at 500 m TVD show a very inhomogeneous distribution, displaying the whole range from thrust to normal faulting. Very high values - indicating a thrust faulting regime - can be found, e.g., at the model edges. Low values, indicating a normal faulting regime, occur, e.g., in the SNB, the URG, the NGB and in the MB. The model section at 1500 m TVD shows a more homogeneous pattern than at 500 m TVD. RSR values larger than 2 occur still at the model edges and within the area of the Glückstadt Graben. The lowest values still occur in the SNB, the URG, the NGB and some areas within the MB. This trend continues at 2500 m TVD. Here, almost the entire SNB show values <0.5 indicating a pure normal faulting regime. As at 1500 m TVD, also the NGB and the southern part of the MB show a normal faulting regime and additionally also the SXZ. In contrast to the 1500 m TVD section, several regions show lower values at 2500 m TVD. The deepest model section shown at 5000 m TVD shows a much more homogeneous distribution than at 500 m with large areas indicating a normal faulting regime. The trends described for 2500 m TVD continues, except within the URG. Up to a TVD of 2500 m the RSR in this area is lower in comparison to the surrounding areas, but at 5000 m TVD the RSR is higher.

5.3.2.5 Stress gradients

Figure 5.12 shows modeling results from three major sedimentary basins in Germany, the NGB, the URG and the MB, in comparison to available data partially also used for calibration. Results and data of the upper 200 m TVD are not displayed to avoid showing data influenced by topography or free surface effects. The model results are displayed as magnitude sets (S_V, S_{hmin} and S_{Hmax}) from virtual wells up to 8 km TVD located at the locations from which measurement data are shown. This results in a compilation of 12 magnitude sets for the MB, five magnitude sets for the URG and 45 magnitude sets for the NGB.

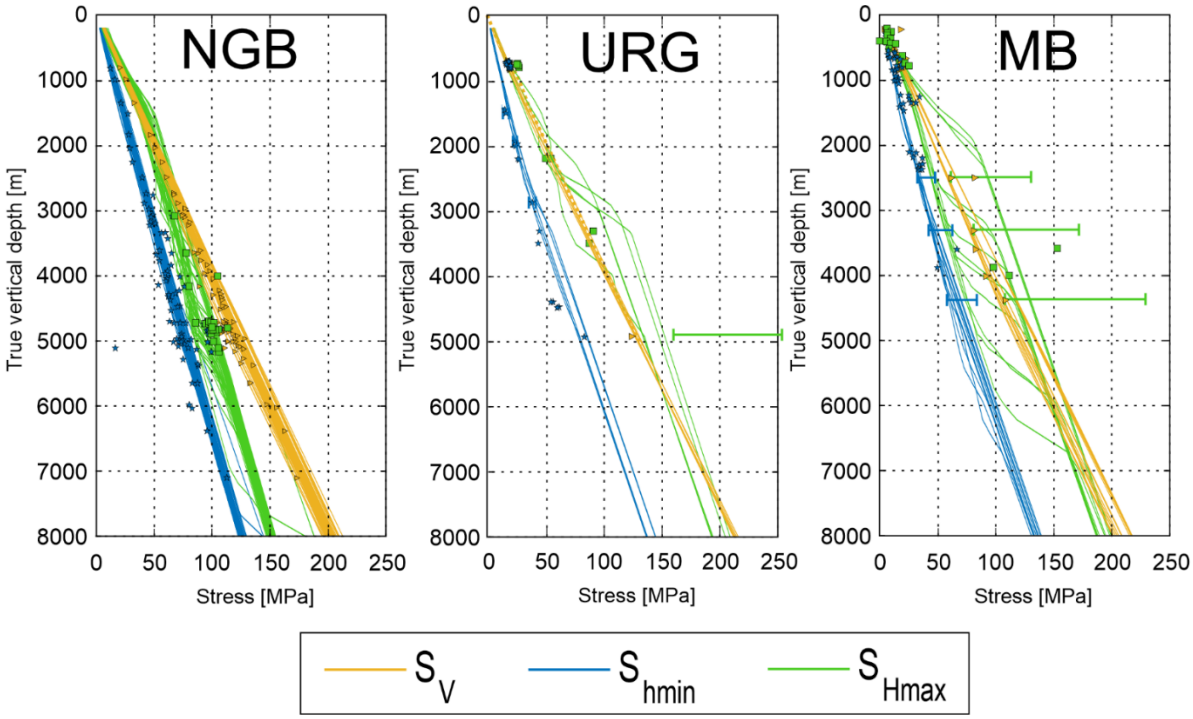

Figure 5.12: Results from multiple virtual wells in the corresponding sedimentary basin of the model in comparison to measured and calculated magnitudes of S_V, S_{hmin}, and S_{Hmax}. The uncertainties of the magnitudes if specified are displayed as error bars. **North German Basin (NGB):** Röckel and Lempp (2003), Fleckenstein et al. (2004), Stöckhert et al. (2013). **Upper Rhine Graben (URG):** Cornet and Burlet (1992), Klee and Rummel (1993), Valley and Evans (2007), Häring et al. (2008), Meixner et al. (2014), Azzola et al. (2019). **Molasse Basin (MB):** nagra (2001), Seithel et al. (2015), Backers et al. (2017), Budach et al. (2017), Drews et al. (2019), Garrard et al. (2021).

The results for the NGB show quite uniform magnitudes for all 45 magnitude sets displayed. The modeled S_{hmin} magnitudes show the smallest range of values with a maximum range of ~10 MPa except for two outliers below ~5000 m TVD. The range of the S_{Hmax} magnitudes are larger with an average range of ~15 MPa, a maximum of ~25 MPa at ~5000 m TVD and again two outliers. The S_V magnitudes show a trend of increasing scattering with depth, starting with a range of <5 MPa at 200 m TVD to a range of ~20 MPa at 8 km TVD.

The five data sets from the URG show similar gradients for S_{hmin} and S_V but significant differences for the S_{Hmax} magnitudes. The S_{Hmax} magnitudes are also the only ones that show significant changes of the gradients with depth. While the S_{hmin} and S_V magnitudes show an almost linear increase with depth, some S_{Hmax} magnitudes between 2000 and 3500 m increase sharply and some even show decreasing or constant values. The compilation of the MB shows the most inhomogeneous results. At about 1000 m TVD, the magnitudes of S_{Hmax} split in two groups. The magnitudes of three virtual wells show an increase to ~40 MPa at 2500 m TVD in contrast to nine virtual wells, which show continuous S_{Hmax} magnitudes. The S_V and S_{hmin} values of these three virtual wells also increase but less obviously to 5 to 10 MPa higher values. With increasing depth at about 2500, 3200, 3700, 4200, 5000 and 6000 m TVD, other virtual wells also show such increasing magnitudes and converge to the higher

magnitude trend. In general, there seems to be a lower and a higher magnitude gradient with a transition zone between 1000 and 6500 m TVD changing from one dominating gradient (0-1000 m TVD) to another (>6500 m TVD). At 8 km TVD, all magnitudes are roughly homogenous with S_{hmin} magnitudes of 130 to 140 MPa, S_{Hmax} magnitudes of 180 to 200 MPa and S_V magnitudes of 200 to 215 MPa.

5.3.2.6 Fracture Potential

As an additional result the Fracture Potential (FP) of four depth sections is displayed in Figure 5.13. The FP based on Connolly and Cosgrove (1999) and Eckert and Connolly (2004) is a dimensionless value indicating how close to failure the stress state is. The calculation is described in detail by Heidbach et al. (2020). The FP is defined *as actual maximum shear stress* divided *by the acceptable shear stress* (Equation 5.6):

$$FP = \frac{actual\ maximum\ shear\ stress}{acceptable\ shear\ stress} \tag{5.6}$$

Therefore, a FP of >1 indicates failure and lower FPs represent a stable state of stress. The *actual maximum shear stress* is calculated as mean of the maximum (σ_1) and minimum (σ_3) principal stress (Equation 5.7):

$$actual\ maximum\ shear\ stress = \frac{1}{2}(\sigma_1 - \sigma_3) \tag{5.7}$$

The acceptable maximum shear stress is calculated as (Equation 5.8):

$$acceptable\ shear\ stress = c\ cos\varphi + \frac{1}{2}(\sigma_1 + \sigma_3)\ sin\ \varphi \tag{5.8}$$

The FP is calculated with individual cohesion (c) and friction angle (φ) for each model unit (Figure 5.13), except for the Zechstein salt unit since salt behaves visco-elastic. Therefore, the regions where Zechstein salt occur are left white in Figure 5.13. The results in Figure 5.13 show a stable stress state with a FP between 0 and 0.6. The highest values of 0.5 to 0.6 occur at 1500 m depth. In general, there is an increase of the FP up to 1500 m TVD. With further increasing depth the FP decreases. At 500 m TVD relative low values are associated with sedimentary units as within the NGB, the SNB or the Mesozoic units in southern Germany. Higher values are mainly associated with outcropping basement units, for example within the Bohemian and Rhenish Massif, the Vosges and the Black Forest. This trend is also visible at 1500 m TVD with a generally higher FP. High values are associated with crystalline basement units, e.g., the MDZ, the MGCH or the Tauern Window, low values are predicted for the NGB, the SNB or the MB. At 2500 m TVD such a clear trend is not visible anymore, but a low FP is still located within in the SNB. An interpretation of the results from the NGB is difficult for this depth section, since the Zechstein salt unit is dominant here. At 5000 m TVD the NGB is still a region with a relative low FP. However, in contrast to the depth sections at 500 or 1500 m TVD

some regions show opposite trends. For example, the Bohemian Massif with former relatively high values or the SNB with former relatively low values.

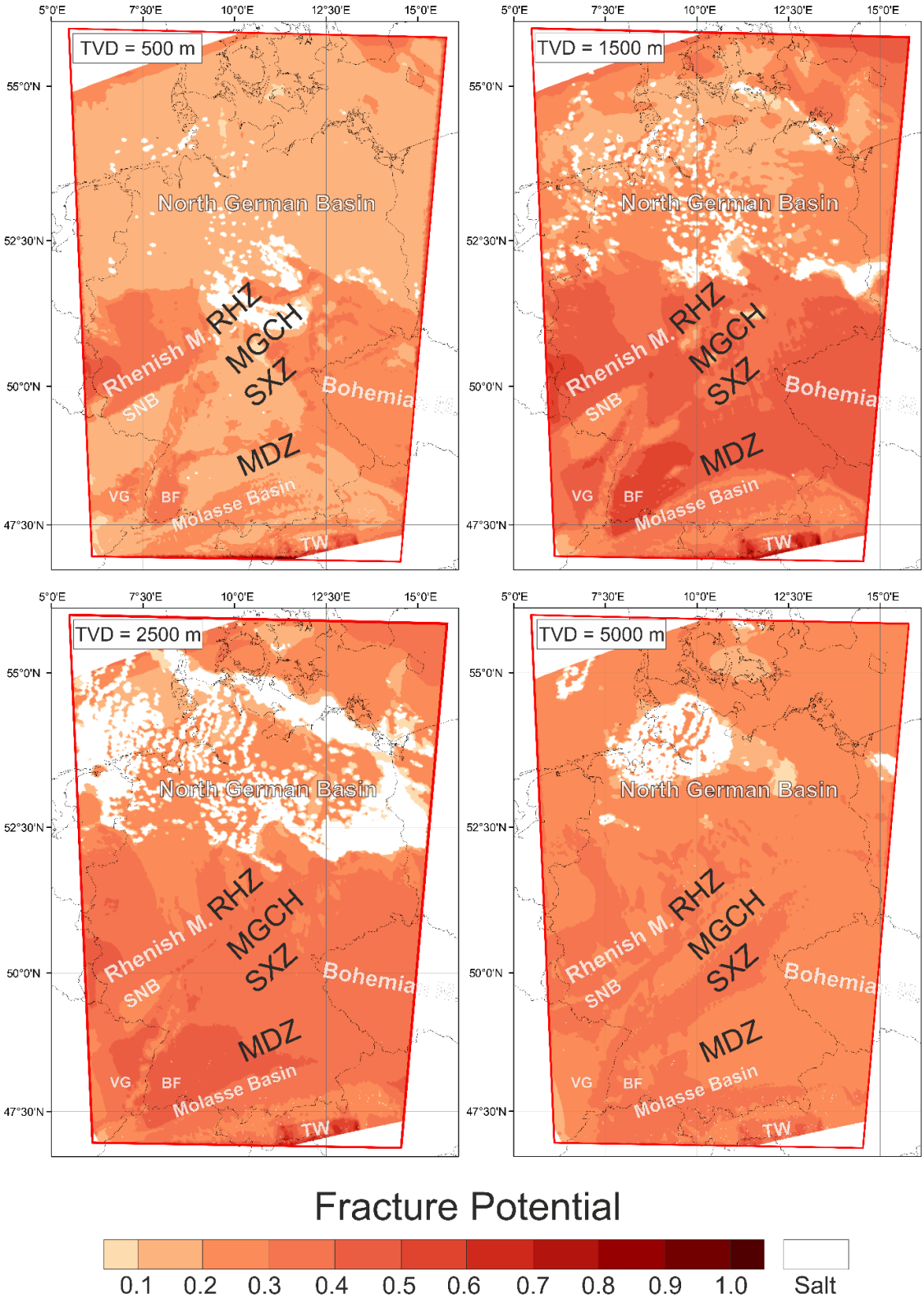

Figure 5.13: Depth sections showing the lateral distribution of the Fracture Potential calculated for the model results. TVD – true vertical depth. Regions where Zechstein salt occurs are left white. Black titles (details in Figure 5.1d): MDZ – Moldanubian

Zone, MGCH – Mid German Crystalline High, RHZ – Rhenoherzynian Zone, SXZ – Saxothuringian Zone. White titles (details in Figure 5.1c): BF – Black Forest, M – Massif, SNB – Saar-Nahe Basin, TW – Tauern Window, VG – Vosges.

5.4 Discussion

5.4.1 Orientation of S_{Hmax}

Although our results lie almost entirely within the standard deviation of the S_{Hmax} orientation derived from the WSM and some additional data of Levi et al. (2019) and a median of deviation of 0.3° suggest a very good fit, a closer look indicates some discrepancies (Figure 5.5). The orientations of S_{Hmax} predicted by our model (Figure 5.5a) show a homogenous NNW-SSE pattern with some small deviation to N-S but the mean S_{Hmax} orientation of the WSM show several regions with divergent patterns, e.g., within the eastern part of the NGB showing NNE-SSW orientations or the central part of Germany with dominant NW-SE orientations. These results indicate that our model does probably not include some relevant factors or our displacement boundary conditions applied are too simple to reproduce the pattern of the orientation of S_{Hmax}. The median deviation of 0.3° and the distribution of the histogram support the former since differing displacements, e.g., at the eastern and western edges would probably only shift the distribution as a whole. Implemented lateral stiffness contrasts do not seem to have a significant impact on the regional stress field, e.g., predicted by Grünthal and Stromeyer (1994), Marotta et al. (2002) or Reiter (2021), despite Young's modulus contrasts of >50 GPa, e.g., at the southern edge of the SNB between weak Rotliegend sediments (15 GPa) and the stiff upper crust (70 GPa). However, laterally there are no contrasts of the Young's modulus in the upper crystalline crust. Thus, the softer units lie on a homogeneous and stiff block. This could be an explanation of the quite homogeneous orientations of S_{Hmax} of our model within in the sedimentary units but also for parts of the crust since our model assumption of linear elasticity does not represents the ductile behavior of lower parts of the crust and the mantle (e.g., Stüwe, 2007).

Processes not included in our model, which may also affect the stress field within the model region, are isostatic buoyancy effects in Scandinavia (Kaiser et al., 2005) or in the south due to erosion, deglaciation and potential slab break off below the Alpine chain (Przybycin et al., 2015; Sternai et al., 2019). In addition, the lithosphere-asthenosphere-boundary (Cacace, 2008) or density contrasts in the lower crust, e.g., the Pritzwalk anomaly (Krawczyk et al., 2008) could explain the misfit in the northeast. Effects due to salt decoupling leading to a regional stress field below and a more local stress field above the Zechstein unit (Roth and Fleckenstein, 2001; Röckel and Lempp, 2003; Heidbach et al., 2007) should have no influence since we did not use the data from the units above.

5.4.2 Absolute stress and stress regime

In general, the predicted S_{hmin} magnitudes fit the values of Morawietz and Reiter (2020) quite well with differences between -20 and +7.5 MPa and a mean of the absolute differences of 4.6 MPa (Figure 5.6) and an overall good fit to additional data in Figure 5.12. However, the depth dependent differences

(Figure 5.6a) and the compilation of the URG and the MB (Figure 5.12) indicate too low magnitudes of S_{hmin} within the upper ~1500 m of the model. Since the shallow calibration data (Figure 5.6b) and additional data of the MB (Figure 5.12) are partly located in young sedimentary units, the Young's modulus in the model could possibly be too high for these units, despite the implemented Young's modulus gradient. Furthermore, unconsolidated sediments can behave in a visco-elastic manner (e.g., Chang and Zoback, 1998, Zoback, 2007), which the linear elastic properties of our model cannot represent. Both, a lower Young's modulus and visco-elastic properties would lead to higher S_{hmin} magnitudes since the S_{hmin} magnitudes would approach the S_V magnitudes. Missing visco-elastic properties can also explain the too low values at ~800 m TVD, data from Wittelsheim, in the southwestern URG (Figure 5.12) measured in an evaporitic layer (Cornet and Burlet, 1992). Another clue to explain the low values could be the geographic distribution of the data. Almost all calibration data used and the data of the MB indicating this trend are located in the southern part of Germany. Available data from the northern part of Germany are sparse, but do not confirm this trend (Figure 5.12). A possible trend to slightly too high values in the lower part of the model indicated by the three deepest values in the general comparison (Figure 5.6) cannot be confirmed by the results in Figure 5.12.

The predicted S_{Hmax} magnitudes also show a good fit to the values of the magnitude database by Morawietz and Reiter (2020) (Figure 5.8) despite a wider range of differences between -20 and +20 MPa and a higher mean of the absolute differences of 6.4 MPa in comparison to the S_{hmin} magnitudes. However, available S_{Hmax} magnitudes are usually calculated and not measured and therefore have larger uncertainties (Morawietz et al., 2020). Furthermore, calibration data from units which are parametrized with mean mechanical properties, e.g., the Triassic unit or from thin units which are numerically not sufficiently represented by our model resolution can explain the wider range. Since, differing stiffnesses have a significantly higher influence on S_{Hmax} magnitudes than on S_{hmin} magnitudes (Figure 5.12). A quantification of the influence of mean properties on the results is possible, e.g., using the HIPSTER tool of Ziegler (2021) but not feasible for such a large-scale model, since thousands of calculations would be necessary for such an estimation.

Although the S_{Hmax} magnitudes of our model do not show a general depth trend as described for the S_{hmin} magnitudes, the differences in the upper 1000 m TVD show a distribution that is very similar to the one of the S_{hmin} magnitudes within this depth range (Figure 5.6 and 5.8). This does not fit to the assumption that the Young's modulus might be too high because too low S_{Hmax} values rather indicate too low Young's modulus values. Incorporation of visco-elastic properties could increase both magnitudes if the S_{Hmax} magnitudes are lower than S_V, which is partly the case indicated by a normal faulting regime in Figure 5.11 and 5.12. Another possibility to increase both horizontal magnitudes at the same time is an increase of the vertical stress, a higher Poisson's ratio, a higher stress input due to the boundary conditions or a higher k ratio of the initial stress. Increasing stresses by increasing the density does not seem to make sense since the fit with the S_V magnitudes (Figure 5.10) is almost perfect. A higher Poisson's ratio for different units within this specific depth interval only is difficult

to explain. The third and fourth possibility, an increased shortening and reduced extension by the displacement boundary conditions or an increased k-ratio within the upper part of the model only, are difficult to implement and are difficult to explain from a tectonic point of view.

Another view inside the model is given by the compilation of virtual wells in Figure 5.12. The magnitudes used for comparison from the NGB are mainly based on two datasets. A compilation of Röckel and Lempp (2003) from the eastern and central part of the NGB and a dataset by Fleckenstein et al. (2004) from the western part of the NGB. The compilation of Röckel and Lempp (2003) only contains S_V and S_{hmin} magnitudes, the compilation of Fleckenstein et al. (2004) all three principal stresses. However, the data sets show some general differences. The data from Fleckenstein et al. (2004) show a near isotropic stress state, particularly well visible between 4750 and 5250 m where the stress magnitudes of S_{hmin}, S_{Hmax} and S_V are very close to each other. The smaller magnitudes of S_{hmin} and also the larger S_V magnitudes visible within this depth range are from Röckel and Lempp (2003). In general, the model results of all virtual wells displayed show a better fit to the data of Röckel and Lempp (2003). However, it is remarkable that the S_{Hmax} magnitudes contrary to the S_{hmin} and S_V magnitudes fit the data by Fleckenstein et al. (2004) quite well. The misfit between these datasets could be explained due to the different location within the NGB. Another possible reason for this discrepancy could be the different measurement methods, since the data by Fleckenstein et al. (2004) are based on core samples while the data of Röckel and Lempp (2003) are in situ measurements. However, despite these inconsistencies the overall fit of the model results to the displayed data within the NGB is good.

The fit of the second virtual well compilation for the URG in comparison to the predicted magnitudes is also good. Regarding the S_{hmin} magnitudes, the results show only significant differences to the measured magnitudes at 800 m TVD and between 3500 and 4500 m TVD. The differences at ~800 m TVD, indicating ~10 MPa too low magnitudes, are probably a result of inappropriate material properties in the model for this area. As mentioned before, these dataset is measured in an evaporitic layer at Wittelsheim (Cornet and Burlet, 1992). However, our model does not include visco-elastic properties. Between 3500 and 4500 m TVD the model results indicate a trend to too high S_{hmin}. However, the deepest data record at 5000 m TVD fits to the model results. The S_{Hmax} data in general show a wider range of values as the S_{hmin} data. At ~800 and ~5000 m TVD our results indicate too low values. However, the value at 5000 m TVD from Basel (Häring et al., 2008) must be interpreted with care due to the very high uncertainty indicated by the error bar. The differences between 2000 and 3500 m TVD show significant deviations up to ~30 MPa but all data records are within the range of our predicted values. At ~2200 m TVD the lowest differences occur for all locations, except the results from Soultz-sous-Forets. Although both measured S_{Hmax} magnitudes shown at 2200 m TVD are from Soultz-sous-Forets (Klee and Rummel, 1993) the model results from this region indicate too high values.. A possible explanation are altered granites in the upper part of the crystalline basement as described by Aichholzer et al. (2016) which are not well represented by our high Young's modulus of 70 GPa. A lower Young's modulus would possibly lead to lower S_{Hmax} and a better fit. However, the altered granites are only about 150 m thick and therefore not able to explain the full discrepancy.

Remarkable are the S_{Hmax} magnitudes between 2500 and 3500 m TVD predicted for Bruchsal, showing a very low gradient leading to ~30 to 40 MPa lower values as predicted for the other locations. This trend can be explained by a thick Rotliegend layer within this region (GeORG-Projektteam, 2013; Meixner et al., 2014), with a low Young's modulus of 15 GPa. In addition, four of the five virtual wells show a significant change of the S_{Hmax} gradients with depth. For example, Rittershoffen and Soultz-sous-Forets - located only ~10 km apart from each other – show almost similar S_{Hmax} values below 3000 m TVD, but the gradient change occur below 1500 m TVD at Soultz-sous-Forets and below 2250 m TVD at Rittershoffen. The depth at which the 'jump' of the S_{Hmax} magnitudes occurs fits quite perfectly to the boundary between the crystalline basement and the sedimentary units of the URG. Rittershoffen is a little east to Soultz-sous-Forets and further away from the western graben shoulder of the URG and therefore the top of the crystalline basement in Rittershoffen is located at ~2250 m TVD and at ~1550 m TVD in Soultz-sous-Forets (Aichholzer et al., 2016).

The S_{hmin} magnitudes of our model within the MB show a good fit to the comparison data displayed below 2000 m TVD. However, as already mentioned, our model results indicate partially too low values in the upper 1500 m. The S_{Hmax} magnitudes again show larger variations. Similar to the results of the URG, in all virtual wells the S_{Hmax} magnitudes increase if the crystalline basement is reached. Thus, since the depth of the crystalline basement differs in almost every virtual well due to the southward increase of the sediment thickness in the MB, the resulting stresses are inhomogeneous. A remarkable outlier is the data record at ~3600 m from Mauerstetten (Backers et al., 2017).

In general, the predicted S_{Hmax} magnitudes of the MB and URG show the impact of the vertical model resolution. The transition zone between sediments and crystalline basement is ~750 m, which corresponds to about three element rows. A higher model resolution could decrease this transition zone significantly.

Since the calibration data (Figure 5.6 and 5.8) and the compilations of Figure 5.12 only show pointwise data the S_{hmin} and S_{Hmax} magnitudes are additionally displayed by several depth sections to focus on the lateral distribution. In general, the depth sections of Figure 5.7 displaying the lateral distribution of the S_{hmin} magnitudes show a more homogeneous pattern than the S_{Hmax} magnitudes in Figure 5.9. However, in both figures high magnitudes of S_{hmin} or S_{Hmax} are associated with crystalline basement units, e.g., the Bohemian Massif in the southeast or the EEC in the northeast and low magnitudes are often related to sedimentary basins, e.g., the NGB or the MB or regions with outcropping low-grade metamorphic sediments, e.g., the RHZ or SXZ. This correlation can be explained by the combination of stiff units with relatively high densities and softer units, which often have lower densities. However, a high stiffness alone is not sufficient for high horizontal stress magnitudes. This is because high stiffness leads to an increase in S_{Hmax} magnitudes as a result of applied shortening but at the same time to a decrease in the S_{hmin} magnitude as a result of applied extension. Accordingly, a higher Young's modulus leads to higher S_{Hmax} magnitudes and lower S_{hmin} magnitudes. This effect can be reduced or increased by the influence of S_V. S_V reduces or increases the S_{hmin} and S_{Hmax} magnitudes equally and,

since it is defined by density, a high density leads to higher horizontal stresses and a lower density to lower horizontal stresses. An example for this combined effect can be seen within the MDZ and MGCH where an inversion of the S_{hmin} magnitudes relative to the adjacent regions occurs between 1500 and 5000 m TVD (Figure 5.7). The MDZ and MGCH are regions with a thin sedimentary cover. Therefore, the low S_{hmin} magnitudes at 1500 m occur due to the high Young's modulus of 70 GPa and a lower magnitude of S_V due to the thin sedimentary cover. The adjacent regions show higher S_{hmin} magnitudes, e.g., the Bohemian Massif with a similar Young's modulus but a higher S_V due to the missing sedimentary cover or the SXZ due to a lower Young's modulus and a higher S_V. At 5000 m TVD the MDZ and MGCH show higher S_{hmin} values than the SXZ but more similar to the ones in the Bohemian Massif. This shows that the effect of the thin sedimentary cover vanishes with depth. Furthermore, the relation between the S_{hmin} magnitudes in the Bohemian Massif and the RHZ and NGB shows that the influence of a higher density (Bohemian Massif > RHZ & NGB) exceeds the effect of a lower Young's modulus (RHZ & NGB < Bohemian Massif). The lateral distribution of the S_{Hmax} magnitudes is easier to explain, since a higher density and a higher Young's modulus result in high stresses and a lower density and a lower Young's modulus in low stresses. Some boundary effects are visible at the northern and southern model edge where the compressional boundary conditions are defined, showing the highest values for S_{hmin} and S_{Hmax}. An exception is the stiff Tauern window (Young's modulus: 70 GPa), showing lower magnitudes of S_{hmin} and S_{Hmax} up to 1500 m TVD than the weaker surrounding thrusted units of the Alps (Young's modulus: 23 GPa) do. This is probably due to the fact, that the Tauern window is pushed into the softer units and the soft units absorb the stress. This is also indicated by the high RSR values within the surrounding units (Figure 5.11, 500 to 2500 m TVD), indicating high horizontal stresses. Furthermore, remarkable low magnitudes of S_{hmin} and S_{Hmax} occur at the boundary between the RHZ and the MGCH up to 2500 m TVD. This might be an effect due to the vertical boundary between these units (Ahlers et al., 2021a).

The prediction of the stress regime and possible stress regime changes are important for the stimulation of geothermal reservoirs (Azzola et al., 2019), borehole stability and for directional drilling (Rajabi et al., 2016). In particular, if the stress regime change leads to an increase of the differential stress, e.g., due to a change from a normal faulting to a strike-slip faulting regime. For this, the RSR indicating lateral and vertical stress regime changes is a useful parameter. For example, the RSR values in the Glückstadt Graben up to 2500 m TVD, which are higher as in the adjacent areas of the NGB. Probably, the predicted strike-slip regime is related to major salt walls within this region (Maystrenko et al., 2005). The low density of salt (2100 kg/m³) leads to a relative low S_V magnitude and, as a result, the horizontal stresses exceed S_V and even a thrust faulting regime at 1500 m TVD is partially established. Very low RSR values at 2500 m TVD in the SNB show an opposite effect. The weak Rotliegend sediments with a Young's modulus of 15 GPa lead to low horizontal stresses and therefore the RSR value decreases, leading to a normal faulting regime. This is also well visible in the depth section at 5000 m TVD in the NGB. The trend towards relatively higher values in the URG than in the surrounding areas at 5 km TVD is related to a lower S_V in comparison to the graben shoulders

because of the sedimentary fill of the URG but similar horizontal stresses. Above 5 km TVD, the horizontal stresses are lower in the URG due to the lower Young's modulus of the sediments. However, at 5 km TVD the basement of the URG is reached with a similar Young's modulus as for the graben shoulders. In general, a trend towards a normal faulting stress regime due to increasing dominance of S_V with depth is visible. Thus, the depth section at 5000 m TVD shows mainly RSR values smaller than 1.0.

This trend is also clearly visible in Figure 5.12. All results displayed show a stress regime change from a dominant strike-slip regime in the uppermost part of the model to a normal faulting regime at 8000 m TVD. However, within the depth range of 200 to 8000 m TVD the results of the individual virtual wells differ sometimes significantly. The results from the NGB show an almost continuous change from a strike-slip regime in the upper 500 m to a normal faulting regime at TVDs >3000 m with a transition zone between 500 and 3000 m TVD where the stress regime is not the same for all virtual wells. The virtual wells located in the URG show a more complex stress regime change with depth, with differences up to 7500 m TVD. In the upper 1500 m, the magnitudes of S_V and S_{Hmax} are almost equal resulting in a strike-slip to reverse faulting regime or transpressional regime, respectively. Between 1500 and 2500 m TVD almost all S_{Hmax} magnitudes get higher than S_V resulting in a strike-slip regime. Between ~5500 and 7500 m TVD, the stress regime changes to a normal faulting regime. An exception are the results at Bruchsal, showing several changes of the stress regime up to 5500 m TVD between strike-slip and normal faulting regimes. The results of the MB show almost similar results as the results from the URG. Starting with a strike-slip to reverse faulting regime within the upper parts of the model, followed by a strike-slip regime and finally a normal faulting regime.

5.5 Conclusions

The model presented is a further step towards a robust prediction of the crustal stress state of Germany with focus on sedimentary basins. It is based on Ahlers et al. (2021a), but significantly improved. An 18-time higher mesh resolution resulting in a lateral resolution of 2.5 km and a vertical resolution of up to 250 m, 15 additional units within the sedimentary layer and an additional model calibration with S_{Hmax} magnitudes, provide a refined prediction of the crustal stress field of Germany. The 3D geomechanical-numerical model provides the complete 3D stress tensor for the entire model volume. Overall, the results show a good fit to all three principal stress magnitudes S_V, S_{hmin} and S_{Hmax} indicated by absolute differences of 0.0 MPa for S_V, 4.6 MPa for S_{hmin} and 6.4 MPa for S_{Hmax}. The differences to the calibration data are mainly within in a range of +/- 10 MPa for the S_{hmin} magnitudes and within a range of +/- 20 MPa for the S_{Hmax} magnitudes. Despite the overall good fit, some data indicate too low S_{hmin} values in the upper 1500 m TVD of our model. However, additional data from the NGB does not confirm a general trend. Apart from the magnitudes we compare our results also with a mean orientation of S_{Hmax} derived from the WSM (Heidbach et al., 2016a) and additional data of Levi et al.

(2019). Our predicted orientations of S_{Hmax} show an overall good fit with a median of 0.3° and our results lie almost entirely within the standard deviation of the derived WSM data. However, our model does not resolve perturbations of S_{Hmax} on smaller local scales as indicated by the data of the WSM.

Some limitations result from the size of our model. Due to the size, it is not possible to define visco-elastic properties, e.g., for the Zechstein salt unit. Furthermore, the vertical resolution is still too low to numerically represent all units sufficiently and at the same time some inhomogeneous units like the Triassic are still combined. Accordingly, sub modeling is a useful method to enable a higher resolution and stratigraphic refinement (e.g., Ziegler et al., 2016). Such smaller models on local or reservoir scale also enable consideration of varying rock properties (e.g., Ziegler, 2021), a quantification of model uncertainties and the implementation of structures that influence the stress field on a local scale, e.g., faults. In addition, more high quality data records, especially magnitude data from north Germany are necessary for a more reliable calibration.

Acknowledgements

This study is part of the SpannEnD Project (http://www.SpannEnD-Projekt.de, last access: 2021/11/29), which is supported by Federal Ministry for Economic Affairs and Energy (BMWI) and managed by Projektträger Karlsruhe (PTKA) (project code: 02E11637A). Calculations for this research were conducted on the Lichtenberg high performance computer of the Technische Universität Darmstadt. Coastlines and borders used in the figures are based on the Global Self-consistent Hierarchical High-resolution Geography (GSHHG) of Wessel and Smith (1996). We acknowledge support by the Deutsche Forschungsgemeinschaft (DFG – German Research Foundation) and the Open Access Publishing Fund of Technische Universität Darmstadt.

Author contribution

Conceptualization of the project was done by AH, TH, KR, OH and BM. Construction, discretization and calibration of the model were done by SA. Data for the model and its calibration were collected and provided by SA, LR, SM, MSW and DA. Evaluation of the model results and their interpretation were performed by SA with the support of AH, TH, KR, BM, LR, OH and SM. SA wrote the paper with help from all coauthors. All authors read and approved the final paper.

Availability of data and materials

The model geometry and the results of our model have been published and are publicly available at: https://tudatalib.ulb.tu-darmstadt.de/handle/tudatalib/2624.5 (see Ahlers et al., 2022b).

6 The analysis of slip tendency of major tectonic faults in Germany

Luisa Röckel[1], Steffen Ahlers[2], Birgit Müller[1], Karsten Reiter[2], Oliver Heidbach[3,4], Andreas Henk[2], Tobias Hergert[2], Frank Schilling[1]

[1]Institute of Applied Geosciences, KIT, 76131 Karlsruhe, Germany

[2]Institute of Applied Geosciences, TU Darmstadt, 64287 Darmstadt, Germany

[3]Helmholtz Zentrum Potsdam, Deutsches GeoForschungsZentrum GFZ, 14473 Potsdam, Germany

[4]Institute of Applied Geosciences, TU Berlin, 10587 Berlin, Germany

Published in Solid Earth (https://doi.org/10.5194/se-13-1087-2022)

Received: 4 March 2022, Accepted: 26 May 2022, Published: 29 June 2022

Abstract

Seismic hazard during subsurface operations is often related to the reactivation of pre-existing tectonic faults. The analysis of the slip tendency, i.e., the ratio of shear to normal stress acting on the fault plane, allows an assessment of the reactivation potential of faults. We use the total stresses that result from a large-scale 3D geomechanical-numerical model of Germany and adjacent areas to calculate the slip tendency for three 3D fault geometry sets with increasing complexity. This allows to draw general conclusions about the influence of the fault geometry on the reactivation potential.

In general, the fault reactivation potential is higher in Germany for faults that strike NW-SE and NNE-SSW. Due to the prevailing normal stress regime in the geomechanical-numerical model results, faults dipping at an angle of about 60° generally show higher slip tendencies in comparison to steeper or shallower dipping faults. Faults implemented with a straight geometry show higher slip tendencies than those represented with a more complex, uneven geometry. Pore pressure has been assumed as hydrostatic and has shown to have a major influence on the calculated slip tendencies. Compared to slip tendency values calculated without pore pressure, the consideration of pore pressure leads to an increase of slip tendency of up to 50 %. The qualitative comparison of the slip tendency with the occurrence of seismic events with moment magnitudes $M_w > 3.5$ shows areas with an overall good spatial correlation between elevated slip tendencies and seismic activity but also highlights areas where more detailed and diverse fault sets would be beneficial.

6.1 Introduction

Seismic activity is a crucial aspect for many subsurface constructions and activities such as the production of oil and gas, coal mining, geothermal energy production, the storage of gas or the construction and safe long term operation of a nuclear waste repository. The occurrence of seismic activity is closely linked to the presence of pre-existing tectonic faults and their reactivation (Sibson, 1985). To estimate the potential to trigger seismic events, knowledge about the reactivation potential of tectonic faults is essential (Moeck et al., 2009a; Worum et al., 2004). Slip on a fault occurs when the resolved shear stress τ is larger than the frictional resistance τ_f (Sibson, 1974; Jaeger et al., 2011):

$$\tau \geq \tau_f = c + \mu \cdot \sigma_{neff} \tag{6.1}$$

where c is the fault cohesion, μ is the coefficient of static friction and σ_{neff} the effective normal stress on the fault. The relevant parameters for the assessment of the fault reactivation potential are therefore: 1) The stress tensor to estimate τ and the absolute normal stress σ_n; 2) The pore pressure required for the calculation of σ_{neff}; 3) The fault orientation that influences the magnitudes of σ_n and τ; 4) The frictional fault properties C and μ that describe the fault's mechanical behavior.

The stress tensor in previous works has mainly been estimated utilizing stress inversion (McFarland et al., 2012; Yukutake et al., 2015; Ferrill et al., 2020), point-wise stress data from field observations (Neves et al., 2009; Lee and Chang, 2009; Moeck et al., 2009a; Morris et al., 2021) or using Monte Carlo Simulation (Healy and Hicks, 2022) for 2D lineaments and in some cases 3D fault geometries. Worum et al. (2004) calculated the 3D stress tensor with an analytical model and used it for the estimation of the fault reactivation potential of 3D faults of the Roer Graben. Stress tensor estimates from 3D geomechanical-numerical models have been used to determine fault reactivation potential on regional scales, e.g., for the Upper Rhine Graben (Peters, 2007) or the Val d'Agri (Italy) (Vadacca et al., 2021), but this has not been achieved for all of Germany. In this study, we focus on the whole of Germany.

Here, we use the first 3D geomechanical-numerical model of Germany by Ahlers et al. (2021b) that provides an estimate of the 3D stress tensor that is variable with depth and lateral extent (Cornet and Röckel, 2012) due to inhomogeneous density and elastic rock properties. Furthermore, we compile three sets of 3D fault geometries with increasing complexity and use the stress tensor from the Germany model to predict the fault reactivation potential. The fault sets can be used not only to derive a first order estimation of the fault reactivation potential, but also to highlight the effect of fault geometry on the fault reactivation potential. We also investigate the impact of hydrostatic pore pressure as well as assumed overpressure on the reactivation potential estimates and compare our results with the spatial distribution of seismic events with moment magnitudes $M_w \geq 3.5$.

6.2 Data and method

6.2.1 Study area

This study focuses on Germany and some adjacent areas. It is subdivided into the three crustal units of the East-European Craton, Avalonia and the Armorican Terrane Assemblage (Meschede and Warr, 2019; Ahlers et al., 2021a) (Figure 6.1a). Most parts of the European basement have an Variscan overprint and can be subdivided into the roughly SW-NE striking regions defined by Kossmat: the Rhenohercynican, the Saxothuringican including the Middle German Crystalline Zone and the Moldanubian Zone (Walter, 2007). North Germany is characterized by the North German Basin as part of the Southern Permian Basin (van Wees et al., 2000) and almost N-S striking Graben structures such as the Glückstadt Graben and SW-SE striking basins (Walter, 2007). Central and south Germany are characterized by several low mountain ranges such as the Black forest, the Harz, the Ore Mountains or the Rhenish Massif and sedimentary basins such as the Upper Rhine Graben and the Molasse Basin. The southernmost part of Germany is dominated by the roughly E-W striking Alps.

Seismicity is mainly observed in the Rhine area, the Swabian Jura and Eastern Thuringia as well as Western Saxony (German Research Centre For Geosciences). Induced seismicity has mainly been documented in the context of gas production (Müller et al., 2020), geothermal energy production (Bönnemann et al., 2010; Stober and Bucher, 2020) and especially mining activities, which caused induced seismic events with local magnitudes of up to 5.6 (Grünthal and Minkley, 2005). Poro-elastic stress changes should be considered for significant pore pressure changes, as shown for production induced earthquakes (Müller et al., 2020). In the case of geothermal sites, fluid injections into the sedimentary rocks have been suggested to not be as seismogenic as injections into crystalline rocks. In general, the presence of faults close to the injection well as fluid pathways increases the risk of seismic events (Evans et al., 2012)

6.2.2 Stress state

Stress data are not evenly distributed throughout Germany (Figure 6.1b) and vary between different regions of Germany both in terms of orientation and the stress magnitudes, thus the stress regime. For the North German Basin, Röckel and Lempp (2003) describe a normal faulting regime and mostly N-S striking S_{Hmax} orientations (S_{Hazi}) with an NNW-SSE influence towards the Dutch border and an NNE-SSW influence towards Poland. For the Upper Rhine Graben (URG) area in southwest Germany, Homuth et al. (2014) calculate a transtensional regime with a strong strike-slip influence with S_{Hazi} around 135°, while modeling results of Buchmann and Connolly (2007) suggest a present day strike-slip reactivation of the URG. For the Molasse Basin in South Germany, S_{Hazi} rotates from striking N-S in southeast Germany to NNW-SSE striking in the southwest (Reinecker et al., 2010) and the stress regime most likely varies between normal faulting and strike slip (Drews et al., 2019; Seithel et al., 2015)

Since these stress data are available only pointwise, we use the stress tensor derived from the 3D geomechanical-numerical model of Germany by Ahlers et al. (2021a) for the assessment of the fault reactivation potential. The model covers Germany and adjacent areas and provides a continuum mechanics based prediction of the stress tensor. The purely elastic finite element (FE) model comprises seven mechanical units, i.e., sediments, four upper crustal units, the lower crust and parts of the lithospheric mantle. The four crustal units represent the crustal framework of Germany as shown in Figure 6.1a and the Alps-Carpathian-Pannonia. The lateral grid resolution is 6 x 6 km² and the vertical resolution decreases from 800 m within the sediments to 7500 m at the model base. Each unit is characterized by its respective density, Young's modulus and Poisson's ratio (Ahlers et al., 2021a).

The model is calibrated with stress magnitude data from the magnitude database by Morawietz et al. (2020) and compared with stress orientations from the World Stress Map database (Heidbach et al. 2016); both data sets are shown in Figure 6.1b. The resulting best fit model provides the 3D absolute stress tensor σ_{ij} within the model domain (Ahlers et al., 2021a), i.e., for Germany and adjacent areas. In order to consider effective stresses, we assume a hydrostatic pore pressure. Even though overpressure is well documented for the Molasse Basin (Drews et al., 2018; Müller et al., 1988), there is not enough spatial information on pore pressure available to justify the usage of different pore pressure gradients in our analysis.

Figure 6.1: (a) Crustal units in Germany are indicated by different shades of blue and labelled with dark grey, capital text. White text labels Variscan units. Modified after Meschede and Warr (2019) and Ahlers et al. (2021a); (b) stress data available in Germany: the rotated line markers represent data on the orientation of the maximum horizontal stress (S_{Hazi}) available in the World Stress Map (Heidbach et al., 2018) and are colored by the stress regime associated with the data points (Normal faulting (NF), strike-slip faulting (SS), thrust faulting (TF) and unknown regime (U)). Plotted alongside are the locations of stress magnitude data (Morawietz and Reiter, 2020) and major tectonic faults in Germany as blue lines with (outcropping) basement structures indicated by grey areas The location of Figure 6.3a and b is indicated by orange squares. BPF: Bavarian Pfahl Fault; EG: Eger Graben; FL: Franconian Line; GG: Glückstadt Graben; HSBF: Hunsrueck Southern border fault; LNF: Landshut-Neuötting Fault; NHBF: Northern Harz Boundary fault; RG: Roer Graben: RT: Rheinsberg Through; URG: Upper Rhine Graben (modified after Kley and Voigt (2008) and Ahlers et al. (2021a)); (c) and (d) The stress regime calculated by the Germany model in 1 km and 8 km depth respectively is indicated by the background color; S_{Hazi} calculated by the Germany model has been averaged along a regular grid. The mean S_{Hazi} of each grid point is indicated by the orientation and color of the marker. For five areas within the model area, fault reactivation stereo plots are shown, displaying what fault orientations and dips are most favorable for reactivation under the given stress conditions. © EuroGeographics for the administrative boundaries.

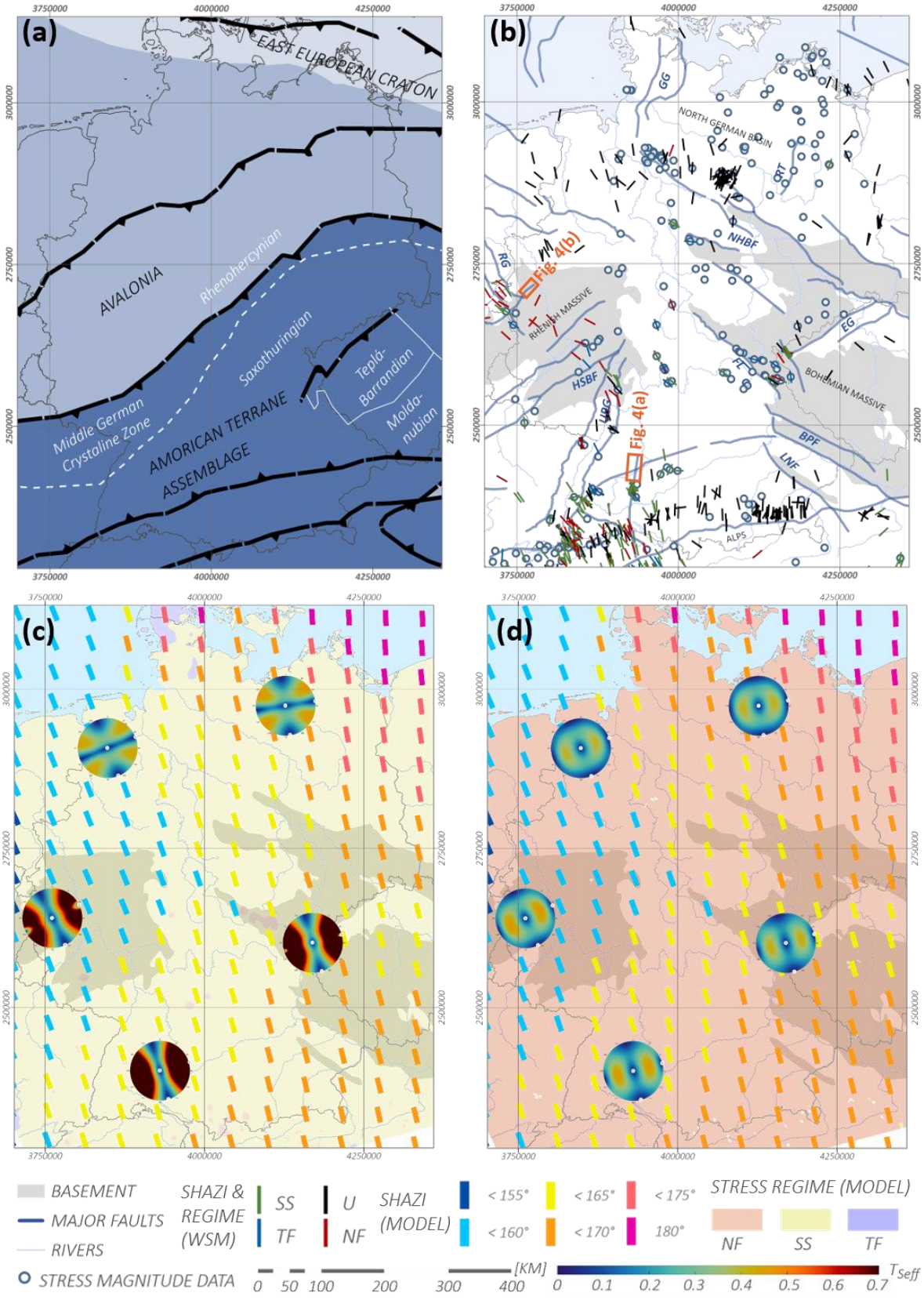

Figure 6.1c and d show the stress regime in the Germany model and S_{Hazi} in 1 km and 8 km depth respectively. In the uppermost km of the model, thrust faulting (TF) and strike-slip (SS) regimes are present. Below 1 km depth, the model is dominated by SS regime with some areas showing normal faulting (NF) regimes. With increasing depth, the NF regime becomes increasingly dominant as can

be seen in Figure 6.1d. In contrast, the stress orientations are almost constant with depth but change noticeably laterally. While S_{Hazi} is almost purely N-S in the northeastern part of the model, the orientation switches more towards a NNE-SSW orientation in the western part of the model. Additionally, the figure shows fault reactivation stereo plots for five regions in Germany. The plots are based on data provided by the model at the respective locations and illustrate the reactivation potential of faults striking between 0° and 360° and dipping between 0° and 90° represented by their normal vectors. They indicate high reactivation potentials in the upper 1 km of the model in south Germany for shallow to moderately dipping and NNE-SSW to SSE-NNW striking faults. The reactivation potential for faults in north Germany is noticeably lower. In 8 km depth, the reactivation potential is predicted as relatively low for all areas and fault orientations. The highest reactivation potential in this depth is predicted for moderately dipping faults striking roughly in NE-SW direction.

6.2.3 Fault data sets

A spatially comprehensive collection of 2D fault lineaments in Germany has been compiled by Schulz et al. (2013). 3D fault geometries are available on a regional scale for some regions in Germany, such as the North German Basin (BGR et al., 2022), the Molasse Basin (GeoMol Team, 2015) in South Germany or in the model of Saxony (Geißler et al., 2014). However, there are no comprehensive 3D fault geometry compilations available for Germany. We created a total of three fault sets of increasing complexity. The first fault set is based the 2D fault collection by Schulz et al. (2013) that comprises the 2D lineaments of 900 faults in Germany. The faults used in the second fault set have been chosen according to selection criteria. The selection criteria comprise the length of the fault (≥ 250 km), the horizontal displacement (≥ 10 km), the vertical displacement (≥ 2.5 km) and the seismic activity of the fault (since 800 CE or later). Furthermore, the general special pattern of fault orientations should be reproduced. In areas, where no faults met the criteria, we selected some additional faults to reproduce the general spatial distribution of faults. This approach lead to a final compilation of 55 faults. For these faults the fault type, namely strike-slip, normal fault or thrust fault, was known from a data collection of (Suchi et al., 2014; Agemar et al., 2016) or respective literature. For the third fault set, we used geological and seismic cross sections in the depth domain to compile data on the 3D geometry of the selected faults. For 23 faults, cross sections with sufficient vertical extent were available. Based on the three described fault sets we generated three different 3D geometry sets of increasing complexity for slip tendency calculation:

1. **Vertical fault set**: All 900 faults of the fault catalogue (Agemar et al., 2016) were implemented as 90° dipping faults extending to the base of the lower crust. The assumption of a vertical dip is an oversimplification due to the lack of data on most faults and introduces significant errors to the calculated reactivation potentials of faults that dip differently in reality. However, it allows the consideration of a large quantity of faults and therefore a more diverse representation in terms of location and strike than the other two sets with more realistic dips.

2. **Andersonian fault set**: The 55 selected faults have been implemented depending on their Andersonian fault type as normal faults, thrust faults or strike-slip faults. For normal faults a dip angle of 60° was assigned, for thrust faults of 30° and for strike-slip of 90°. The faults reach the base of the lower crust. The supplementary Table S1 lists the implemented faults with a corresponding ID.
3. **Semi-Realistic fault set**: For 23 faults, a more complex geometry on the basis of seismic and geological cross sections is used. The depth of the faults is not constant as in the Vertical and Andersonian fault sets, but is chosen in accordance with the depths given in the sections used. The vertical cross sections used for the generation of the semi-realistic fault set are compiled in Table 6.1. The quantity of available cross sections per fault varied considerably. For many faults, only one cross section was available leading to a uniform geometry over the entire length of the fault.

Table 6.1: Sources with suitable geological and seismic cross sections for the generation of semi-realistic fault geometries and the specific faults they were used for.

Fault	Source
Albstadt Shear Zone	Derived from Reinecker and Schneider, 2002
Allertal Lineament	Littke et al., 2008
Alpine Thrust	Brückl et al., 2007
Finne Fault	Reinhold, 2005
Franconian Line	Reinhold, 2005
Gardelegen Fault	Littke et al., 2008, Reinhold, 2005
Haldesleben Fault	Littke et al., 2008, Reinhold, 2005
Harz Northern Boundary fault	Reinhold, 2005
Hunsrueck Southern Border fault	Henk, 1993
Kyffhäuser Fault	Reinhold, 2005
Lausitz Escarpement	Reinhold, 2005
Lausitz Thrust	Behr et al., 1994
Midi-Aachen Thrust	Ribbert and Wrede, 2005, Cazes et al., 1985
Osning Fault	Duin et al., 2006, Drozdzewski and Dölling, 2018
Roer Graben	Duin et al., 2006, Geluk et al., 1994
Siegen Thrust	Franke et al., 1990
Swabian Lineament	Pfiffner, 2017
Teisseyre–Tornquist Zone	Narkiewicz et al., 2015
Upper Rhine Graben	Brun et al., 1992, GeORG-Projektteam, 2013
Wittenberg Fault	Reinhold, 2005

6.2.4 Three-dimensional slip tendency analysis

To estimate the fault reactivation potential we use definitions and terms of Morris et al. (1996). Assuming that cohesion can be neglected, they defined the parameter slip tendency as the ratio between τ and σ_n. We use this definition as a first slip tendency type:

$$T_S = \frac{\tau}{\sigma_n} \tag{6.2}$$

We further use three additional slip tendency parameters for our analysis. T_{Seff} considers σ_{neff} that takes the influence of pore pressure on σ_n (Jaeger et al., 2011) into account.

$$T_{seff} = \frac{\tau}{\sigma_{neff}} \tag{6.3}$$

A normalization to μ has been used for example by Peters (2007) and is additionally calculated as T_{Snorm} and $T_{Snormeff}$. We choose μ as 0.57 which is in the middle of the range reported by Jaeger et al. (2011). For T_{Snorm} and $T_{Snormeff}$ slip is likely to occur if they approach values around 1 or larger.

$$T_{Snorm} = \frac{\frac{\tau}{\sigma_n}}{\mu} \tag{6.4}$$

$$T_{Snormeff} = \frac{\frac{\tau}{\sigma_{neff}}}{\mu} \tag{6.5}$$

The pore pressure P_p for the calculation of σ_{neff} is computed from the depth z [m] (which is the true vertical depth below the topographic surface of the German stress model), gravity g [9.81 m s^{-2}] and the fluid density ρ [1000 kg m^{-3}]:

$$P_p = \rho \cdot g \cdot z \tag{6.6}$$

To estimate the slip tendencies, the fault geometries are discretized as surfaces with triangles with a side length of 800 m. Then the 3D stress tensor components from the geomechanical-numerical model of Ahlers et al. (2021b) are mapped on the corner nodes of the triangles using *Tecplot 360 EX v2019* and the AddOn *Geostress* (Heidbach et al., 2020). The mean stress tensor of the three nodes is multiplied with the normal vector of each triangle to estimate τ and σ_n. With the hydrostatic pore pressure the four slip tendency parameters are calculated.

6.3 Results

6.3.1 Vertical fault set

The results for the Vertical fault set are shown for all four slip tendency parameters in Figure 6.2. As the faults are vertical, the top view only shows the values along the fault top. T_S of the Vertical fault set ranges mainly between 0 and 0.5 (histograms are shown in Figure S2 in the Supplement). Higher T_S values are reached for the uppermost parts of some faults as can be seen in Figure 6.2a. With increasing depth T_S decreases rapidly to nearly 0 for all faults. Faults striking NNE-SSW and NW-SE

show elevated T_S values in the uppermost parts of the faults when compared to faults of other strike directions.

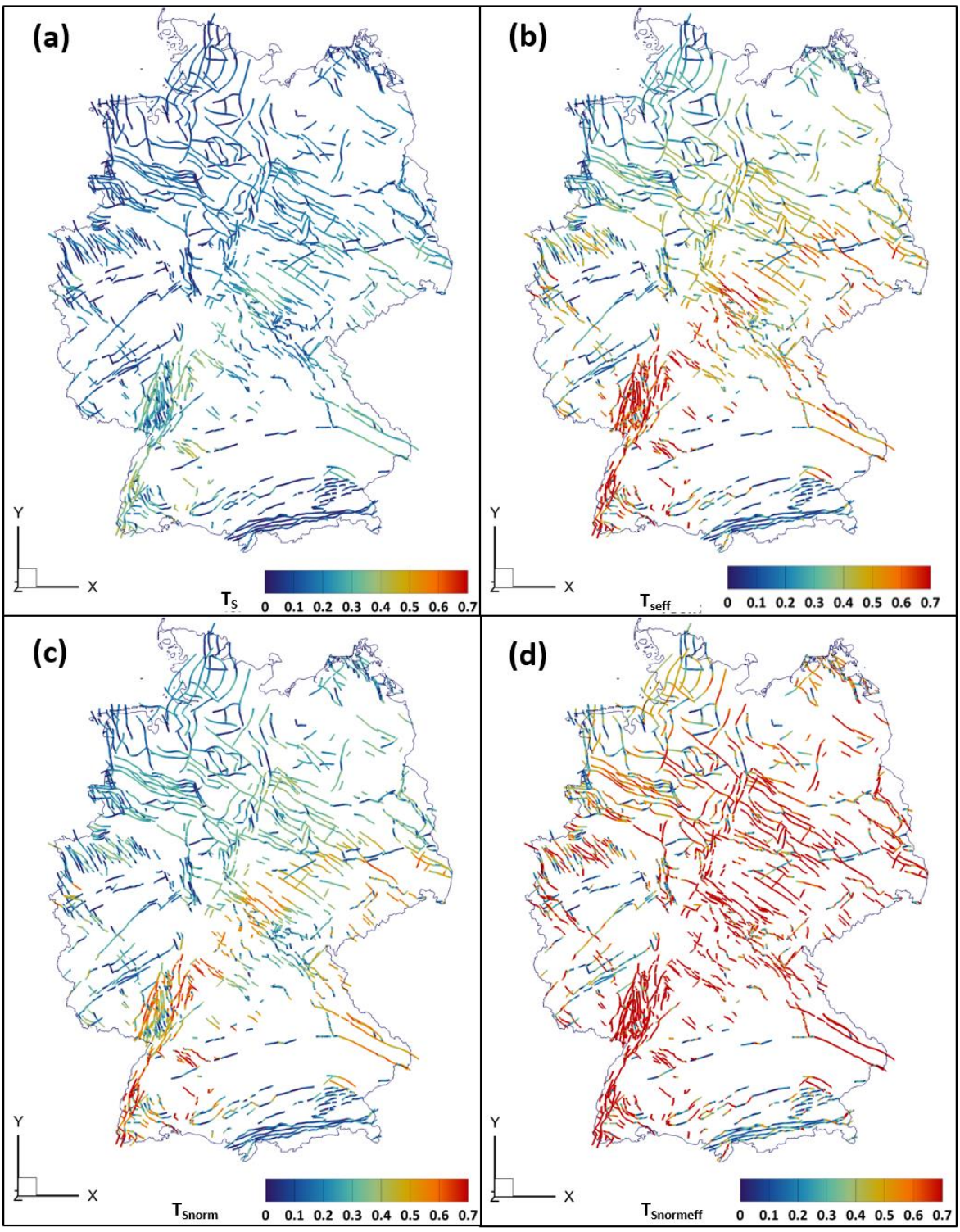

Figure 6.2: Topview of the slip tendency of the vertical fault set calculated for four cases. Due to the vertical nature of the faults only the uppermost parts of the faults are visible. (a) T_S; (b) T_{Seff} (with effective normal stresses); (c) T_{Snorm} (normalized to a coefficient of friction of 0.57); (d) $T_{Snormeff}$ (with effective normal stresses and normalized to a coefficient of friction of 0.57). © EuroGeographics for the administrative boundaries.

T_{Seff} is higher than T_S and ranges mainly between 0 and 0.7. T_{Seff} is highest in the uppermost fault parts and decreases rapidly with increasing depth as well. NW-SE and especially NNE-SSW striking faults show higher T_{Seff} than faults of other strike. T_{Snorm} values mainly range between 0 and 0.7 and $T_{Snormeff}$ ranges mostly between 0 and 1. The same trends for depth and fault strike apply as for T_S and T_{Seff}. T_{Snorm} and $T_{Snormeff}$ are however higher in the uppermost parts of the faults than T_{Seff}.

6.3.2 Andersonian fault set

The resulting slip tendencies of the Andersonian fault set are shown for all four slip tendency types in Figure 6.4 (additional histograms are given in Figure S3 in the Supplement). T_S ranges mainly between 0 and 0.2. Only the uppermost parts of some NNW-SSE and NE-SW striking faults such as the URG, the Albstadt Shear Zone and the Landshut-Neuoetting Fault show slightly higher values.

T_{Seff} mostly ranges between 0 and 0.4. Only 5 % of the values are higher than 0.4. T_{Seff} is generally elevated for faults and fault segments striking in NNE-SSW and NW-SE direction such as the URG, the Franconian Line, the Albstadt Shear Zone, the Wittenberg Fault, the Rheinsberg Through, the Landshut-Neuoetting Fault and the Roer Graben. The influence of fault strike direction is especially prominent for faults with segments of varying orientation. The NW-SE striking parts of the Rheder Moor-Blenhorst Fault show elevated T_{Seff} values when compared to the more WNW-ESE striking segments of the fault. For strike-slip faults, T_{Seff} strongly decreases within the uppermost fault parts and keeps decreasing with increasing depth as shown for parts of the Albstadt Shear Zone Figure 6.3a. T_{Seff} slightly increases with depth after the initial strong decrease for some normal and thrust faults. This is shown for the Midi-Aachen-Thrust in Figure 6.3b. T_{Snorm} ranges mainly between 0 and 0.3 and shows an overall similar behavior to T_{Seff}. While the high $T_{Snormeff}$ values reach up to 1.0, areas with low $T_{Snormeff}$ show values in the same range as for the other three slip tendency parameters. The spatial distribution of areas of low and high $T_{Snormeff}$ values is similar to T_{Snorm} and T_{Seff}.

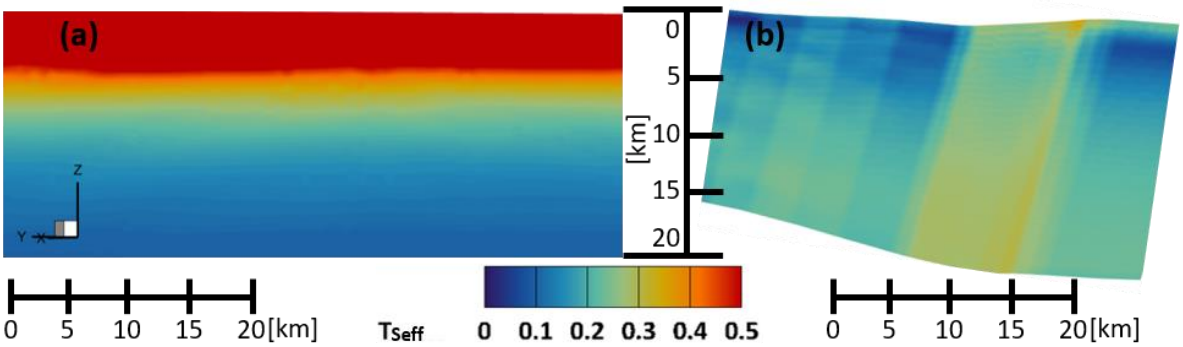

Figure 6.3: Vertical section of T_{Seff} along faults. (a) T_{Seff} of a northern part of the Albstadt Shear Zone decreases over the entire depth; (b) T_{Seff} of an eastern part of the Midi-Aachen Thrust slightly increases again (after an initial strong decrease) as indicated by the shift from blue to greenish colors in greater depths. Colorbar applies to both (a) and (b).

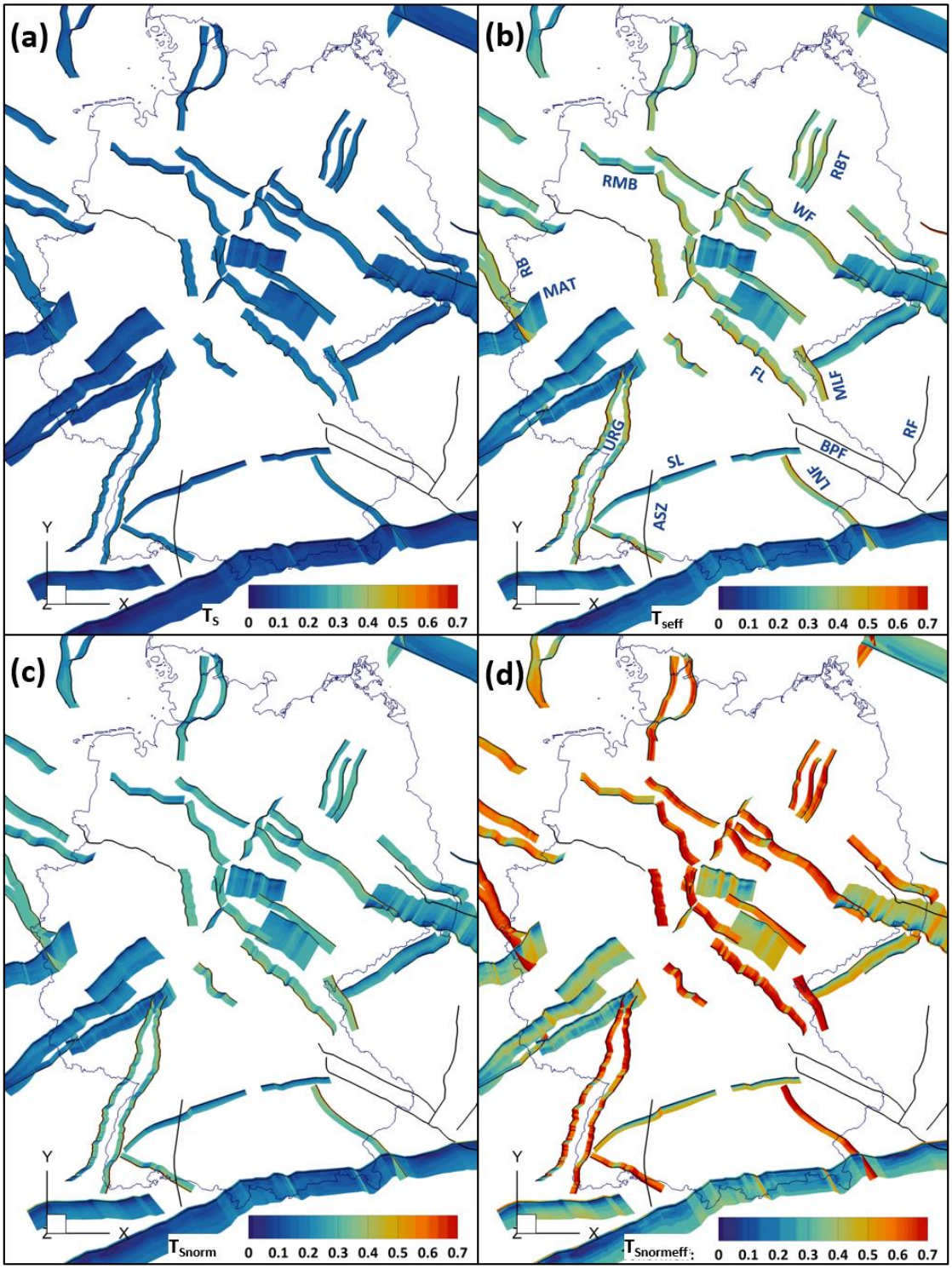

Figure 6.4: Topview of the slip tendency of the Andersonian fault set calculated for four slip tendency types. (a) T_S; (b) T_{Seff} (with effective normal stresses); (c) T_{Snorm} (normalized to a coefficient of friction of 0.57); (d) $T_{Snormeff}$ (with effective normal stresses and normalized to a coefficient of friction of 0.57). ASZ: Albstadt Shear Zone (not visible in map view due to the vertical geometry); BPF: Bavarian Pfahl Fault; FL: Franconian Line; LNF: Landshut-Neuoetting Fault; MAT: Midi-Aachen Thrust; MLF: Mariánské Lázne Fault; URG: Upper Rhine Graben; RB: Roer Basin; RBT: Rheinsberg Through; RF: Rodl Fault; RMB: Rheder Moor-Blenhorst Fault; SL: Swabian Lineament; WF: Wittenberg Fault. © EuroGeographics for the administrative boundaries.

6.3.3 Semi-realistic fault set

Figure 6.5 shows the results of the slip tendency calculations for the Semi-Realistic fault set; additional histograms are shown in Figure S4 in the Supplement. T_S ranges mainly between 0 and 0.2. For the Semi-Realistic fault set, the NNE-SSW and NW-SE striking faults show elevated T_S compared to faults of other orientations. The highest T_S can be observed at the uppermost steeply dipping sections of the URG, the Franconian Line, the Albstadt Shear Zone, the Wittenberg Fault and the Roer Graben. For most faults, T_S decreases with increasing depth. However, most faults are significantly less deep than in the Andersonian fault set.

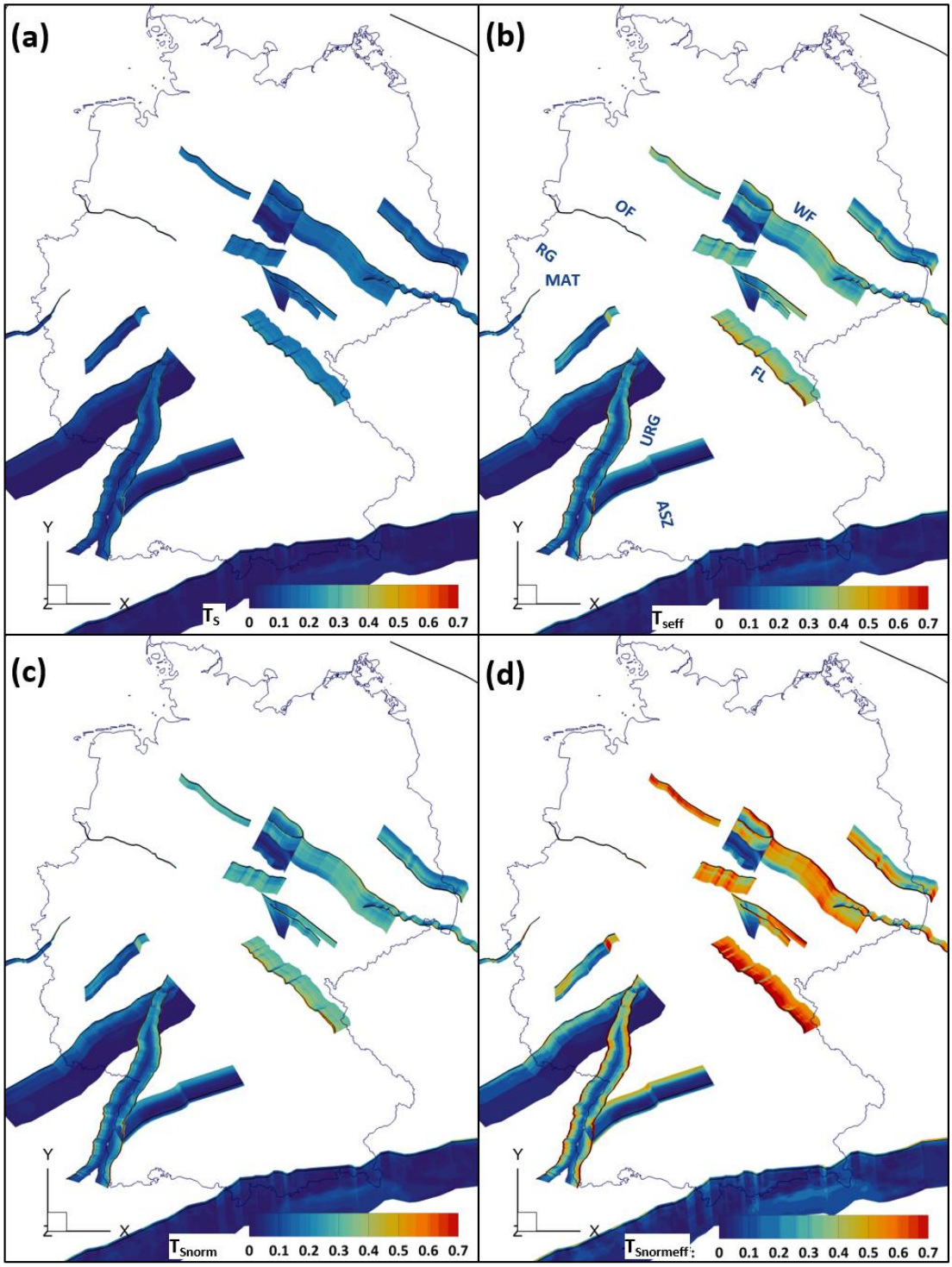

Figure 6.5: The semi-realistic fault geometries are color-coded by their slip tendency for four cases. (a) TS; (b) T_{Seff} (with effective normal stresses); (c) T_{Snorm} (normalized to a coefficient of friction of 0.57); (d) $T_{Snormeff}$ (with effective normal stresses and normalized to a coefficient of friction of 0.57). ASZ: Albstadt Shear Zone: FL: Franconian Line; MAT: Midi-Aachen Thrust; OF: Osning Fault; URG: Upper Rhine Graben; RG: Roer Graben; WF: Wittenberg Fault. © EuroGeographics for the administrative boundaries.

T_{Seff} ranges mainly between 0 and 0.4 with 5 % of values 0.5 or higher. Faults striking in NNW-SSE and NE-SW direction such as the URG, the Franconian Line, the Albstadt Shear Zone, the Wittenberg Fault and the Roer Graben show elevated T_{Seff} as compared to faults of other strike directions. This influence is especially noticeable for the Franconian Line where the WNW-ESE striking segments of the fault show lower T_{Seff} than the NNW-SSE striking ones. For sections of the uppermost parts of the URG and the Roer Graben T_{Seff} exceeds values of 1. The decrease in T_{Seff} with increasing depth is especially prominent for faults that have been implemented with a listric geometry (such as the URG or the Hunsrueck Southern Border Fault). While the listric URG geometry shows some of the highest T_{Seff} values for the Semi-Realistic fault set in its uppermost parts, T_{Seff} decreases drastically with depth. The same decrease can be observed for the listric Hunsrueck Southern Border Fault. In contrast, T_{Seff} increases drastically in the lowermost part of the Swabian Lineament after a steady decrease of T_{Seff} with increasing depth for the most part of the fault. T_{Snorm} mainly ranges between 0 and 0.4 The T_{Snorm} distribution is almost identical to the one of T_{Seff}. $T_{Snormeff}$ mainly ranges between 0 and 0.8. The high $T_{Snormeff}$ values mainly occur on the NW-SE and NNE-SSE striking faults while the areas with low $T_{Snormeff}$ show values similar to the other slip tendency types in the respective areas.

6.4 Discussion

6.4.1 Influence of fault strike on slip tendency

To investigate the influence of the spatial orientation of the faults on the slip tendency, we prepared scatter plots of T_{Seff} as a function of fault strike for all faults of each of the three fault sets (Figure 6.6). The normal faults, thrust faults and strike-slip faults of the Andersonian set are displayed in separate subfigures (Figure 6.6b, c and d, respectively).

Overall, the minimum T_{Seff} values occur consistently at strikes of 75° for all fault types, i.e., the reactivation potential is generally the lowest for ENE-WSW striking faults, as could be expected in the context of the stress orientation shown in Figure 6.1c and d. Vertical faults also show a low reactivation potential on NNW-SSE striking segments (corresponding to strikes of 165°). The maximum T_{Seff} occurs for strikes of 5°-25° for all fault types, i.e., the reactivation potential is generally highest for N-S to NNE-SSW striking faults; these faults strike at an angle of 25° to S_{Hazi} with an orientation between 160° and 175°. The vertical faults also have a high reactivation potential for NW-SE strikes, the Andersonian normal faults for NNW-SSE striking segments. Due to the uniform

dip of the Vertical fault set, dip is not a variable of influence for this fault set and only the location in the stress field and the strike of the fault lead to differences in slip tendency.

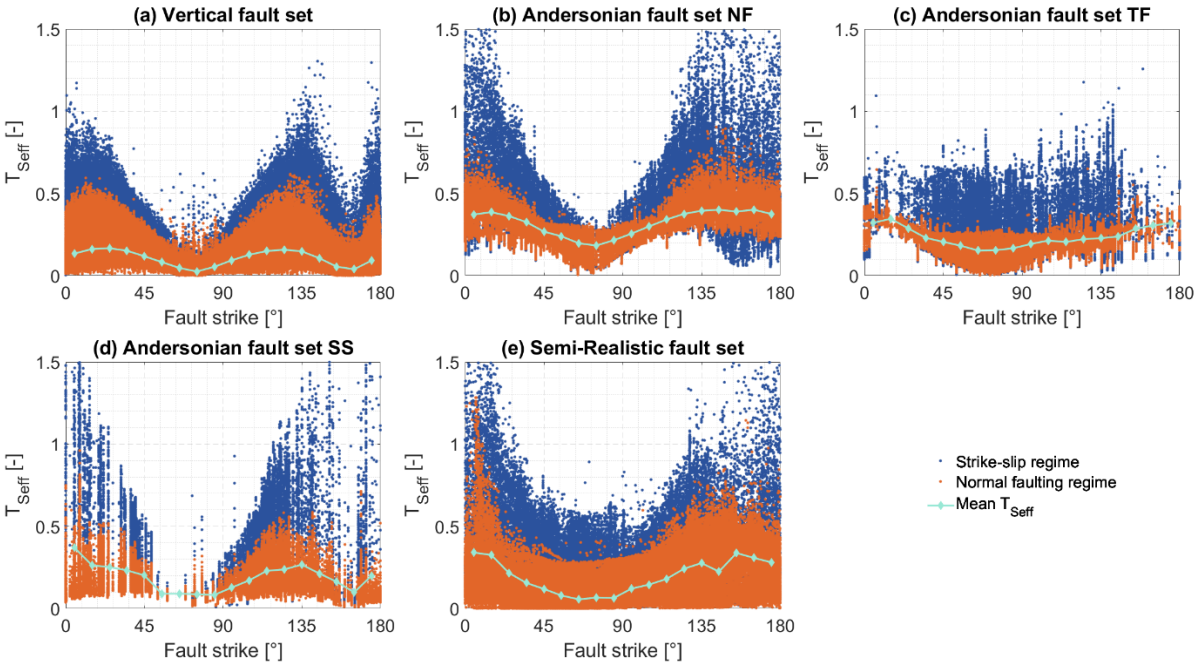

Figure 6.6: Scatterplots showing T_{Seff} and the fault strike of each node of the fault mesh. Additionally, the stress regime the data points are subjects to is indicated by its color (blue for strike-slip regime, orange for normal faulting regime). The mean T_{Seff} in 10° fault strike steps is plotted as a mint colored line. (a) vertical fault set; (b) normal faults of the Andersonian fault set; (c) Thrust faults of the Andersonian fault set; (d) Strike-slip faults of the Andersonian fault set; (e) Semi-Realistic fault set.

6.4.2 Influence of depth and shear stress on slip tendency

For all three fault sets, a strong decrease in the slip tendencies can be observed from the surface to a depth of 5-10 km as shown in Figure 6.7 and 6.8 for the Vertical and Andersonian fault set, respectively. In greater depths, the slip tendency gradient is low. This is the case for all four slip tendency types. For the Vertical fault set (Figure 6.7), slip tendency decreases steadily for all four slip tendency types with the exception of a dent between 32 km and 38 km. However, since only very few fault segments reach this depth, the influence of fault strike strongly superimposes the depth dependency for these depths. For the Andersonian fault set (Figure 6.8), the same trends apply in general as for the Vertical fault set. However, for the thrust and normal faults the initial strong decrease in slip tendency occurs within the uppermost 3–4 km. In this depth, the stress regime switches from a strike-slip regime to a normal faulting regime in most parts of the model. The slip tendencies of the strike-slip faults are generally higher than the ones of the thrust and normal faults in the upper 5–10 km but generally lower in greater depths. In contrast to the strike-slip faults, both normal and

thrust faults show a slight increase of the mean slip tendency with increasing depth below 5 km depth. The mean slip tendency increase with depth is higher for the thrust faults than for the normal faults.

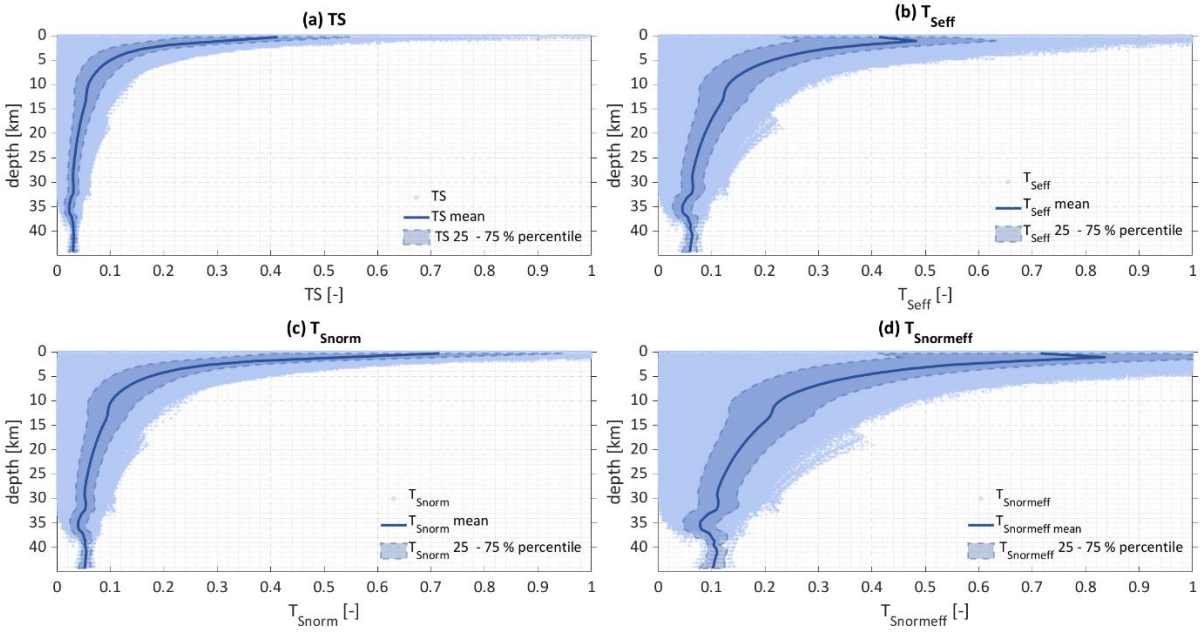

Figure 6.7: All slip tendency data are plotted vs. depth for the vertical fault set. The mean slip tendency is plotted as a solid line; the 25 %-75 % percentile is shown as a shaded area.

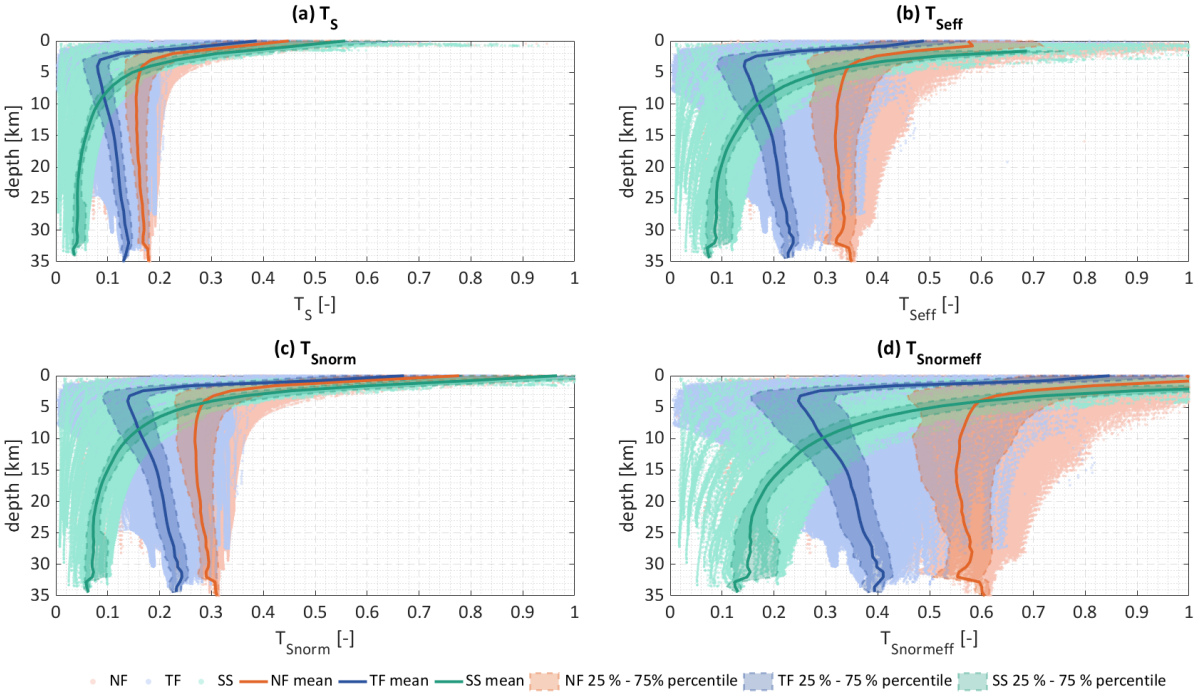

Figure 6.8: All four slip tendency types at each data point of the Andersonian fault set are plotted vs. their depth. The mean slip tendency is plotted as a solid line; the 25 %-75 % percentile is shown as a shaded area. Due to the different behavior of normal, thrust and strike-slip faults, the three fault types are colored individually. Data corresponding to the normal faults are shown in orange, data corresponding to

thrust faults are shown in blue and data corresponding to strike-slip faults are shown in mint color.

For normal, thrust and strike-slip faults σ_n increases at a similar rate with increasing depth. On the other hand, τ on strike-slip faults and the faults of the Vertical fault set increases less strongly. Since slip tendency has been defined as τ/σ_n, low τ leads to low slip tendencies for the strike-slip faults and the faults of the Vertical fault set. Figure 6.9 shows τ for the Vertical fault set. Additionally, σ_{neff}, τ and the resulting T_{Seff} of the Landshut-Neuoetting Fault are shown exemplarily. While σ_{neff} increases to over 250 MPa, τ only increases to around 20 MPa at a depth of 30 km (note that the range of the color bar of σ_{neff} is 10 times the range of the τ). This results in T_{Seff} strongly decreasing with increasing depth for all faults regardless of their strike direction in the Vertical fault set.

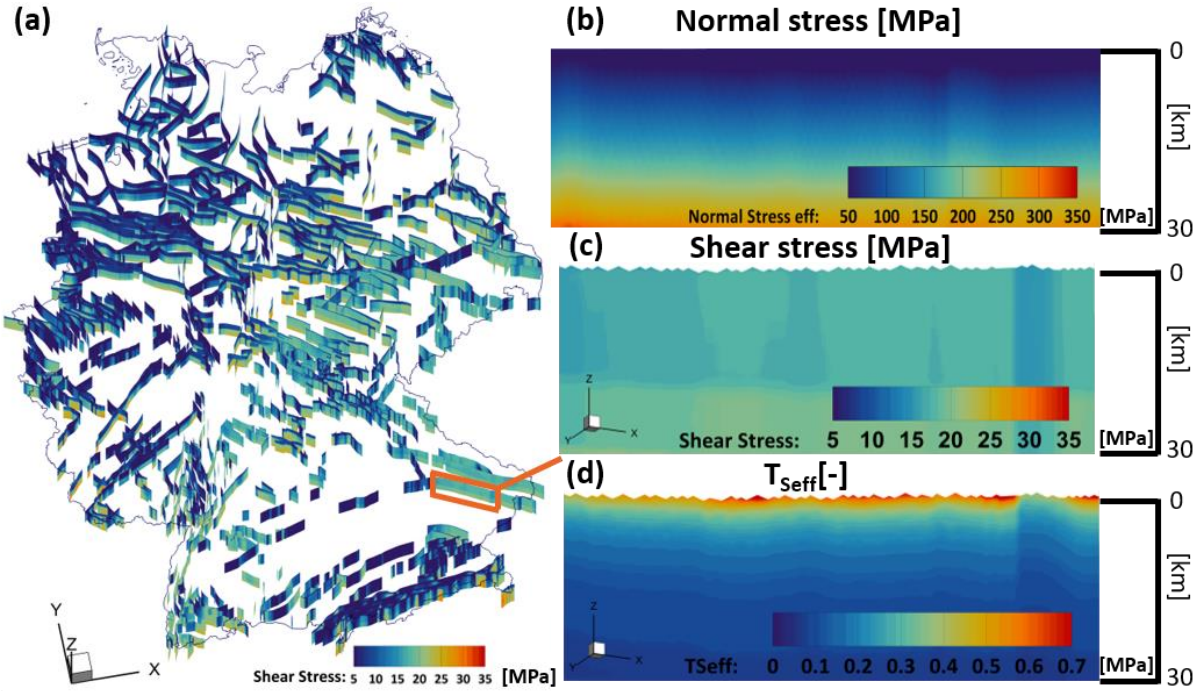

Figure 6.9: (a) Shear stress τ in MPa of the Vertical fault set with the color map ranging from 5 to 35 MPa (oblique view). (b)-(d): zoomed in view of the Landshut-Neuoetting Fault normal to the strike reaching to a depth of around 30 km; (b) effective normal stress σ_{neff} with the color map ranging from 50 to 350 MPa; (c) shear stress τ with the color map ranging from 5 to 35 MPa; (d) T_{Seff} of the Landshut-Neuoetting Fault is shown with the color map ranging between 0 and 0.7. © EuroGeographics for the administrative boundaries.

6.4.3 Influence of fault dip

In order to investigate the influence of the 3D fault geometry, we compare the slip tendency histograms of the Vertical (blue), Andersonian (orange) and Semi-Realistic (mint) fault set (Figure 6.10). For all four slip tendency types, the Vertical fault set shows a right skewed bell shape, the Semi-Realistic fault set displays as J-shape and the Andersonian fault set shows a bimodal distribution. The

bimodal character of the Andersonian fault set is more distinct for T_{Seff} and $T_{Snormeff}$. The slip tendency values of the first peak are mainly concentrated on the thrust faults whereas the slip tendency values of the second peak are mainly present on normal faults. As the normal faulting regime is predominant in most parts of the Germany model (especially in depths greater than 4 km) in general σ_n is lower for normal faults than for thrust faults, which have been implemented with a dip of 60° and 30° respectively in the Andersonian fault set, leading to the bimodal distribution of T_S.

The more prominent bimodal distribution of T_{Seff} and $T_{Snormeff}$ in the Andersonian fault set results from the influence of the calculation of the pore pressure as a function of depth. In combination with the normal faulting regime in most parts of the Germany model this leads to a stronger relative reduction of σ_{neff} for normal faults than for thrust faults.

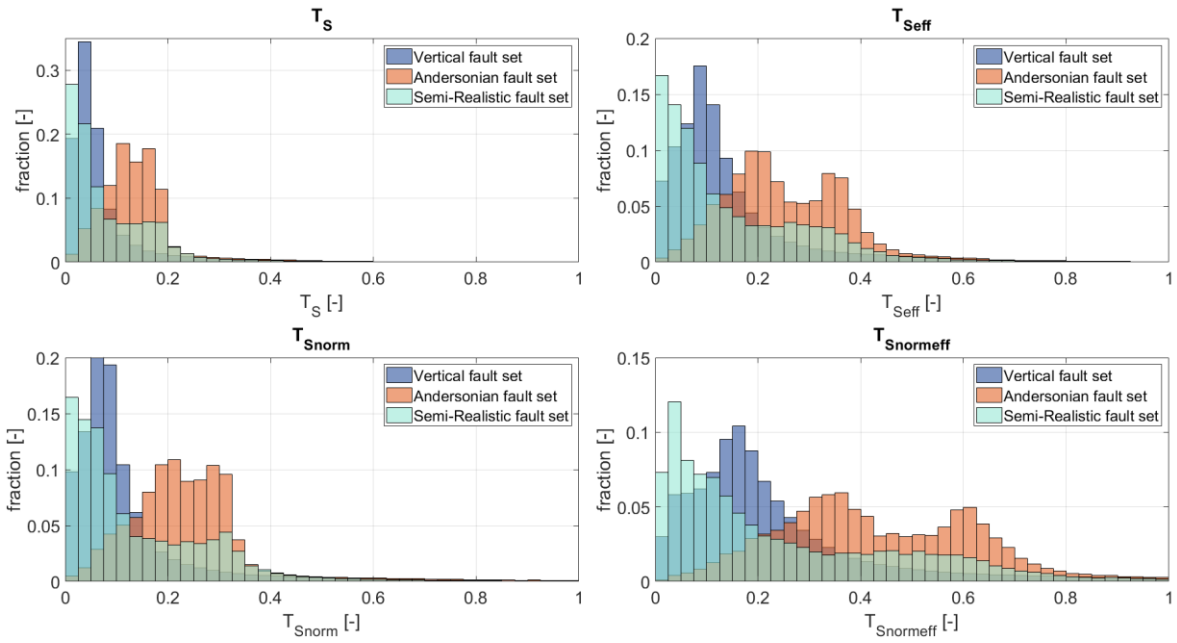

Figure 6.10: Comparison of the slip tendency histograms of the Vertical (blue), Andersonian (orange) and Semi-Realistic (mint) fault set for the four slip tendency types. Slip tendency values greater than 1 are not shown. The slip tendency values have been calculated on the nodes of the fault mesh; mesh resolution is 800 m for all three fault sets. Bin size is 0.025.

The listric geometry of the URG in the Semi-Realistic fault set is based on DEKORP 9N (Brun et al., 1992). The URG shows high T_{Seff} values in the uppermost parts for both the Andersonian and the Semi-Realistic fault set. With increasing depth, the dip of the Semi-Realistic URG faults decreases until it becomes sub-horizontal. This decrease in dip coincides with a significant T_{Seff} decrease. In contrast, T_{Seff} for the Andersonian fault geometries decreases at a significantly lower rate. This results from the fact that while σ_{neff} increases at a similar rate for both fault types, τ of the Semi-Realistic URG increases at a much lower rate than it does for the Andersonian URG (also shown in Figure S5 in th Supplement). Results from the Hunsrueck Southern Border Fault, another listric fault, (derived from DEKORP 9N and 1C, Henk, 1993) show a similar behavior.

The overall low slip tendency values of the vertical fault set were to be expected due to the prevailing normal faulting regime in most parts of the model and the uniform 90° dip of the Vertical fault set. The low values do not properly reflect the actual fault reactivation potential of faults with different dips in reality. The reactivation potential for faults with other dips in reality is underestimated in areas with normal and thrust faulting regimes and overestimated in a strike-slip regime.

6.4.4 Influence of pore pressure

The use of a hydrostatic pore pressure is a major simplification since the pore pressure is not hydrostatic everywhere in Germany. Considerable overpressures have been shown for example in the Molasse basin (Drews et al., 2018; Müller et al., 1988). Müller et al. (1988) describes pore pressure gradients of up to 24 MPa km^{-1} in the vicinity of the lineament of the Alpine thrust. Figure 6.11shows T_{Seff} for the Alpine Thrust for pore pressure gradients of (a) 10 MPa km^{-1} (hydrostatic) (b) 16 MPa km^{-1} and (c) 22 MPa km^{-1}. T_{Seff} increases drastically with increasing pore pressure. For the gradient of 16 MPa km^{-1} T_{Seff} reaches values of up to 0.7 for favorably oriented segments of the fault. For a pore pressure gradient of 22 MPa km^{-1} T_{Seff} increases to over 0.7 for almost all parts of the fault and reaches values well in excess of 1 over large areas. Even though these pore pressure gradients are unlikely to occur over large areas of the fault, this highlights the crucial impact of the pore pressure on the fault reactivation potential.

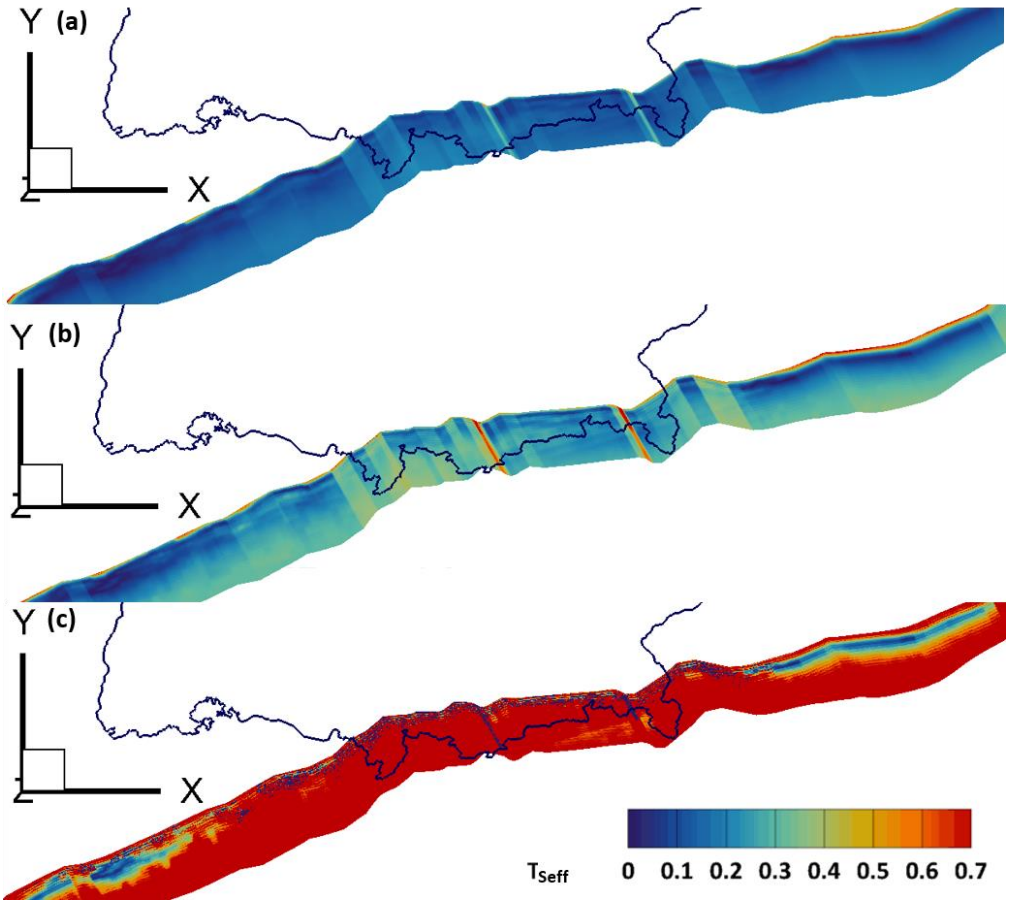

Figure 6.11: T_{Seff} of the Alpine Thrust for different pore pressures. (a) T_{Seff} with hydrostatic pore pressure corresponding to a gradient of 10 MPa km^{-1}; (b) T_{Seff} for an overpressured pore pressure with a gradient of 16 MPa km^{-1}; (c) T_{Seff} for an overpressured pore pressure with a gradient of 22 MPa km^{-1}. The color bar applies to all three cases. © EuroGeographics for the administrative boundaries

6.4.5 Comparison between slip tendency and seismicity

In order to evaluate our slip tendency results, we test them qualitatively against the distribution of tectonic earthquakes. The earthquakes are taken from the EMEC seismic event catalogue of Grünthal and Wahlström (2012) that covers the period between 1000 to 2006 CE in the investigation area and provides earthquakes with magnitudes $M_w \geq 3.5$. We added events to this compilation with $M_w \geq 3.5$ for the years 2007-2021 from the GEOFON data center at the GFZ German research Centre (Quinteros et al., 2021). For the events with a given hypocentral depth, the majority occur at 8 km (refer to Figure S6 in the Supplement) and the largest moment magnitudes are observed at 8 to 10 km depth. Therefore, we use the slip tendency values at a cross section at 8 km depth for the comparison with seismic events.

Figure 6.12a shows the location of the seismic events with $M_w \geq 3.5$ color-coded by their moment magnitude alongside a horizontal cross section through the Vertical fault set at a depth of 8 km. The faults are color-coded by their T_{Seff} values. The overall T_{Seff} in this depth is very low with values of only up to 0.3 as the 90° dip is unfavorable for reactivation in the normal faulting regime in this depth. However, the NNE-SSW striking faults of the seismically active Upper Rhine area show slightly higher T_{Seff} values than other areas with low seismicity. While several seismic events in east Germany are localized close to faults with elevated T_{Seff}, there are several faults with similar or higher values where no seismicity is documented. The seismicity in the Roer Graben area and its SE trending elongation is localized along faults where only some segments show slightly elevated T_{Seff} values or where no faults at all have been mapped. While the Vertical fault set is based on a very comprehensive fault selection it is apparent from the distribution of seismic events, that some relevant structures are likely still missing.

This is not surprising when considering the results of fault detection using photolineations derived from high resolution data of satellite missions such as (ERS) 1/2. For example Franzke and Wetzel (2001) present in their work for southern Germany that there are numerous additional fault networks on smaller scale that could potentially serve as faults for the catalogued seismicity with small magnitudes. However, if we would use only large events with $M_w > 6$ instead that have according to empirical relations rupture length of > 10 km (Wells and Coppersmith, 1994) these would fit better to our resolution, but in a low strain area these magnitudes do not occur very often and even the largest recorded event in Germany from year 1911 with M_w 5.8 in the Albstadt Shear Zone would not be usable, but only the historical events where the epicenter estimation based on intensity reports is highly uncertain.

A cross section through the Andersonian fault set at a depth of 8 km is shown in Figure 6.12b, the same color-codes as for Figure 6.12a apply. The occurrence of seismic events is in good accordance with the elevated T_{Seff} of the URG, the Roer Graben, the Mariánské Lázne Fault and the Randen-Bonndorf Fault. However, especially in east Germany and in the SE trending elongation of the Roer Graben there are areas without faults despite numerous seismic events. Furthermore, T_{Seff} is rather low along the Albstadt Shear Zone, one of the seismically most active areas in Germany due to the implementation as a 90° dipping strike-slip fault. In contrast, there are also areas with T_{Seff} in the same range as, e.g., the URG with no or only very little seismicity, especially in northern Germany. Here, T_{Seff} is either overestimated in comparison to seismically active areas or stress relief is achieved by other processes.

Since only a subset of the Andersonian fault set could be implemented in the Semi-Realistic fault set, there are many areas where earthquakes occur but no fault geometry is considered (Figure 6.12c). While the shallow sections of the URG and the Albstadt Shear Zone show T_{Seff} of 0.6 and higher, T_{Seff} is relatively low in a depth of 8 km. In general, T_{Seff} is lower at the 8 km depth cross section for the Semi-Realistic fault set than for the Andersonian fault set.

While some of the seismogenic areas show elevated T_{Seff} values, the absolute values are rather low, especially in 8 km depth and deeper, where most of the considered seismic events take place. If μ is low enough, seismicity can still occur even with T_{Seff} in the range below 0.4. The range of μ of faults can vary greatly and even reach values below 0.4 for faults with fault gouge (Numelin et al., 2007; Haines et al., 2014) as a compilation by Ferrill et al. (2017) shows. For higher μ, as they have been shown for different locations (Zoback and Healy, 1992; Zoback and Healy, 1985; Brudy et al., 1997) and collected by Peters (2007), T_{Seff} would need to reach higher values in order to explain seismic events. This could be achieved through higher τ or lower σ_n. In order to achieve these either significant changes regarding the stress tensor from the geomechanical model of Germany or changes in the fault geometry would be required. The changes to the stress tensor required would not be warranted by the calibration data used for the model of Germany. In order to elevate T_{Seff} of the Franconian Line to values of 0.7 and higher, an additional 30 MPa of τ would be required in 8 km depth. The required stress changes however would not fit the data from the *Kontinentale Tiefbohrung* (KTB) nearby that has been used for the model calibration. On the other hand, the fault geometries are subject to major uncertainties due to the sparse data available on the geometries in greater depths. As shown above, both fault strike and fault dip drastically impact the resulting slip tendency and the uncertainties regarding the 3D fault geometries could therefore at least partly explain the overall low values.

Figure 6.12: Seismic events with M_w > 3.5 color-coded by their moment magnitude (yellow to red) displayed on horizontal cross sections through the fault sets color-coded by T_{Seff} (hydrostatic pore pressure) in 8 km depth.Vertical fault set; (b) Andersonian fault set; (c) Semi-Realistic fault set. The color bars of T_{seff} and M_w apply to (a) - (d); (d) Andersonian fault set with fault plane solutions from the GFZ GEOFON catalogue (GEOFON Data Centre) visualized using the focalmech script (Conder, 2022). ASZ:

Albstadt Shear Zone; BT: Boppard Thrust; LNF: Landshut-Neuoetting Fault; MLF: Mariánské Lázne Fault; RBF: Randen-Bonndorf Fault; RB: Roer Basin; SL: Swabian Lineament; URG: Upper Rhine Graben. © EuroGeographics for the administrative boundaries.

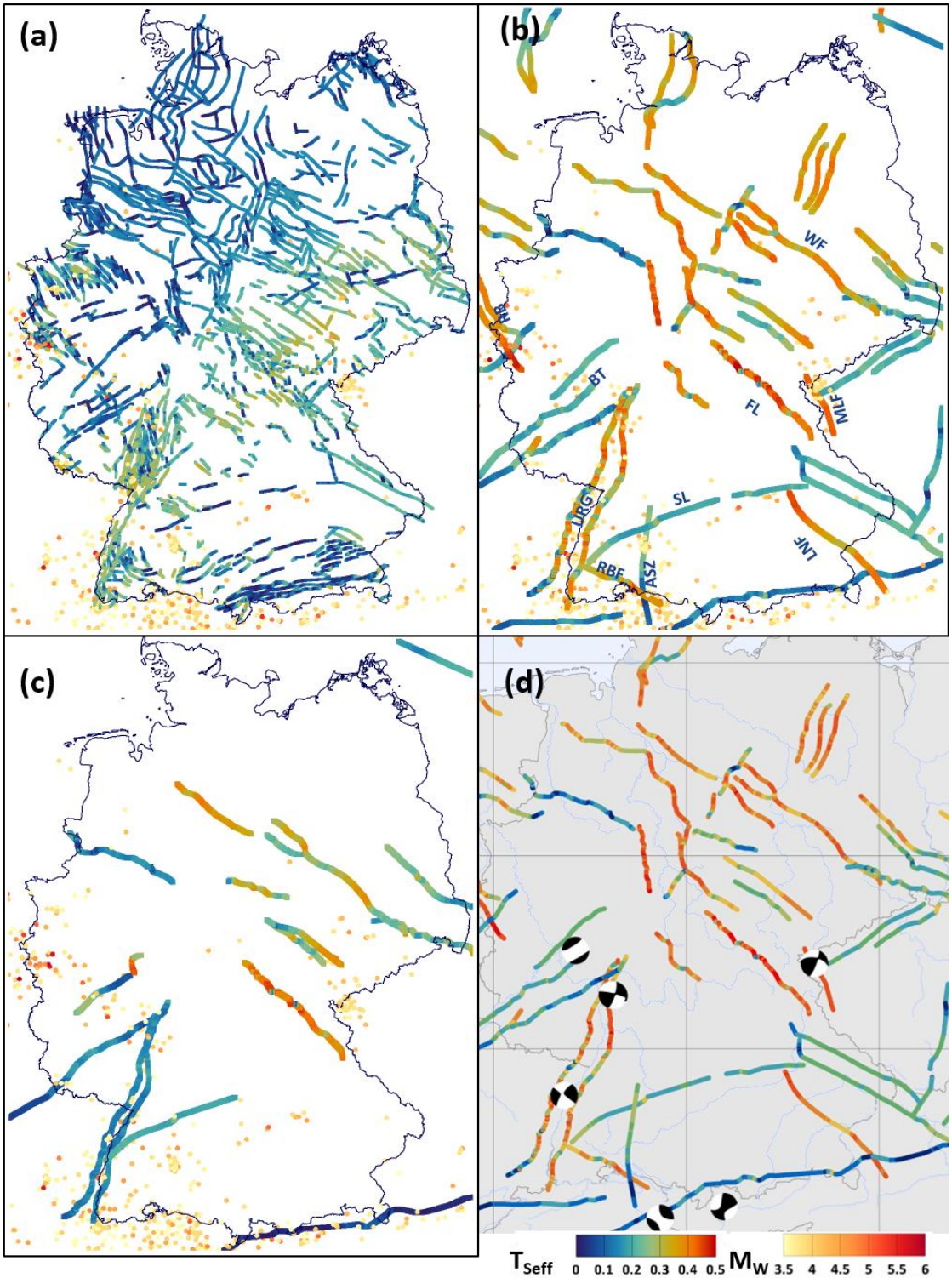

A comparison of the faults of the Andersonian fault set with 3 fault plane solutions (GEOFON Data Centre) (Figure 6.12d) shows that one of the nodal planes' strike is (sub-) parallel to the URG, even

though the corresponding dips are steeper at around 75° than they were assumed for the URG in the Andersonian fault set. For the Alpine Thrust, one fault plane solution in the fault's proximity shows a parallel strike of 78° but a much steeper dip of 71° than the 30° dip that had been assumed for the Alpine Thrust with another fault plane solution indicating reactivation along a fault that is not present in the fault set. A fault plane solution close to the NNW-SSE striking Mariánské Lázne Fault indicates seismicity linked to a NNE-SSW striking fault. Reactivation along a fault striking in NNW-SSE direction rather than NE-SW direction is indicated by a fault plane solution in the area of the NE-SW striking Boppard Thrust. Such faults are present in the Vertical fault set, even though their slip tendencies are rather low due to the 90° dip in the normal faulting regime. Even though the Andersonian fault set roughly replicates the general fault pattern documented for Germany, a more diverse fault set in terms of strike, location and dip is required for a more comprehensive comparison with the seismic events.

6.4.6 Data limitations

The relevant data for this slip tendency analysis are the stress tensor, pore pressure, frictional fault properties and fault geometry. The model by Ahlers et al. (2021b), which provides the 3D absolute stress tensor for our study, has a coarse resolution and only implements a single sediment layer as well as only four upper crustal units. Tectonic faults are not implemented and thus local stress variations due to their presence are not considered in the model. Ahlers et al. (2021a) describe a good fit to the stress magnitude data that are used for the model calibration. However, these are located in the uppermost kilometers of the model where we predict the overall highest slip tendencies. At greater depths, where our slip tendency results are visibly lower, no calibration data were available for the geomechanical model.

Wide regions and depth intervals of the numerical model indicate a prevailing normal faulting stress regime. However, focal mechanisms of seismic events (Heidbach et al. 2018) indicate a possible strike-slip regime also at greater depths. In such a regime, an overestimation of the minimum horizontal stress S_{hmin} reduces the slip tendencies. Similarly, the underestimation of the maximum stress (either the vertical stress S_v in normal faulting stress regime or the maximum horizontal stress S_{Hmax} in a strike-slip stress regime) might explain the low slip tendencies.

A second major source of uncertainty results from the limited data available regarding the 3D fault geometries of the selected faults with sufficient depth extension (mostly >5 km). Only few seismic sections and geological cross sections could be used for the 3D fault geometry generation. Due to the sparse data available for most faults the 3D geometry has been deduced from only one section. The resulting geometries are therefore unlikely to properly represent the real 3D fault geometries (dip, strike, depth extent) over the entire fault lengths. As shown above, strike and dip have major influences on the resulting slip tendency.

Pore pressure data are too sparse to justify the discrimination of areas of distinct pore pressure gradients and thus only a hydrostatic pore pressure could be assumed for the estimation of T_{Seff} and $T_{Snormeff}$ with the above mentioned effects. Since data on the frictional fault properties were not available, we assumed the faults to be cohesionless. If the considered faults have cohesion greater than 0, the resulting slip tendencies would be further reduced.

6.4.7 Comparison with earlier studies

Peters (2007) analyzed the slip tendency of the URG with the help of a numerical model. Using a dip of 60° for faults with a known dip direction and assuming hydrostatic pore pressure calculated slip tendencies reached values up to 0.8 in a depth of 2.5 km and with a normalization to a coefficient of friction of 0.4. Even though the slip tendency in this study has been normalized to a higher coefficient of friction of 0.6 the overall slip tendency values in this study are around 0.2 higher than the results in Peters (2007). However, the URG boundary faults show elevated values for similar segments as the ones in the study by Peters (2007). The study of Worum et al. (2004) calculates T_{Seff} values between 0.2 and 0.4 for the Roer Graben using an analytical model for faults reaching depths of around 2-3 km for comparable S_{hmin}/S_{Hmax}-ratios and the strike-slip regime that is present in the Germany model at the before mentioned depths. T_{Seff} of the Roer Graben boundary faults in this study ranges between 0.6 for the southernmost parts of the faults and 0.2 at the northern parts, which is in contrast to the trends displayed in Worum et al. (2004) where the southern parts of the faults show the lowest T_{Seff} values. However, the high T_{Seff} values appear on short segments with ideal orientation for reactivation under the given strike-slip regime with S_{Hazi} around 155°. Slightly less well oriented segments show values that are in better agreement with the results by Worum et al. (2004).

6.5 Main outcome and recommendations

The slip tendency analysis on basis of the 3D absolute stress tensor from the geomechanical-numerical model of Germany (Ahlers et al., 2021b) allowed the identification of regions with a higher reactivation potential and regions where faults are more stable. Elevated slip tendencies have been found especially for NNE-SSW and NW-SE striking faults such as the URG, the Franconian Line, the Albstadt Shear Zone, the Wittenberg Fault, the Rheinsberg Through, the Landshut-Neuoetting Fault and the Roer Graben. However, a comparison with focal mechanisms points towards reactivation of a more diverse set of faults which should be subject to further studies.

The major influence of fault geometry on the calculated slip tendency has been shown by the comparison of three fault sets. High quality information on fault geometry can be provided for example by interpreted seismic sections for large scale faults. To improve this kind of analysis, faults should be characterized by multiple seismic cross sections. The analysis also has shown the crucial influence of the pore pressure on slip tendencies for the fault sets considered. However, no spatially comprehensive

pore pressure data for the entire area of Germany are available. The same applies for the frictional properties of faults, which are only poorly restrained. Lastly, further and more information on the stress state in Germany is crucial for a more reliable slip tendency analysis.

Data availability

The fault geometries are available under https://doi.org/10.5445/IR/1000143465.

Supplement

The supplement related to this article is available online at: https://doi.org/10.5194/se-13-1087-2022-supplement.

Author contribution

Conceptualization of the project was done by AH, TH, KR, OH, FS and BM. Research and collection of fault information was done by SA and LR. Generation of 3D fault geometries and slip tendency analysis were done by LR. Evaluation and interpretation of the slip tendency results were done by LR with the support of BM, OH, KR, TH, SA and AH. LR wrote this paper with the help of all coauthors. All authors read and approved the final paper.

Acknowledgements

This study is part of the SpannEnD Project (http://www.SpannEnD-Projekt.de, last access: 25.02.2022), which is supported by Federal Ministry for Economic Affairs and Energy (BMWI) and managed by Projektträger Karlsruhe (PTKA) (project code: 02E11637A). We acknowledge support by the KIT-Publication Fund of the Karlsruhe Institute of Technology.

7 Discussion

7.1 Orientation of S_{Hmax}

The results of the geomechanical-numerical models of Ahlers et al. (2021a) and (2022a) - presented in Chapter 4 and 5 - show almost equal orientations of S_{Hmax}. For both models, the orientation is almost homogeneous and does not show significant regional perturbations, e.g., in the North East German Basin (NEGB) or north of the Alpine front. However, the results show a good fit with the mean S_{Hmax} orientation derived from the WSM (Heidbach et al., 2016a) and some additional data of Levi et al. (2019). The 2021 model shows a mean of the absolute differences of 15.6° and a median of 5.6° (Figure 4.7). The 2022 model shows a slightly better mean of the absolute differences of 14.9° and a median of 3.8° (Figure 7.2). Within the central part of the model - containing the higher stratigraphic resolution - the differences are significant lower with a mean of the absolute differences of 11.9° and a median of 0.3° (Figure 5.5). Almost all results are below 15° and therefore within the range of the uncertainties assumed for the best-ranked data (quality A) of the WSM (Heidbach et al. 2016). In addition, all orientations of S_{Hmax} predicted by the 2022 model lie within the standard deviation of the mean WSM data (Figure 5.5).

Figure 7.1 and 7.2 display the results of former models described in Chapter 2.2.2 in comparison to the mean orientation of S_{Hmax} used for this study derived from the WSM and additional data of Levi et al. (2019). It should be noted, that the state of knowledge of the stress state increased significantly since the first model published in 1986 (Grünthal and Stromeyer, 1986). For example, the fanlike pattern in north Germany has been mentioned for the first time by Roth and Fleckenstein (2001). Furthermore, significant different model approaches, e.g., elastic vs plastic properties are used and the area of interest varies significantly in region and size, e.g., whole Eurasia (Warners-Ruckstuhl et al., 2013) and NEGB (Marotta et al., 2002). The results of the first and very simple model of Grünthal and Stromeyer (1986) with homogeneous properties and without faults, show a quite good fit with a mean of the absolute differences of 11.4° and a median of 7.8°. The updated version with implemented stiffness contrasts (BM and Adriatic Intender) of Grünthal and Stromeyer (1992) shows a significant better fit with a mean of the absolute differences of 12.9° and a median of 0.3°, which is the best median of all model results shown. However, the differences in the southeastern area are worse. The second update (Grünthal and Stromeyer, 1994) with an extensional feature within the Pannonian Basin and a shear zone at the northeastern margin of the BM shows significantly poorer results for the entire area. The mean of the absolute differences (29.1°) and the median (-13.3°) support this.

Another quite simple model with homogeneous material properties of Goelke and Coblentz (1996) shows also good results with a mean of the absolute differences of 6.5° and median of 4.4°. The parallels to the results of the studies in Chapter 4 and 5 are remarkable: A very homogeneous stress field with anti-clockwise rotations in the area of the NEGB and in the southeast of the model area and counterclockwise deviations in Belgium.

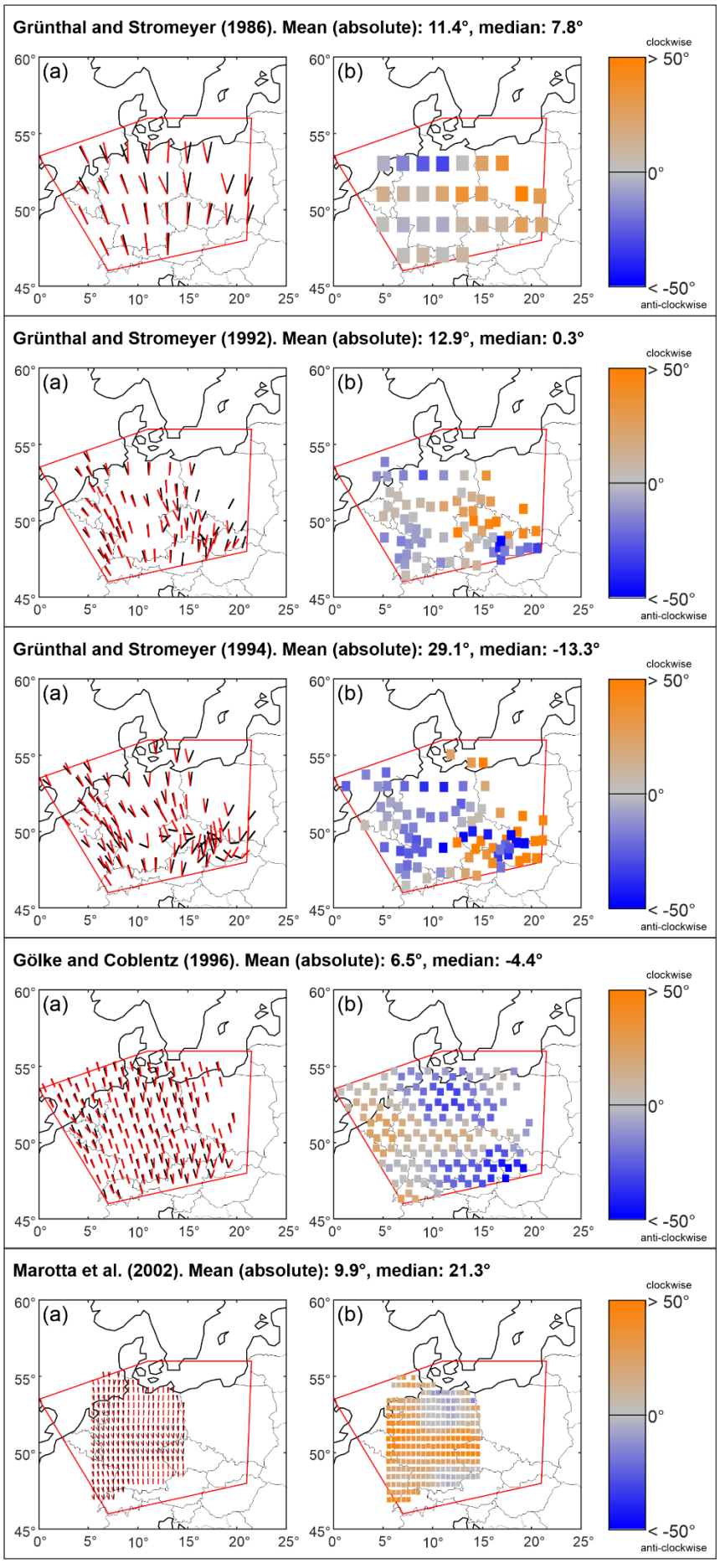

Figure 7.1: Comparison of S_{Hmax} orientations of former numerical models, part 1. The results of Grünthal and Stromeyer (1986, 1992; 1994), Goelke and Coblentz (1996) and Marotta et al. (2002) are compared with a mean S_{Hmax} orientation derived from WSM data (Heidbach et al., 2016a) and additional data of Levi et al. (2019). For the mean S_{Hmax} orientations that have a WSM quality of A to C are used only and averaged on a regular 0.5° grid by the tool stress2grid (Ziegler and Heidbach, 2019b) based on the statistics of bi-polar data (Mardia, 1972). The S_{Hmax} data records are weighted according to their quality and their distance to the grid points. Each grid point requires at least ten data points within a fixed search radius of 200 km. (a) Orientation of the mean S_{Hmax} derived (red) in comparison to model results (black). (b) Deviation of the model result relative to the mean S_{Hmax} orientation.

The results of Marotta et al. (2002) show a clear trend of clockwise deviations indicated by a median of 21.3°. However, the area of focus is the NEGB where a stiff lithosphere is implemented and within this area the deviations are very small. Another study with focus on northern Germany is the study of Kaiser et al. (2005). It includes ~20 faults and fault zones and GPS measurements are used as boundary conditions. However, the results of this study show significant higher deviations within the NEGB and also the overall fit - with a mean of the absolute differences of 33.9° and a median of 3.1° - is not good. In contrast, the study by Jarosiński et al. (2006), which also implement faults, shows significantly better results with a mean of the absolute differences of 9.7° and a median of -3.7°. In particular, the results in the southern part in front of the Alps are in a very good agreement with the mean WSM data. It is remarkable that the relative deviations of the stress field almost resemble a negative of Kaiser et al. (2005). The results of Cacace (2008) - also focusing on the NEGB - show a similar pattern of deviations as Marotta et al. (2002). However, with a significantly larger mean of the absolute differences of 18.0°. The worst results are shown by the study of Warners-Ruckstuhl et al. (2013) with very large deviations especially in the eastern part of the model area, where the differences are clearly above 45° almost everywhere. However, this study does focus on entire Eurasia and therefore, this figure only shows a small part of their results.

The fact that quite simple models with uniform or almost uniform material properties, e.g., by Grünthal and Stromeyer (1986, 1992) or Goelke and Coblentz (1996), are in good agreement with the observed stress pattern, indicates a quite consistent and stable stress field. This is also supported by the results of our study, which predict a very homogeneous stress field despite inhomogeneous material properties (density, Young's modulus and Poisson's ratio). This is in agreement with plate boundary forces as dominant stress source in Western Europe (e.g., Müller et al., 1992; Heidbach et al., 2007). This may also explain the large deviations of Kaiser et al. (2005), which use GPS measurements as boundary conditions. However, Warners-Ruckstuhl et al. (2013) use plate boundary forces and their results show even larger deviations.

Studies predicting a homogeneous field (Goelke and Coblentz, 1996; Ahlers et al., 2021a; 2022a) may provide an indication of regions where low-order stress sources are responsible for deviations. One region, on which a number of studies also focus (Marotta et al., 2002; Kaiser et al., 2005; Cacace, 2008), is the NEGB at the border between Avalonia and the EEC. The two studies (Marotta et al., 2002; Cacace, 2008) - with the best results for this region - see both the cause in stiffness contrasts. Marotta et al. (2002) hold a stiff lithosphere responsible, while Cacace (2008) could furthermore show a significant influence of the depth of the LAB. Furthermore, stiffness contrasts may also explain the deviations of this study (Ahlers et al., 2021a; 2022a) in the vicinity of the Bohemian and Rhenish Massif. However, the results of this studies do not show a significant impact of stiffness contrasts on the pattern of the orientation of S_{Hmax}, despite Young's modulus contrasts of up to 55 GPa, e.g., between Rotliegend sediments and the upper crustal units. However, some small deviations on small spatial scales occur but they are not visbile in the comparison with the mean WSM data since a grid of 0.5° is used here.

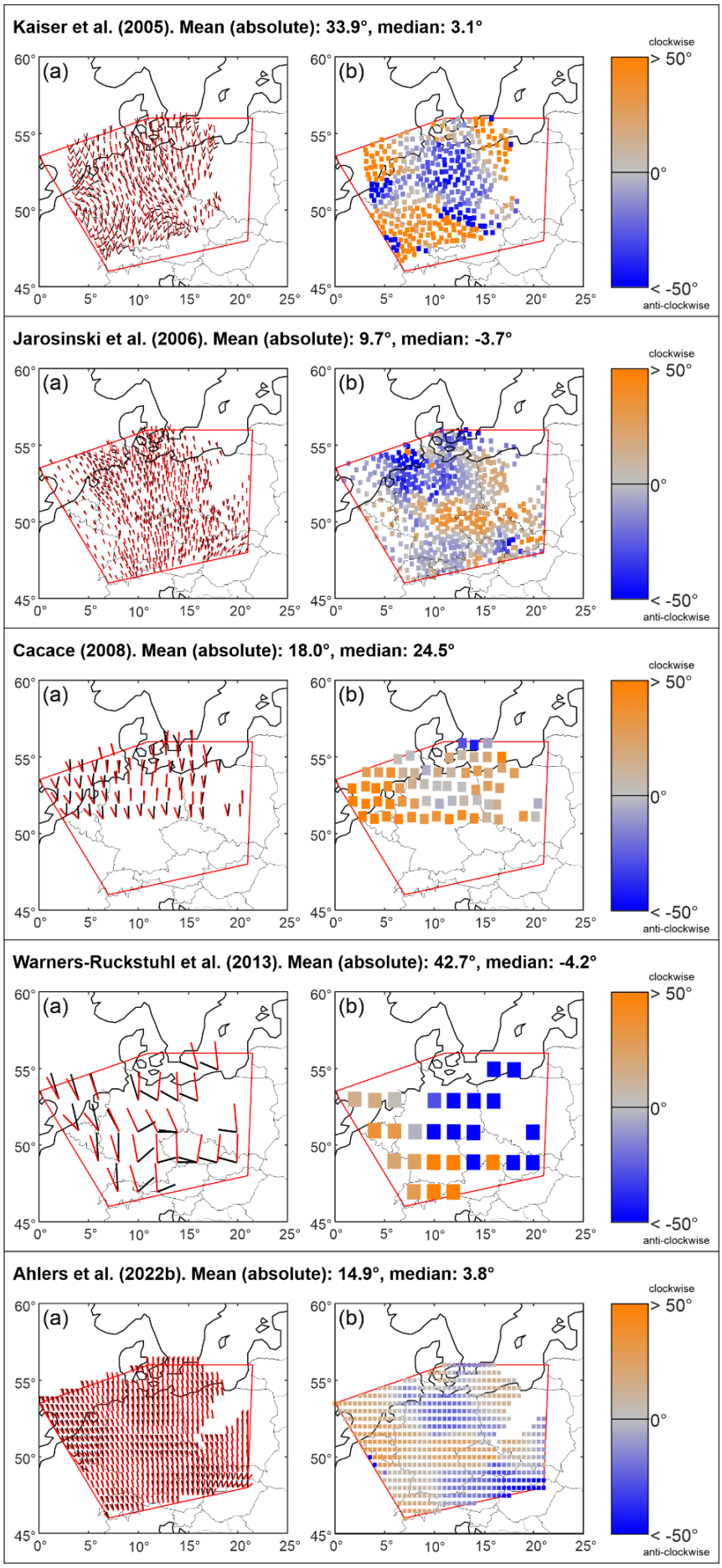

Figure 7.2: Comparison of S_{Hmax} orientations of former numerical models, part 2. The results of Kaiser et al. (2005), Jarosiński et al. (2006), Cacace (2008), Warners-Ruckstuhl et al. (2013) and Ahlers et al. (2022b) are compared with a mean S_{Hmax} orientation derived from WSM data (Heidbach et al., 2016a) and additional data of Levi et al. (2019). For the mean S_{Hmax} orientations that have a WSM quality of A to C are used only and averaged on a regular 0.5° grid by the tool stress2grid (Ziegler and Heidbach, 2019b) based on the statistics of bi-polar data (Mardia, 1972). The S_{Hmax} data records are weighted according to their quality and their distance to the grid points. Each grid point requires at least ten data points within a fixed search radius of 200 km. (a) Orientation of the mean S_{Hmax} derived (red) in comparison to model results (black). (b) Deviation of the model result relative to the mean S_{Hmax} orientation. The results of Ahlers et al. (2022b) are from a depth of 5 km.

An attempt to visualize small perturbations of the orientation of S_{Hmax} is shown in Figure 7.3, where the differences between the standard 0.5° grid and a much higher resolution grid (~1 km) at 5 km depth are shown. The results of the 0.5° grid represent a regional average, while the results of the higher resolved grid show also very small deviations on a scale of single elements. Since the regional average (0.5° grid) also shows slight variations, sometimes a rectangular pattern is visible in the figure. Some differences displayed, are therefore less due to small-scale variations than to larger-scale variations.

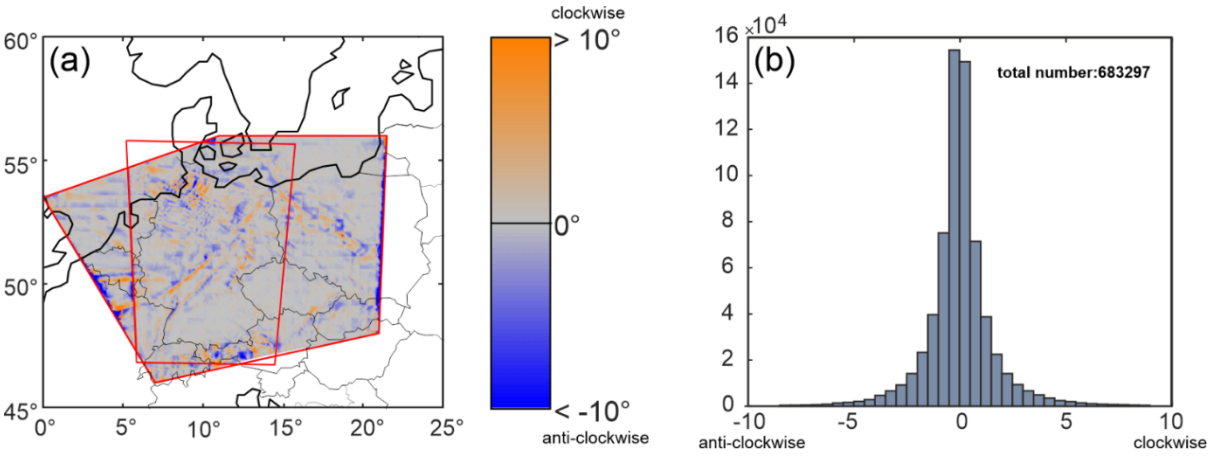

Figure 7.3: Perturbations of the orientation of S_{Hmax} between a local and an averaged stress field of Ahlers et al. (2022b) at 5 km depth. Displayed are the perturbation of the local-scale from the averaged stress field. (a) Relative differences. (b) Histogram of the differences.

Nevertheless, some patterns can be identified. Small-scale reorientations of rarely more than 5° occur for example in high mountains (Alps, Carpathians), at the transition between the Variscan units RHZ, MDCH, SXT, the boundary between Avalonia and the EEC and in the GG. The reorientations in the Carpathians and Alps can be attributed to the strong topography and the reorientations within the GG to strong density contrasts between large halokinetic structures (Maystrenko et al., 2005; Warsitzka et al., 2017). The two remaining areas most likely show effects of stiffness contrasts. In both cases between 'soft' sediments and the stiffer crystalline basement. Although the orientations at the boundary between Avalonia and the EEC would also fit well to crustal contrasts, it is the contrast between deep sedimentary basins and the EEC crust, since all units of the upper crust have the same Young's modulus. However, there are many indications for a stiffer crust of the EEC (e.g., Fischer et al., 2004). In order to test the influence of such a stiffness contrast between two upper crustal units the Young's modulus of the EEC unit is increased from 70 GPa to 110 GPa. The results are shown in Figure 7.4 as deviations to the model with uniform upper crustal stiffnesses. Some effects are visible over the entire EEC. However, the deviations within the EEC are not uniform, but show an irregular distribution of clockwise and anti-clockwise rotations, respectively. At the border between EEC and Avalonia a clearer trend is visible, where the anti-clockwise and clockwise deviations are opposed to each other. In general, the perturbations are small with deviations up to +/- 5°. Remarkable are the small anti-clockwise (blue) rotations which extent over half of the model area. However, the results of

this model variation show in general, only minor effects (<5°) despite an increase of the Young's modulus of 40 GPa and the main effects within the EEC region are probably due to the contrast between sedimentary and crystalline units and not due to the contrast between the upper crustal units of EEC and Avalonia. The only effect which could probably be a result of this contrast are the reorientations at the boundary and the far field effect. However, a uniform clockwise rotation, which could reduce the deviations of the models of this study, is not achieved.

Another possible influence is the depth of the LAB and their influence on the temperature field and rock properties, respectively as shown by Cacace (2008). However, since no temperature dependent material properties are used in this study, it is not possible to test this factor. However, a comparison between the depth of the LAB (e.g., Anikiev et al., 2019) with the deviations of the model results shows a remarkable correlation between larger depths of the LAB and anti-clockwise rotations and smaller depths of the LAB and clockwise rotations. In general, visco-elastic properties for the deeper units of the model could lead to more pronounced differences between individual crustal units, as they would be decoupled from the deeper units.

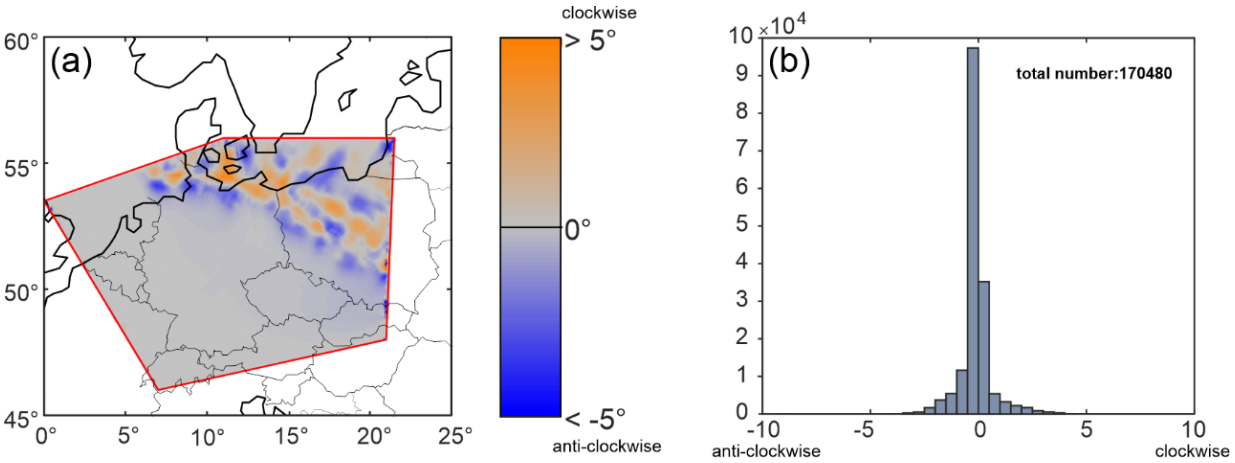

Figure 7.4: Perturbations of the orientation of S_{Hmax} at 5 km depth between the stress field of Ahlers et al. (2022b) and a modified version of this model with a higher stiffness of 110 GPa within the upper crustal unit of the EEC. (a) Relative perturbations. (b) Histogram of the deviations.

An additional source influencing the stress field are faults. However, the results of the former models shown (Figure 7.1 and 7.2) do not provide a consistent indication of whether faults have a significantly effect on the stress field within the model area. While Jarosiński et al. (2006) postulates a very strong influence, clearly above that of stiffness contrasts, and, e.g., north of the Alps with very good results, the study of Kaiser et al. (2005) does not show very good results. However, as already mentioned, the GPS boundary conditions could also be a reason. However, the fan-shaped pattern in front of the Alpine Chain is also produced well by Grünthal and Stromeyer (1986, 1992; 1994), without any faults. Some tests with single, vertical, large (100s of kilometers) faults implemented in the 2021s model showed also an impact on the stress field. However, only up to a distance of ~25 km on both sides of the fault, which corresponds to only four element rows (6km each). These results are also consistent

with observations, e.g., from Yale (2003), results of Warners-Ruckstuhl et al. (2013) and the classification of faults as third- or fourth-order stress sources (Chapter 2.1.2; Rajabi et al., 2017). Furthermore, stress perturbations due to stiffness contrasts can vanish if they are separated by weak faults as shown by Reiter (2021).

Other sources, which may affect the stress field in the model region are isostatic buoyancy effects in Scandinavia due to the deglaciation (e.g., shown by Grollimund and Zoback, 2005) or in the vicinity of the Alps due to erosion, deglaciation and potential slab break off (Przybycin et al., 2015; Sternai et al., 2019). In addition, the uplift of the Rhenish Massif (Reicherter et al., 2008) or the Pritzwalk anomaly (Krawczyk et al., 2008) could explain the misfit in the western part of our model or in the NEGB, respectively

7.2 Stress magnitudes

In contrast to the orientations of S_{Hmax}, the magnitudes of S_{hmin} and S_{Hmax} show significantly larger differences between the model versions of 2021 and 2022. The differences of the vertical model resolution, the different stratigraphic resolution in the central model area with more differentiated material properties in the 2022 model, the Young's modulus gradient integrated in the 2022 model and the use of different calibration data and values can be seen.

7.2.1 S_{hmin} magnitudes

In order to compare the results of the two model variants more easily, the differences - regarding the calibration data - of the S_{hmin} magnitudes of both model variants 2021 (Figure 4.8) and 2022 (Figure 5.6) are displayed together in Figure 7.5. The differences are calculated as model results minus calibration value, i.e., positive differences indicate too high model values and negative values accordingly too low magnitudes predicted by the model. The results of the two model variants do not differ significantly. However, the differences of the 2022 model are slightly higher, with a mean value of the absolute differences of 4.6 MPa and an unweighted median of -3.7 MPa. The trend indicated by the unweighted median is supported by the depth-dependent differences shown, which almost exclusively show too low S_{hmin} magnitudes predicted by the 2022 model in the uppermost 1.5 km TVD. Regarding the differences shown and the statistical values, the agreement with the calibration data appears slightly worse for the 2022 model, but the 2021 model did not take into account the uneven depth distribution of the calibration data, so the many shallow-lying data are over-represented. Despite these differences in calibration, both models show very good agreement with the magnitudes of S_{hmin} from the magnitude database of Morawietz and Reiter (2020). A quality-dependent distribution cannot be observed. Furthermore, no significant influence of the Young's modulus gradient can be detected for the S_{hmin} differences of the 2022 model.

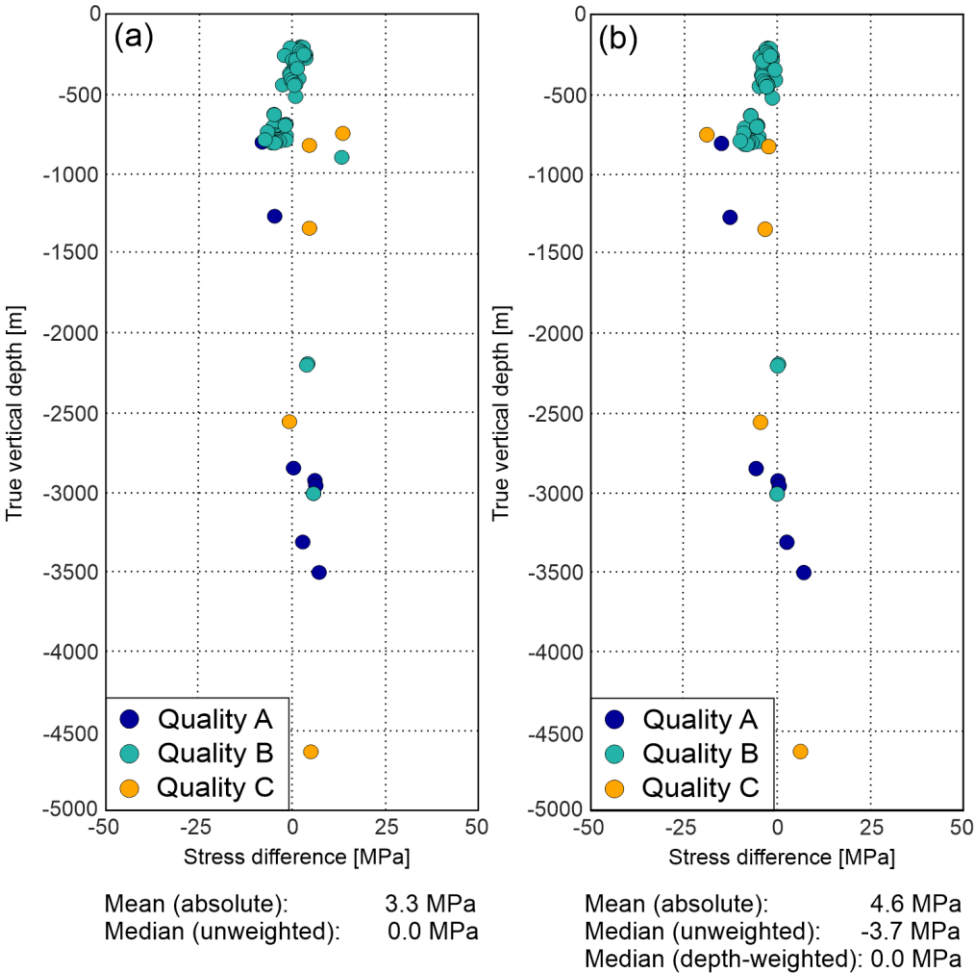

Figure 7.5: Comparison of S_{hmin} magnitudes of the 2021 (a) and 2022 (b) models with the calibration data of Morawietz and Reiter (2020). The differences are calculated as model results minus calibration value, i.e., positive differences indicate too high model results and negative values accordingly too low magnitudes predicted by the model. The differences are color-coded regarding their quality. (Reiter et al., 2022)

In order to check whether the trend towards too low values in the uppermost part is possibly due to a specific rock type or a locality, the differences for the 2022 model are shown again in Figure 7.6, this time color-coded according to these properties. However, no lithological dependency (Figure 7.6a) is recognizable and no dependency on location (Figure 7.6b), i.e., no rock type or location occurs separately or shows a trend deviating from the majority. This supports the observation that there is a general trend of too low S_{hmin} magnitudes in the upper part of the model. However, the statement is somewhat limited regarding the rock types, since there are only values of sedimentary units up to ~1400 m TVD, deeper only values from crystalline units.

Even if this does not disprove the general trend, there are possible explanations for the too low values for two rock types at ~750 m TVD (Figure 7.6b). The orange colored values (sandstone/schist/greywacke) include rock types that can behave mechanical different, but the rock types are not specified more precisely in the corresponding publications (Kohlbeck et al., 1980; Cornet

and Burlet, 1992). However, all three values are located within the PrePerm unit parameterized with a Young's modulus of 40 GPa. Which, for example, is a too high value for schists (e.g., Alber et al., 2015: ~25 GPa). In this case, a lower value would lead to higher S_{hmin} magnitudes and a better fit. A second rock type, which is obviously not well parameterized, is salt. However, some calibration data from Wittelsheim in the URG are taken from such an evaporitic salt-dominated sequenz (Figure 7.6; Cornet and Burlet, 1992).

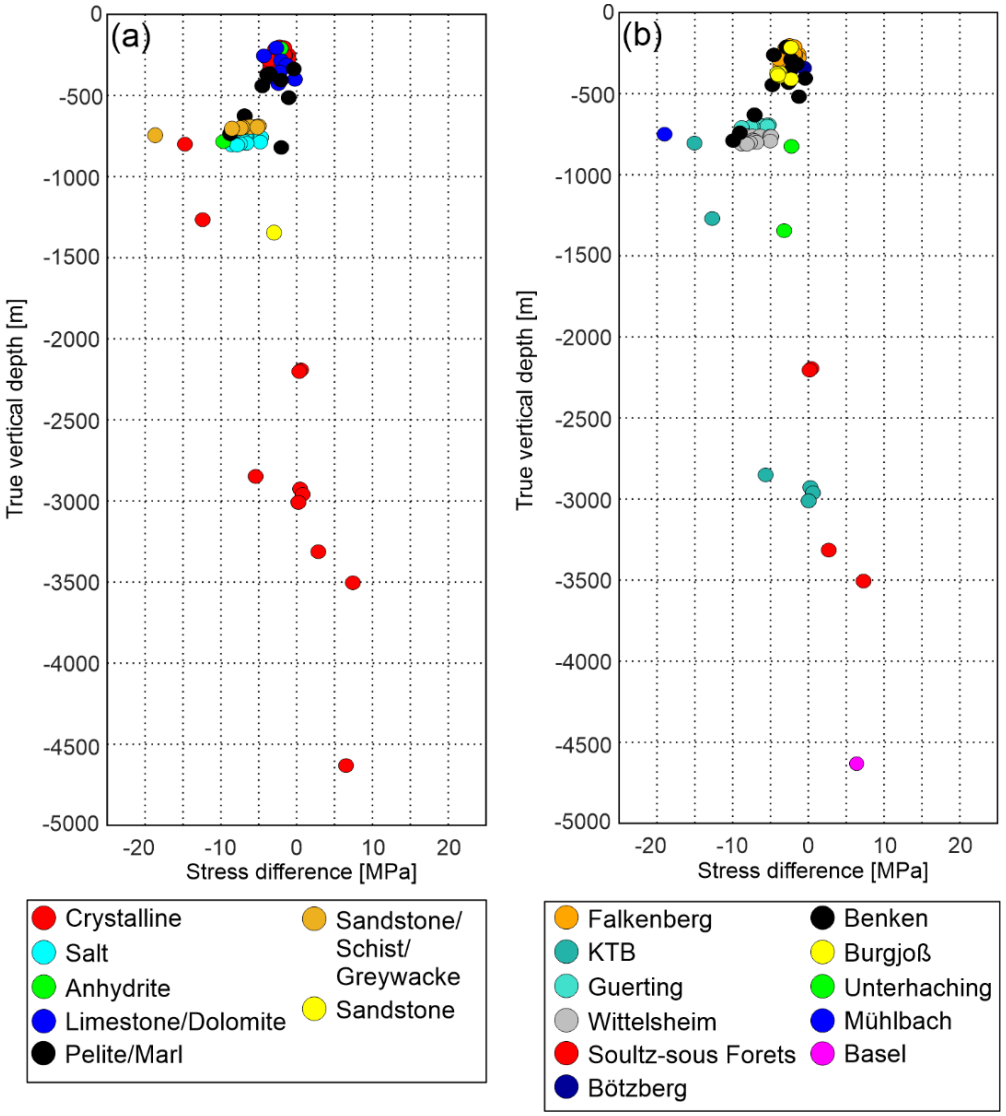

Figure 7.6: Differences of S_{hmin} magnitudes of the 2022 model to the calibration data of Morawietz and Reiter (2020) color-coded according to lithology (a) and locality (b).

To show the effect on the S_{hmin} magnitudes of visco-elastic salt properties - not implemented in the models - the differences of S_{hmin} are shown in Figure 7.7 assuming a lithostatic stress state for the data of Wittelsheim, which is typical for salt (e.g., Dusseault et al., 2004 or Ahlers et al., 2019). The corresponding data are at ~750 m TVD and are marked with a red outline.

The recalculated differences show an almost perfect fit with the calibration data. This also improves the overall fit of the mean of the absolute differences from 4.6 MPa to 3.6 MPa and the unweighted

median from -3.7 MPa to -2.4 MPa. The depth-weighted median, however, worsens slightly from 0.0 MPa to 0.2 MPa.

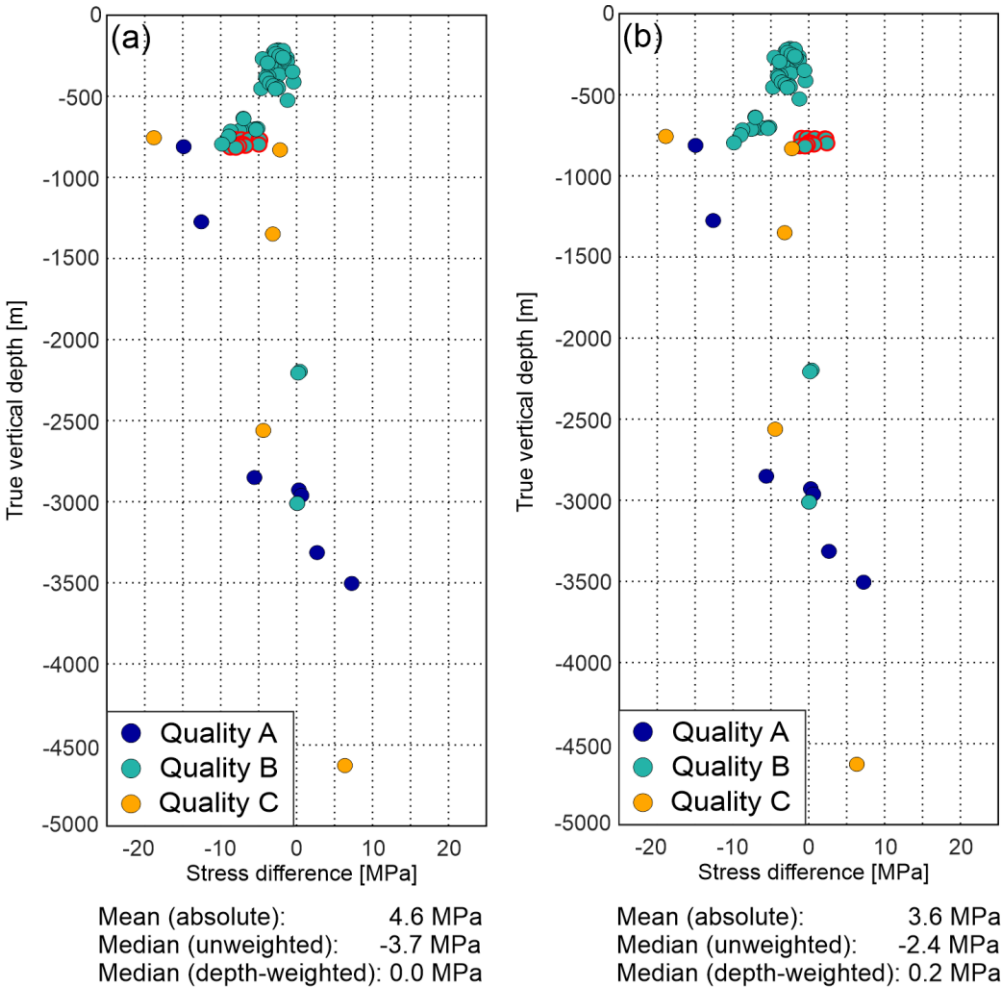

Figure 7.7: Differences of S_{hmin} magnitudes of the 2022 model (a) with calibration data of Morawietz and Reiter (2020) in comparison to recalculated model results (b) assuming a lithostatic stress state for Wittelsheim. The data from Wittelsheim (Cornet and Burlet, 1992) in ~750 m TVD are marked with a red outline. These are not model results; this is only a calculation made on the existing results of the 2022 model under the assumption that S_{hmin} is equal to S_V.

7.2.2 S_{Hmax} magnitudes

The S_{Hmax} results displayed in Figure 7.8 show, in contrast to the S_{hmin} magnitudes, significantly larger differences between the 2021 and 2022 model variants, a fact that is primarily due to its use as a calibration data in case of the 2022 model. The comparison of the unweighted median of 19.3 MPa (2021 model) to -0.9 MPa (2022 model) and the mean of the absolute differences of 20.6 MPa to 6.4 MPa show this. The differences in the upper kilometer of the models illustrate this too. While the 2021 model (Figure 7.8a) predicts up to 40 MPa too high values in this range, the deviations of the 2022 model (Figure 7.8b) rarely exceed 15 MPa. A quality-dependent distribution is not evident in either case. The results of the 2021 model show a clear tendency of increasing overestimation with

decreasing depth in the uppermost 1000 m TVD. The Young's modulus gradient, which reduces the magnitudes of S_{Hmax} especially in the uppermost part of the model reduce this tendency. However, a trend is still visible, which seems to be similar to the trend of the S_{hmin} magnitudes.

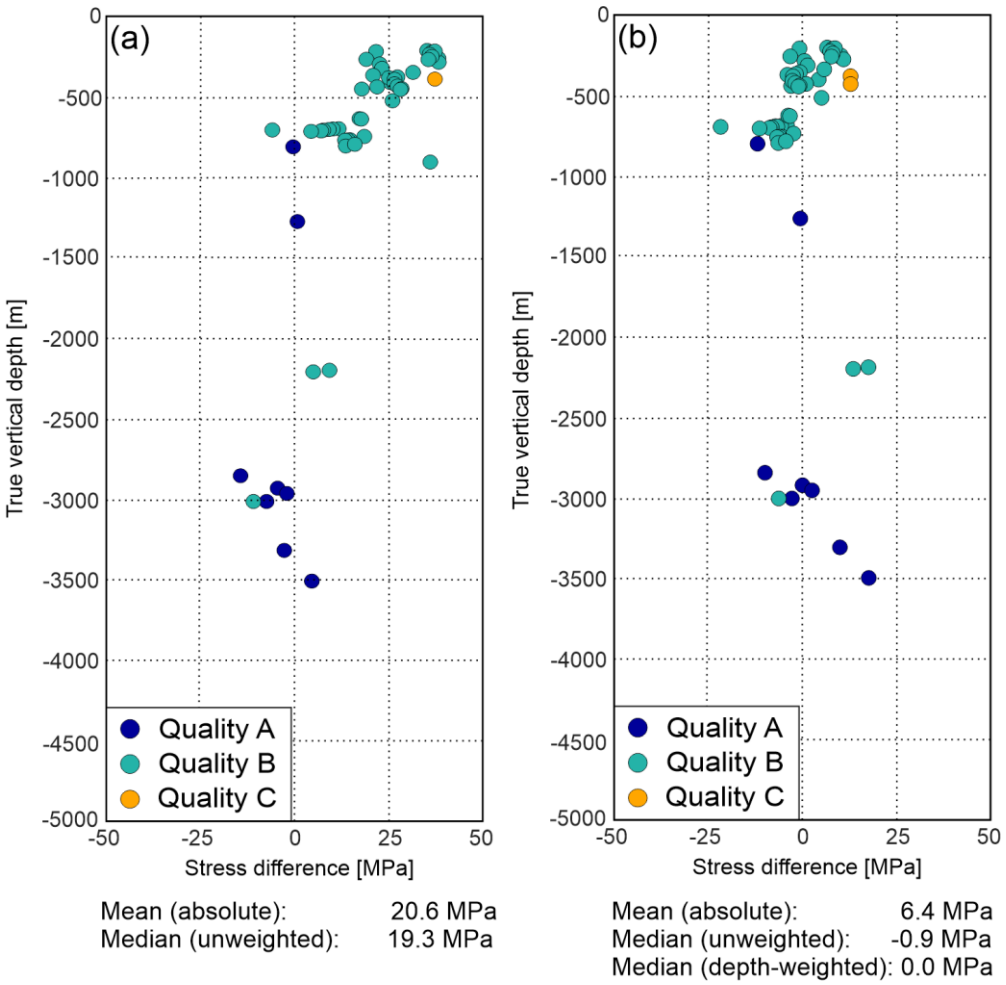

Figure 7.8: Comparison of S_{Hmax} magnitudes of the 2021 (a) and 2022 (b) models with the calibration data of Morawietz and Reiter (2020). The differences are calculated as model results minus calibration value, i.e., positive differences indicate too high model results and negative values accordingly too low magnitudes predicted by the model. The differences are color-coded regarding their quality. (Reiter et al., 2022)

As for the S_{hmin} magnitudes, the differences for the 2022 model are shown color-coded according to their lithology and localities in Figure 7.9. The results from Falkenberg differ slightly (Figure 7.9b), but since there are no other values from the crystalline at this depth, it must not be a location effect. Below 1500 m TVD, a location-dependent difference of ~15 MPa between Soultz-Sous-Forets and KTB is indicated. A possible cause, which is not considered by the model, could be the different thermal gradient, since the crust in the URG is much thinner than in the vicinity of the KTB (e.g., Anikiev et al. 2019). However, this differences could also be due to the rock type, since the crystalline (upper crustal units) are not further subdivided, but the magnitudes of the KTB are measured in amphibolite and in Soultz-Sous-Forets in granite. As for the differences of S_{hmin} the values from the PrePerm unit

(orange values: sandstone/schist/greywacke) indicate too low magnitudes. This does not fit to the assumption that the assumed Young's modulus might be too high, because too low S_{Hmax} values rather indicate too low value.

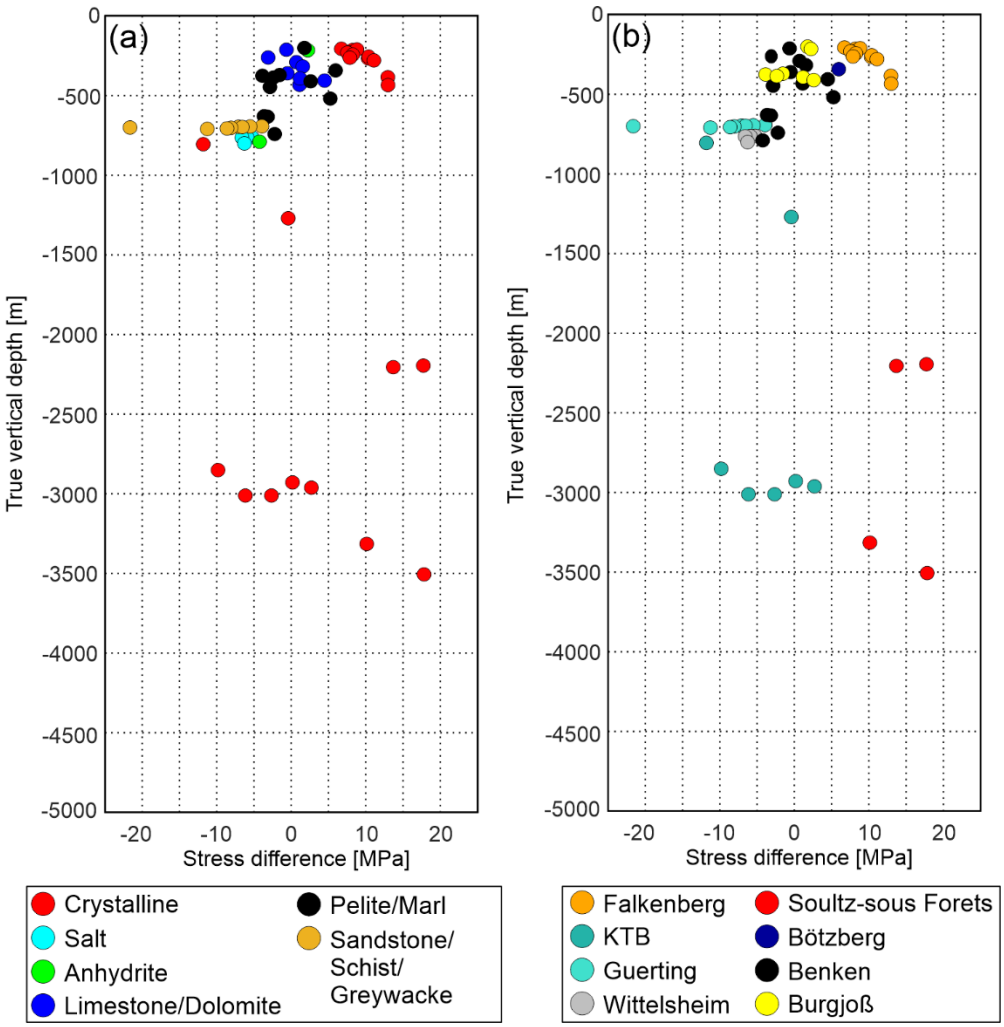

Figure 7.9: Differences of S_{Hmax} magnitudes of the 2022 model to the calibration data of Morawietz and Reiter (2020) color-coded according to lithology (a) and locality (b).

A possibility to increase both magnitudes is the incorporation of visco-elastic properties, e.g., for salt, if the horizontal magnitudes are lower than S_V, i.e., a normal faulting regime. Therefore, the effect of visco-elastic properties on the S_{Hmax} magnitudes in the 2022 model is shown in Figure 7.10 assuming a lithostatic stress state for the data of Wittelsheim (Cornet and Burlet, 1992). The corresponding data are at ~750 m TVD and are marked with a red outline. The recalculated differences show a slight decrease of the S_{Hmax} magnitudes and therefore a deterioration of the fit. Accordingly, the S_{Hmax} magnitudes are - within our model at the location of Wittelsheim - higher than the S_V magnitudes, i.e., a strike-slip regime. Therefore, missing visco-elastic properties cannot explain the misfit between model results and calibration data for this depth range.

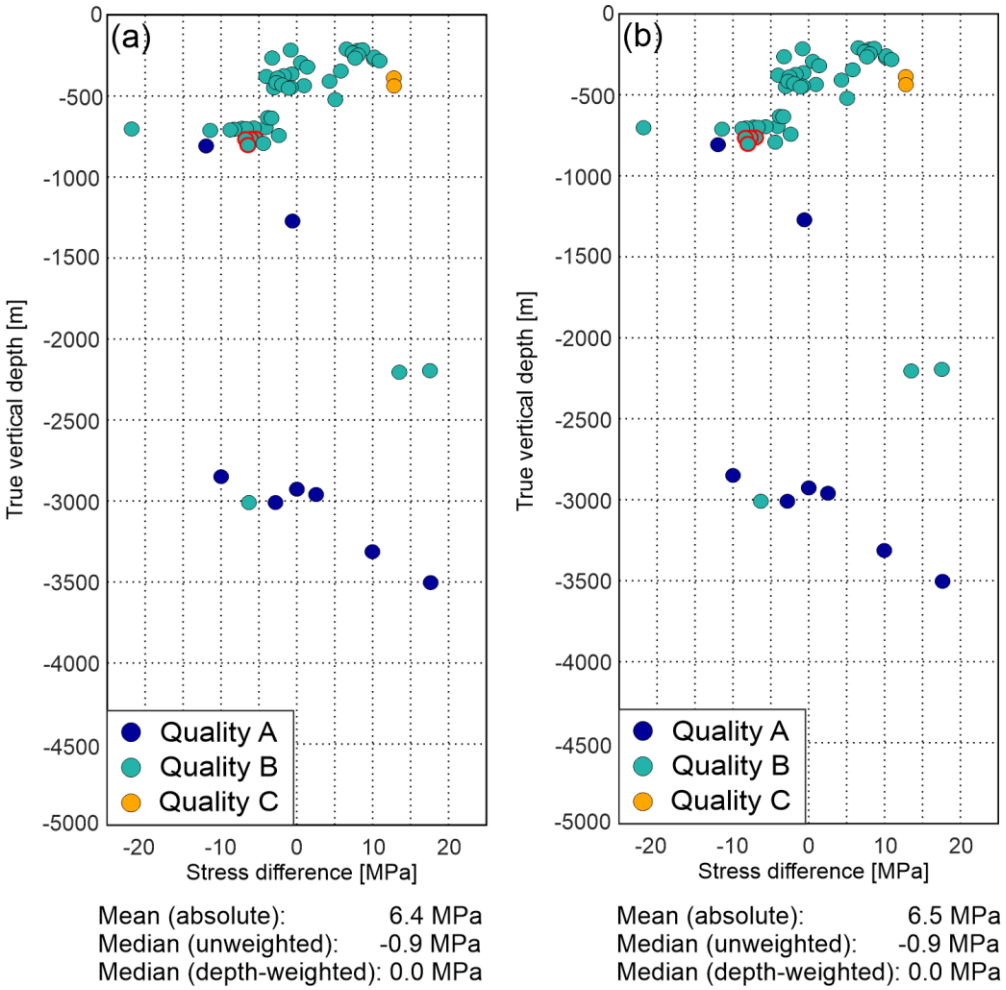

Figure 7.10: Differences of S_{Hmax} magnitudes of the 2022 model (a) with calibration data of Morawietz and Reiter (2020) in comparison to recalculated model results (b) assuming a lithostatic stress state for Wittelsheim. The data from Wittelsheim (Cornet and Burlet, 1992) in ~750 m TVD are marked with a red outline. These are not model results, this is only a calculation made on the existing results of the 2022 model under the assumption that S_{Hmax} is equal to S_V.

In summary, it can be said that the predicted S_{hmin} and S_{Hmax} magnitudes probably show a systematic deviation within the upper 750 m TVD of the model. Within this part, the results show a trend of decreasing differences regarding the calibration data, i.e., the magnitudes of S_{hmin} and S_{Hmax} increases with depth less than the calibration data. This results in too low S_{Hmax} magnitudes between 500 and 750 m TVD and too low S_{hmin} magnitudes for the entire part (0 – 750 m TVD). A systematic dependency of quality, lithology or locality is not detectable for this depth range. Unsuitable material properties – visco-elastic properties or too high Young's moduli – are also unlikely to explain this trend. Other possibilities to increase both horizontal magnitudes, such as higher density, higher Poisson's ratio, different boundary conditions or a different initial stress state are also not very promising as discussed in Chapter 5.4.2. However, it can also not be excluded that there is a regional or lithological effect that is not visible due to the small amount of data. For example, only one calibration value from the NGB could be used and there is no data from sedimentary units deeper than

1500 m TVD. However, it may also be the other way around that it only appears as if there is a systematic deviation due to the paucity of data. Since, the calibration data shown in Figure 2.9 indicate slightly different gradients of values up to ~750 m TVD and below. A trend which is not visible for the S_{hmin} magnitudes if all data qualities are plotted (Figure 7 in Morawietz et al., 2020).

7.3 Stress regime

The stress regime can differ significantly between regions, e.g., as shown in Figure 5.11. Therefore, the following discussion is subdivided with regard to individual regions. For this discussion, only the results of the model with the higher stratigraphic resolution of Ahlers et al. (2022b) are used.

7.3.1 Molasse Basin (MB)

Drews et al. (2019) describes a stress regime variation with depth within in the MB from a normal faulting regime in the upper Cenozoic basin fill to a strike-slip regime in the crystalline basement with a transition zone within the Mesozoic sediments in between based on their study and on studies of Megies and Wassermann (2014), Seithel et al. (2015) and Budach et al. (2017). This stress regime variation with depth fits results presented in Figure 5.12 almost perfect. All results along well paths within the MB - with a sediment-crystalline transition between 2.5 und 5 km TVD - show this trend, from a normal faulting regime in the upper sedimentary units to a strike-slip regime in the crystalline basement. However, in addition, our results show a second transition from strike-slip to a normal faulting regime below 7 to 8 km TVD (Figure 5.12).

7.3.2 North German Basin (NGB)

For the NGB, there are only few studies describing the absolute stress state and thus allow a determination of the stress regime. The studies of Moeck et al. (2009a; 2009b) describe a normal faulting regime for a depth of 4.1 km and a strike-slip regime in 4.2 km depth. However, S_{Hmax} and S_V magnitudes are almost equal with a stress difference of 2 MPa each. The results of Fleckenstein et al. (2004) show a continuous normal faulting regime between 3 and 5.2 km depth, again with very small differences between S_{Hmax} and S_V. In addition, Röckel and Lempp (2003) describe the tendency to a normal faulting regime in the subsalt, i.e., in the deeper parts of the NGB.

The results of the 2022 model (Figure 5.12) show a consistent normal faulting regime below 3 km depth. In the upper 3 km the model predicts a regime between strike-slip and normal faulting. Accordingly, the results of Moeck et al. (2009a; 2009b) do fit only partly to the model results, but the stress data of Fleckenstein et al. (2004) and the interpretation of Röckel and Lempp (2003) correspond to the predicted stress regime. However, the model results predicts significantly higher differential stresses than described by Moeck et al. (2009a; 2009b) and Fleckenstein et al. (2004).

7.3.3 Upper Rhine Graben (URG)

Klee and Rummel (1993), Cornet et al. (2007), Valley and Evans (2007) and Azzola et al. (2019) describe a normal to strike-slip regime at Rittershoffen and Soultz-sous-Forest which is in agreement with our model results which show this varying stress conditions in the northern part of the URG (Figure 5.11 and 5.12). For Bruchsal further to the north, Meixner et al. (2014) also predicts such a stress regime.

In addition, also the data of Häring et al. (2008) predicting a consistent strike-slip regime for Basel - in the south of the URG - differing slightly from the transitional regime in the northern URG, fits to our model results, which show an almost continuous strike-slip regime in this part of the model (Figure 5.12).

7.3.4 Albstadt and Ruhr Region

Two additional studies are chosen for discussion. A study of Mader et al. (2021) is used, since the Albstadt shear-zone is the most active fault in Germany and a study of Kruszewski et al. (2022), since they recently published an outstandingly good data set for the Ruhr Region not included in the magnitude database of Morawietz and Reiter (2020) so far and not used for the studies in Chapter 4 and 5.

Mader et al. (2021), predicts, that S_{Hmax} exceeds S_V in the upper part of the crust, i.e., a strike-slip regime and that S_V is dominant below 7 to 8 km, i.e., a normal faulting regime. This fits the model results within the region of Albstadt of the 2022 model quite well. However, the model results predict a normal faulting regime in the upper 500 m TVD and the transition from a strike-slip to a normal faulting occurs already in ~4.5 km TVD.

For the Ruhr Region the data of Kruszewski et al. (2022) show a normal faulting to strike-slip regime - dominated by a strike-slip regime - between ~500 to 2000 m. This is in agreement with our model results (e.g., Figure 5.11) which predict a dominant strike-slip regime within the upper 1500 m TVD for this region.

7.4 Fracture potential (FP) and slip tendency (T_S)

During this study, two analyses were carried out dealing with the failure probability of the rock mass and faults and the occurrence of earthquakes, respectively. On the one hand, the FP for the 2022 model (Chapter 5.3.2.6) has been calculated, on the other hand the T_S on existing faults has been extensively studied (Chapter 6).

The T_S-analysis shows clear dependencies of the strike, the dip and the cohesion of faults and pore pressure. Spatially, T_S fits quite well to the occurrence of earthquakes compiled by Grünthal and Wahlström (2012) and Quinteros et al. (2021), even though there are areas where the correlation is

clearly lacking. The FP does not show a clear trend. Although the predicted FP for northern Germany tends to be lower than for southern Germany, which correlates roughly with the earthquake distribution, the differences could more likely be explained by lithology contrasts, e.g., between sedimentary units and the crystalline basement (Figure 5.13 and corresponding explanations).

However, both analyses (T_S and FP) predict the highest failure probabilities at much shallower depths than the earthquakes whose majority occur at ~8 km depth. In addition, the consistently stable stress state with a maximum FP of 0.6 does not match the occurrence of earthquakes either. However, the geomechanical-numerical models also do not provide effective stresses, which are necessary to achieve critical T_S in the analysis of Röckel et al. (2022b). In general, T_S analysis predicts a critical role of pore pressure on fault failure. T_{Seff} of more than 1 are generally predicted only if overpressure is assumed. How often such overpressure prevails and whether there is a spatial link to observed earthquakes is difficult to say because area-wide data are missing. However, individual data from the MB support such a condition (Müller et al., 1988; Drews et al., 2018). For example, to increase T_S to the values of T_{Seff} without pore pressure along the Franconian Line, the model results of Ahlers et al. (2021a) (Chapter 4) would have to show a 30 MPa higher τ at 8 km depth. However, the required stress change would not fit the data from the KTB in the vicinity of the Franconian Line (Figure 4.10). However, data from depths greater than 4 km were not used for model calibration and the only two values from the KTB measured at 'typical' earthquake depths (~8 and ~9 km depth) should be viewed with caution, as the HFs were probably not successful (Brudy et al., 1997).

7.5 General model uncertainties

Due to the size of the model - 1000 x 1250 x 100 km, max. 11.1 million elements - and the associated high computation times, it is not yet possible to quantify uncertainties, e.g., regarding the calibration data (Ziegler and Heidbach, 2020). Nevertheless, in the following some uncertainties shall be listed, which can potentially influence the reliability of the model results.

The model geometry consists besides consistent data sets (Anikiev et al., 2019; Maystrenko and Scheck-Wenderoth, 2013; Tašárová et al., 2016) of several different data sets, whose quality and uncertainties are very difficult to estimate. In particular, which have been used for the creation of the top of the crystalline basement. In addition, the data density is sometimes very poor, e.g., in central Germany (Figure 4.4).

For the parameterization of the model units - also in the 2022 model - averaged values are used, which contain partly very different mechanical layers, e.g., the Triassic or the Jurassic unit. Furthermore, there are no lateral differences that could describe facies changes. This is on the one hand due to the lack of data for such a differentiation and on the other hand due to the limited model resolution. The 2022 model, for example, requires 750 m (3 elements of 250m each) to fully represent a layer mechanically. However, the largest uncertainties probably arise from the purely elastic parameters.

This concerns on the one hand sedimentary layers, like salt (especially in northern Germany: e.g., Röckel and Lempp, 2003, Heidbach et al., 2007, Ahlers et al., 2019) and unconsolidated sediments that can behave in a visco-elastic manner (e.g., Chang and Zoback, 1998, Zoback, 2007). On the other hand, the deeper units of the models below the brittle-ductile transition in Germany, e.g., in the vicinity of the KTB at ~10 km depth (e.g., Zang and Stephansson, 2010), in regions with a higher thermal gradient like the URG correspondingly shallower. Therefore, a large part of our model would probably be better parameterized with visco-elastic properties. However, the focus of this study is on the uppermost part of the crust and the deepest available calibration data used are from a depth of 4 km.

In general, the quantity and quality of the calibration data is a problem, since for example from northern Germany only one data record with a reliable quality of A to C is available. Despite all uncertainties, it should be taken into account that the models of this study try to represent the regional longwave stress field and therefore not all local variations have to be included.

8 Conclusion and outlook

The geomechanical-numerical 3D models presented in this study are the first models, which allow for a continuous prediction of the complete stress tensor of the recent upper crustal stress state of Germany. The results of the second, updated version (Ahlers et al., 2022a; Chapter 5) are in a good agreement with several different stress datasets and studies available for Germany, which are used for calibration and validation. The predicted orientation of S_{Hmax} within the central part of the model - covering entire Germany - in comparison to mean WSM data and some additional of Levi et al., 2019 shows a median of deviation of 0.3° and a mean of the absolute deviation of 11.6°. This mean of the absolute deviation is smaller than the uncertainties of the best data of the WSM used (A: <15°; Heidbach et al., 2018) and the model results lie entirely within the standard deviation of the mean data used for comparison. All three principal stress magnitudes (S_V, S_{hmin} and S_{Hmax}) show a good fit to the data used of Morawietz and Reiter (2020) with means of the absolute differences of 0.0 MPa for S_V, of 4.6 MPa for S_{hmin} and of 6.4 MPa for S_{Hmax}. The differences to the calibration data (S_{hmin} and S_{Hmax}) are mainly within in a range of +/- 10 MPa for the S_{hmin} magnitudes and within a range of +/- 20 MPa for the S_{Hmax} magnitudes. Furthermore, the results show good agreement with additional stress data from the NGB, MB, and URG that were not used for calibration and observed stress regimes within these regions. The results of the third study (Röckel et al., 2022b; Chapter 6) - for which the results of the first model (Chapter 4) are used - also confirm the overall good model results, as they show a good spatial correlation with elevated T_S and earthquakes of Grünthal and Wahlström (2012) and Quinteros et al. (2021).

However, the results also show some limitations of the models but also of the available data and unresolved issues that need to be improved and further investigated. The orientations of S_{Hmax} predicted by both models are almost homogeneous and do not show some regional trends of the observed stress field, e.g., within the NEGB, in central Germany or northeast of the Alps. Furthermore, the magnitudes of S_{hmin} and S_{Hmax} show probably systematic deviations to the calibration data within the uppermost 750 m of the model and the depth position of the highest T_S and earthquakes do not match.

One of the biggest limitation for this study is the lack of high quality magnitude data. 56 S_{Hmax} and 73 S_{hmin} magnitudes - with a quality ranking of A to C and from a depth >200 m - from about ten localities could be used for calibration. Especially for the northern half of Germany from which only one value is available. More magnitude data usable for calibration would improve the reliability of our model results and would allow a much more detailed data analysis. In addition, more pore pressure data, fault geometry data and friction properties of faults are of crucial importance for an improved T_S analysis.

Improvements that could still be made to the current model would include vertical and lateral parameter variations, the integration of visco-elastic and temperature dependent material parameters (associated with a temperature field), the implementation of new higher resolution structural models,

e.g., the TUNB model (BGR et al., 2022) and the incorporation of faults. However, many of these improvements require significantly higher mesh resolution, which further reduces the handling capability of the model. One way to build much more complex models is the submodeling approach, where information from large-scale, simple models can be transferred to small-scale, complex models (e.g., Ziegler et al., 2016). Another point that would improve the reliability of the model is the quantification of model uncertainties.

Appendix

DVD containing the results and geometries of Ahlers et al. (2021b, 2022b) and Röckel et al. (2022a), with the following folders and files:

Ahlers_et_al_2021:
- _Readme_Ahlers_et_al_2021.dat
- Stress_tensor_Ahlers_et_al_2021.dat

Ahlers_et_al_2022:
- _Readme_Ahlers_et_al_2022
- Modell_geometry_Ahlers_et_al_2022.inp
- Stress_tensor_Ahlers_et_al_2022.dat

Röckel_et_al_2022:
- _Readme_Röckel_et_al_2022.dat
- Andersonian_Normal_Faults.txt
- Andersonian_Strike_Slip_Faults.txt
- Andersonian_Thrust_Faults.txt
- Semi_Realistic_Normal_Faults.txt
- Semi_Realistic_Strike_Slip_Faults.txt
- Semi_Realistic_Thrust_Faults.txt
- Vertical_Fault set.txt

Detailed information to each file can be found in the Readme files.

References

Adams, J. and Bell, J. S.: Crustal stresses in Canada, in: Neotectonics of North America, edited by: Slemmons, D. B., Engdahl, E. R., Zoback, M. D., and Blackwell, D. D., Geological Society of America, U.S.A, 367–386, https://doi.org/10.1130/DNAG-CSMS-NEO.367, 1991.

Agemar, T., Alten, J.-A., Gorling, L., Gramenz, J., Kuder, J., Suchi, E., Moeck, I., Weber, J., V. Hartmann, H., Stober, I., Hese, F., and Thomsen, C.: Verbundsvorhaben "StörTief": Die Rolle von tiefreichenden Störungszonen bei der geothermischen Energienutzung, Endbericht, 2016.

Ahlers, S., Röckel, L., Hergert, T., Reiter, K., Heidbach, O., Henk, A., Müller, B., Morawietz, S., Scheck-Wenderoth, M., and Anikiev, D.: The crustal stress field of Germany: a refined prediction, Geotherm Energy, 10, https://doi.org/10.1186/s40517-022-00222-6, 2022a.

Ahlers, S., Henk, A., Hergert, T., Reiter, K., Müller, B., Röckel, L., Heidbach, O., Morawietz, S., Scheck-Wenderoth, M., and Anikiev, D.: The Crustal stress state of Germany - Results of a 3D geomechnical model v2, TUdatalib [data set], https://doi.org/10.48328/tudatalib-437.5, available at: https://tudatalib.ulb.tu-darmstadt.de/handle/tudatalib/2624.5, 2022b.

Ahlers, S., Henk, A., Hergert, T., Reiter, K., Müller, B., Röckel, L., Heidbach, O., Morawietz, S., Scheck-Wenderoth, M., and Anikiev, D.: 3D crustal stress state of Germany according to a data-calibrated geomechanical model, Solid Earth, 12, 1777–1799, https://doi.org/10.5194/se-12-1777-2021, 2021a.

Ahlers, S., Henk, A., Hergert, T., Reiter, K., Müller, B., Röckel, L., Heidbach, O., Morawietz, S., Scheck-Wenderoth, M., and Anikiev, D.: The Crustal stress state of Germany - Results of a 3D geomechnical model, TUdatalib [data set], https://doi.org/10.48328/tudatalib-437, 2021b.

Ahlers, S., Hergert, T., and Henk, A.: Numerical Modelling of Salt-Related Stress Decoupling in Sedimentary Basins–Motivated by Observational Data from the North German Basin, Geosciences, 9, https://doi.org/10.3390/geosciences9010019, 2019.

Aichholzer, C., Duringer, P., Orciani, S., and Genter, A.: New stratigraphic interpretation of the Soultz-sous-Forêts 30-year-old geothermal wells calibrated on the recent one from Rittershoffen (Upper Rhine Graben, France), Geothermal Energy, 4, 1–26, https://doi.org/10.1186/s40517-016-0055-7, 2016.

Alber, M. and Solibida, C.: Geomechanical Characterization of a Host Rock for Enhanced Geothermal System in the North-German Basin, Procedia Engineering, 191, 158–163, https://doi.org/10.1016/j.proeng.2017.05.167, available at: http://www.sciencedirect.com/science/article/pii/S187770581732307X, 2017.

Alber, M., Backers, T., Bartmann, K., Brenne, S., Dinter, S., Dresen, G., Gipper, P., Grühser, C., Heft, S., Meier, T., Molenda, M., Röske, F., and Stöckhert, F.: Abschlussbericht zum Verbundprojekt: Erforschung der Mechanismen und Simulation hydraulisch induzierter Risse in geklüfteten Gesteinen für die Optimierung des Aufschlusses geothermischer Lagerstätten, Ruhr-Universität Bochum, geomecon GmbH, 2015.

Altmann, J. B., Müller, B., Müller, T. M., Heidbach, O., Tingay, M., and Weißhardt, A.: Pore pressure stress coupling in 3D and consequences for reservoir stress states and fault reactivation, Geothermics, 52, 195–205, https://doi.org/10.1016/j.geothermics.2014.01.004, 2014.

Amadei, B. and Stephansson, O.: Rock Stress and Its Measurement, Springer Netherlands, Dordrecht, 490 pp., 1997.

Anderson, E. M.: The dynamics of faulting, Transactions of the Edinburgh Geological Society, 8, 387–402, https://doi.org/10.1144/transed.8.3.387, 1905.

Andeweg, B.: Cenozoic tectonic evolution of the Iberian Peninsula: Effects and causes of changing stress fields, Ph. D. thesis, Faculty of Earth Sciences, Vrije Universiteit, Amsterdam, 178 pp., 2002.

Angelier, J.: Determination of the mean principal directions of stresses for a given fault population, Tectonophysics, 56, T17-T26, https://doi.org/10.1016/0040-1951(79)90081-7, 1979.

Anikiev, D., Lechel, A., Gomez Dacal, M. L., Bott, J., Cacace, M., and Scheck-Wenderoth, M.: A three-dimensional lithospheric-scale thermal model of Germany, Adv. Geosci., 49, 225–234, https://doi.org/10.5194/adgeo-49-225-2019, 2019.

Asch, K.: The 1:5 Million International Geological Map of Europe and Adjacent Areas (IGME5000), Bundesanstalt für Geowissenschaften und Rohstoffe, Hannover, 2005.

Azzola, J., Valley, B., Schmittbuhl, J., and Genter, A.: Stress characterization and temporal evolution of borehole failure at the Rittershoffen geothermal project, Solid Earth, 10, 1155–1180, https://doi.org/10.5194/se-10-1155-2019, 2019.

Backers, T., Meier, T., Gipper, P., Munsch, P., Bücken, D., Nokar, K., Dinter, S., Grühser, C., Heft, S., and Röske, F.: Abschlussbericht zum Teilprojekt B: Struktur- und Spannungsfeld im Verbundprojekt MAFA: Parametrisierung von Fazies, Diagenese, Struktur- und Spannungsfeld sowie Optimierung der Testabläufe im Malm zur Verringerung des Erfolgsrisikos, geomecon GmbH, 44 pp., 2017.

Bada, G., Horváth, F., Cloetingh, S., Coblentz, D. D., and Tóth, T.: Role of topography-induced gravitational stresses in basin inversion: The case study of the Pannonian basin, Tectonics, 20, 343–363, https://doi.org/10.1029/2001TC900001, 2001.

Bada, G., Cloetingh, S., Gerner, P., and Horváth, F.: Sources of recent tectonic stress in the Pannonian region: Inferences from finite element modelling, Geophys. J. Int., 134, 87–101, https://doi.org/10.1046/j.1365-246x.1998.00545.x, 1998.

Bär, K., Reinsch, T., and Bott, J.: The PetroPhysical Property Database (P^3) – a global compilation of lab-measured rock properties, Earth Syst. Sci. Data, 12, 2485–2515, https://doi.org/10.5194/essd-12-2485-2020, 2020.

Barth, A., Reinecker, J., and Heidbach, O.: Guidelines for the analysis of earthquake focal mechanism solutions, in: WSM quality ranking scheme, database description and analysis guidelines for stress indicator, GFZ German Research Centre for Geosciences, 13–26, https://doi.org/10.2312/wsm.2016.001, 2016.

Barton, C. A., Zoback, M. D., and Burns, K. L.: In-situ stress orientation and magnitude at the Fenton Geothermal Site, New Mexico, determined from wellbore breakouts, Geophys. Res. Lett., 15, 467–470, https://doi.org/10.1029/GL015i005p00467, 1988.

Baumgärtner, J., Rummel, F., and Zhaotan, C.: Wireline hydraulic fracturing stress measurements in the Falkenberg granite massif, Geol. Jb., E 39, 83–99, 1987.

Behr, H. J., Duerbaum, H. J., Bankwitz, P., Bankwitz, E., Benek, R., Berger, H. J., Brause, H., Conrad, W., Foerste, K., Frischbutter, A., Gebrande, H., Giese, P., Goethe, W., Guertler, J., Haenig, D., Haupt, M., Heinrichs, T., Horst, W., Hurtig, E., and Kaempf, H.: Crustal structure of the Saxothuringian Zone; results of the deep seismic profile MVE-90(East), Z. Geol. Wissenschaft., 22, 647–770, 1994.

Bell, J. S.: Practical methods for estimating in situ stresses for borehole stability applications in sedimentary basins, J. Petrol. Sci. Eng., 38, 111–119, https://doi.org/10.1016/S0920-4105(03)00025-1, 2003.

Bell, J. S.: Petro geoscience 2. In situ stresses in sedimentary rocks (part 2): Applications of stress measurements, Geoscience Canada, 23, 135–153, available at: https://www.scopus.com/inward/record.uri?eid=2-s2.0-0030423139&partnerID=40&md5=c54789a3a5aab7d087fb328b97a87eba, 1996.

BGR: Abriss der Standortauswahl und Darstellung der angewandten geowissenschaftlichen Kriterien bei den Endlagerprojekten in den Ländern Schweiz, Frankreich, Schweden, Belgien und USA, Hannover, 126 pp., 2015.

BGR, LAGB, LBEG, LBGR, LLUR, and LUNG: 3D-Modell des geologischen Untergrundes des Norddeutschen Beckens (Projekt TUNB): Erstveröffentlichung 2021, Version 2022, https://gst.bgr.de, last access: 15 June 2022, 2022.

Bokelmann, G. and Bianchi, I.: Imaging the Variscan suture at the KTB deep drilling site, Germany, Geophys. J. Int., 213, 2138–2146, https://doi.org/10.1093/gji/ggy098, 2018.

Bönnemann, C., Schmidt, B., Ritter, J., Gestermann, N., Plenefisch, T., and Wegler, U.: Das seismische Ereignis bei Landau vom 15. August 2009 - Abschlussbericht der Expertengruppe Seismisches Risiko bei hydrothermaler Geothermie, Bundesanstalt für Geowissenschaften und Rohstoffe, Hannover, 2010.

Bormann, P., Bankwitz, P., Apitz, E., Bankwitz, E., and Franzke, H. J.: Komplexinterpretation des Profilnetzes ZENTROSEIS - Abschlussbericht, Zentralinstitut für Physik der Erde, Potsdam, Bericht der SAG Tiefenerkundung (G4), 162 pp., 1986.

Brady, B. H. and Brown, E. T.: Rock Mechanics for underground mining, 3th, Springer Netherlands, Dordrecht, 628 pp., 2004.

Brooke-Barnett, S., Flottmann, T., Paul, P. K., Busetti, S., Hennings, P., Reid, R., and Rosenbaum, G.: Influence of basement structures on in situ stresses over the Surat Basin, southeast Queensland, J. Geophys. Res., 120, 4946–4965, https://doi.org/10.1002/2015JB011964, 2015.

Brown, E. T. and Hoek, E.: Trends in relationships between measured in-situ stresses and depth, International Journal of Rock Mechanics and Mining Sciences & Geomechanics Abstracts, 15, 211–215, https://doi.org/10.1016/0148-9062(78)91227-5, 1978.

Brückl, E., Behm, M., Decker, K., Grad, M., Guterch, A., Keller, G. R., and Thybo, H.: Crustal structure and active tectonics in the Eastern Alps, Tectonics, 29, TC2011, https://doi.org/10.1029/2009TC002491, 2010.

Brückl, E., Bleibinhaus, F., GOSAR, A., Grad, M., Guterch, A., Hrubcová, P., Keller, G. R., Majdański, M., Šumanovac, F., Tiira, T., Yliniemi, J., Hegedűs, E., and Thybo, H.: Crustal structure due to collisional and escape tectonics in the Eastern Alps region based on profiles Alp01 and Alp02 from the ALP 2002 seismic experiment, Journal of Geophysical Research: Solid Earth, 112, 1109, https://doi.org/10.1029/2006JB004687, 2007.

Brudy, M., Zoback, M. D., Fuchs, K., Rummel, F., and Baumgärtner, J.: Estimation of the complete stress tensor to 8 km depth in the KTB scientific drill holes: Implications for crustal strength, J. Geophys. Res., 102, 18453–18475, https://doi.org/10.1029/96JB02942, 1997.

Brun, J. P., Gutscher, M.-A., and dekorp-ecors teams: Deep crustal structure of the Rhine Graben from dekorp-ecors seismic reflection data: A summary, Tectonophysics, 208, 139–147, https://doi.org/10.1016/0040-1951(92)90340-C, 1992.

Buchmann, T. J. and Connolly, P. T.: Contemporary kinematics of the Upper Rhine Graben: A 3D finite element approach, Global Planet. Change, 58, 287–309, https://doi.org/10.1016/j.gloplacha.2007.02.012, 2007.

Budach, I., Moeck, I., Lüschen, E., and Wolfgramm, M.: Temporal evolution of fault systems in the Upper Jurassic of the Central German Molasse Basin: case study Unterhaching, Geol Rundsch, 107, 635–653, https://doi.org/10.1007/s00531-017-1518-1, 2017.

Cacace, M.: Stress and Strain modelling of the Central European Basin System, Ph. D. thesis, Freie Universität Berlin, Berlin, 167 pp., 2008.

Cacace, M., Bayer, U., and Marotta, A. M.: Strain localization due to structural in-homogeneities in the Central European Basin System, Geologische Rundschau, 97, 899–913, https://doi.org/10.1007/s00531-007-0192-0, 2008.

Carruthers, D., Cartwright, J., Jackson, M. P., and Schutjens, P.: Origin and timing of layer-bound radial faulting around North Sea salt stocks: New insights into the evolving stress state around rising diapirs, Marine and Petroleum Geology, 48, 130–148, https://doi.org/10.1016/j.marpetgeo.2013.08.001, 2013.

Cazes, M., Torreilles, G., Bois, C., Damotte, B., Galdeano, A., Hirn, A., Mascle, A., Matte, P., van Ngoc, P., and Raoult, J. F.: Structure de la croute hercynienne du Nord de la France; premiers resultats du profil ECORS, Bulletin de la Société Géologique de France, 8, 925–941, https://doi.org/10.2113/gssgfbull.I.6.925, 1985.

Chang, C. T. and Zoback, M. D.: Viscous Rheology and State of Stress in Unconsolidated Sands, Rock Mechanics in Petroleum Engineering, Trondheim, Norway, July 1998., 465–473, https://doi.org/10.2118/47401-MS, 1998.

Conder, J.: focalmech James Conder (2022). focalmech(fm, centerX, centerY, diam, varargin), MATLAB Central File Exchange, 2022.

Connolly, P. and Cosgrove, J.: Prediction of static and dynamic fluid pathways within and around dilational jogs, Geological Society, London, Special Publications, 155, 105–121, https://doi.org/10.1144/GSL.SP.1999.155.01.09, 1999.

Cornet, F. H. and Burlet, D.: Stress field determinations in France by hydraulic tests in boreholes, J. Geophys. Res.-Sol. Ea., 97, 11829–11849, https://doi.org/10.1029/90JB02638, 1992.

Cornet, F. H., Bérard, T., and Bourouis, S.: How close to failure is a granite rock mass at a 5km depth?, Int. J. Rock Mech. Min, 44, 47–66, https://doi.org/10.1016/j.ijrmms.2006.04.008, 2007.

Cornet, F. H. and Röckel, T.: Vertical stress profiles and the significance of "stress decoupling", Tectonophysics, 581, 193–205, https://doi.org/10.1016/j.tecto.2012.01.020, 2012.

Crameri, F.: Scientific colour maps, https://doi.org/10.5281/zenodo.1243862, 2021.

Desroches, J., Peyret, E., Gisolf, A., Wilcox, A., Di Giovanni, M., Jong, A. S. de, Sepehri, S., Garrard, R., and Giger, S.: Stress Measurement campaign in scientific deep boreholes: focus on tool and methods, SPWLA 62nd Annual Logging Symposium, May 17-20, https://doi.org/10.30632/SPWLA-2021-0056, 2021.

Diebold, P., Naef, H., and Ammann, M.: NTB 90-04: Zur Tektonik der zentralen Nordschweiz - Interpretation aufgrund regionaler Seismik, Oberflächengeologie und Tiefbohrungen, nagra, Wettingen, 277 pp., 1991.

Diederichs, M., Kaiser, P., and Eberhardt, E.: Damage initiation and propagation in hard rock during tunnelling and the influence of near-face stress rotation, Int. J. Rock Mech. Min, 41, 785–812, https://doi.org/10.1016/j.ijrmms.2004.02.003, 2004.

Drews, M., Bauer, W., and Stollhofen, H.: Porenüberdruck im Bayrischen Molassebecken, Overpressure in the Bavarian Molasse Basin, Erdöl Erdgas Kohle, 308–310, https://doi.org/10.19225/180703, 2018.

Drews, M. C., Seithel, R., Savvatis, A., Kohl, T., and Stollhofen, H.: A normal-faulting stress regime in the Bavarian Foreland Molasse Basin? New evidence from detailed analysis of leak-off and formation integrity tests in the greater Munich area, SE-Germany, Tectonophysics, 755, 1–9, https://doi.org/10.1016/j.tecto.2019.02.011, 2019.

Drozdzewski, G. and Dölling, M.: Elemente der Osning-Störungszone (NW-Deutschland): Leitstrukturen einer Blattverschiebungszone, scriptum online, 7, Geologischer Dienst Nordrhein-Westfalen, 39 pp., 2018.

Dubelaar, C. W. and Nijland, T. G.: Early Cretaceous Obernkirchen and Bentheim Sandstones from Germany used as dimension stone in the Netherlands: geology, physical properties, architectural use and comparative weathering, in: Geomaterials in construction and their sustainability: understanding their role in modern society, edited by: Přikryl, R., Török, Á., Theodoridou, M., Gomez-Heras, M., and Miskovsky, K., 163–181, https://doi.org/10.1144/SP416.13, 2016.

Duin, E., Doornenbal, J. C., Rijkers, R., Verbeek, J. W., and Wong, T.: Subsurface structure of the Netherlands - results of recent onshore and offshore mapping, Netherlands Journal of Geosciences, 85, 245–276, https://doi.org/10.1017/S0016774600023064, 2006.

Dusseault, M. B., Maury, V., Sanfilippo, F., and Santarelli, F. J.: Drilling Around Salt: Risks, Stresses, And Uncertainties, in: ARMA Conference Paper - 2004, Houston, Texas, 5-6 June 2004, 2004.

Eckert, A. and Connolly, P.: 2D finite element modelling of regional and local fracture networks in the Eastern California shear zone and coso range, California USA, Transactions - Geothermal Resources Council, 28, 643–648, 2004.

Evans, K. F., Zappone, A., Kraft, T., Deichmann, N., and Moia, F.: A survey of the induced seismic responses to fluid injection in geothermal and CO2 reservoirs in Europe, Geothermics, 41, 30–54, https://doi.org/10.1016/j.geothermics.2011.08.002, 2012.

Eynatten, H. von, Kley, J., Dunkl, I., Hoffmann, V.-E., and Simon, A.: Late Cretaceous to Paleogene exhumation in central Europe – localized inversion vs. large-scale domal uplift, Solid Earth, 12, 935–958, https://doi.org/10.5194/se-12-935-2021, 2021.

Feist-Burkhardt, S., Götz, A. E., Szulc, J., Borkhataria, R., Geluk, M., Haas, J., Hornung, J., Jordan, P., Kempf, O., Michalik, J., Nawrocki, J., Reinhardt, L., Ricken, W., Röhling, H.-G., Rüffer, T., Török, Á., and Zühlke, R.: Triassic, in: The Geology of Central Europe Volume 1: Precambrian and Palaeozoic; Volume 2: Mesozoic and Cenozoic, edited by: McCann, T., The Geological Society of London, 749–821, https://doi.org/10.1144/CEV2P.1, 2008.

Ferrill, D. A., Smart, K. J., and Morris, A. P.: Resolved stress analysis, failure mode, and fault-controlled fluid conduits, Solid Earth, 11, 899–908, https://doi.org/10.5194/se-11-899-2020, 2020.

Ferrill, D. A., Morris, A. P., McGinnis, R. N., Smart, K. J., Wigginton, S. S., and Hill, N. J.: Mechanical stratigraphy and normal faulting, Journal of Structural Geology, 94, 275–302, https://doi.org/10.1016/j.jsg.2016.11.010, 2017.

Fischer, K. and Henk, A.: A workflow for building and calibrating 3-D geomechanical models - a case study for a gas reservoir in the North German Basin, Solid Earth, 4, 347–355, https://doi.org/10.5194/se-4-347-2013, 2013.

Fischer, K., Jahr, T., and Jentzsch, G.: Evolution of the Variscan foreland-basin: modelling the interactions between tectonics and surface processes, Physics and Chemistry of the Earth, Parts A/B/C, 29, 665–671, https://doi.org/10.1016/j.pce.2004.03.004, 2004.

Fleckenstein, P., Reuschke, G., and Müller, B., and Connolly, P.: Predicting stress re-orientations associated with major geological structures in sedimentary sequences, DGMK, 593-5, 90 pp., 2004.

Franke, W., Bortfeld, R. K., Brix, M., Drozdzewski, G., Dürbaum, H. J., Giese, P., Janoth, W., Jödicke, H., Reichert, C., Scherp, A., Schmoll, J., Thomas, R., Thünker, M., Weber, K., Wiesner, M. G., and Wong, H. K.: Crustal structure of the Rhenish Massif: results of deep seismic reflection lines Dekorp 2-North and 2-North-Q, Geol Rundsch, 79, 523–566, https://doi.org/10.1007/BF01879201, 1990.

Franke, W.: The Variscan orogen in Central Europe: Construction and collapse, in: European Lithosphere Dynamics, edited by: Gee, D. R. and Stephenson, R., Geological Society of London, London, 333–343, https://doi.org/10.1144/GSL.MEM.2006.032.01.20, 2006.

Franke, W.: Tectonostratigraphic units in the Variscan belt of central Europe, GSA Special Papers, 230, 67–90, https://doi.org/10.1130/SPE230-p67, 1989.

Franzke, H.-J. and Wetzel, H.-U.: Geologische Interpretation eines ERS-1 Radarmosaiks von Deutschland, Publikationen der Deutschen Gesellschaft für Photogrammetrie und Fernerkundung, 10, 503–510, available at: https://gfzpublic.gfz-potsdam.de/pubman/faces/ViewItemOverviewPage.jsp?itemId=item_228436, 2001.

Freeman, R. and Mueller, S. (Eds.): A continent revealed: The European geotraverse, Cambridge Univ. Pr, Cambridge [u.a.], 275 pp., 1992.

Garrard, R., Gonus, J., Desroches, J., and Bailey, E.: TBO Bülach-1-1: Data Report - Dossier VI Wireline Logging and Microhydraulic Fracturing, nagra, Arbeitsbericht NAB, 20-08, 2021.

Gaucher, E., Schoenball, M., Heidbach, O., Zang, A., Fokker, P. A., van Wees, J.-D., and Kohl, T.: Induced seismicity in geothermal reservoirs: A review of forecasting approaches, Renewable and Sustainable Energy Reviews, 52, 1473–1490, https://doi.org/10.1016/j.rser.2015.08.026, 2015.

Geißler, V., Gauer, A., and Görne, S.: Innovative digitale Geomodelle 2020 - Teil 1, Dresden, 2014.

Geluk, M. C., Duin, E., Dusar, M., Rijkers, R., van den Berg, M. W., and van Rooijen, P.: Stratigraphy and tectonics of the Roer Valley Graben, Geologie en Mijnbouw, 73, 129–141, 1994.

GEOFON Data Centre: GEOFON Seismic Network, https://doi.org/10.14470/TR560404.

GeoMol Team: GeoMol – Assessing subsurface potentials of the Alpine Foreland Basins for sustainable planning and use of natural resources – Project Report, LfU, 192 pp., 2015.

GeORG-Projektteam: Geopotentiale des tieferen Untergrundes im Oberrheingraben: Fachlich-Technischer Abschlussbericht des INTERREG-Projekts GeORG, Teil 4, Freiburg i. Br., 104 pp., 2013.

Geothermieatlas Bayern: Grundgebirge (Prä-Perm) (Verbreitung und Tiefenlage), Bayerisches Staatsministerium für Wirtschaft, Landesentwicklung und Energie, 2004.

German Research Centre For Geosciences: Seismicity in Germany in global context, https://www.gfz-potsdam.de/en/section/seismic-hazard-and-risk-dynamics/topics/where-in-germany-does-the-earth-quake/seismicity-in-germany-in-global-context, last access: 11 May 2022.

Goelke, M. and Coblentz, D.: Origins of the European regional stress field, Tectonophysics, 266, 11–24, https://doi.org/10.1016/S0040-1951(96)00180-1, 1996.

Grad, M., Brückl, E., Majdański, M., Behm, M., and Guterch, A.: Crustal structure of the Eastern Alps and their foreland: seismic model beneath the CEL10/Alp04 profile and tectonic implications, Geophys. J. Int., 177, 279–295, https://doi.org/10.1111/j.1365-246X.2008.04074.x, 2009a.

Grad, M., Tiira, T., and ESC Working Group: The Moho depth map of the European Plate, Geophys. J. Int., 176, 279–292, https://doi.org/10.1111/j.1365-246X.2008.03919.x, 2009b.

Grollimund, B. and Zoback, M. D.: Impact of glacially induced stress changes on fault-seal integrity offshore Norway: Discussion, Bulletin, 89, 271–274, https://doi.org/10.1306/03300403128, 2005.

Grote, R.: Die rezente horizontale Hauptspannungsrichtung im Rotliegenden und Oberkarbon in Norddeutschland, Erdöl-Erdgas-Kohle, 114, 478–483, 1998.

Grünthal, G. and Wahlström, R.: The European-Mediterranean Earthquake Catalogue (EMEC) for the last millennium, J Seismol, 16, 535–570, https://doi.org/10.1007/s10950-012-9302-y, 2012.

Grünthal, G. and Minkley, W.: Bergbauinduzierte seismische Aktivität als Quelle seismischer Belastungen - Zur Notwendigkeit der Ergänzung der Karte der Erdbebenzonen der DIN 4149: 2005-04, Bautechnik, 82, 508–513, https://doi.org/10.1002/bate.200590167, 2005.

Grünthal, G. and Stromeyer, D.: The recent crustal stress field in Central Europe sensu lato and its quantitative modelling, Geologie en Mijnbouw, 73, 173–180, 1994.

Grünthal, G. and Stromeyer, D.: The recent crustal stress field in central Europe: trajectories and finite element modeling, Journal of geophysical research, 97, 1992.

Grünthal, G. and Stromeyer, D.: Stress pattern in Central Europe and adjacent areas, Gerlands Beiträge zur Geophysik, 95, 443–452, 1986.

Haimson, B. C. and Cornet, F. H.: ISRM Suggested Methods for rock stress estimation—Part 3: hydraulic fracturing (HF) and/or hydraulic testing of pre-existing fractures (HTPF), Int. J. Rock Mech. Min. Sci., 40, 1011–1020, https://doi.org/10.1016/j.ijrmms.2003.08.002, 2003.

Haines, S., Marone, C., and Saffer, D.: Frictional properties of low-angle normal fault gouges and implications for low-angle normal fault slip, Earth and Planetary Science Letters, 408, 57–65, https://doi.org/10.1016/j.epsl.2014.09.034, 2014.

Häring, M. O., Schanz, U., Ladner, F., and Dyer, B. C.: Characterisation of the Basel 1 enhanced geothermal system, Geothermics, 37, 469–495, https://doi.org/10.1016/j.geothermics.2008.06.002, 2008.

Healy, D. and Hicks, S. P.: De-risking the energy transition by quantifying the uncertainties in fault stability, Solid Earth, 13, 15–39, https://doi.org/10.5194/se-13-15-2022, 2022.

Heidbach, O., Reinecker, J., Tingay, M., Müller, B., Sperner, B., Fuchs, K., and Wenzel, F.: Plate boundary forces are not enough: Second- and third-order stress patterns highlighted in the World Stress Map database, Tectonics, 26, TC6014, https://doi.org/10.1029/2007TC002133, 2007.

Heidbach, O., Ziegler, M., and Stromeyer, D.: Manual of the Tecplot 360 Add-on GeoStress v2.0, World Stress Map Technical Report, 20-02, GFZ German Research Centre for Geosciences, 62 pp., 2020.

Heidbach, O., Rajabi, M., Cui, X., Fuchs, K., Müller, B., Reinecker, J., Reiter, K., Tingay, M., Wenzel, F., Xie, F., Ziegler, M. O., Zoback, M.-L., and Zoback, M.: The World Stress Map database release 2016: Crustal stress pattern across scales, Tectonophysics, 744, 484–498, https://doi.org/10.1016/j.tecto.2018.07.007, 2018.

Heidbach, O., Rajabi, M., Reiter, K., Ziegler, M., and WSM Team: World Stress Map Database Release 2016 v1.1, GFZ Data Services [data set], https://doi.org/10.5880/WSM.2016.001, 2016a.

Heidbach, O., Barth, A., Müller, B., Reinecker, J., Stephansson, O., Tingay, M., and Zang, A.: WSM quality ranking scheme, database description and analysis guidelines for stress indicator, GFZ German Research Centre For Geosciences, World Stress Map Technical Report, 16-01, 2016b.

Heidbach, O., Hergert, T., Reiter, K., and Giger, S.: NAB 13-88: Local Stress field sensitivity analysis - Case study Nördlich Langen, Wettingen, 50 pp., 2014.

Heidbach, O., Tingay, M., Barth, A., Reinecker, J., Kurfeß, D., and Müller, B.: Global crustal stress pattern based on the World Stress Map database release 2008, Tectonophysics, 482, 3–15, https://doi.org/10.1016/j.tecto.2009.07.023, 2010.

Heinemann, B.: Results of scientific investigations at the HDR test site Soultz-sous-Forêts: Alsace (1987-1992), SOCOMINE report, 126 pp., 1994.

Heinrichs, T., Giese, P., Bankwitz, P., and Bankwitz, E.: Dekorp 3/MVE-90(West) - preliminary geological interpretation of a deep near-vertical reflection profile between the Rhenish and the Bohemian Massifs, Germany, Z. Geol. Wissenschaft., 22, 771–801, 1994.

Henk, A.: Perspectives of Geomechanical Reservoir Models - Why Stress is Important, Oil Gas: European Magazine, 125, OG20-OG24, 2009.

Henk, A.: Subsidenz und Tektonik des Saar-Nahe-Beckens (SW-Deutschland), Geol Rundsch, 82, 3–19, https://doi.org/10.1007/BF00563266, 1993.

Hergert, T., Heidbach, O., Reiter, K., Giger, S. B., and Marschall, P.: Stress field sensitivity analysis in a sedimentary sequence of the Alpine foreland, Northern Switzerland, Solid Earth, 6, 533–552, https://doi.org/10.5194/se-6-533-2015, 2015.

Hergert, T.: Numerical modelling of the absolute stress state in the Marmara region - a contribution to seismic hazard assessment, Dissertation, Universität Karlsruhe, 152 pp., 2009.

Hergert, T. and Heidbach, O.: Geomechanical model of the Marmara Sea region-II. 3-D contemporary background stress field, Geophys. J. Int., 185, 1090–1102, https://doi.org/10.1111/j.1365-246X.2011.04992.x, 2011.

Hettema, M.: Analysis of mechanics of fault reactivation in depleting reservoirs, Int. J. Rock Mech. Min, 129, 104290, https://doi.org/10.1016/j.ijrmms.2020.104290, 2020.

Hickman, S. and Zoback, M. D.: Stress orientations and magnitudes in the SAFOD pilot hole, Geophysical Research Letters, 31, 9373, https://doi.org/10.1029/2004GL020043, 2004.

Hillis, R. R. and Nelson, E. J.: In situ stresses in the North Sea and their applications: Petroleum geomechanics from exploration to development, in: Petroleum Geology: North-West Europe and Global Perspectives—Proceedings of the 6th Petroleum Geology Conference, 551–564, 2005.

Hirschmann, G.: KTB - The structure of a Variscan terrane boundary: seismic investigation - drilling - models, Tectonophysics, 264, 327–339, https://doi.org/10.1016/S0040-1951(96)00171-0, 1996.

Homuth, B., Rümpker, G., Deckert, H., and Kracht, M.: Seismicity of the northern Upper Rhine Graben — Constraints on the present-day stress field from focal mechanisms, Tectonophysics, 632, 8–20, https://doi.org/10.1016/j.tecto.2014.05.037, 2014.

Hübner, W., Wellbrink, M., Röckel, T., Steuer, S., Krug, S., and Tischner, T.: Stress rotation in the suprasalt beneath Hanover (North German Basin) derived from image logs of the deep well Groß Buchholz Gt1, Z. Dtsch. Ges. Geowiss., 166, 361–373, https://doi.org/10.1127/zdgg/2015/0038, 2015.

Hudson, J. A. and Harrison, J. P.: Rock mass classification, in: Engineering Rock Mechanics: An Introduction to the Principles, edited by: Hudson, J. A. and Harrison, J. P., Elsevier, 193–206, https://doi.org/10.1016/B978-008043864-1/50009-4, 1997a.

Hudson, J. A. and Harrison, J. P.: Rock masses, in: Engineering Rock Mechanics: An Introduction to the Principles, edited by: Hudson, J. A. and Harrison, J. P., Elsevier, 141–148, https://doi.org/10.1016/B978-008043864-1/50009-4, 1997b.

Hurtig, E., Cermak, V., Haenel, R., and Zui, V.: Geothermal atlas of Europe, Haack, Gotha (Germany), 156 pp., 1992.

IAEA: Geological Disposal Facilities for Radioactive Waste, Specific Safety Guides, INTERNATIONAL ATOMIC ENERGY AGENCY, Vienna, 2011.

Ingebritsen, S. E. and Manning, C. E.: Geological implications of a permeability-depth curve for the continental crust, Geol, 27, 1107, https://doi.org/10.1130/0091-7613(1999)027%3C1107:GIOAPD%3E2.3.CO;2, 1999.

Jaeger, J. C., Cook, N. G. W., and Zimmerman, R. W.: Fundamentals of rock mechanics, 4. ed., Blackwell Publ, Malden, MA, 475 pp., 2011.

Janik, T., Grad, M., Guterch, A., Vozár, J., Bielik, M., Vozárova, A., Hegedűs, E., Kovács, C. A., Kovács, I., and Keller, G. R.: Crustal structure of the Western Carpathians and Pannonian Basin: Seismic models from CELEBRATION 2000 data and geological implications, J. Geodyn., 52, 97–113, https://doi.org/10.1016/j.jog.2010.12.002, 2011.

Jarosiński, M., Beekman, F., Bada, G., and Cloetingh, S.: Redistribution of recent collision push and ridge push in Central Europe: insights from FEM modelling, Geophys. J. Int., 167, 860–880, https://doi.org/10.1111/j.1365-246X.2006.02979.x, 2006.

Kaiser, A., Reicherter, K., Huebscher, C., Gajewski, D., Marotta, A. M., and Bayer, U.: Variation of the present-day stress field within the North German Basin; insights from thin shell FE modeling based on residual GPS velocities, Tectonophysics, 397, 55–72, https://doi.org/10.1016/j.tecto.2004.10.009, 2005.

King, R., Backé, G., Tingay, M., Hillis, R., and Mildren, S.: Stress deflections around salt diapirs in the Gulf of Mexico, in: Faulting, Fracturing and Igneous Intrusion in the Earth's Crust, edited by: Healy, D., Sibson, R. H., Shipton, Z., and Butler, R., 141–153, https://doi.org/10.1144/SP367.10, 2012.

Kirsch, M., Kroner, U., Hallas, P., and Stephan, T.: 3D Model of the Erzgebirge - Crustal-Scale 3D Modelling of the Allochthonous Domain of the Saxo-Thuringian Zone, https://tu-freiberg.de/geo/tectono/3d-erzgebirge, 2017.

Klee, G. and Rummel, F.: Hydrofrac stress data for the European HDR research project test site Soultz-Sous-Forets, Int. J. Rock Mech. Min, 30, 973–976, https://doi.org/10.1016/0148-9062(93)90054-H, 1993.

Kley, J., Franzke, H.-J., Jähne, F., Krawczyk, C., Lohr, T., Reicherter, K., Scheck-Wenderoth, M., Sippel, J., Tanner, D., and van Gent, H.: Strain and Stress, in: Dynamics of complex intracontinental basins: The Central European basin system, edited by: Littke, R., Bayer, U.,

Gajewski, D., and Nelskamp, S., Springer, Berlin, Heidelberg, 97–124, https://doi.org/10.1007/978-3-540-85085-4_3, 2008.

Kley, J. and Voigt, T.: Late Cretaceous intraplate thrusting in central Europe: Effect of Africa-Iberia-Europe convergence, not Alpine collision, Geology, 36, 839–842, https://doi.org/10.1130/G24930A.1, 2008.

Kohlbeck, F., Rock, K., and Scheidegger, A.: In Situ measurements in Austria, Rock Mechanics, Supplement 9:21-29, 1980.

Konstantinovskaya, E., Malo, M., and Castillo, D. A.: Present-day stress analysis of the St. Lawrence Lowlands sedimentary basin (Canada) and implications for caprock integrity during CO2 injection operations, Tectonophysics, 518-521, 119–137, https://doi.org/10.1016/j.tecto.2011.11.022, 2012.

Korsch, R. J. and Schäfer, A.: The Permo-Carboniferous Saar-Nahe Basin, south-west Germany and north-east France: basin formation and deformation in a strike-slip regime, Geol. Rundschau, 84, 293–318, https://doi.org/10.1007/BF00260442, 1995.

Kossmat, F.: Gliederung des variszischen Gebirgsbaus, Abh. Sächs. Geol. Landesamtes, 1, 1–39, 1927.

Krawczyk, C. M., Rabbel, W., Willert, S., Hese, F., Götze, H.-J., Gajewski, D., and SPP-Geophysics Group: Crustal structures and properties in the Central European Basin system from geophysical evidence, in: Dynamics of complex intracontinental basins: The Central European basin system, edited by: Littke, R., Bayer, U., Gajewski, D., and Nelskamp, S., Springer, Berlin, Heidelberg, 67–95, https://doi.org/10.1007/978-3-540-85085-4_3, 2008.

Kristiansen, T. G.: Drilling Wellbore Stability in the Compacting and Subsiding Valhall Field, IADC/SPE Drilling Conference, 2-4 March, Dallas, Texas, https://doi.org/10.2118/87221-MS, 2004.

Kroner, U., Romer, R. L., and Linnemann, U.: The Saxo-Thuringian Zone of the Variscan Orogen as part of Pangea, in: Pre-Mesozoic geology of Saxo-Thuringia: From the Cadomian active margin to the Variscan orogen, edited by: Linnemann, U. and Romer, R. L., Schweizerbart, Stuttgart, 3–16, 2010.

Kruszewski, M., Klee, G., Niederhuber, T., and Heidbach, O.: In situ stress database of the greater Ruhr region (Germany) derived from hydrofracturing tests and borehole logs [preprint], https://doi.org/10.5194/essd-2022-196, 2022.

Lee, J. B. and Chang, C.: Slip tendency of Quaternary faults in southeast Korea under current state of stress, Geosci J, 13, 353–361, https://doi.org/10.1007/s12303-009-0033-1, 2009.

Levi, N., Habermueller, M., Exner, U., Piani, E., Wiesmayr, G., and Decker, K.: The stress field in the frontal part of the Eastern Alps (Austria) from borehole image log data, Tectonophysics, 769, 228175, https://doi.org/10.1016/j.tecto.2019.228175, 2019.

Lindner, E. N. and Halpern, J. A.: In-situ stress in North America: A compilation, International Journal of Rock Mechanics and Mining Sciences & Geomechanics Abstracts, 15, 183–203, https://doi.org/10.1016/0148-9062(78)91225-1, 1978.

Lindner, H., Scheibe, K., Seidel, K., and Hoffmann, N.: Berechnung von Relief, Tiefenlage und Magnetisierung des magnetisch wirksamen Kristallins für das Norddeutsche Becken, Z. Angew. Geol., 50, 65–74, 2004.

Linnemann, U. and Romer, R. L. (Eds.): Pre-Mesozoic geology of Saxo-Thuringia: From the Cadomian active margin to the Variscan orogen, Schweizerbart, Stuttgart, 485 pp., 2010.

Linnemann, U., D'Lemos, R., Drost, K., Jeffries, T., Gerdes, A., Romer, R. L., Samson, S. D., and Strachan, R. A.: Cadomian tectonics, in: The Geology of Central Europe Volume 1: Precambrian and Palaeozoic; Volume 2: Mesozoic and Cenozoic, edited by: McCann, T., The Geological Society of London, 103–154, https://doi.org/10.1144/CEV1P.3, 2008.

Litt, T., Schmincke, H.-U., Frechen, M., and Schluchter, C.: Quaternary, in: The Geology of Central Europe Volume 1: Precambrian and Palaeozoic; Volume 2: Mesozoic and Cenozoic, edited by: McCann, T., The Geological Society of London, 1287–1340, https://doi.org/10.1144/CEV2P.8, 2008.

Littke, R., Bayer, U., Gajewski, D., and Nelskamp, S. (Eds.): Dynamics of complex intracontinental basins: The Central European Basin System, Springer, Berlin Heidelberg, 2008.

Ljunggren, C., Chang, Y., Janson, T., and Christiansson, R.: An overview of rock stress measurement methods, Int. J. Rock Mech. Min, 40, 975–989, https://doi.org/10.1016/j.ijrmms.2003.07.003, 2003.

Lund, B. and Zoback, M.: Orientation and magnitude of in situ stress to 6.5 km depth in the Baltic Shield, Int. J. Rock Mech. Min. Sci., 36, 169–190, https://doi.org/10.1016/S0148-9062(98)00183-1, 1999.

Mader, S., Ritter, J. R. R., and Reicherter, K.: Seismicity and seismotectonics of the Albstadt Shear Zone in the northern Alpine foreland, Solid Earth, 12, 1389–1409, https://doi.org/10.5194/se-12-1389-2021, 2021.

Mardia, K. V.: Statistics of Directional Data: Probability and Mathematical Statistics, Academic Press, London, 380 pp., 1972.

Marotta, A. M., Bayer, U., Thybo, H., and Scheck, M.: Origin of the regional stress in the North German Basin - results from numerical modelling, Tectonophysics, 360, 245–264, https://doi.org/10.1016/S0040-1951(02)00358-X, 2002.

Marotta, A. M., Bayer, U., Scheck, M., and Thybo, H.: The stress field below the NE German Basin; effects induced by the Alpine collision, Geophysical Journal International, F8-F12, 2001.

Maystrenko, Y., Bayer, U., and Scheck-Wenderoth, M.: The Glueckstadt Graben, a sedimentary record between the North and Baltic Sea in north Central Europe, Tectonophysics, 397, 113–126, https://doi.org/10.1016/j.tecto.2004.10.004, 2005.

Maystrenko, Y. P. and Scheck-Wenderoth, M.: 3D lithosphere-scale density model of the Central European Basin System and adjacent areas, Tectonophysics, 601, 53–77, https://doi.org/10.1016/j.tecto.2013.04.023, 2013.

Mazur, S., Mikolajczak, M., Krzywiec, P., Malinowski, M., Buffenmyer, V., and Lewandowski, M.: Is the Teisseyre-Tornquist Zone an ancient plate boundary of Baltica?, Tectonics, 34, 2465–2477, https://doi.org/10.1002/2015TC003934, 2015.

McCann, T. (Ed.): The Geology of Central Europe Volume 1: Precambrian and Palaeozoic; Volume 2: Mesozoic and Cenozoic, The Geological Society of London, 1449 pp., 2008.

McCann, T., Kiersnowski, H., Krainer, K., Vozarova, A., Peryt, T. M., Oplustil, S., Stollhofen, H., Schneider, J., Wetzel, A., Boulvain, F., Dusar, M., Torok, A., Haas, J., Tait, J., and Korner, F.: Permian, in: The Geology of Central Europe Volume 1: Precambrian and Palaeozoic; Volume 2: Mesozoic and Cenozoic, edited by: McCann, T., The Geological Society of London, 531–597, https://doi.org/10.1144/CEV1P.10, 2008.

McFarland, J. M., Morris, A. P., and Ferrill, D. A.: Stress inversion using slip tendency, Computers & Geosciences, 41, 40–46, https://doi.org/10.1016/j.cageo.2011.08.004, 2012.

Megies, T. and Wassermann, J.: Microseismicity observed at a non-pressure-stimulated geothermal power plant, Geothermics, 52, 36–49, https://doi.org/10.1016/j.geothermics.2014.01.002, 2014.

Meissner, R. and Bortfeld, R. K.: DEKORP-Atlas: Results of Deutsches Kontinentales Reflexionsseismisches Programm, Springer Berlin Heidelberg, Berlin, Heidelberg, 21 pp., 1990.

Meixner, J., Schill, E., Gaucher, E., and Kohl, T.: Inferring the in situ stress regime in deep sediments: an example from the Bruchsal geothermal site, Geotherm Energy, 2, https://doi.org/10.1186/s40517-014-0007-z, 2014.

Merkel, M. and Öchsner, A.: Eindimensionale Finite Elemente, Springer Berlin Heidelberg, Berlin, Heidelberg, 428 pp., 2014.

Meschede, M. and Warr, L. N.: The Geology of Germany, Springer, 304 pp., 2019.

Moeck, I., Kwiatek, G., and Zimmermann, G.: Slip tendency analysis, fault reactivation potential and induced seismicity in a deep geothermal reservoir, Journal of Structural Geology, 31, 1174–1182, https://doi.org/10.1016/j.jsg.2009.06.012, 2009a.

Moeck, I., Schandelmeier, H., and Holl, H.-G.: The stress regime in a Rotliegend reservoir of the Northeast German Basin, Geol Rundsch, 98, 1643–1654, https://doi.org/10.1007/s00531-008-0316-1, 2009b.

Morawietz, S. and Reiter, K.: Stress Magnitude Database Germany v1.0, GFZ Data Services [data set], https://doi.org/10.5880/wsm.2020.004, 2020.

Morawietz, S., Heidbach, O., Reiter, K., Ziegler, M., Rajabi, M., Zimmermann, G., Müller, B., and Tingay, M.: An open-access stress magnitude database for Germany and adjacent regions, Geothermal Energy, 8, https://doi.org/10.1186/s40517-020-00178-5, 2020.

Morin, R. H. and Wilkens, R. H.: Structure and stress state of Hawaiian island basalts penetrated by the Hawaii Scientific Drilling Project deep core hole, J. Geophys. Res., 110, https://doi.org/10.1029/2004JB003410, 2005.

Morris, A., Ferrill, D. A., and Henderson, D. B.: Slip-tendency analysis and fault reactivation, Geology, 24, 275, https://doi.org/10.1130/0091-7613(1996)024<0275:STAAFR>2.3.CO;2, 1996.

Morris, A. P., Hennings, P. H., Horne, E. A., and Smye, K. M.: Stability of basement-rooted faults in the Delaware Basin of Texas and New Mexico, USA, Journal of Structural Geology, 149, 104360, https://doi.org/10.1016/j.jsg.2021.104360, 2021.

Müller, B., Scheffzük, C., Schilling, F., Westerhaus, M., Zippelt, K., Wampach, M., Röckel, T., Lempp, C., and Schöner, A.: Reservoir-management and seismicity: Strategies to reduce induced seismicity = Reservoir-Managemant und Seismizität Strategien zur Verringerung der induzierten Seismizität, Als Manuskript gedruckt, DGMK-research report, 776, DGMK e.V, Hamburg, 88 Blätter, 2020.

Müller, B., Zoback, M. L., Fuchs, K., Mastin, L., Gregersen, S., Pavoni, N., Stephansson, O., and Ljunggren, C.: Regional patterns of tectonic stress in Europe, Journal of geophysical research, 97, 11783, https://doi.org/10.1029/91JB01096, 1992.

Müller, M., Nieberding, F., and Wanninger, A.: Tectonic style and pressure distribution at the northern margin of the Alps between Lake Constance and the River Inn, Geol Rundsch, 77, 787–796, https://doi.org/10.1007/BF01830185, 1988.

nagra: Vorschlag geologischer Standortgebiete für das SMA- und das HAA-Lager. Begründung der Abfallzuteilung, der Barrieresysteme und der Anforderungen an die Geologie. Bericht zur Sicherheit und technischen Machbarkeit: NTB 08-05, nagra, Wettingen, 2008.

nagra: Sondierbohrung Benken: Technical Report NTB 00-01, nagra, 288 pp., 2001.

Narkiewicz, M., Maksym, A., Malinowski, M., Grad, M., Guterch, A., Petecki, Z., Probulski, J., Janik, T., Majdański, M., Środa, P., Czuba, W., Gaczyński, E., and Jankowski, L.: Transcurrent nature of the Teisseyre–Tornquist Zone in Central Europe: results of the POLCRUST-01 deep reflection seismic profile, Int J Earth Sci (Geol Rundsch), 104, 775–796, https://doi.org/10.1007/s00531-014-1116-4, 2015.

Neves, M. C., Paiva, L. T., and Luis, J.: Software for slip-tendency analysis in 3D: A plug-in for Coulomb, Computers & Geosciences, 35, 2345–2352, https://doi.org/10.1016/j.cageo.2009.03.008, 2009.

Numelin, T., Marone, C., and Kirby, E.: Frictional properties of natural fault gouge from a low-angle normal fault, Panamint Valley, California, Tectonics, 26, n/a-n/a, https://doi.org/10.1029/2005TC001916, 2007.

Oncken, O., Plesch, A., Weber, J., Ricken, W., and Schrader, S.: Passive margin detachment during arc-continent collision (Central European Variscides), in: Orogenic Processes: Quantification and

Modelling in the Variscan Belt, edited by: Franke, W., Haak, V., Oncken, O., and Tanner, D., London, 199–216, https://doi.org/10.1144/GSL.SP.2000.179.01.13, 2000.

Oncken, O.: Transformation of a magmatic arc and an orogenic root during oblique collision and it's consequences for the evolution of the European Variscides (Mid-German Crystalline Rise), Geol. Rundschau, 86, 2–20, https://doi.org/10.1007/s005310050118, 1997.

Peterek, A., Rauche, H., Schröder, B., Franzke, H.-J., Bankwitz, P., and Bankwitz, E.: The late-and post-Variscan tectonic evolution of the Western Border fault zone of the Bohemian massif (WBZ), Geol. Rundschau, 86, 191–202, https://doi.org/10.1007/s005310050131, 1997.

Peters, G.: Active tectonics in the Upper Rhine Graben: Integration of paleoseismology, geomorphology and geomechanical modeling, Zugl.: Amsterdam, Vrije Univ., Diss, 2007, Logos-Verl., Berlin, 270 pp., 2007.

Pfiffner, O. A.: Thick-skinned and thin-skinned tectonics: A global perspective, Geosciences, 7, https://doi.org/10.3390/geosciences7030071, 2017.

Pharaoh, T.: The Anglo-Brabant Massif: Persistent but enigmatic palaeo-relief at the heart of western Europe, P. Geol. Assoc., 129, 278–328, https://doi.org/10.1016/j.pgeola.2018.02.009, 2018.

Pienkowski, G., Schudack, M. E., Bosak, P., Enay, R., Feldman-Olszewska, A., Golonka, J., Gutowski, J., Herngreen, G., Jordan, P., Krobicki, M., Lathuiliere, B., Leinfelder, R. R., Michalik, J., Monnig, E., Noe-Nygaard, N., Palfy, J., Pint, A., Rasser, M. W., Reisdorf, A. G., Schmid, D. U., Schweigert, G., Surlyk, F., Wetzel, A., and Wong, T. E.: Jurassic, in: The Geology of Central Europe Volume 1: Precambrian and Palaeozoic; Volume 2: Mesozoic and Cenozoic, edited by: McCann, T., The Geological Society of London, 823–922, https://doi.org/10.1144/CEV2P.2, 2008.

Pierdominici, S. and Heidbach, O.: Stress field of Italy — Mean stress orientation at different depths and wave-length of the stress pattern, Tectonophysics, 532-535, 301–311, https://doi.org/10.1016/j.tecto.2012.02.018, 2012.

Przybycin, A. M., Scheck-Wenderoth, M., and Schneider, M.: Assessment of the isostatic state and the load distribution of the European Molasse Basin by means of lithospheric scale 3D structural and 3D gravity modelling, Int. J. Earth Sci., 104, 1405–1424, https://doi.org/10.1007/s00531-014-1132-4, 2015.

Quinteros, J., Strollo, A., Evans, P. L., Hanka, W., Heinloo, A., Hemmleb, S., Hillmann, L., Jaeckel, K.-H., Kind, R., Saul, J., Zieke, T., and Tilmann, F.: The GEOFON Program in 2020, Seismological Research Letters, 92, 1610–1622, https://doi.org/10.1785/0220200415, 2021.

Rajabi, M., Tingay, M., Heidbach, O., Hillis, R., and Reynolds, S.: The present-day stress field of Australia, Earth-Science Reviews, 168, 165–189, https://doi.org/10.1016/j.earscirev.2017.04.003, 2017.

Rajabi, M., Tingay, M., and Heidbach, O.: The present-day state of tectonic stress in the Darling Basin, Australia: Implications for exploration and production, Mar. Petrol. Geol., 77, 776–790, https://doi.org/10.1016/j.marpetgeo.2016.07.021, 2016.

Rasser, M. W., Harzhauser, M., Anistratenko, O. Y., Anistratenko, V. V., Bassi, D., Belak, M., Berger, J.-P., Bianchini, G., Cicic, S., Cosovic, V., Dolakova, N., Drobne, K., Filipescu, S., Gürs, K., Hladilova, S., Hrvatovic, H., Jelen, B., Kasinski, J. R., Kovac, M., Kralj, P., Marjanac, T., Marton, E., Mietto, P., Moro, A., Nagymarosy, A., Nebelsick, J. H., Nehyba, S., Ogorelec, B., Oszcypko, N., Pavelic, D., Pavlovec, R., Pavsic, J., Petrova, P., Piwocki, M., Poljak, M., Pugliese, N., Redzepovic, R., Rifelj, H., Roetzel, R., Skaberne, D., Sliva, L., Standke, G., Tunis, G., Vass, D., Wagreich, M., and Wesselingh, F.: Palaeogene and Neogene, in: The Geology of Central Europe Volume 1: Precambrian and Palaeozoic; Volume 2: Mesozoic and Cenozoic, edited by: McCann, T., The Geological Society of London, 1031–1139, https://doi.org/10.1144/CEV2P.5, 2008.

Reicherter, K., Froitzheim, N., Jarosinski, M., Badura, J., Franzke, H.-J., Hansen, M., Hubscher, C., Müller, R., Poprawa, P., Reinecker, J., Stackebrandt, W., Voigt, T., Eynatten, H. von, and Zuchiewicz, W.: Alpine tectonics north of the Alps, in: The Geology of Central Europe Volume 1:

Precambrian and Palaeozoic; Volume 2: Mesozoic and Cenozoic, edited by: McCann, T., The Geological Society of London, 1233–1285, https://doi.org/10.1144/CEV2P.7, 2008.

Reinecker, J. and Schneider, G.: Zur Neotektonik der Zollernalb: Der Hohenzollerngraben und die Albstadt-Erdbeben, Jahresberichte und Mitteilungen des Oberrheinischen Geologischen Vereins, 84, 391–417, https://doi.org/10.1127/jmogv/84/2002/391, 2002.

Reinecker, J., Tingay, M., and Müller, B.: Guidelines for borehole breakout analysis from four-arm caliper logs, in: WSM quality ranking scheme, database description and analysis guidelines for stress indicator, GFZ German Research Centre for Geosciences, 27–32, https://doi.org/10.2312/wsm.2016.001, 2016.

Reinecker, J., Tingay, M., Müller, B., and Heidbach, O.: Present-day stress orientation in the Molasse Basin, Tectonophysics, 482, 129–138, https://doi.org/10.1016/j.tecto.2009.07.021, 2010.

Reinhold, K.: Tiefenlage der "Kristallin-Oberfläche" in Deutschland - Abschlussbericht, Bundesanstalt für Geowissenschaften und Rohstoffe, Hannover, 89 pp., 2005.

Reiter, K. and Heidbach, O.: 3-D geomechanical–numerical model of the contemporary crustal stress state in the Alberta Basin (Canada), Solid Earth, 5, 1123–1149, https://doi.org/10.5194/se-5-1123-2014, 2014.

Reiter, K., Ahlers, S., Röckel, L., Morawietz, S., Henk, A., Hergert, T., Heidbach, O., Müller, B., and Schilling, F.: SpannEnD — Abschlussbericht: Abschlussbericht des Projektes SpannEnD — Geomechanisch-numerische Modellierungen zur Charakterisierung des tektonischen Spannungszustandes für die Entsorgung radioaktiver Abfälle in Deutschland, 157 pp., 2022.

Reiter, K., Heidbach, O., Reinecker, J., Müller, B., and Röckel, T.: Spannungskarte Deutschland 2015, Erdöl-Erdgas-Kohle, 131, 437–442, 2015.

Reiter, K.: Stress rotation – impact and interaction of rock stiffness and faults, Solid Earth, 12, 1287–1307, https://doi.org/10.5194/se-12-1287-2021, 2021.

Reiter, K., Heidbach, O., Müller, B., Reinecker, J., and Röckel, T.: Stress Map Germany 2016, https://doi.org/10.5880/WSM.Germany2016_en, 2016.

Reyer, D.: Outcrop analogue studies of rocks from the Northwest German Basin for geothermal exploration and exploitation: Fault zone structure, heterogeneous rock properties, and application to reservoir conditions, PhD, 108 pp., 2013.

Ribbert, K.-H. and Wrede, V.: Stratigrafische und tektonische Ergebnisse der Grundgebirgsbohrungen im Umfeld des Braunkohle-Tagebaus Hambach, in: Der tiefere Untergrund der Niederrheinischen Bucht: Ergebnisse eines Tiefbohrprogramms im Rheinischen Braunkohlenrevier, edited by: Geologischer Dienst Krefeld, Obermann GmbH & Co KG, Krefeld, 33–66, 2005.

Richardson, R. M.: Ridge forces, absolute plate motions, and the intraplate stress field, Journal of geophysical research, 97, 11739–11748, https://doi.org/10.1029/91JB00475, 1992.

Röckel, L., Müller, B. I. R., Ahlers, S., Reiter, K., Hergert, T., Henk, A., Heidbach, O., and Schilling, F.: 3D fault sets of Germany and adjacent areas, https://doi.org/10.5445/IR/1000143465, 2022a.

Röckel, L., Ahlers, S., Müller, B., Reiter, K., Heidbach, O., Henk, A., Hergert, T., and Schilling, F.: The analysis of slip tendency of major tectonic faults in Germany, Solid Earth, 13, 1087–1105, https://doi.org/10.5194/se-13-1087-2022, 2022b.

Röckel, T. and Lempp, C.: Der Spannungszustand im Norddeutschen Becken, Erdöl-Erdgas-Kohle, 119, 73–80, 2003.

Roth, F. and Fleckenstein, P.: Stress orientations found in NE Germany differ from the West European trend, Terra Nova, 13, 289–296, https://doi.org/10.1046/j.1365-3121.2001.00357.x, 2001.

Rupf, I. and Nitsch, E.: Das Geologische Landesmodell von Baden-Württemberg: Datengrundlagen, technische Umsetzung und erste geologische Ergebnisse, Freiburg i. Br., LGRB-Informationen, 21, 81 pp., 2008.

Scheck-Wenderoth, M. and Lamarche, J.: Crustal memory and basin evolution in the Central European Basin System - new insights from a 3D structural model, Tectonophysics, 397, 143–165, https://doi.org/10.1016/j.tecto.2004.10.007, 2005.

Scheck-Wenderoth, M., Krzywiec, P., Zuhlke, R., Maystrenko, Y., and Froitzheim, N.: Permian to Cretaceous tectonics, in: The Geology of Central Europe Volume 1: Precambrian and Palaeozoic; Volume 2: Mesozoic and Cenozoic, edited by: McCann, T., The Geological Society of London, 999–1030, https://doi.org/10.1144/CEV2P.4, 2008.

Schintgen, T.: The Geothermal Potential of Luxembourg - Geological and thermal exploration for deep geothermal reservoirs in Luxembourg and the surroundings, Ph. D. thesis, Universität Potsdam, Potsdam, 313 pp., 2015.

Schmid, S. M., Fügenschuh, B., Kissling, E., and Schuster, R.: Tectonic map and overall architecture of the Alpine orogen, Eclogae Geolog. Helv., 97, 93–117, https://doi.org/10.1007/s00015-004-1113-x, 2004.

Schmitt, D. R., Currie, C. A., and Zhang, L.: Crustal stress determination from boreholes and rock cores: Fundamental principles, Tectonophysics, 580, 1–26, https://doi.org/10.1016/j.tecto.2012.08.029, 2012.

Schulz, Suchi, Dittmann, Knopf, and Müller: Geothermie-Atlas zur Darstellung möglicher Nutzungskonkurrenzen zwischen CCS und Tiefer Geothermie, 2013.

Schutjens, P., Snippe, J. R., Mahani, H., Turner, J., Ita, J., and Mossop, A. P.: Production-induced stress change in and above a reservoir pierced by two salt domes: A geomechanical model and its applications, SPE J, 17, 80–97, https://doi.org/10.2118/131590-PA, 2012.

Segall, P. and Fitzgerald, S. D.: A note on induced stress changes in hydrocarbon and geothermal reservoirs, Tectonophysics, 289, 117–128, https://doi.org/10.1016/S0040-1951(97)00311-9, 1998.

Seithel, R., Steiner, U., Müller, B., Hecht, C., and Kohl, T.: Local stress anomaly in the Bavarian Molasse Basin, Geotherm Energy, 3, https://doi.org/10.1186/s40517-014-0023-z, 2015.

Shen, B.: Borehole Breakouts and In Situ Stresses, in: SHIRMS 2008: Proceedings of the First Southern Hemisphere International Rock Mechanics Symposium, edited by: Potvin, Y., Carter, J., Dyskin, A., and Jeffrey, R., Perth, 407–418, https://doi.org/10.36487/ACG_repo/808_145, 2008.

Sheorey, P. R.: A theory for In Situ stresses in isotropic and transverseley isotropic rock, Int. J. Rock Mech. Min, 31, 23–34, https://doi.org/10.1016/0148-9062(94)92312-4, 1994.

Sibson, R. H.: A note on fault reactivation, Journal of Structural Geology, 7, 751–754, https://doi.org/10.1016/0191-8141(85)90150-6, 1985.

Sibson, R. H.: Frictional constraints on thrust, wrench and normal faults, Nature, 249, 542–544, https://doi.org/10.1038/249542a0, 1974.

Simpson, R. W.: Quantifying Anderson's fault types, J. Geophys. Res., 102, 17909–17919, https://doi.org/10.1029/97JB01274, 1997.

Smart, K. J., Ofoegbu, G. I., Morris, A. P., McGinnis, R. N., and Ferrill, D. A.: Geomechanical modeling of hydraulic fracturing: Why mechanical stratigraphy, stress state, and pre-existing structure matter, AAPG Bulletin, 98, 2237–2261, https://doi.org/10.1306/07071413118, 2014.

Smith, W. H. F. and Sandwell, D. T.: Global Sea Floor Topography from Satellite Altimetry and Ship Depth Soundings, Science, 277, 1956–1962, https://doi.org/10.1126/science.277.5334.1956, 1997.

Sommaruga, A.: Décollement tectonics in the Jura forelandfold-and-thrust belt, Mar. Petrol. Geol., 16, 111–134, https://doi.org/10.1016/S0264-8172(98)00068-3, 1999.

Sperner, B., Lorenz, F., Bonjer, K., Hettel, S., Müller, B., and Wenzel, F.: Slab break-off - abrupt cut or gradual detachment? New insights from the Vrancea Region (SE Carpathians, Romania), Terra Nova, 13, 172–179, https://doi.org/10.1046/j.1365-3121.2001.00335.x, 2001.

StandAG: Gesetz zur Suche und Auswahl eines Standortes für ein Endlager für hochradioaktive Abfälle (Standortauswahlgesetz), 2017.

Sternai, P., Sue, C., Husson, L., Serpelloni, E., Becker, T. W., Willett, S. D., Faccenna, C., Di Giulio, A., Spada, G., Jolivet, L., Valla, P., Petit, C., Nocquet, J.-M., Walpersdorf, A., and Castelltort, S.: Present-day uplift of the European Alps: Evaluating mechanisms and models of their relative contributions, Earth-Science Reviews, 190, 589–604, https://doi.org/10.1016/j.earscirev.2019.01.005, 2019.

Stober, I. and Bucher, K.: Potentielle Umweltauswirkungen bei der Tiefen Geothermie, in: Geothermie, 3. Aufl. 2020, edited by: Stober, I. and Bucher, K., Springer Berlin Heidelberg, Berlin, Heidelberg, 243–274, https://doi.org/10.1007/978-3-662-60940-8_11, 2020.

Stöckhert, F., Brenne, S., Molenda, M., Bartmann, K., Hoenig, S., and Alber, M.: Geomechanische Charakterisierung von Vulkaniten und Sedimenten des Rotliegenden im Norddeutschen Becken für die Optimierung des Aufschlusses geothermischer Lagerstätten, 19. Tagung für Ingenieurgeologie mit Forum für junge Ingenieurgeologen, München 2013, 2013.

Stollhofen, H., Bachmann, G., Barnasch, J., Bayer, U., Beutler, G., Franz, M., Kästner, M., Legler, B., Mutterlose, J., and Radies, D.: Basin Fill - Upper Rotliegend to Early Cretaceous basin development, in: Dynamics of complex intracontinental basins: The Central European basin system, edited by: Littke, R., Bayer, U., Gajewski, D., and Nelskamp, S., Springer, Berlin, Heidelberg, 181–210, https://doi.org/10.1007/978-3-540-85085-4_4, 2008.

Stromeyer, D. and Heidbach, O.: Tecplot 360 Add-on GeoStress, GFZ Data Services, 2017.

Stüwe, K.: Geodynamics of the Lithosphere, Springer Berlin Heidelberg, Berlin, Heidelberg, 493 pp., 2007.

Suchi, E., Dittmann, J., Knopf, S., Müller, C., and Schulz, R.: Geothermal Atlas to visualise potential conflicts of interest between CO2 storage (CCS) and deep geothermal energy in Germany, Zeitschrift der Deutschen Gesellschaft für Geowissenschaften, 165, 439–453, https://doi.org/10.1127/1860-1804/2014/0070, 2014.

Tašárová, Z. A., Fullea, J., Bielik, M., and Środa, P.: Lithospheric structure of Central Europe: Puzzle pieces from Pannonian Basin to Trans-European Suture Zone resolved by geophysical-petrological modeling, Tectonics, 35, 722–753, https://doi.org/10.1002/2015TC003935, 2016.

Tingay, M.: State and origin of present-day stress fields in sedimentary basins, in: Australian Society of Exploration Geophysicists Extended Abstracts, Adelaide, Perth, Feb 22 2009, 2009.

Tingay, M., Reinecker, J., and Müller, B.: Guidelines for borehole breakout and drilling-induced fracture analysis from image logs, in: WSM quality ranking scheme, database description and analysis guidelines for stress indicator, GFZ German Research Centre for Geosciences, 33–41, https://doi.org/10.2312/wsm.2016.001, 2016.

Tingay, M., Bentham, P., Feyter, A. de, and Kellner, A.: Present-day stress-field rotations associated with evaporites in the offshore Nile Delta, GSA Bulletin, 123, 1171–1180, https://doi.org/10.1130/B30185.1, available at: http://dx.doi.org/10.1130/B30185.1, 2011.

Tingay, M., Morley, C., King, R., Hillis, R., Coblentz, D., and Hall, R.: Present-day stress field of Southeast Asia, Tectonophysics, 482, 92–104, https://doi.org/10.1016/j.tecto.2009.06.019, 2010.

Turcotte, D. L. and Schubert, G.: Geodynamics, 3. ed., Cambridge Univ. Press, Cambridge, 623 pp., 2014.

Urai, J. L., Schléder, Z., Spiers, C. K., and Kukla, P. A.: Flow and Transport Properties of Salt Rocks, in: Dynamics of complex intracontinental basins: The Central European basin system, edited by: Littke, R., Bayer, U., Gajewski, D., and Nelskamp, S., Springer, Berlin, Heidelberg, 277–290, 2008.

Vadacca, L., Rossi, D., Scotti, A., and Buttinelli, M.: Slip Tendency Analysis, Fault Reactivation Potential and Induced Seismicity in the Val d'Agri Oilfield (Italy), J. Geophys. Res., 126, https://doi.org/10.1029/2019JB019185, 2021.

Valasek, P. and Mueller, S.: A 3D tectonic model of the Central Alps based on an integrated interpretation of seismic refraction and NRP 20 reflection data, in: Deep structure of the Swiss alps: results of NRP 20, edited by: Pfiffner, O. A., Lehner, P., Heitzmann, P., Mueller, S., and Steck, A., Birkhauser Verlag, Basel, 302–325, 1997.

Valley, B. and Evans, K. F.: Stress State at Soultz-Sous-Forêts to 5 km Depth from wellbore failure and hydraulic observations, in: Thirty-Second Workshop on Geothermal Reservoir Engineering, 22-24 January 2007, 2007.

van Mount, S. and Suppe, J.: State of stress near the San Andreas fault: Implications for wrench tectonics, Geol, 15, 1143, https://doi.org/10.1130/0091-7613(1987)15%3C1143:SOSNTS%3E2.0.CO;2, 1987.

van Wees, J.-D., Stephenson, R., Ziegler, P., Bayer, U., McCann, T., Dadlez, R., Gaupp, R., Narkiewicz, M., Bitzer, F., and Scheck, M.: On the origin of the Southern Permian Basin, Central Europe, Marine and Petroleum Geology, 17, 43–59, https://doi.org/10.1016/S0264-8172(99)00052-5, 2000.

Voigt, S., Wagreich, M., Surlyk, F., Walaszczyk, I., Ulicny, D., Cech, S., Voigt, T., Wiese, F., Wilmsen, M., Niebuhr, B., Reich, M., Funk, H., Michalik, J., Jagt, J. W., Felder, P. J., and Schulf, A. S.: Cretaceous, in: The Geology of Central Europe Volume 1: Precambrian and Palaeozoic; Volume 2: Mesozoic and Cenozoic, edited by: McCann, T., The Geological Society of London, 923–997, https://doi.org/10.1144/CEV2P.3, 2008.

Wagner, G. A., Coyle, D. A., Duyster, J., Henjes-Kunst, F., Peterek, A., Schröder, B., Stöckhert, B., Wemmer, K., Zulauf, G., Ahrendt, H., Bischoff, R., Hejl, E., Jacobs, J., Menzel, D., Lal, N., van den haute, P., Vercoutere, C., and Welzel, B.: Post-Variscan thermal and tectonic evolution of the KTB site and its surroundings, J. Geophys. Res., 102, 18221–18232, https://doi.org/10.1029/96JB02565, 1997.

Wagner, M., Kissling, E., and Husen, S.: Combining controlled-source seismology and local earthquake tomography to derive a 3-D crustal model of the western Alpine region, Geophys J Int, 191, 789–802, https://doi.org/10.1111/j.1365-246X.2012.05655.x, 2012.

Walsh, F. R. and Zoback, M. D.: Probabilistic assessment of potential fault slip related to injection-induced earthquakes: Application to north-central Oklahoma, USA, Geol, 44, 991–994, https://doi.org/10.1130/G38275.1, 2016.

Walter, R.: Geologie von Mitteleuropa, 7., vollständig neu bearbeitete Auflage, Schweizerbart, Stuttgart, 511 pp., 2007.

Warners-Ruckstuhl, K. N., Govers, R., and Wortel, R.: Tethyan collision forces and the stress field of the Eurasian Plate, Geophys J Int, 195, 1–15, https://doi.org/10.1093/gji/ggt219, 2013.

Warsitzka, M., Kley, J., Jähne-Klingberg, F., and Kukowski, N.: Dynamics of prolonged salt movement in the Glückstadt Graben (NW Germany) driven by tectonic and sedimentary processes, International Journal of Earth Sciences, 106, 131–155, https://doi.org/10.1007/s00531-016-1306-3, 2017.

Wells, D. L. and Coppersmith, K. J.: New Empirical Relationships among Magnitude, Rupture Length, Rupture width, Rupture Area, and Surface Displacement, Bulletin of the Seismological Society of America, 974–1002, 1994.

Wenting, L., Völkner, E., Minkley, W., and Popp, T.: Zusammenstellung der Materialparameter für THM-Modellberechnungen - Ergebnisse aus dem Vorhaben KOSINA, BGR, Hannover, 88 pp., 2017.

Wenzel, F. and Brun, J. P.: A deep reflection seismic line across the Northern Rhine Graben, Earth Planet. Sc. Lett., 104, 140–150, https://doi.org/10.1016/0012-821X(91)90200-2, 1991.

Wessel, P. and Smith, W. H. F.: A global, self-consistent, hierarchical, high-resolution shoreline database, J. Geophys. Res., 101, 8741–8743, https://doi.org/10.1029/96JB00104, 1996.

White, A. J., Traugott, M. O., and Swarbrick, R. E.: The use of leak-off tests as means of predicting minimum in-situ stress, Petroleum Geoscience, 8, 189–193, https://doi.org/10.1144/petgeo.8.2.189, 2002.

Williams, J., Fellgett, M. W., Kingdon, A., and Williamson, J. P.: In-situ stress orientations in the UK Southern North Sea: Regional trends, deviations and detachment of the post-Zechstein stress field, Marine and Petroleum Geology, 67, 769–784, https://doi.org/10.1016/j.marpetgeo.2015.06.008, 2015.

Worum, G., van Wees, J.-D., Bada, G., van Balen, R. T., Cloetingh, S., and Pagnier, H.: Slip tendency analysis as a tool to constrain fault reactivation: A numerical approach applied to three-dimensional fault models in the Roer Valley rift system (southeast Netherlands), Journal of Geophysical Research: Solid Earth, 109, 233, https://doi.org/10.1029/2003JB002586, 2004.

Yale, D. P.: Fault and stress magnitude controls on variations in the orientation in situ stress, in: Fracture and in-situ stress characterization of hydrocarbon reservoirs, edited by: Ameen, M. S., Geological Society of London, London, 55–64, https://doi.org/10.1144/GSL.SP.2003.209.01.06, 2003.

Yukutake, Y., Takeda, T., and Yoshida, A.: The applicability of frictional reactivation theory to active faults in Japan based on slip tendency analysis, Earth and Planetary Science Letters, 411, 188–198, https://doi.org/10.1016/j.epsl.2014.12.005, 2015.

Zang, A. and Stephansson, O.: Stress Field of the Earth's Crust, Springer Netherlands, Dordrecht, 322 pp., 2010.

Ziegler, M. and Heidbach, O.: Manual of the Matlab Script Stress2Grid v1.1, 2019a.

Ziegler, M. O.: Python Script HIPSTER v1.3, GFZ Data Services [code], 2021.

Ziegler, M. O. and Heidbach, O.: The 3D stress state from geomechanical–numerical modelling and its uncertainties: a case study in the Bavarian Molasse Basin, Geothermal Energy, 8, https://doi.org/10.1186/s40517-020-00162-z, 2020.

Ziegler, M. O. and Heidbach, O.: Matlab Script Stress2Grid v1.1, GitHub [code], 2019b.

Ziegler, M. O., Ziebarth, M., and Reiter, K.: Python Script Apple PY v1.0, GFZ Data Services [code], 2019.

Ziegler, M. O., Heidbach, O., Reinecker, J., Przybycin, A. M., and Scheck-Wenderoth, M.: A multi-stage 3-D stress field modelling approach exemplified in the Bavarian Molasse Basin, Solid Earth, 7, 1365–1382, https://doi.org/10.5194/se-7-1365-2016, 2016.

Ziegler, P. A. and Dèzes, P.: Crustal evolution of Western and Central Europe, Geological Society, London, Memoirs, 32, 43–56, https://doi.org/10.1144/GSL.MEM.2006.032.01.03, 2006.

Zienkiewicz, O. C., Taylor, R. L., and Zhu, J. Z.: The Finite Element Method: its Basis & Fundamentals, 7th, Elsevier, 714 pp., 2013.

Zoback, M. D. and Healy, J. H.: Friction, faulting, and 'in situ' stress, International Journal of Rock Mechanics and Mining Sciences & Geomechanics Abstracts, 22, 119, https://doi.org/10.1016/0148-9062(85)93053-0, 1985.

Zoback, M. D.: Reservoir Geomechanics, Cambridge University Press, Cambridge, 449 pp., 2007.

Zoback, M. D. and Healy, J. H.: In situ stress measurements to 3.5 km depth in the Cajon Pass Scientific Research Borehole: Implications for the mechanics of crustal faulting, J. Geophys. Res., 97, 5039, https://doi.org/10.1029/91JB02175, 1992.

Zoback, M. L.: First- and second-order patterns of stress in the lithosphere: The World Stress Map Project, J. Geophys. Res.-Sol. Ea., 97, 11703–11728, https://doi.org/10.1029/92JB00132, 1992.

Zulauf, G.: Brittle deformation events at the western border of the Bohemian Massif (Germany), Geol Rundsch, 82, 489–504, https://doi.org/10.1007/BF00212412, 1993.